

SLAC-185  
UC-34a

ABSTRACT

ELECTRON SCATTERING OFF HYDROGEN AND DEUTERIUM  
AT 50° AND 60° \*

WILLIAM BRADFORD ATWOOD  
STANFORD LINEAR ACCELERATOR CENTER  
STANFORD UNIVERSITY  
Stanford, California 94305

PREPARED FOR THE  
U.S. ENERGY RESEARCH AND DEVELOPMENT ADMINISTRATION  
UNDER CONTRACT NO. E(04-3)-515

June 1975

The inelastic scattering of electrons for both protons and neutrons has been measured at scattering angles of fifty and sixty degrees and for incident energies between 6.5 GeV and 19.5 GeV. Elastic scattering from protons was also observed. The measurements were made at the Stanford Linear Accelerator Center using the 1.6-GeV spectrometer located in End Station A. The experimental techniques used in making the measurements are detailed. The resulting cross sections are large, indicative of a charged point-like substructure within the nucleon and match the extrapolation from previous measurements to the new kinematic region to within forty percent. The measurements are found to be compatible with some existing theoretical expectations. The  $W_1$  structure function is not found to "scale" in previously suggested scaling variables. The introduction of propagator scale breaking is investigated and shown to be compatible with the measurements. An alternative scaling variable is proposed in which  $W_1$  is found to scale. The elastic scattering measurements are consistent with an inverse fourth power dependence on four-momenta transfer. The measured neutron-proton ratio is in agreement with previous measurements.

Printed in the United States of America. Available from National Technical Information Service, U.S. Department of Commerce, 5285 Port Royal Road, Springfield, Virginia 22161. Price: Printed Copy \$7.50; Microfiche \$1.45.

\* Ph.D. Dissertation.

Dedicated to my father, William Faulkner Atwood, who  
awakened within me an interest in the physical sciences.

#### ACKNOWLEDGMENTS

The person who had the greatest influence on this work was my advisor, Professor Richard E. Taylor of SLAC. Under his guidance, I was exposed to almost all the aspects of the high energy experimental physics business including proposal writing, equipment design and construction, scheduling and running the experiment, data analysis and interpretation and formal presentation of the data. Dick allowed me much freedom to pursue the experiment as I wished, making available to me many of the resources that SLAC has to offer. Dick has taught me to question the fundamental notions we are investigating and how our discoveries fit into the overall theoretical framework from which we perceive the world. But, more than fulfilling the formal role as advisor, he has become a trusted and dear friend upon whom I have relied heavily during the trying times of the past five years. I am truly grateful for having the good fortune to have Dick Taylor as my advisor.

I wish to express my appreciation of the major contributions Hobey DeStaebler made to E-89. Hobey has, by example, taught me the power of facts and logical argument to dispel mysteries. I am grateful to Hobey for always being willing to listen to my ideas calmly and thoughtfully, no matter how crazy they were.

The construction of the two principal counters for the 1.6 (the gas Cerenkov counter and lead glass TA) was accomplished by D. Trines, G. Johnson and myself. The three of us worked closely together for one and one-half years, and their contributions to the success of the experiment are numerous.

Leon Rochester and I performed the data analysis. His efforts resulted in our understanding many subtle features of the equipment, and

he eliminated many "mysterious effects." I also sincerely thank Leon for his careful perusal of this manuscript.

I gratefully acknowledge the rest of Group-A at SLAC, including C. Y. Prescott, S. Stein, R. L. A. Cottrell, E. D. Bloom and, in particular, my office-mate M. Mestayer, all of whom were involved in the planning, designing and running of E-89. Connie Logg deserves special recognition for her wonderful computer programs with which the radiative corrections and smearing corrections were done. Sunnie Sund and Ken Eymann's help in organizing the data tapes and initial off-line analysis is gratefully acknowledged. Thanks are due E. Allton for many discussions and clever computer programs with which to calculate various radiation processes.

Many thanks are due Mary Lou Arnold for typing this manuscript. I express my gratitude to Pamala Barbour Klundt for typing Chapter V and struggling through innumerable corrections, making it possible for me to make the deadline.

Finally, I wish to express my sincere thanks to my ex-wife, Marilyn Corbeille for her loyalty, honesty and the home she made and provided for me during most of my stay at Stanford.

## TABLE OF CONTENTS

CHAPTER I	-	Introduction . . . . .	Page 1
		First Remarks on Phenomenology.	Page 4
		The Experiment . . . . .	Page 12
		Chap. I References. . . . .	Page 19
CHAPTER II	-	Overview of the Experiment. . .	Page 22
		The Beam . . . . .	Page 24
		Beam Monitors . . . . .	Page 32
		The Target . . . . .	Page 33
		The 1.6 Spectrometer . . . . .	Page 43
		Counter Package . . . . .	Page 48
		Electronics . . . . .	Page 54
		Chap. II References . . . . .	Page 63
CHAPTER III	-	Electron Counting and Experimental Corrections . . .	Page 64
		Pulse Height Analysis . . . . .	Page 66
		Tracking and Codes . . . . .	Page 80
		Accidentals . . . . .	Page 85
		Over One Correction . . . . .	Page 85
		Event Binning . . . . .	Page 86
		Run Weeding . . . . .	Page 88
		Testing the Analysis Procedure .	Page 89
CHAPTER IV	-	Measured Corrections . . . . .	Page 93
		Calculated Corrections . . . . .	Page 97

TABLE OF CONTENTS (continued)

	Elastic Tail Subtraction . . . . .	Page 97
	Inelastic Radiative Corrections. . . . .	Page 100
	Smearing Corrections . . . . .	Page 105
	The Extraction of $W_1$ . . . . .	Page 107
	Summary of Systematic Errors . . . . .	Page 110
	Table IV-4 - Final Cross Sections . . . . .	Page 114
	Chap. IV References . . . . .	Page 124
CHAPTER V -	Introduction . . . . .	Page 125
	Elastic Scattering . . . . .	Page 127
	The $W_1$ Structure Function of the Proton . . . . .	Page 131
	The Proton Cross Sections for $W < 2.0$ GeV . . . . .	Page 144
	Neutron/Proton Comparison . . . . .	Page 144
	Summary of the Physics Results . . . . .	Page 148
	Chap. V References . . . . .	Page 151
APPENDIX A -	The Cerenkov Counter . . . . .	Page 153
	Appendix A References . . . . .	Page 160
APPENDIX B -	Design Considerations for Lead Glass Shower Counters . . . . .	Page 161
	Appendix B References . . . . .	Page 178
APPENDIX C -	A Quasi-Elastic Approach to Smearing . . . . .	Page 179
	Appendix C References . . . . .	Page 192

TABLE OF CONTENTS (continued)

APPENDIX D -	Wire Orbit of the 1.6 GeV Spectrometer . . . . .	Page 193
	Appendix D References . . . . .	Page 211

## LIST OF TABLES

I - 1	Data acquisition chronology.	Page 17
II - 1	Summary of beam parameters and errors	Page 34
II - 2	Summary of radiators for the 1.6 GeV spectrometer for before and after the center of the target.	Page 38
II - 3	Density reduction from vapor bulb pressure for the average density.	Page 41
II - 4	Gross counter properties for the 1.6 instrument package.	Page 51
III - 1	Analysis scheme - a summary of the 4 passes over the data to produce final cross sections.	Page 65
III - 2	A 4 x 4 x 4 x 4 matrix showing various cut effects for TAL, CT, MULT and TFT. For each cut combination the two entries are 1) electron detection efficiency and 2) pion contamination.	Page 79
III - 3	Cut definitions of the six PHS classes used in the analysis.	Page 81
III - 4	Hodoscope codes, first entry is the fraction of electrons, second entry $\pi/e$ ratio (counts < 95 TASUM/counts > 95 TASUM).	Page 84
III - 5	Hodoscope code classes; class 6 are the cleanest events (one slat in each hodoscope); class one are the "Z00" events. The data were analyzed using code classes 4, 5 and 6.	Page 84
III - 6	Table of cross sections relative to the analysis class for the six code classes and six PHS's classes.	Page 90
IV - 1	The functional forms and parameters used to make the empty target and positron corrections. Also given are the $\chi^2$ for the fits.	Page 95

## LIST OF TABLES (continued)

IV - 2	A summary of the point-to-point systematic error contributions to the data.	Page 111
IV - 3	A summary of the overall systematic errors.	Page 112
IV - 4	The final cross sections and $W_1$ structure functions for P, D and N measured at 50° and 60°. The neutron error includes all the deuterium errors as well as the error from unsmearing and smeared proton subtraction.	Page 114
V - 1	The final elastic cross sections for 50° and 60°.	Page 130
V - 2	Various functions fit to the elastic data with parameters and $\chi^2$ . The minimum error was taken to be $\pm 2.5\%$ of the cross section.	Page 133
V - 3	Functions fit to the data with $W > 2.0$ GeV using different values of R. Only statistical counting errors were used in evaluating $\chi^2$ .	Page 138
V - 4	The measured N/P ratios for 50° and 60°. The systematic errors include target uncertainties and smearing errors.	Page 147

## LIST OF TABLES

A - 1	Some physical properties of several gases considered for filling the gas Cerenkov counter.	Page 156
B - 1	Some physical properties of various commercial lead glasses.	Page 164
B - 2 a,b,c	The charge particle path length, $\bar{\tau}$ , for shower particles with more than 1 MeV of energy. Table entries are the fraction of $\bar{\tau}$ contained inside the boundaries of that shower bin $\pm$ the RMS deviations of $\bar{\tau}$ for that bin.	Page 169
C - 1	Definition of the variables used in the equations of Appendix C.	Page 181
D - 1	Definitions of co-ordinates used by their index number, Group A and Group F.	Page 197
D - 2	Optics coefficients to transform input variables to the counter cave variables.	Page 200
D - 3	Optics coefficients to transform counter cave co-ordinates to the input variables.	Page 201
D - 4	Error estimates in the optics coefficients and offsets.	Page 203

## LIST OF FIGURES

I - 1	Feynman diagram of single photon exchange for $e + p \rightarrow e' + X$ and laboratory schematic of the same process.	Page 5
I - 2	Kinematic region in $W^2$ and $Q^2$ of the measurements at $50^\circ$ and $60^\circ$ .	Page 13
I - 3	$\epsilon$ contours (curved lines) for $60^\circ$ and $\eta'$ contours overplotted on the kinematic region of the data.	Page 15
II - 1	The beam transport system from the accelerator to End Station-A.	Page 25
II - 2	Photographs of closed circuit T.V. monitors for the three zinc sulfide screens RS1, RS2 and RS3.	Page 28
II - 3	Photograph of oscilloscope traces of the "good" spill counter (lower trace) and the "bad" spill counter (upper trace).	Page 30
II - 4	Photograph of target assembly	Page 35
II - 5	Schematic of the target showing the circulation path and driving fan.	Page 36
II - 6	Scatter plots of hydrogen and deuterium liquid densities versus beam current.	Page 40
II - 7	1.6 GeV spectrometer schematic	Page 44
II - 8	Counter array used to detect electrons in the 1.6 counter cave. The Pb glass hodoscope, pre-radiator, TA1 and TA2 formed the total absorption counter.	Page 49
II - 9	Pulse height distribution of the sum of the two photomultiplier signals from the Cerenkov counter. The kinematics correspond to elastic scattering off hydrogen.	Page 53
II - 10	Pulse height distribution of hardware sum of signals from TA package. The kinematics correspond to elastic scattering off hydrogen.	Page 55

## LIST OF FIGURES (continued)

II - 11	A schematic diagram of the fast electronics used for the 1.6.	Page 58
III - 1	Pulse height analysis flow chart.	Page 68
III - 2	The six PHS's used in the analysis.	Page 72
III - 3	Scatterplot of TFT versus TAl for a) deuterium run at $E_0 = 19.5$ GeV, $\theta = 60^\circ$ , $E' = 1.196$ GeV. (This setting had the largest $\pi/e$ ratio, $\approx 2500:1$ ). b) elastic scattering off hydrogen for $E_0 = 1.5$ GeV, $\theta = 50^\circ$ , $E' = .96$ GeV.	Page 73
III - 4	Scatterplot of CT versus TASUM for the same data shown in Fig. III-3 after the TFT and TAl cuts have been applied. Again a) is deuterium for $E_0 = 19.5$ GeV, $\theta = 60^\circ$ and $E' = 1.196$ . b) elastic scattering off hydrogen for $E_0 = 1.5$ GeV, $\theta = 50^\circ$ and $E' = .96$ GeV.	Page 75
III - 5	A plot of TASUM before and after the TFT, TAl and CT cuts have been applied.	Page 76
III - 6	Plot TASUM showing cut position, $x_c$ , and fits used to estimate the electron detection efficiency and the pion subtraction factor.	Page 77
III - 7	Hodoscope hit patterns and codes.	Page 83
III - 8	Hodoscope distributions.	Page 87
III - 9	A histogram of the residuals $R_{ij}$ . The curve is what one expects normally distributed data to give.	Page 92
IV - 1	The elastic radiative tail fraction for representative lines at $50^\circ$ and $60^\circ$ . The arrows at the top of the graph indicate where a missing mass, $W$ , of 2.5 GeV falls for $E_0 = 6.5, 13.3$ and 19.5 GeV at $60^\circ$ and $W = 2.5$ for $E_0 = 7.0$ GeV and $W = 3.5$ for $E_0 = 19.5$ GeV at $50^\circ$ .	Page 99

## LIST OF FIGURES (continued)

IV - 2	Logic flowchart for the radiative correction procedure.	Page 102
IV - 3	The radiative correction ratios for representative incident energies at $50^\circ$ and $60^\circ$ . The ratios are plotted for $W > 1.75$ GeV.	Page 104
IV - 4	Logic flowchart for the unsmearing procedure.	Page 108
IV - 5	The smearing ratios ( $\sigma_{\text{model}}/\sigma_{\text{model smeared}}$ ) for the neutron, $S_N$ , and the proton, $S_P$ .	Page 109
V - 1	The measured elastic peak cross sections off hydrogen and the empty target cross sections for $Q^2 = 21.8$ GeV <sup>2</sup> and 33.4 GeV <sup>2</sup> .	Page 129
V - 2	A plot of $Q^4 G_M^S/\mu_p$ versus $Q^2$ . The dashed line is the dipole fit and the solid line is the ad hoc fit.	Page 132
V - 3	$2MW_1$ (for $R = .18$ ) plotted versus $x'$ . The lines indicate the predicted values of $2MW_1$ for $E_0 = 6.5$ GeV and $E_0 = 19.5$ GeV.	Page 135
V - 4	The $2MW_1$ data interpolated to fixed values of $x'$ (indicated on the right) plotted against $Q^2$ .	Page 136
V - 5	$\nu R$ extracted from the data (assuming $\nu W_2$ given by Eq. 5.4) plotted against $Q^2$ for various values of $x'$ .	Page 140
V - 6	a) $2MW_1/(1-x_s)^4$ plotted against $Q^2$ . b) $2MW_1/(1-x_s)^4$ plotted versus $x_s$ . The lines indicated what the third (solid line) and the fifth powers (dashed line) would look like.	Page 143
V - 7	The slope in $Q^2$ for fixed values of the scaling variable for values of $M_S^2 = 0, M^2$ , and 1.42. The poor $\chi^2$ for $M_S^2 = 0$ and $M^2$ indicate that the $Q^2$ dependence is not well parameterized by a straight line.	Page 145

## LIST OF FIGURES (continued)

V - 8	Resonance region data for $6.9 \text{ GeV}^2 < Q^2 < 9.2 \text{ GeV}^2$ .	Page 146
V - 9	The N/P ratio plotted versus $x'$ .	Page 149
A - 1	A layout of the isobutane threshold gas Cerenkov counter used in E-89.	Page 154
B - 1	Transmission curves for lead glass types 1a, 2, 3, 4, 5a (see Table B-1). Dashed lines and right-hand scale show AVP and DVP photocathode response.	Page 165
B - 2a	Number of photons produced from a 1 GeV electron shower and transmitted through a $16 \chi_0$ long counter.	Page 166
2b	Number of photoelectrons expected for a 1 GeV shower for various glass types. No light collection efficiency has been included in the calculation.	Page 166
B - 3 a & b	Fractional containment of showers for 1, 2, 5, 10 and 20 GeV incident electrons versus a) counter length and b) counter radius.	Page 172
B - 4 a & b	Shower fluctuations for 1, 2, 5, 10 and 20 GeV incident electrons versus a) counter length and b) counter width.	Page 173
B - 5	Calculated RMS resolution for a lead glass counter (see text) using 20% light collection efficiency.	Page 174
B - 6	Plot of $\bar{r}$ versus cosine of its angle from particle's direction for 1, 10 and 20 GeV electrons.	Page 176
C - 1	Feynman diagram of electron-deuterium scattering in the impulse approximation.	Page 180
C - 2 a & b	Graphs of the convolution function $\Gamma_\omega$ for input $\omega$ 's of a) 1.2 and b) 2.2 for various values of $Q^2$ .	Page 187
C - 2 c & d	Graphs of the convolution function $\Gamma_\omega$ for input ( $\omega'$ )'s of a) 1.2 and b) 2.2 for various values of $Q^2$ .	Page 187

## LIST OF FIGURES (continued)

C - 3 a & b	The convolution function $\Gamma_W$ for input $W$ 's of a) 1.5 GeV and b) 2.5 GeV for various values of $Q^2$ .	Page 188
C - 4	The function $\Gamma_{p_s}$ shows where the contributions to smearing come from in the squared momentum wave function.	Page 190
D - 1	Definitions of the various co-ordinate systems used to describe the 1.6 GeV spectrometer optics.	Page 195
D - 2 a,b,c,d	Histograms of the residuals for the fits to the optics coefficients. The mean, $\mu$ , and RMS deviations, $\sigma$ , of each histogram is shown.	Page 204
D - 3	Calculated resolutions of the optics for the 1.6 using the fitted optics coefficients and hodoscope bin widths.	Page 205
D - 4	Calculated values of $p_{0c}$ for various values of $(1/\text{tension})_0$ .	Page 208
D - 5	The limiting apertures of the 1.6 GeV spectrometer for a) $\phi_i$ (vertical projected scattering angle) versus $\delta$ (deviation in momentum from the central ray), b) $X_i$ (target length) versus $\theta_i$ (horizontal projected scattering angle).	Page 209



CHAPTER I  
INTRODUCTION

Particle scattering experiments done by Rutherford (Ref. I-1) foreshadowed the development of particle physics. The use of this technique has grown immensely during this century and has become a major source of information about the structure of the world on the scale of atoms and nuclei. Rutherford's low energy alpha particles allowed him to "see" atomic structure, revealing the presence of a charged point-like core, the nucleus. Hofstadter and co-workers during the 1950's performed similar experiments (Ref. I-2) replacing the low energy alpha particles with a high energy electron beam.

In both experiments the fundamental interaction used to probe the target structure was electromagnetism. Due to the comparatively weak coupling of photons to charged particles (characterized by a coupling constant  $\alpha = 1/137$ ), this type of probe can pass unaffected deep inside a target particle. The electron, believed to be a point-like charged particle, interacts with matter primarily through electromagnetism and does not participate in strong interactions (characterized by a coupling constant of approximately 15), hence the problem of strong interactions masking substructure is not present. Rutherford could not have successfully examined nuclear structure, because strong interaction between the alpha particles and the nucleus would not allow these projectiles to penetrate. The alpha particle proved adequate for examining atomic structure where the nucleus can be regarded as a point-like object on the scale of atomic dimensions.

For scattering at a fixed angle, raising the energy of the incident particle decreases the distance of closest approach to the target particle. Thus, increasing the energy of the probe may reveal structure inside the target on a smaller distance scale. Point-like charged particles are the most effective targets to scatter incident electrons (or muons) via electromagnetic interactions. Deviation from a point-like target is discussed in terms of the form factor which has a value of one for point-like particles and is in general smaller for more tenuous charge distributions. In an impressive series of experiments, Hofstadter and his co-workers found that nuclei have a finite size roughly determined by the number of nucleons contained, and that the charge distribution inside the nucleus was nearly uniform. But, perhaps, the most remarkable observation was that the proton itself was not a simple point-like object. It, too, displayed an internal structure giving rise to an elastic form factor decreasing from unity rapidly as the momentum transfer to the proton was increased (Ref. I-3).

With the completion of SLAC in the late 1960's, electron energies up to 20 GeV became available to continue this exploration. The first experiments using electrons to probe nucleons at SLAC examined elastic scattering at higher energies. The inability of the proton to elastically scatter high energy electrons to large angles persisted with much the same dependence on momentum transfer as observed at lower energies (Ref. I-4).

At incident electron energies in the GeV range, the proton can be excited inelastically, as well as scattering elastically, resulting in the production of many new particles such as  $\pi$  mesons. A big surprise came in the discovery that this inelastic cross section was very large (Ref. I-5). As the elastic cross section died away with increasing momentum transfer, the relative inelastic cross section increased. The total scattering strength at a fixed angle and incident energy of all inelastic states was quite large and suggested the existence of a substructure of charged point-like constituents within the nucleon that was responsible for the total scattering strength of this system. Models of nucleon structure based on point-like constituents suggest that the data should exhibit a "scaling" phenomenon explaining the inelastic form factor's constancy with respect to momentum transfer (Ref. I-6). Other models also offer explanations of the scaling behavior of the inelastic form factor (Ref. I-7).

Later experiments included electron-deuteron scattering as well as continuing the electron proton scattering program. The objective here was to compare the neutron to the proton in the inelastic region. The deuteron cross sections showed that the neutron inelastic form factor "scaled" like that of the proton (Ref. I-8). Again the possible presence of a substructure revealed itself. Although the neutron/proton cross section ratio scaled, it showed a nontrivial dependence on the scaling variable. In particular  $N/P \leq 1$  everywhere. The inelastic electroproduction cross sections were not merely diffractive

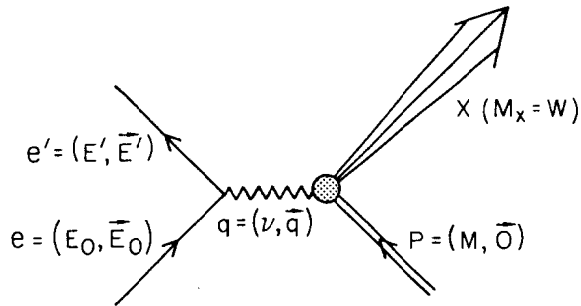
scattering of virtual photons off the target nucleon.

The present work continues the investigation of electron nucleon scattering, both elastic and inelastic, to large scattering angles and extends the kinematic range of the data near the boundary imposed by a maximum incident beam energy of 20 GeV. The experiments are in principle very simple. An electron beam of measured energy,  $E_0$ , and flux is directed onto a liquid hydrogen (or deuterium) target. Detectors are set up to count the number of electrons scattered as a function of the deflection angle,  $\theta$ , and scattered energy,  $E'$ . In practice the experiment becomes increasingly difficult as the angle  $\theta$  is increased, for two reasons. First (as Rutherford could have told us!) the cross section quickly becomes small. At  $50^\circ$  and  $60^\circ$  the typical size is  $10^{-35} \text{ cm}^2$  per GeV per steradian at SLAC energies. Second, the background of particles other than scattered electrons produced by the beam striking the target increases with respect to the signal.

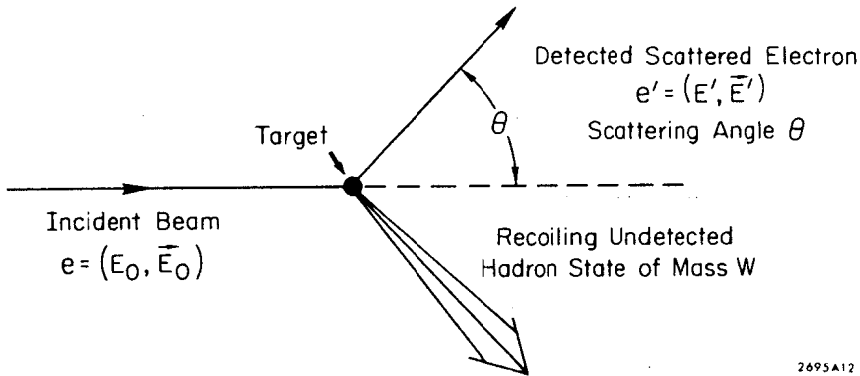
#### FIRST REMARKS ON PHENOMENOLOGY

The canonical diagram used to describe the inelastic electron scattering process is shown in Fig. I-1. The electric current  $e \rightarrow e'$  is the source of a virtual photon,  $\gamma$ , of measured energy and momentum. The photon couples to the target (initially at rest in the laboratory) producing a recoiling final state of mass  $W$ . Due to the weakness of the electromagnetic coupling, the single photon exchange is believed to dominate as higher order processes (two or more photon exchanges) would be weaker still at each order by the coupling constant.

FEYNMAN DIAGRAM OF SINGLE PHOTON EXCHANGE



LABORATORY SCHEMATIC



2695A12

FIG. I-1

Feynman diagram of single photon exchange for  $e + p \rightarrow e' + X$  and laboratory schematic of the same process.

Experiments indicate that the general angular dependence of the observed cross sections is what one expects for the single photon exchange mechanism. The observation that the cross section is independent of the sign of the charge of the incident electron provides more confirmation that two photon exchange mechanisms are suppressed (Ref. I-9).

The relativistic invariants used to describe the target vertex are:

$$-q^2 = Q^2 = -(e_\mu - e'_\mu)^2 = 4 E_0 E' \sin^2 \theta/2$$

$$P \cdot q = M\nu = M(E_0 - E')$$

$$W^2 = M^2 + 2M\nu - Q^2$$

Following the standard prescriptions of quantum electrodynamics the matrix element describing the one photon exchange process is

$$m = i\sqrt{\alpha} \bar{e} \gamma_\mu e \frac{1}{q^2} J_\mu$$

where  $J_\mu = \sqrt{\alpha} \sum_{i,f} \langle f | j_\mu | i \rangle$  is the electric current within the hadron ( $i, f$  signify initial and final states). The electric current of the incoming and outgoing electron when squared in the matrix element (averaged over initial spin states and summed over final spin states) yields the tensor:

$$k_{\mu\nu} = (e_\mu e'_\nu + e'_\mu e_\nu - \delta_{\mu\nu} e \cdot e')$$

This tensor is contracted against a  $W_{\mu\nu}$  tensor describing the photon-target coupling. A general Lorentz covariant formulation for  $W_{\mu\nu}$  (again only the symmetric part remains after summing over spin states) assuming one photon exchange and gauge invariance is

$$W_{\mu\nu} = -W_1 \left( \delta_{\mu\nu} - \frac{q_\mu q_\nu}{q^2} \right) + \frac{W_2}{M^2} \left( P_\mu - \frac{P \cdot q}{q^2} q_\mu \right) \left( P_\nu - \frac{P \cdot q}{q^2} q_\nu \right)$$

The squared matrix element resulting from contracting these two tensors yields the cross section:

$$\frac{d\sigma}{d\Omega dE'} = \sigma_{\text{Mott}} \left( W_2 + 2 \tan^2 \theta/2 W_1 \right)$$

where

$$\sigma_{\text{Mott}} = \frac{\alpha^2 \cos^2 \theta/2}{4 E_0^2 \sin^4 \theta/2}$$

An analysis of the cross section in terms of photon polarization,  $\epsilon_\mu$ , parallel and perpendicular to  $\vec{q}$  is instructive (Ref. I-10). The total photoabsorption cross section is proportional to  $\epsilon_\mu \epsilon_\nu W^{\mu\nu}$ . Gauge invariance requires  $\epsilon_\mu q^\mu = 0$ . Choosing  $\vec{q}$  along the z-direction, the two polarization cases are:

TRANSVERSE:  $\epsilon_z = \epsilon_t = 0$ . Both  $q$  and  $P$  are perpendicular to  $\epsilon_\mu$ . All terms in  $W_{\mu\nu}$  containing either  $P$  or  $q$  vanish. Only  $W_1$  remains.

$$\sigma_t = \frac{4\pi^2 \alpha}{K} W_1$$

where  $K = (W^2 - M^2) / 2M$

is the energy of an equivalent on mass-shell photon to produce the final mass state  $W$ .

LONGITUDINAL:  $\epsilon_z = v / \sqrt{Q^2}$ ,  $\epsilon_t = q / \sqrt{Q^2}$ , only  $\epsilon_\mu q^\mu = 0$

Terms in  $W_1$  and  $W_2$  are both present.

$$\sigma_s = \frac{4\pi^2 \alpha}{K} \left( W_2 \left( 1 + \frac{v^2}{Q^2} \right) - W_1 \right)$$

Often the  $\sigma_s$  and  $\sigma_t$  contributions are discussed in terms of  $\sigma_s/\sigma_t$ . Simple substitutions into the previous cross section expression gives

$$\frac{d\sigma}{d\Omega dE'} = \Gamma_t \left( \sigma_t + \epsilon \sigma_s \right)$$

where  $\epsilon = 1 / (1 + 2 \tan^2 \theta/2 (1 + v^2/Q^2))$

is the photon polarization parameter and

$$\Gamma_t = \frac{\alpha}{4\pi^2} \frac{2KE'}{Q^2 E_0 (1 - \epsilon)}$$

is interpreted as the effective flux of virtual photons. Dividing this photon flux factor into the data yields a total virtual photoabsorption cross section,  $\sigma_t + \epsilon \sigma_s$ . These cross sections then are plotted versus  $\epsilon$  for fixed  $W$  and  $Q^2$ . As the range of  $\epsilon$  is  $0 \rightarrow 1$  the intercepts of a straight line fit yield  $\sigma_t$  and  $\sigma_t + \sigma_s$  respectively. Increasing the spread of the data in  $\epsilon$  for fixed  $W$  and  $Q^2$  makes possible more accurate the extraction of  $\sigma_s$  and  $\sigma_t$  (or equivalently  $W_1$  and  $W_2$ ). Large angle data populates very small values of  $\epsilon$  ( $50^\circ$  and  $60^\circ$  have  $\langle \epsilon \rangle = .12$  for the incident energy range of 6-20 GeV). Previous electroproduction data in the deep inelastic region covered  $\epsilon = .3$  to  $\epsilon = .9$ , and usually for any given  $W$  and  $Q^2$  the spread in  $\epsilon$  was considerably less than 0.5.

Much confidence in a model of the nucleon based on a substructure composed of point-like particles, called partons, is founded on the scaling behavior of the deep inelastic data (Ref. I-11). Scaling

means that the structure functions,  $W_1$  and  $\nu W_2$ , depend only on the ratio  $2M\nu/Q^2$  as  $\nu$  and  $Q^2$  both get "large." This behavior has a simple interpretation within the parton model, namely quasi-elastic scattering off point-like constituents. Most "proofs" of scaling in the parton model set  $W_{\mu\nu}$  for the parton (and thus for the fundamental interaction) proportional to a delta function,  $\delta((p+q)^2 - m^2)$ , to impose the quasi-elastic constraint. The assumption is made that the parton carries a fraction  $x$  of the nucleon's momentum. This assumption is formulated as  $p = xP$ , and it should become more valid as the energies in the problem get large compared to mass terms. Integrating over the parton distribution function  $f(x)$  ( $f(x) dx =$  no. of partons between  $x$  and  $x + dx$  each weighted by its  $(\text{charge})^2$ ) yields the following three conclusions:

- 1)  $x = Q^2/2M\nu$  and  $\omega = 1/x$
- 2)  $\nu W_2 = xf(x)$  for both spin 0 partons and for spin  $\frac{1}{2}$  partons
- 3)  $2M W_1 = f(x)$  for spin  $\frac{1}{2}$  partons  
 $= 0$  for spin 0 partons

In the parton model  $W_1$  measures the spin  $\frac{1}{2}$  parton distribution (assuming no spin 1 partons) as transversely polarized photons do not couple to spin 0 particles. On the other hand,  $\nu W_2$  measures the distribution in  $x$  of spin  $\frac{1}{2}$  and spin 0 partons. Scaling is observed in  $x$  for  $\nu W_2$  to about  $\pm 10\%$  over a dynamic range of about 1000 in the size of  $\nu W_2$  (Ref. I-12). The kinematic region where this phenomenon is observed to begin occurs at relatively low energies,  $Q^2 > 1.5 \text{ GeV}^2$  and  $W > 2.5 \text{ GeV}$ .

The phenomenological lore of scaling starts from the variable  $x$  introduced by J. D. Bjorken (Ref. I-6). Later, Bloom and Gilman suggested a modified scaling variable  $\omega' = \omega + M^2/Q^2$  (Ref. I-13). Holding a scaling variable fixed while allowing  $W$  and  $Q^2$  to vary traces out contours in the  $W^2$  vs.  $Q^2$  plane. Constant  $x$  contours are straight lines all intersecting at  $Q^2 = 0$  and  $W = M$ . Photo-production occurs at  $x = 0$ , and all elastic scattering lies along  $x = 1$ . The  $x'$  ( $1/\omega'$ ) variable produces contours which are also straight lines all intersecting at  $W^2 = Q^2 = 0$ . Elastic scattering does not occur at fixed  $x'$  as it does in  $x$ . This allows for the connection of the inelastic to the elastic in a natural way (for  $\nu W_2 \propto (1-x')^n$  we have  $W_2(\text{el}) \propto 1/(Q^2)^{n+1}$  which is the Drell-Yan-West relation (Ref. I-14)). The data when plotted in  $x'$  exhibits more "precocious" scaling than when plotted against  $x$ , extending the scaling region down to  $Q^2 > 1 \text{ GeV}^2$  and  $W > 2 \text{ GeV}$ .

For scaling to begin at such low energies was a puzzle. Nothing in the parton theories sets an absolute energy scale. As no one has yet produced or observed a free parton in the laboratory, one might conclude that partons must be very massive objects bound extremely tightly inside the nucleon. The neglected mass terms in the traditional scaling derivation could then be important.

Recently it has been demonstrated experimentally (Ref. I-15) that the connection to photoproduction can be achieved through a "closure approximation" stolen from nuclear physics (Ref. I-16).

$$\nu W_2 = (1 - W_2(\text{el})) F_2(\omega')$$

where

$$W_2(e1) = (G_E^2 + \tau G_M^2) / (1 + \tau), \quad \tau = Q^2 / 4M^2$$

and  $G_E$  and  $G_M$  are the electric and magnetic form factors of the proton.

$F_2(\omega')$  is the scaling function using the  $\omega'$  variable.

The above factorization yields the original Gottfried (Ref. I-17) sum rule:

$$\int W_2 d\nu = (1 - W_2(e1)) \sum_i Q_i^2$$

where the  $Q_i$  are the parton charges.

This sum rule is a formulation of the transition that a many particle system makes going from the region where elastic scattering dominates (coherent scattering) to the region where scattering off the constituents is most important (incoherent scattering). The sum rule saturates quickly with increasing  $Q^2$  (at  $Q^2 = 1 \text{ GeV}^2, (1 - W_2(e1)) = .925$ ) and sets a reasonable energy where scaling phenomena (scattering off individual partons) should become important.

Recently some theorists predicted scale breaking should become important rapidly just beyond the measured kinematic region (Ref. I-18). This scale breaking was to arise from the form factors of the partons themselves. We shall return to this question in some detail in Chapter V.

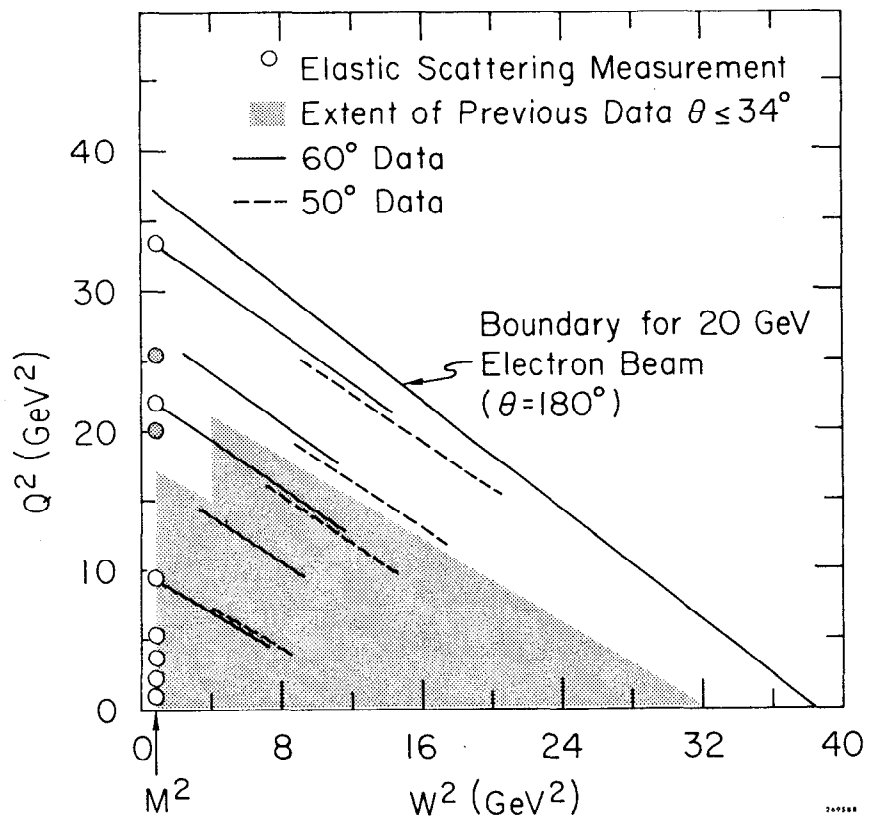
Neutron-proton comparisons provide further tests of theories. The Gottfried sum rule interprets the integral of the structure function as the sum of the squares of the charges of the nucleon's constituents at high  $Q^2$ . In a popular version of the parton model, the quark model of Gell-Mann and Zweig (Ref. I-19) there are 3 quarks

within a nucleon. The proton has two p quarks of charge +2/3 and one n quark of charge -1/3. The neutron has one p quark and two n quarks. The charge-squared sum rule evaluated over the available data (Ref. I-15) has a value of about 1.05 for the proton and .85 for the neutron giving approximately the correct ratio for this simple fractionally-charged-quark model. The N/P ratio as a function of  $x$  should not go below 1/4 as  $x \rightarrow 1$  for parton models. Bloom and Gilman predict  $N/P \rightarrow (\mu_N / \mu_P)^2$  as  $x \rightarrow 1$ . Unfortunately the neutron picture is complicated, particularly near  $x = 1$ , due to the neutron cross section's extraction from deuterium data. (Appendix C covers the Fermi motion problem in some detail.) The present data extend the N/P measurement to high  $Q^2$  in the small  $\omega$  region and slightly increases the measured region in  $\omega$  (see Chp. V).

#### THE EXPERIMENT

The experiment (officially called E-89) was a double spectrometer experiment (the spectrometers were not run in coincidence). The two spectrometers were the 1.6-GeV spectrometer and the 20-GeV spectrometer. Both instruments are located in End Station A at SLAC. In the experiments, the two spectrometers shared the same beam and target with the 1.6-GeV spectrometer taking data at  $50^\circ$  and  $60^\circ$  and the 20-GeV spectrometer taking data at a variety of angles from  $6^\circ$  to  $20.6^\circ$ . This thesis is concerned with the 1.6-GeV spectrometer measurements at the large angles; the 20-GeV spectrometer experiment is described elsewhere (Ref. I-20).

Figure I-2 is a  $W^2$  vs.  $Q^2$  diagram depicting the kinematic range



Kinematic region in  $W^2$  and  $Q^2$  of the measurements at  $50^\circ$  and  $60^\circ$ .

FIG. I-2

of the  $50^\circ$  and  $60^\circ$  data. The  $60^\circ$  data were taken at 5 different incident energies and the  $50^\circ$  data were taken at 4 energies. Data taken at one incident energy and angle are referred to as a "line." The low  $E'$  cut off of the data (corresponding to a  $W < 4.5$  GeV) was dictated by the rising experimental corrections as  $E'$  decreased. The dots on Fig. I-2 indicate where elastic scattering data were taken. During the experimental checkout period many low  $Q^2$  elastic peaks were measured mostly at  $50^\circ$  with incident energies from 1.5 GeV to 4.5 GeV.

The  $W_1$  contribution to the cross section outweighs the  $W_2$  portion by about 6:1 at  $50^\circ$  and  $60^\circ$ . In the language of total virtual photoabsorption cross sections this means we are measuring  $\sigma_t$  with very little contamination from  $\sigma_s$ . The  $\epsilon$  parameter is typically .12, thus the effect of  $\sigma_s$  when multiplied by  $\epsilon$  in the total cross section is reduced by nearly an order of magnitude. The correction applied to the measured cross section to extract  $W_1$  is quite insensitive to  $R$ . In Fig. I-3 contours of constant  $\epsilon$  (curve lines) calculated for  $60^\circ$  and of constant  $\omega'$  are shown.

The data taking proceeded as follows. A beam of electrons from the accelerator was delivered to the End Station. The spectrometer was set to its highest value of  $E'$  for that incident energy. Data were taken on each of the three targets, hydrogen, deuterium, and the empty target cell. The central momentum of the spectrometer was then lowered, and data taking continued as for the first setting. The spectrometer accepts particles within  $\pm 5\%$  of the

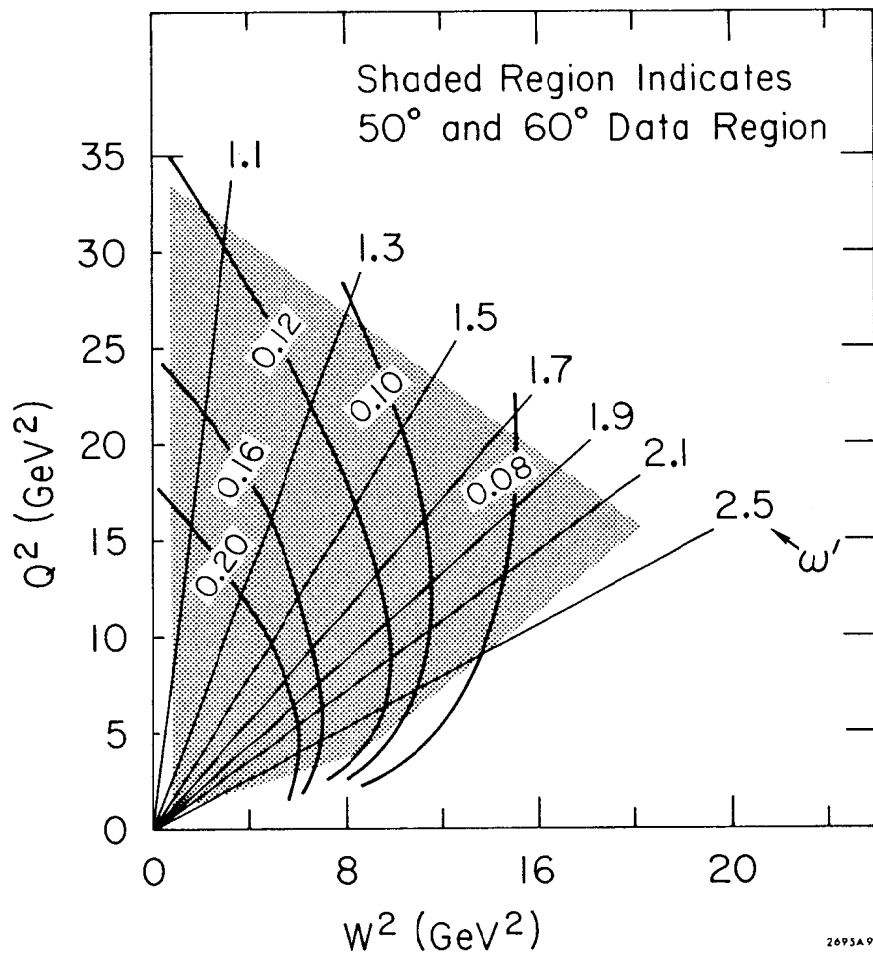


FIG. I-3

$\epsilon$  contours (curve lines) for  $60^\circ$  and  $\omega'$  contours overplotted on the kinematic region of the data.

central momentum. Each new setting was lower in central momentum by 3.33%. Thus, each cross section was measured in three separate runs at three different locations in the detector.

The main data taking occurred in two periods. During the first, fall of 1973, most of the  $60^\circ$  data were completed. In the second cycle, winter of 1974, the  $50^\circ$  data were accumulated, the  $60^\circ$  data completed, the high  $Q^2$  elastic points run and an interesting comparison of  $e^+/e^-$  made to values of  $Q^2$  as high as  $15 \text{ GeV}^2$  (Ref. I-21). The cross section data were bracketed by "check point" data of two types: 1) 1.5 GeV elastic scattering at  $50^\circ$  and 2) 6.5 GeV cross sections at  $60^\circ$ . These check runs tested the reproducibility of the measurements. A complete run chronology is given in Table I-1.



TABLE I

DATA ACQUISITION  
CHRONOLOGY

DATE	RUN NO.	TO RUN NO.	$E_0$	$\theta$	COMMENT
9/22/73	302	323	1.5	50°	Elastic check point
	324	364	1.5	60°	Elastic check point
	365	385	1.5	50°-60°	Elastic sweep in $\theta$
9/26/73	386	397	2.5	50°	Elastic check
	398	417	3.5	50°	Elastic check
	418	420	4.5	50°	Elastic check
	421	424	2.5	50°	Elastic check
	425	522	19.5	53.3°-60°	Check out data
10/9/73	523	532	1.5	50°	Elastic check point
	533	557	19.5	53.3°-60°	Check out data
End Check Out -----					
10/13/73	1001	1232	6.5	60°	Data
10/22/73	1233	1297	19.5	60°	Data
11/2/73	1349	1449	13.3	60°	Data
11/8/73	1450	1557	16.0	60°	Data
11/13/73	1558	1637	10.4	60°	Data
11/16/73	1638	1647	6.5	60°	Check point data
11/16/73	1648	1664	19.5	60°	Data
11/17/73	1665	1682	1.5	50°	Elastic check point

TABLE I (continued)

DATA ACQUISITION  
CHRONOLOGY

DATE	RUN NO.	TO RUN NO.	$E_0$	$\theta$	COMMENT
1/10/74	2001	2011	1.5	50°	Elastic check point
1/12/74	2012	2026	6.5	60°	Check point data
1/13/74	2027	2099	7.0	50°	Data
1/14/74	2101	2191	13.5	50°	Data
1/17/74	2192	2272	16.0	50°	Data
1/20/74	2273	2474	19.5	50°	Data
1/31/74	2475	2585	13.3	50°	Data
	2586	2592	13.3	50°	Dummy target checks
2/5/74	2593	2673	16.0	60°	Data
2/10/74	2674	2720	13.9	50°	e <sup>+</sup> /e <sup>-</sup> comparison
2/16/74	2721	2845	19.5	60°	Data
2/26/74	2846	2857	6.5	60°	Check point data
2/28/74	2858	2861	6.5	39°	Optics test

CHAPTER I - REFERENCES

1. "The Scattering of Alpha and Beta Particles by Matter and the Structure of the Atom," E. Rutherford, Phil. Mag. Vol. 21, 669 (1911).  
Also see A. Bodek, Ph.D. Thesis, M.I.T. Laboratory for Nuclear Science, Report No. C00-3069-116 (1972).
2. R. Hofstadter, H. R. Fechter and J. A. McIntyre, Phys. Rev. 72, 978 (1953).  
R. Hofstadter, B. Hahn, A. W. Knudsen and J. A. McIntyre, Phys. Rev. 95, 512 (1954).
3. R. Hofstadter and L. W. McAllister, Phys. Rev. 98, 217 (1955).  
R. Hofstadter, F. Bumiller and M. A. Yearian, Rev. Modern Physics 30, 482 (1958).
4. First publication of data: D. H. Coward et al., Phys. Rev. Lett 20, 292 (1968).  
Final publication of data: P. N. Kirk et al., Phys. Rev. D 8, 63 (1973).
5. E. D. Bloom et al., Phys. Rev. Lett 23, 930 (1969) and M. Breidenbach et al., Phys. Rev. Lett. 23, 935 (1969).
6. J. D. Bjorken, Phys. Rev. 179, 1547 (1969).  
J. D. Bjorken and E. A. Paschos, Phys. Rev. 185, 1975 (1969).
7. Such models as Vector Dominance are reviewed in: J. J. Sakurai, "Vector-Meson Dominance - Present Status and Future Prospects," 1969 International Conference on Electron and Photon Interactions at High Energies, Daresbury, England, 1969.
8. E. D. Bloom et al., "Recent Results in Inelastic Electron Scattering," SLAC-PUB-796, 1970; (A report presented to the XV International Conference on High Energy Physics, Kiev, U.S.S.R., 1970).
9. J. Mar et al., Phys. Rev. Lett. 21, 482
10. An excellent review of electroproduction phenomenology is: R. P. Feynman, Photon Hadron Interactions, W. A. Benjamin Inc., 1972.  
Also, L. N. Hand, Phys. Rev. 129, 1834 (1963).
11. Ref. 5 and G. Miller, "Inelastic Electron Scattering at Large Angles," Ph.D. Thesis, SLAC Report No. 129 (1971).
12. See, for example: E. M. Riordan, "An Experimental Study of the Nucleon Structure Functions," M.I.T. Ph.D. Thesis, Laboratory for Nuclear Science Report No. C00-3069-176 (1973).
13. E. D. Bloom and F. Gilman, Phys. Rev. Lett. 25, 1140 (1970)
14. G. B. West, Phys. Rev. Lett 24, 1206 (1970).  
S. D. Drell and T.-M. Yan, Phys. Rev. Letters 24, 181 (1970).
15. S. Stein et al., "Electron Scattering at  $4^\circ$  with Energies of 4.5 - 20 GeV," SLAC-PUB-1528 (1975).
16. V. Z. Jankus, Phys. Rev. 102, 1586 (1956).
17. K. Gottfried, Phys. Rev. Lett 18, 1174 (1967).
18. M. Chanowitz and S. D. Drell, Phys. Rev. Lett 30, 307 (1973).  
M. Chanowitz and S. D. Drell, Phys. Rev. D9, 2078 (1974).  
G. B. West, Stanford University Preprint (unpublished).

## CHAPTER II

### OVERVIEW OF THE EXPERIMENT

19. M. Gell-Mann, Phys. Letters 8, 214 (1964).
20. M. Mestayer, Stanford University Ph.D. Thesis
21. L. S. Rochester et al., (to be published).

The experiment is conceptually very simple. The Stanford Linear Accelerator produces a beam of high energy electrons (Ref. II-1). The principal element in the LINAC is a 10000 foot disk-loaded copper waveguide. Prior to the injection of electrons from a high current electron gun, the waveguide is filled with R.F. power from up to 245 klystrons. Some of the injected electrons are caught on the crests of the travelling R.F. wave in the waveguide and are accelerated with an energy gain of approximately 2 MeV per foot. The resulting electron beam has an R.F. structure reflecting the 2856 MHz microwave radiation used to power the waveguide (the bunch structure has approximately 10 cm spacing). The total pulse duration is from 1.2 to 1.6 usec., and the accelerator can run at a repetition rate of up to 360 pulses per second (or a maximum duty cycle of about 1:1700). Although the pulses are short, currents over the beam spill can exceed 60 mA above 13 GeV (a single 20 GeV pulse can have almost 2000 joules of energy).

The beam from the accelerator is channeled to various experimental areas via the Beam Switch Yard (BSY) on a pulse to pulse basis. As many as 8 independent beams have been delivered in this fashion, each sharing a fraction of the available pulses. For End Station A (ESA), the BSY deflects the beam north to the "A-line." Here, a symmetric series of bending magnets and quadrupole focusing elements complete the 24.5 degree bend into ESA. High power momentum selection slits located half way through "A Bend"

determine the incident energy and resolution.

In the End Station the beam passes through a target mounted on the "pivot." Three large spectrometers sit on circular railroad tracks centered on the pivot making angle positioning of these cumbersome instruments easy. Most of the beam suffers little deflection in the target and passes out the rear of the End Station and into a beam dump buried in the hill behind the End Station.

The 1.6 GeV spectrometer is located on the north side of the beam and is the lowest momentum spectrometer of the three in ESA (Ref. II-2). It consists of a single 90 degree bending magnet weighing approximately 80 tons. Scattered electrons from the target pass through a tungsten slit at the magnet entrance which partially defines the spectrometer's acceptance. Slanted entrance and exit pole faces cause wedge focusing, yielding point to point imaging in the vertical plane, dispersing different momenta at the "p-focus," and parallel to point focusing in the horizontal plane. The line target source is focused to a point with the various allowed angles dispersed.

Particle detectors were located within a 5' (diameter) by 11' (high) enclosure shielded by over 200 tons of concrete. Particle identification was made with a threshold gas Cerenkov counter (CT) followed by a multi-segmented lead glass Total Absorption counter (TA). Particle tracking information was provided by three hodoscopes, one located in front of the Cerenkov counter and two sandwiched between the Cerenkov counter and the TA package.

A particle traversing the counters produced various signals which were transmitted to the "counting house" where they were processed by fast electronic circuits. Subsequently information from the electronics was recorded by an XDS 9300 computer on magnetic tape for each event. In addition, target information, 1.6 spectrometer status information, and beam information were recorded at regular intervals. The computer's other duties were to perform an online analysis of the experiment, to monitor the functioning of the various pieces of apparatus associated with the experiment and announce any malfunctions detected. The computer also provided experimenters (often to their annoyance) with a preprogrammed agenda. This agenda directed the data taking, calling for changes in initial and scattered energy settings, and prompting the inattentive when sufficient incident flux had been accumulated for a given kinematical setting.

#### THE BEAM

The beam transport system is shown in Fig. II-1. Accelerated electrons from the LINAC are collimated to a spot size determined by the high power slits C0 and C1 at the entrance to the BSY. These slits were typically set at 9mm x 9mm. Pulsed bending magnets then deflect the beam 0.5 deg. into the "A-line." Eight bending magnets and five quadrupole magnets are the primary magnetic elements. These are placed symmetrically about high power momentum slits, SL10/SL11, with pairs of "quads" beginning and ending the sequence.

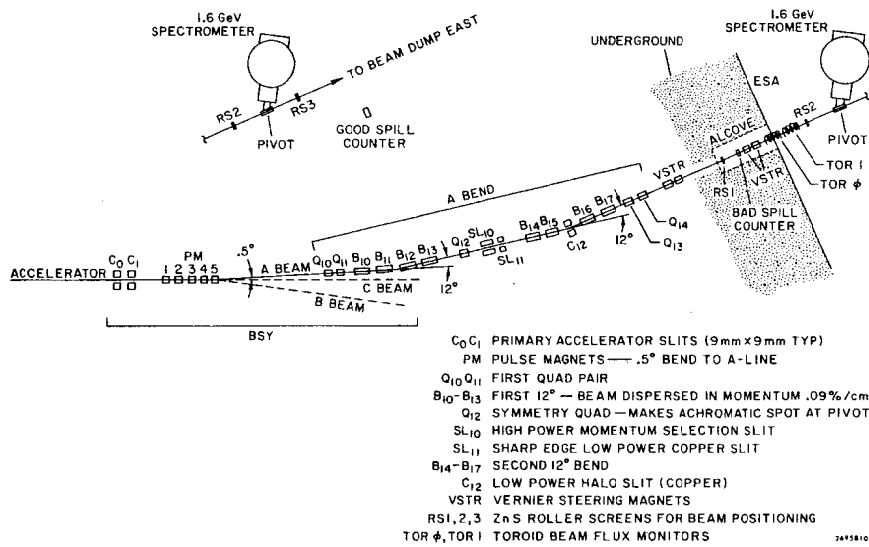


FIG. II-1

The beam transport system from the accelerator to End Station-A.

This arrangement disperses the beam in momentum at SL10. The experiment was run with SL10 set to a width corresponding to  $\pm 0.38\%$  energy resolution. The focusing properties of A-line produced an image of the slit C0 at the pivot, where the beam is again achromatic (x - y position within the beam spot is not correlated with energy) due to the effect of Q12 just in front of SL10. The energy of the beam is set by measuring the magnetic field with a "flip coil" in a 9th identical bending magnet connected in series with the 8 in A-line. The absolute energy calibration for the center of SL10 is  $\pm 0.1\%$  (Ref. II-3).

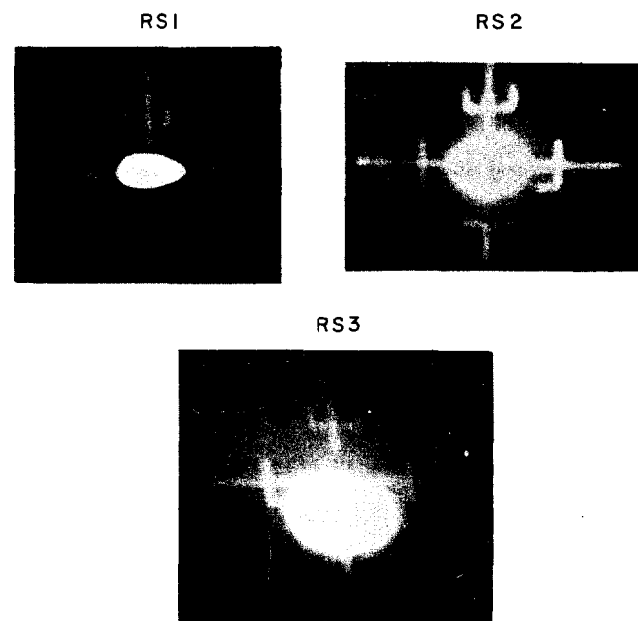
The uncertainty in the size of the cross sections at 60 degrees due to the energy spread in the incident beam is usually less than  $\frac{1}{4}$  that of the statistical errors of the recorded data. The incident energy spread washes out missing mass structure only on the tens of MeV level. A shift in  $E_0$  of 0.38% typically corresponds to a change in the  $w'$  variable of 0.3% and results in a possible cross section change of at most 0.8%. The resulting shift in the missing mass for a 0.38% change in  $E_0$  is small and quite insensitive to the value of W (for  $E_0 = 16$  GeV,  $E' = 1.38$  GeV, and  $W = 2.5$  GeV gives  $\Delta W = 6.1$  MeV). A transmission scan at the end of the full data taking period showed that for a typical running condition (19.5 GeV, 50 mA) more than 80% of the beam lay inside a  $\pm .2\%$  slit opening instead of the  $\pm 0.38\%$  for the full slit opening used in this experiment. The cross section measurements are more sensitive to an error in  $E'$ , and this is dominated

by the hodoscope slat widths ( $E'$  was resolved with the hodoscopes to about  $\frac{1}{2}\%$ ).

The fine steering adjustments of the beam were done using four steering magnets, controlling both the pitch and the position of the beam at the pivot. Two zinc sulfide screens located 10.8' and 42.3' upstream of the target were used for this alignment. For a positioning uncertainty of 1 mm on the screens, the resulting angle misalignment would be .1 mrad (0.004 deg.). These screens were normally removed during data runs to reduce beam halo at the target. Sixteen feet downstream of the target a third screen (RS3) was left in the beam during data taking to provide continuous beam position and spot shape information. The waist of the beam was adjusted to occur near RS2. The three zinc sulfide screens were remotely monitored in the counting house by closed circuit T.V. (see Fig. II-2). On the target assembly itself an aluminum oxide screen was precisely positioned with respect to the targets. Checking the beam alignment relative to this screen after steering with the other screens assured us that the target positioning was correct.

The average beam spot size was measured using two independent techniques besides visual inspection of the roller screens. The critical parameters were the horizontal spot size and position, since the liquid target cells were long and narrow (17.7 cm x 1.9 cm). Measuring the local beam intensity by observing the secondary electron emission from a wire mounted on the target assembly showed the spot to be approximately Gaussian in intensity with a horizontal

Photographs of closed circuit T.V. monitors for the three zinc sulfide screen RS1, RS2 and RS3.



Tick marks are 1 cm spacing. Visual spots are much larger than actual spots as the ZnS screens quickly saturate.

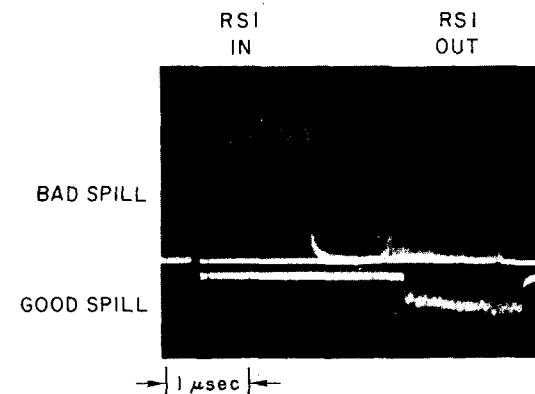
2695A3

FIG. II-2

sigma of 1.0 mm (this confirmed observations made of the beam burn spots on the screens). After the experiment autoradiographs of the entry and the exit beam burn spots on the target cells were made by holding X-ray film against the ends of the cells. Measuring the resulting exposures showed optical densities approximately Gaussian in both horizontal and vertical directions. The measured sigmas were: hydrogen - 1.35 mm (Hor.) x 0.99 mm (vert.); deuterium 1.36 mm (hor.) x 1.09 mm (vert.). The autoradiographs were made approximately one week after the second data run. The principal isotope contributing to the residual radioactivity is  $V^{48}$  (half life of 23 days). Thus, these measurements represent a long term average spot size including broadening due to any steering errors. The spot positions were checked by measuring the center of the autoradiographs, and no significant deviation ( $\pm 2$  mm) from the center of the ends of the targets was found.

The beam spill was monitored in the End Station using two lucite Cerenkov counters (1" (dia.) x 0.5" lucite cylinders glued to 56AVP photomultiplier tubes). One was placed downstream of the pivot and called "good spill" (see Fig. II-1 and Fig. II-3). This counter was exposed to the high flux of secondary particles produced by the beam striking the target. Any irregularity in intensity or spill width was easily detectable on an oscilloscope trace of this signal. The typical spill width was measured to be 1.5  $\mu$ sec using this counter. The second spill monitor, called "bad spill," was placed in the entry alcove to the End Station

Photograph of oscilloscope traces of the "good" spill counter (lower trace) and the "bad" spill counter (upper trace).



Bad spill trace is inverted. Putting RSI in the beam gave a reference signal to calibrate the bad spill.

2695A2

FIG. II-3

(see Fig. II-1) just upstream of a shield which provided about 16" of iron to attenuate the room noise from "downstream." This counter detected beam halo striking beam line elements near the counter. The counter was located a few feet downstream of RS1, and putting RS1 into the beam resulted in a very large signal from the bad spill counter (see Fig. II-3) which was used as a reference signal. In tuning the beam, we tried to minimize the bad spill signal with RS1 removed. We found this counter to be sensitive to many beam faults, some of which were: focusing in the accelerator, scraping beam on CO in front of the BSY, mis-steering in the pulsed magnets in the switch yard, any collimator scraping in the A-line, and a poor vacuum in the A-line. "Gulches" in the good spill usually corresponded to spikes in the bad spill, presumably due to beam loss on SL10 or some other collimator. It became clear early in the experiment that a well tuned beam produced a small bad spill. The bad spill was used as a primary indication of beam quality.

For the greater part of the experiment, the beam currents were run at the maximum current the accelerator could produce. In the upper half of its energy range currents over the beam spill in excess of 50 mA were usually achieved, sometimes reaching as high as 60 mA. The beam current was adjusted to keep particle counting rates in the two spectrometers at an acceptable level and was not allowed to exceed 2 per pulse for electron running (4 per pulse for positron running) in the 1.6-GeV spectrometer.

#### BEAM MONITORS

The incident flux of electrons for the experiment was measured by two independent, identical precision toroid charge monitors, TORO and TOR1 (see Fig. II-1 for position and Ref. II-4 for a detailed description). The detection element of the toroid system is a ferrite core toroid located upstream of the pivot. The beam passes through the toroid forming an equivalent one turn primary winding. A secondary winding is directly connected across a capacitor. The resulting LC circuit has a resonance frequency of 5.25 kHz which is slow compared with the beam pulse length. A beam pulse shock excites this LC circuit. After a delay time selected to minimize spill width effects and noise effects, the amplified wave form is sampled, digitized, and accumulated on a pulse to pulse basis in a bi-directional scaler.

The toroid monitors were frequently calibrated by "dumping" a precision capacitor charged to a precisely determined voltage through a one turn winding on the ferrite core to simulate a beam pulse. The calibration pulse shape resembles the beam pulse shape, and differences can be somewhat compensated for by appropriately adjusting the sampling delay time. Agreement, after gain shift compensation between the two toroids, was better than 0.5%, and both agreed with the total charge put through the one turn winding to the same accuracy. Although this technique is not a convincing absolute calibration, it does provide an excellent



TABLE II - 1  
SUMMARY OF BEAM PARAMETERS AND ERRORS

QUANTITY	VALUE	CAL. & MEAS.	RANDOM ERROR	SYSTEMATIC ERROR
$E_0$	1.5-19.5 GeV	A-Bend, Flip Coil, A-Bend shunt voltage.	$\pm 0.38\%$ SL10 Setting	$\pm 0.1\%$ Absolute Cal. of A-Bend.
Spot Size ( $\sigma$ ) and Shape	1.36mm (hor.)x 1.00mm (vert.)	Zinc-sulfide screens, SEM scan, Auto Radiographs	$\pm 0.5$ mm (variation in optics over run).	
Spill	1.5 usec (typ.) flat top	Oscilloscope trace of spill counters	$\pm 0.1$ usec pulse to pulse variation.	
Current	1mA-60mA	Toroids, Faraday Cup	$\pm 0.5\%$ Fluctuation in Toroid cal.	$\pm 0.6\%$ Faraday Cup, Toroid cal.
Steering and Beam Alignment		Zinc-sulfide screens, SEM, Auto Radiographs, $Al_2O_3$ Screen on Target Assembly.	$\pm 0.004^\circ$	$\pm 0.002^\circ$ Survey Error $\pm 0.5$ mm.
Halo	$\leq 0.5\%$ contrib. to cross section.	$\frac{1}{4}$ " $Fe$ Halo Hole Target, Bad Spill Monitor.	$\pm 0.2\%$	$\pm 0.2\%$

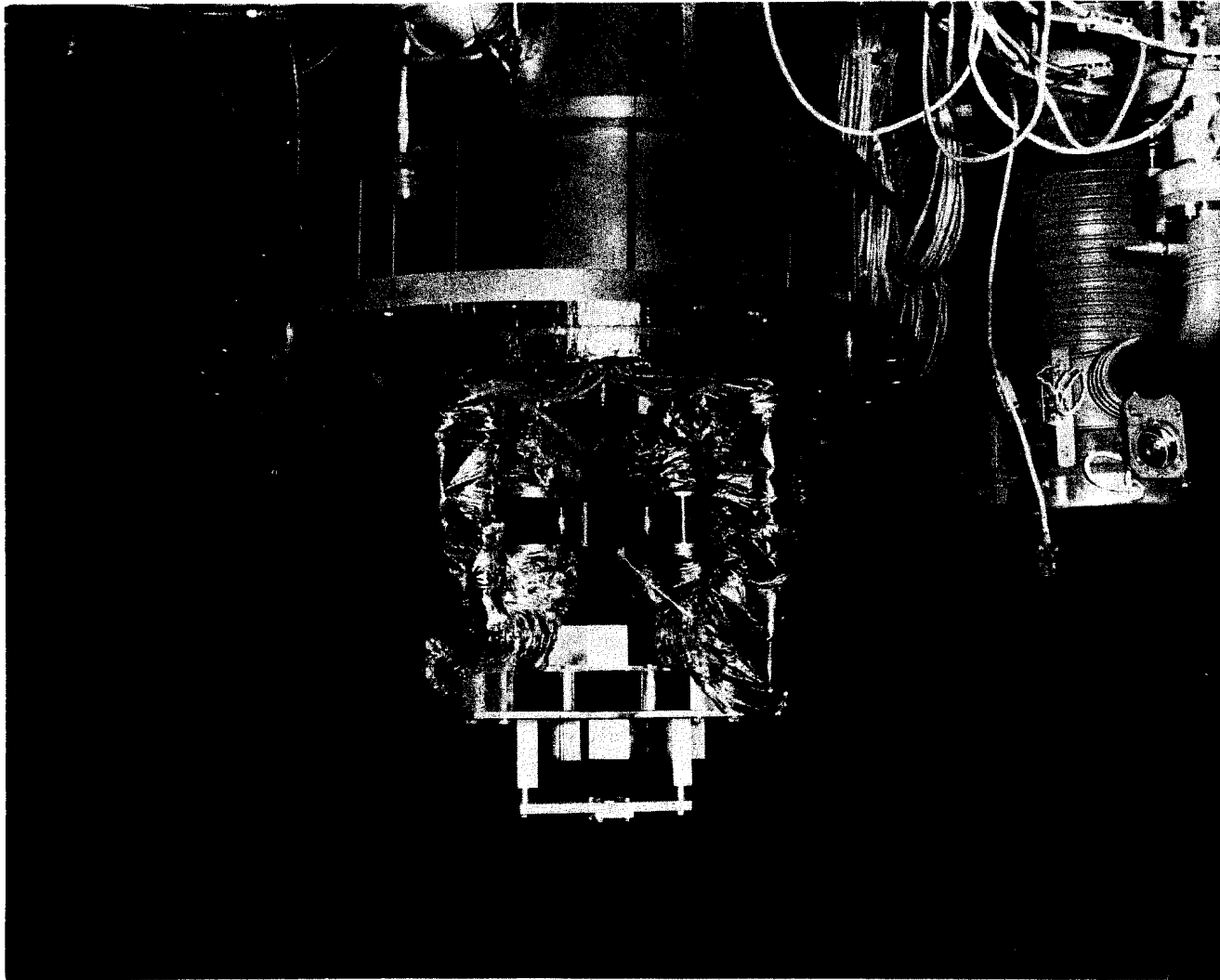
means of monitoring drifts and malfunctions of these devices over a long experiment.

An absolute flux calibration of the toroids was done approximately once per incident beam energy change using a Faraday Cup located about 80' downstream of the pivot. The total charge incident on the Faraday Cup was accumulated by an integrating digital voltmeter. The Faraday Cup has an average power limitation of about 1 kW so the tests were made at a repetition rate of a few per second. All gain ranges on the toroids used in E-89 were compared to a Faraday Cup measurement. These calibrations agreed with both toroids to  $\pm 0.5\%$ , and the Faraday Cup itself is believed to have an absolute accuracy of  $\pm 0.2\%$  (Ref. II-5). Beam properties are summarized in Table II-1.

#### THE TARGET

To withstand the high intensity beams used in E-89, the liquid targets for the experiment were fan driven recirculating liquid targets developed for high power dissipation (Ref. II-6). The target cells were the only new feature of the target assembly compared with previous experiments. A picture of the target is shown in Fig. II-4 and a schematic in Fig. II-5.

The long, narrow shape of the cells evolved from two considerations. To maximize the rate the targets were made as long as the 1.6 could "see" with its full  $\theta$  acceptance ( $7.00'' = 17.8$  cm) at 60 degrees. To minimize the production of electrons by secondary particles, the amount of radiator (material) between the beam and



2695A36

FIG. II-4

Photograph of target assembly

Schematic of the target showing the circulation path and driving fan.

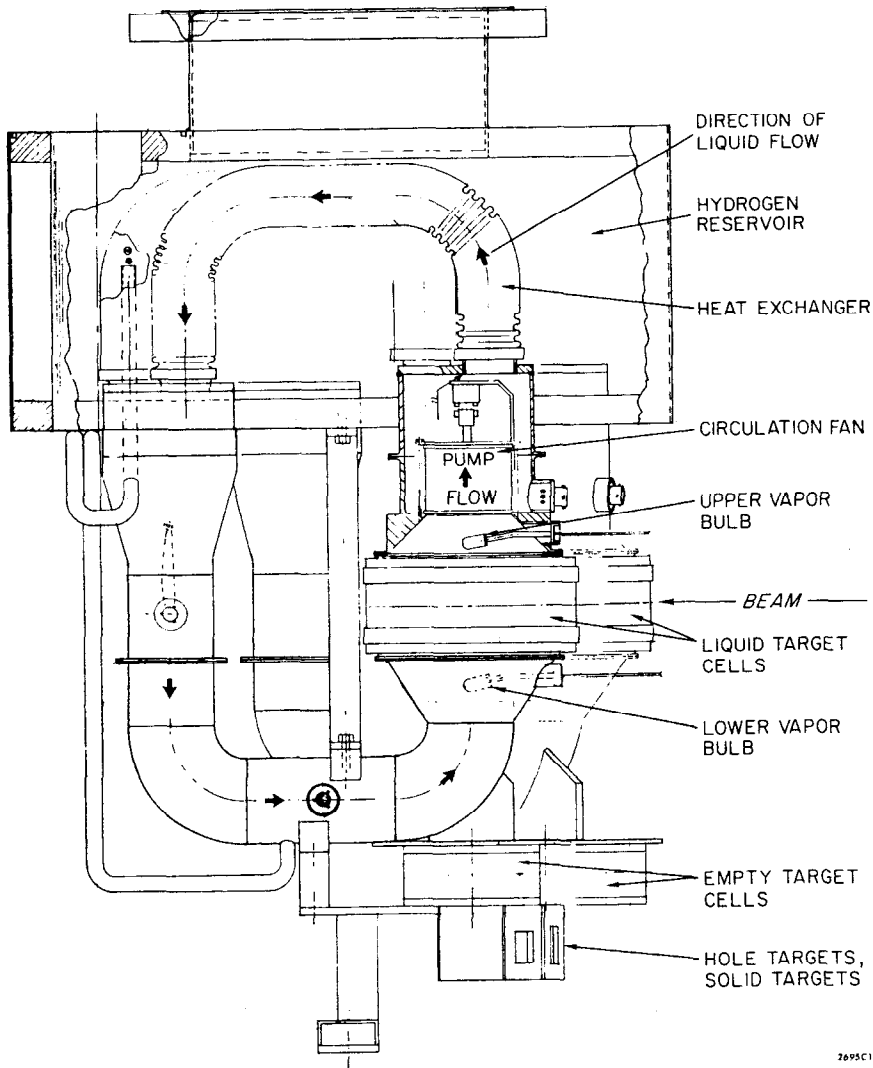


FIG. II-5

the 1.6-GeV spectrometer was made as small as possible. The target cells were about 2 cm wide made from .0017" (.0043 cm) stainless steel foil. The only other material between the target and the 1.6 magnet was a thin H-film (.002" plastic film) window to separate the vacuum tank of the spectrometer from the high vacuum of the scattering chamber in which the cells were located.

A summary of the material in the path of the electrons is presented in Table II-2. It is parameterized in terms of the radiation lengths ( $\chi_0$ ) before ( $t_b$ ) and after ( $t_a$ ) the center of the target. The  $t_b$  includes  $\frac{1}{2}$  the radiation length of the target cell and an anticondensation foil. The  $t_a$  includes the average length of the liquid between the beam line and the spectrometer, the cell wall, and the H-film. This amount of material ( $t_a$ ) produces about 1/3 of the total positron signal arising from  $\pi^0$  production with subsequent conversion of the decay gammas. Neutral pion decay and other charge symmetric processes contribute equally to  $e^-$  and  $e^+$  rates. For  $\pi^0$ 's the yield is proportional to  $7/9 t_a + 1/86$  (the 1/86 comes from Dalitz decay,  $\pi^0 \rightarrow \gamma e^+ e^-$ ).

The liquid temperatures were monitored by hydrogen vapor bulbs placed in the liquid flow above and below each of the two liquid target cells. Measuring the vapor pressure in these bulbs with pressure transducers provided target temperature information. The voltage reading from the transducer was converted to (psia) using calibration data and then to  $P(\text{atm}) = P(\text{psia}) \times .0680457$ .

TABLE II-2

## SUMMARY OF RADIATORS FOR 1.6 GeV SPECTROMETER

Quantity	$t_b(x_o)$	$t_a(x_o)$	
		50°	60°
Anti-Condensation Coil	.0004		
Target Walls	.002557 (.0017" Fe)	.00328	.00295
Liquid Radiators	LH <sub>2</sub> .00997	.00166 } 1.47cm	.00147 } 1.30cm
	LD <sub>2</sub> .01157		
$\left. \begin{array}{l} \text{LH}_2 \\ \text{LD}_2 \end{array} \right\} \left( \frac{17.68\text{cm}}{2} \right)$			
H-Film Vac. Isolation		.00017 (.002 Mylar)	.00017
<hr/>			
Totals			
LH <sub>2</sub>	.01293	.00511	.00459
LD <sub>2</sub>	.01453	.00538	.00482

Summary of radiators for the 1.6 GeV spectrometer for before and after the center of the target.

The relation

$$\log_{10} (P(\text{atm})) = 2.00062 - 50.09708/(T(^{\circ}\text{K}) + 1.0044) + .01748495 \times T(^{\circ}\text{K})$$

taken from Ref. II-7 can be inverted to yield the target temperature. The hydrogen density was obtained using polynomial fits (Ref. II-8) to publish the hydrogen and deuterium densities (Ref. II-9). The fits used were:

$$\rho_H = .07714 + .000443 T - .00003866 T^2$$

$$\rho_D = (.1853 + .0006677 T - .000068727^2) \frac{2}{2.015}$$

The densities  $\rho_i$  are in atomic weights/cc, and the temperature  $T$  is in degrees Kelvin.

The target densities were calculated for every run for both the upper and the lower vapor bulb measurements. The densities were found to slightly depend on the power input into the target from the beam. The power input was parameterized as repetition rate (in pulses per second) times beam current (in mA). Scatter plots for all the data runs versus this power parameter are displayed in Fig. II-6. These densities were used to calculate the number of nuclei per  $\text{cm}^2$  for each run.

In Table II-3, the density reduction for the average of all runs is given. The sources of systematic error are pressure transducer calibration (for the vapor bulb pressure), formula error (for the temperature-pressure relation), and the quoted accuracy

TABLE II - 3

A SUMMARY OF THE LIQUID TARGET PROPERTIES  
(AVERAGED OVER ALL RUNS)

Quantity	LH <sub>2</sub>		LD <sub>2</sub>	
	Value	Error*	Value	Error*
Vapor Pressure (psia)				
Upper	16.583		16.774	
Lower	16.317		16.731	
Temperature (°K)				
Upper	20.08	±.1% (S)	20.72	±.1% (S)
Lower	20.63		20.72	
Density ( $\frac{\text{Atm. Wt.}}{\text{cc}}$ )				
Upper	.06973	±.3% (R)	.1684	±.3% (R)
Lower	.06982	±.3% (S)	.1684	±.6% (S)
Contamination	-		.3%(H)	±.1% (S)
Target Length (cm)	17.674	±.5% <sup>**</sup> (S)	17.631	±.5% <sup>**</sup> (S)
No. of Nuclei per cm <sup>2</sup>	7.431x10 <sup>23</sup>		8.942x10 <sup>23</sup>	
Total Error	.6% (S)		.9% (S)	
	.3% (R)		.3% (R)	

Density reduction from vapor bulb pressure for the average density.

\* For the errors (S) denotes Systematic Error and (R) denotes Random Error.

\*\* Note on systematic error on target length - this ½% is mostly a guessed possible 1/32" in the optical determination of the overall length. Since the H and D cells were measured in the same way at the same time, most of the ½% is common to both and wouldn't propagate into N/P ratios very much.

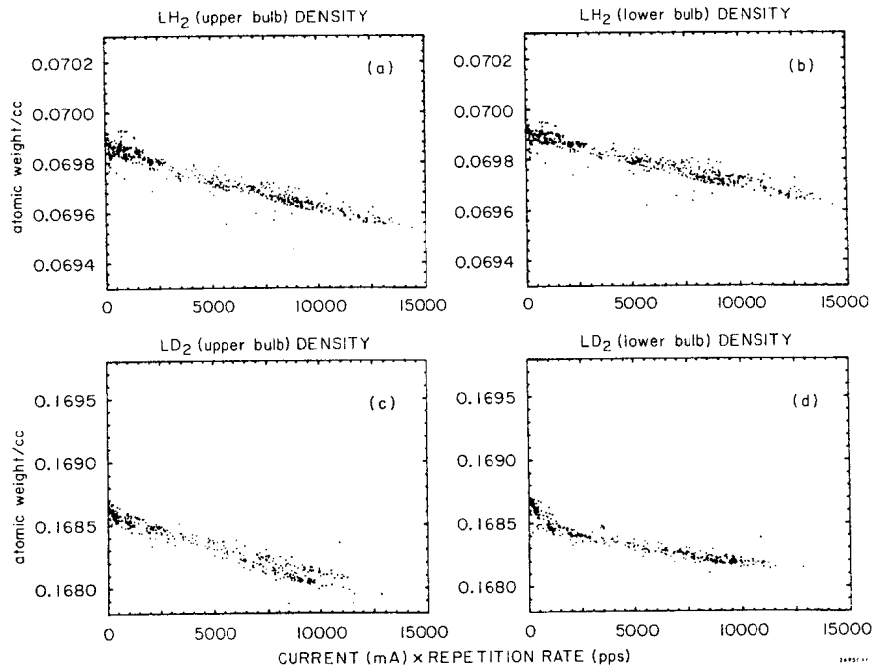


FIG. II-6

Scatter plots of hydrogen and deuterium liquid densities versus beam current.

of temperature versus density measurements. The random error is taken to be  $\pm\frac{1}{2}$  of the full width of the typical spread of the data.

The density used in calculating cross sections was that calculated from the lower vapor bulb measurement. This should be the density of the hydrogen just before the 1.5  $\mu$ sec beam pulse strikes the target. The circulation rate is supposed to move the liquid fast enough so that the beam strikes a fresh portion of liquid on each pulse, even at 360 pps. Density changes during the beam pulse are neglected.

The two liquid cells were positioned directly underneath the liquid hydrogen reservoir used to cool the recirculation loops. Beneath them were various dummy targets. Measurements of electrons and positrons off these were used to correct the full target yield for scattering from the cell walls. The principal dummy target used in the experiment was approximately 5.5 times thicker than the actual target cell walls and was constructed to have the same radiators ( $t_a$  and  $t_b$ ) as the liquid cells. The number of nucleons for the thick dummy was roughly the same as the full cells, thus the counting rates were comparable.

An additional solid angle factor has to be applied to the dummy subtraction since the spectrometer didn't have full acceptance for the ends of the targets (the thick dummy was distributed in thin foils along the 17.7 cm length). This factor was calculated by Monte Carlo techniques using a model

of the spectrometer and checked experimentally by measuring the ratio of a "long" dummy (2 - .010" steel foils, 17.7 cm apart) to a "short" dummy (2 - .010" steel foils, 2.0 cm apart). The solid angle reduction factor was .78 for 60 deg. and .92 for 50 deg. The measurements agreed with these calculated ratios to within 5% and well within statistical errors.

Below the dummy targets were an  $Al_2O_3$  screen, the SEM wire (see Chp. II, The Beam), a  $\frac{1}{4}$ " steel hole target (for measuring effects of beam halo), and some solid targets. The whole target assembly could be moved up and down and rotated by remote control from the counting house allowing accurate positioning ( $\pm 0.1$  mm (vert.) x  $\pm 0.1$  mm (hor.)) of any of the targets in the beam. Usually the targets were driven into position automatically under computer control.

#### THE 1.6 SPECTROMETER

The 1.6-GeV spectrometer is shown in Fig. II-7. A single 90 degree bend magnet transports particles scattered into its acceptance to the "counter cave." The focusing properties employ wedge focusing giving point to point imaging in the vertical plane for particles of the same momentum. This focusing effect is achieved by the different path lengths through the dipole magnetic field for different  $\phi$  angles ( $\phi = y/z =$  "vertical projected angle"). The slanted pole faces also produce magnetic fringe fields that have a non-zero y component. This produces

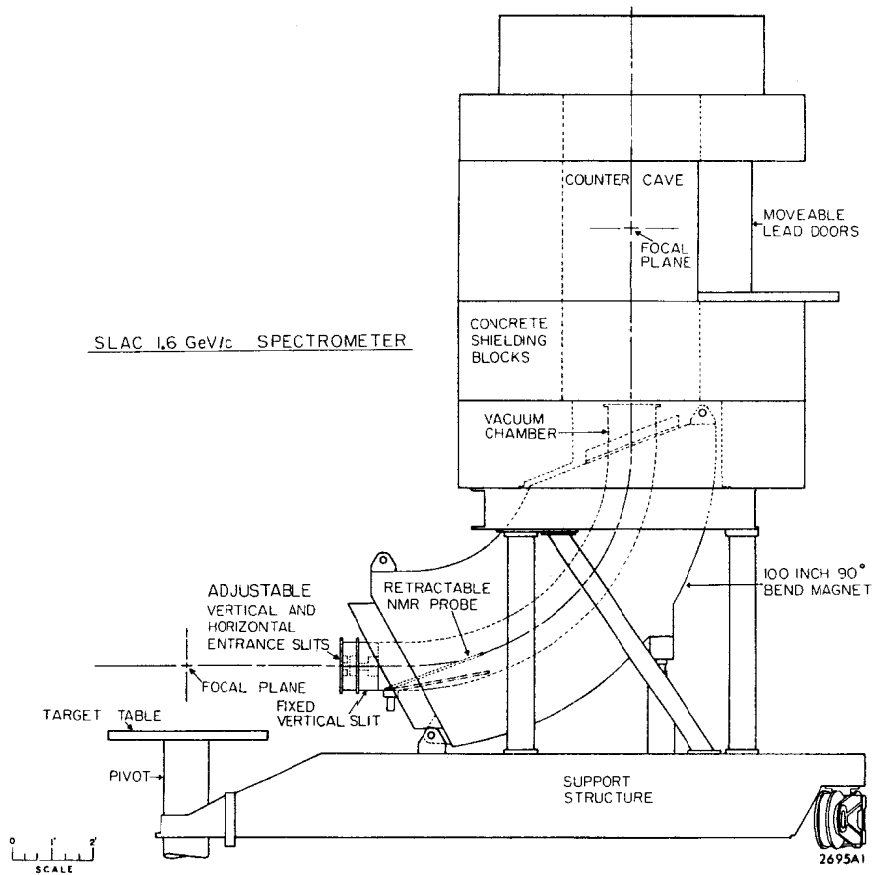


FIG. II-7

1.6 GeV Spectrometer Schematic

quadrupole focusing in the horizontal plane. The field is such that particles are first focused at the entrance then defocused at the exit. The net result is line to point focusing in the horizontal plane. This takes particles from the line source target scattered at the same angle and focuses them to a "point" at the focus in the counter cave.

The two focusing properties are obviously coupled. To make the two focal planes coincident in the cave, sextupole corrections are used. This is introduced by curved pole faces in three regions in the magnet called "beta lenses." The original idea was to be able to use a single rotatable hodoscope at the p-focus to measure missing mass spectra, but we used fixed p and  $\theta$  hodoscopes in E-89.

The momentum of the 1.6 was set by measuring the magnetic field near the center of the aperture just past the first beta lens region. A nuclear magnetic resonance (NMR) probe was raised into position by a remotely operated boom to make the field measurement. The NMR would be tuned to the frequency corresponding to the desired magnetic field (and thus the momentum). Then the power supply for the magnet was adjusted to find the signal. This procedure was easily accomplished as the 1.6 followed a known current-field relation very well. The NMR frequency was recorded along with the magnet current, magnet temperature, and the voltage measured from the two Hall probes located inside the magnet at the beginning and end of every run.

An aperture defining slit was located at the entrance of the magnet. This fixed slit was accurately constructed from lead with tungsten jaws. The top and bottom tungsten pieces were angled toward the target and spaced from the center line so that rays outside of +40 mrad and -50 mrad were completely blocked. Two tungsten pieces on the sides defined the  $\theta$ -target length limits and completed the frame.

Particles traversed a large aluminum vacuum tank (7 15/16" x 21 15/32") which passes through the magnet to the counter cave. The tank limits parts of the acceptance for some rays. The large  $\theta$  trajectories from the ends of the targets are intercepted by the top flange of the tank. For large  $p$  and  $\phi$  near the top of the tank the orbits grazed the aluminum. Two tungsten baffles were placed inside the tank to obstruct such rays. The limiting apertures were accurately measured during a wire float measurement of the optics of the 1.6 (see Appendix D).

The 1.6-GeV spectrometer counter cave is formed by a stack of three concrete doughnuts above the magnet. A 5' x 11' cylindrical cavity results. Two large lead filled doors located halfway up the wall away from the target provide the principal access. The whole structure is capped with a 3'thick circular concrete lid, which can be removed to load counters into the cave using the overhead crane in End Station A.

In the first checkout run, much experimenting was done to

reduce background in the counter cave by adding shielding outside, particularly between the cave and the target. The extra shielding blocks reduced the singles rates at the p-focus by a factor of 2.5. Most of the remaining counting rate was coming up the vacuum tank as verified by closing a pair of movable slits located directly in front of the fixed slit. The singles rates were most severe near the magnet exit at the bottom of the cave presumably due to soft spray from particles striking the aluminum vacuum pipe. More extensive baffling might have improved this situation.

In 1970, the 1.6 suffered an unfortunate accident. The magnet was run without water cooling. Much of the epoxy insulation melted off the coil. Subsequently, in 1971, two of the 144 turns of the coil shorted. To compensate, two symmetric turns on the other side of the aperture were shorted. Measurements of the elastic proton peak showed no detectable difference from the measurements using the original coil when the remaining turns were excited to achieve the same field.

In view of this history, we decided to measure the properties of the magnet using the floating wire technique at the completion of the experiment to independently measure the optics coefficients. These results are given in Appendix D. No large differences were found from the original optical properties published in Ref. II-2.



### COUNTER PACKAGE

The counters used to detect scattered electrons are shown in Fig. II-8. They were physically separated into two parts: a TA package that included all counters down to the  $\theta$  hodoscope and the gas Cerenkov counter and the Y hodoscope. The TA package was hung from a rotatable mount secured at the top of the counter cave while the CT and Y hodoscope rested on the floor of the cave. Rotation of the TA package was necessary to service the equipment. Gross counter properties are summarized in Table II-4.

The counters were aligned by using the laser system designed by SLAC Group-F. On each side of the magnet an optical laser imaged a cross hair through a lens system, pointing toward the ceiling of the End Station. The cross hairs and lenses were set so that a line connecting them split the center of the exit aperture of the magnet in the direction of the p dispersion. The point half way between the cross hairs located the center of the aperture in the  $\theta$  dispersion direction. Both optical systems were supported 1" off the iron return yoke of the magnet and were affixed to it. The two bright cross images described two vertical reference lines. Lucite screens attached to the various counters and TA package linked the co-ordinate systems of the spectrometer to that of the counters.

Both the p and  $\theta$  hodoscopes had coarse hodoscopes behind

Counter array used to detect electrons in the 1.6 counter cave. The Pb glass hodoscope, pre-radiator, TA1 and TA2 formed the total absorption counter.

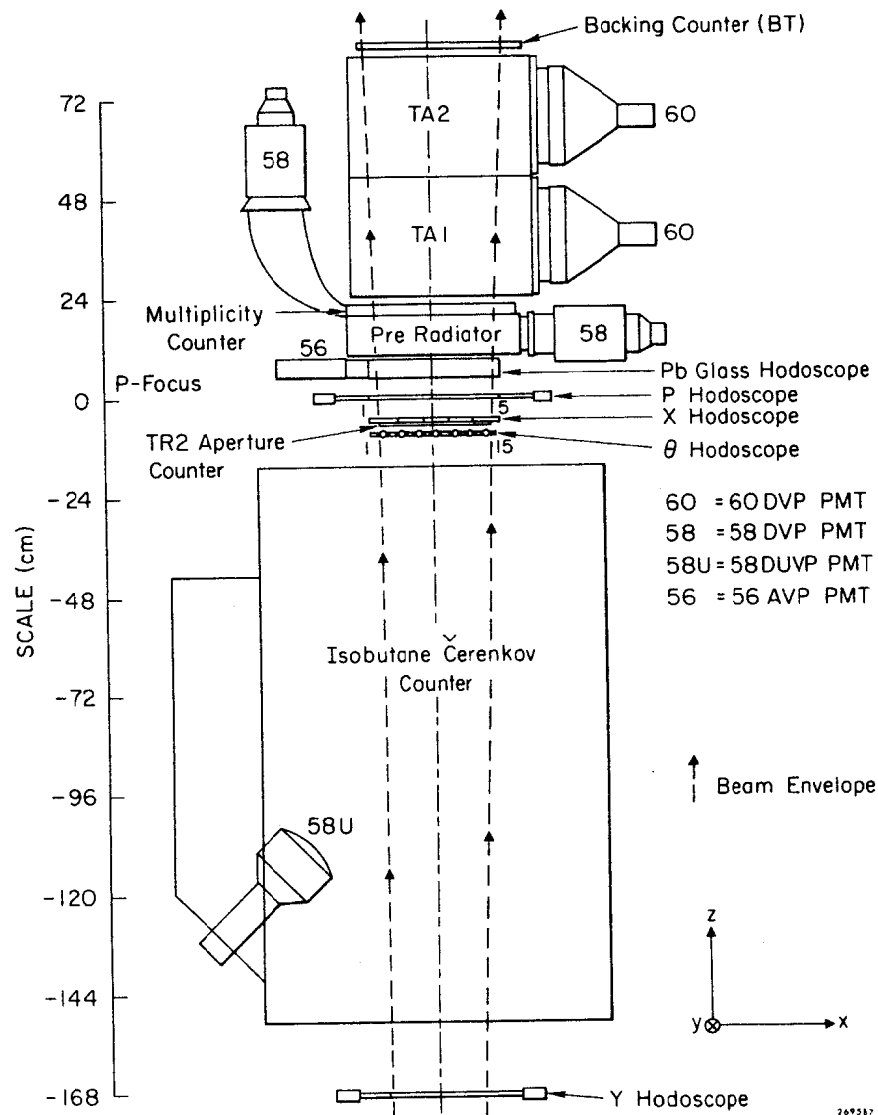
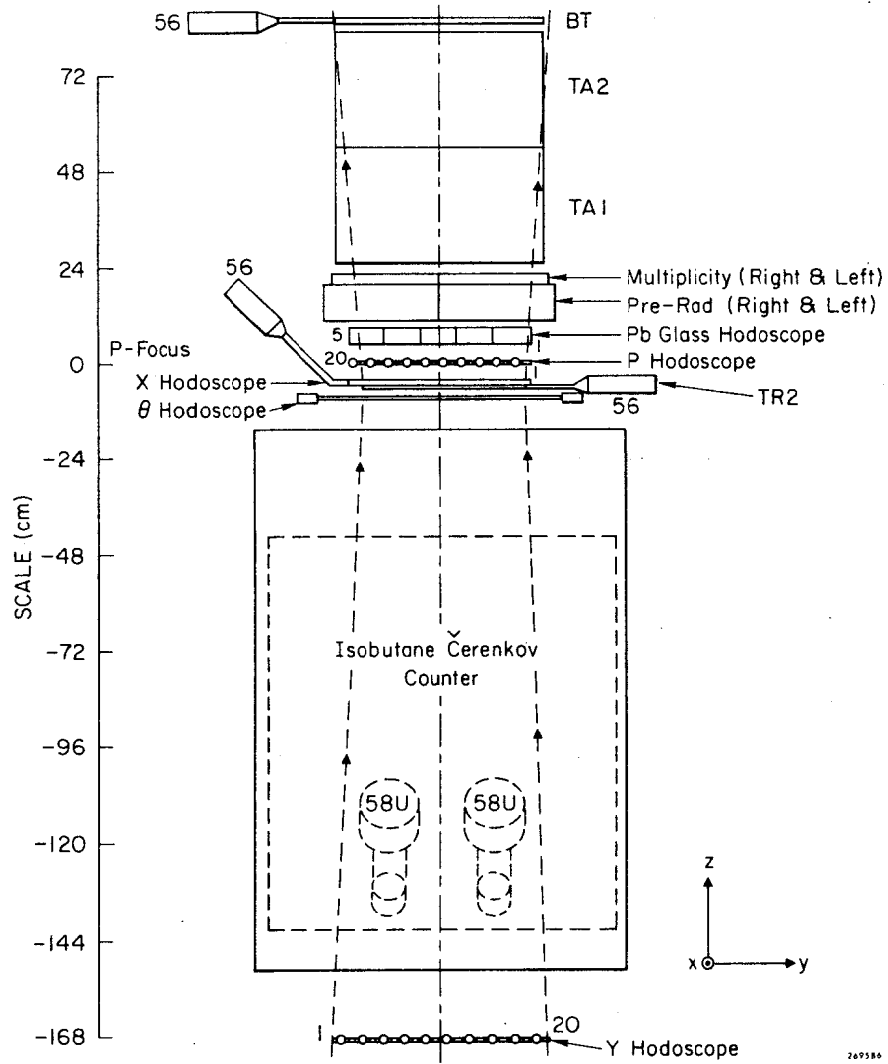


FIG. II-8a



THIS PAGE LEFT BLANK

FIG. II-8b

TABLE II-4

## 1.6 Counters

Name	X-Limits (cm)	Y-Limits (cm)	Material	gr/cm <sup>2</sup>	X <sub>0</sub> (Rad.Len.)	Distance of Nearest Sur- face to Focus (cm)	Comment
Y-Hodo	+11.43	+27.19	.32cm Scint.	.33	.0074	-168.9	2.72cm Bin Width
Cerenkov	+41.9	+45.7	134.cm ISOB 2/3 cm Lu- cite. Two .002" Al windows.	.34 .76 .03	.008 .018 .001	- 22.8	Effective Cerenkov path length (window to mirror) 124 cm.
Ø-Hodo	+15.98	+30.54	.64cm Scint.	.66	.015	- 10.3	2.13cm Bin Width
TR2	+13.89	+20.73	.64cm Scint.	.66	.015	- 3.8	
X-Hodo	+16.03	+22.00 -24.05	1.27cm Scint.	1.32	.030	- 2.5	6.39cm Bin Width
P-Hodo	+23.08	+22.90	.64cm Scint.	.66	.015	+ .52	2.30cm Bin Width
G-Hodo	+15.98	+23.09	4.0cm Pb Glass	14.4	1.25	6.0	9.20cm Bin Width
Pre-Rad	+20.95	+29.00	10cm Pb Glass	36.1	3.13	10.60	Two blocks-each 29cm in Y direction.
Multi- plicity	+20.00 -21.00	+27.00	2.54 cm Scint.	2.64	.060	21.3	Two pieces(LF & RT) each 27cm in Y dir- ection.
TA1	+24.04 -20.04	+26.04	29.2cm Pb Glass	104.7	9.13	25.7	
TA2	+24.07 -20.07	+26.07	29.0cm Pb Glass	105.4	9.06	55.0	
BT	+21.27 -18.73	+26.00	1.27cm Scint.	1.32	.030	89.5	

Physical dimensions of 1.6 counters and positions within the counter cave.

them. The Pb glass hodoscope (G-HODO) was matched to the p hodoscope with a 4:1 bin width ratio. The X-hodoscope (X-HODO,  $\frac{1}{4}$ " plastic scintillator) gave 3:1 binning of the  $\theta$  hodoscope. It was found that approximately 75% of the "multiple slat" events could be resolved using the coarse bin information (see Chap. III - Tracking and Codes).

The TR2 scintillator defined the counter package aperture. It covered p bins 2-19 and  $\theta$  bins 2-14. A signal from TR2 defined the event to be within the aperture used in calculating the cross sections. The stacking order of the hodoscopes and TR2 was done to minimize track reconstruction problems caused by knock-on electrons. The p hodoscope was located at the p-focus. TR2 was placed in front of the X-HODO to absorb knock-on electrons produced in either the  $\theta$  hodoscope or in the Cerenkov counter's mirror.

The Cerenkov counter and the TA package made up the electron detection system. The CT had an average flight path for particles of about 1.24 meters. The gas filling was isobutane at atmospheric pressure. A mirror made from  $\frac{1}{4}$ " lucite, slump molded and coated with approximately 2500 Å of aluminum and overcoated with 200 Å  $MgF_2$  imaged the Cerenkov light onto two quartz window 5" photomultipliers. An electron traversing this counter produced an average of 26 photoelectrons. In Fig. II-9 the distribution of the sum of the pulse heights from the two

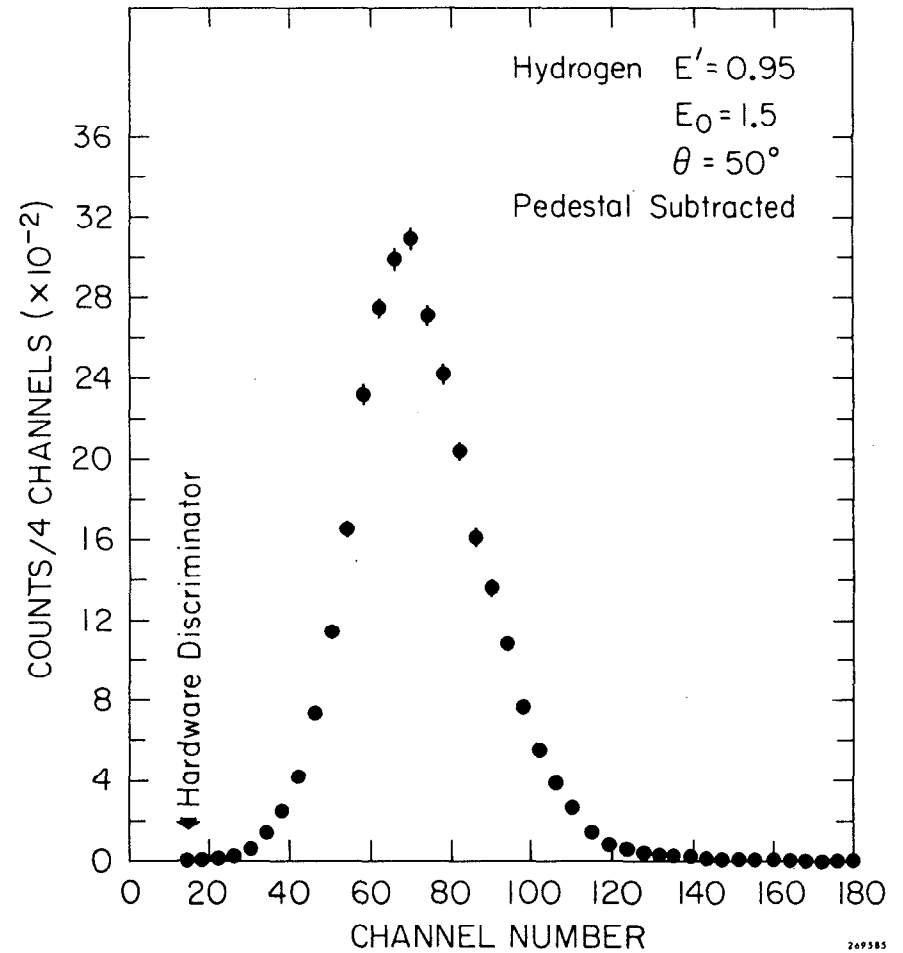


FIG. II-9

Pulse height distribution of the sum of the two photomultiplier signals from the Cerenkov counter. The kinematics correspond to elastic scattering off hydrogen.

phototubes is shown (no position correction has been made). The kinematics were set for elastic scattering to ensure we were observing electrons. The position of the hardware discriminator cut is indicated by the arrow. This cut resulted in about 250:1  $\pi/e$  rejection.

The TA package had 5 elements along the beam path (see Table II-4). The shower material was a low density lead glass (see Appendix B). This glass had good transmission far into the blue end of the spectrum. The most important elements for the total absorption signal were the PRERAD (3 rad.lengths) and TAL (9 rad.lengths) as a 1.3-GeV showers deposited about half its energy in each counter. Each element by itself produced a rather broad pulse height distribution, but the correlation of the signals produced by electrons was quite sharp (see Chap. III). A crude hardware TA signal, SUPS, was formed using passive adders and attenuators (see Fig. II-10). The arrow in Fig. II-10 indicates the position of the hardware discriminator threshold just above the minimum ionizing peak which yields an approximate 3:1  $\pi/e$  separation. This signal in coincidence with the CT signal was used as the main trigger interrupt in the experiment.

#### ELECTRONICS

Signals from the phototubes in the counter cave were transmitted to the counting house on RG-58 co-axial cable. Inverted dynode signals from the counters went directly to 8 bit pulse height analyzers. The anode signals were fed to

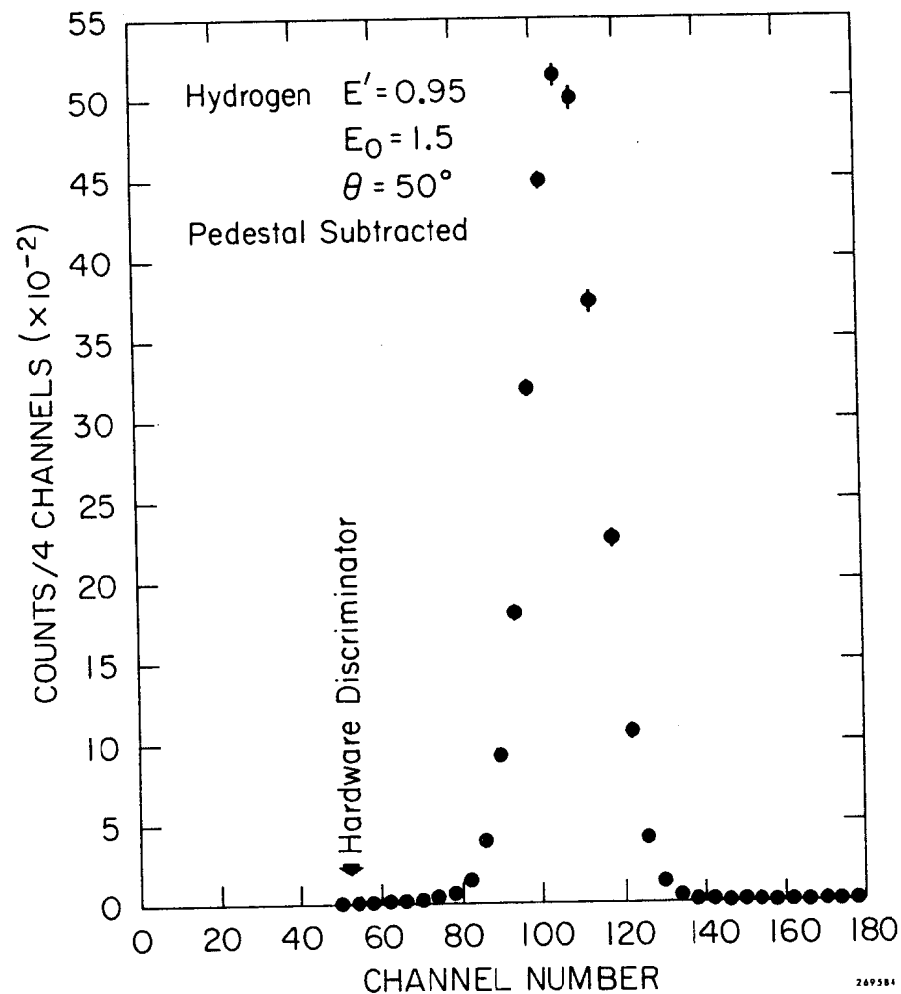


FIG. II-10

Pulse height distribution of hardware sum of signals from TA package. The kinematics correspond to elastic scattering off hydrogen.

the fast logic circuits. Some of the anode and dynode signals were passively added in the counter cave before transmission to the Counting House.

A schematic diagram of the electronics is shown in Fig. II-11. All discriminators were run in clipped mode. Signals from elements of the TA package were passively added to form a total energy absorption signal, SUPS (see Fig. II-10). This SUPS signal and the initial shower development signal, PRERAD, in conjunction with the Cerenkov signal (CT - see Fig. II-9) formed the various triggers for the experiment.

The main trigger, ORT, for the experiment was a coincidence between CT and SUPS (the discriminated SUPS signal was called GL) with hardware discriminator cuts as shown in Fig. II-9, 10. The electron detection efficiency was very close to 100% as determined from runs made at the elastic peak where the particles incident on the counters are predominantly electrons. The timing was set by the CT signal. Two identical trigger systems were used as the main triggers, each monitoring the electronics of the other (e.g., CT1, CT2 - GL1, GL2, etc.). During the experiment, monitoring of scaler ratios from these discriminators and coincidence units quickly revealed malfunctions such as double pulsing and dead units.

An ORTK signal was made by latching a coincidence circuit for the duration of the beam spill once an ORT trigger was received. Thus ORTK could fire at most once per pulse. This

ORTK circuit was reset at the beginning of each beam pulse. By using the ratio  $ORT/ORTK$ , an over-one correction for missed events was measured. Of course, many other over-one corrections factors can be constructed using flag and scaler information. All over-one corrections were found to be consistent except when malfunctions in one of the arms of the trigger occurred.

As the CTA1 and CTA2 rates were very low for the entire experiment, little fast electronics dead time is expected. The CT discriminators usually ran about 0.3/pulse almost independent of  $E'$  and polarity while the GL discriminator rates were dependent on  $E'$  and polarity, and these rates reached as high as 0.7/pulse. Both CT2 and GL2 were monitored for dead time by several discriminators having fixed dead times out to 180 nsec. Since most of the signals in CT2 are uncorrelated to those in GL2 (demonstrated by the small coincidence rate between them) their dead times should be added together. Straight line fits to the GL2 dead time scalers verses dead time when combined with the GL2 scaler information indicated approximately 33.4 nsec dead time for this signal. This measurement was confirmed by examining oscilloscope photographs of the pulses going into the GL2 discriminator. The CT2 dead time was found to be about 10 nsec. From these two dead times a correction to the data was made which was usually about 0.2% and always less than 2.0% for electron running.

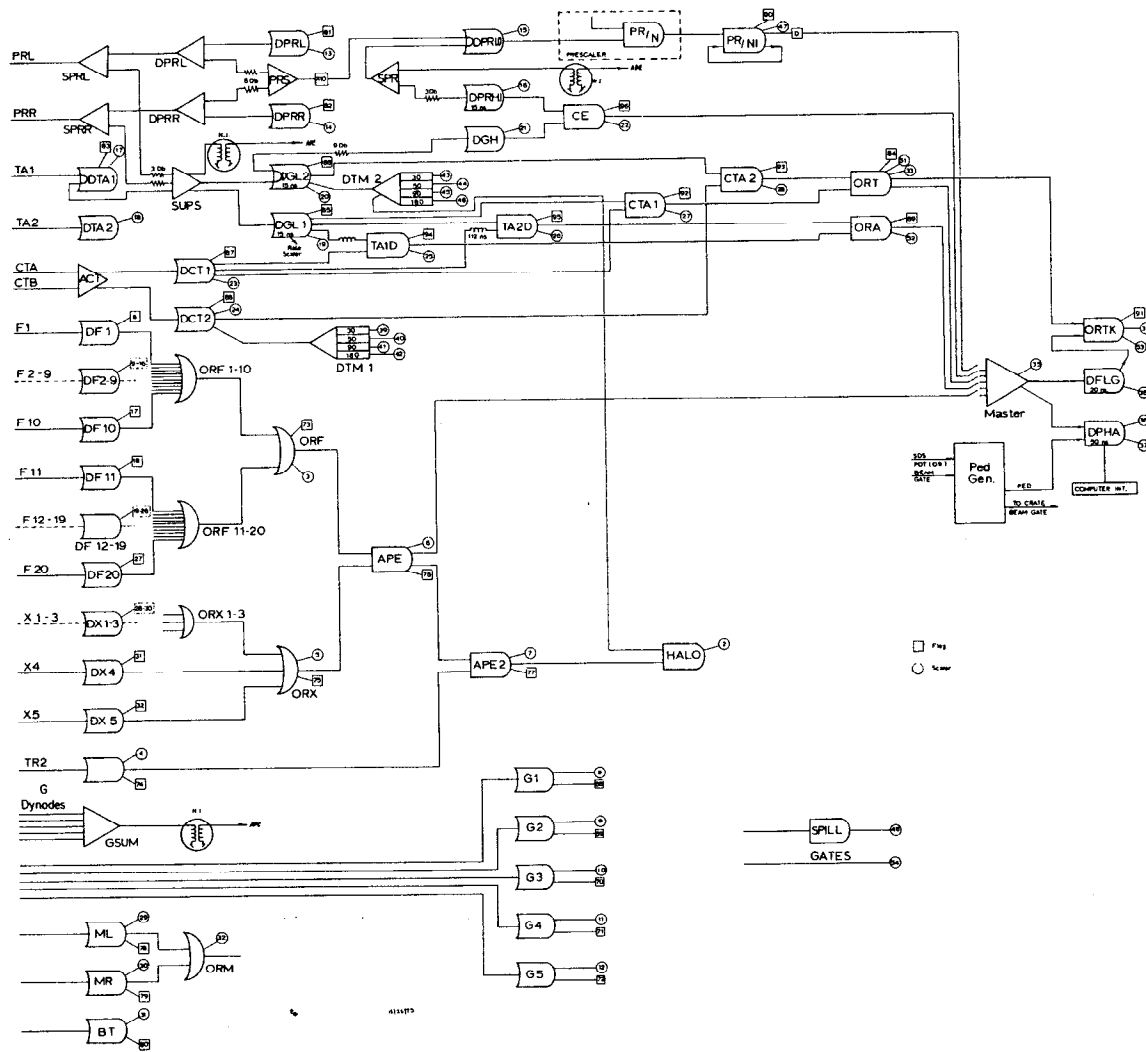


FIG.II-11

A schematic diagram of the fast electronics used for the 1.6.

In an experiment with a high background to signal ratio, measurement of chance events simulating real events is important. The accidental trigger, ORA, was made from two out-of-time coincidences, TA1D (GL1 delayed by 112 nsec with respect to CT1) and TA2D (CT1 delayed by 112 nsec with respect to GL1). The principal accidental trigger is taken to be TA2D as it strobed data into the PHA's and flag units in time with a pulse in the glass counters. As the associated CT signal is out of time by 112 nsec its PHA does not necessarily contain any information about the signal that fired its discriminator. Events gotten from TA1D were used to simulate the missing CT signals in the TA2D events.

With such an accidental scheme a correction must be made since chance coincidence can only occur 112 nsec after the beginning and before the end of each beam pulse (this correction =  $((1500-224)/1500) = 1./1.176$ ).

Three other triggers were also used to gather data. A CE trigger made by a coincidence between a high cut on the PRERAD and a high cut on SUPS produced data with about 80% detection efficiency for electrons, but did not require CT information. The purpose of this trigger was to monitor the CT. This data has too poor  $\sqrt{e}$  discrimination to clearly monitor the Cerenkov efficiency for most of the running and is therefore useless. A "junk" trigger made by prescaling a low threshold PRERAD discriminator on beam gates (usually 1:1000) also gen-

erated data. By using this trigger in the analysis associated with the flag information, biases could be investigated in the main trigger, ORT. Finally a simple scintillator trigger made by a coincidence between ORF and ORX, called APE, was used occasionally to record pion data. This APE trigger was also used for elastic peak checkout runs so as not to bias efficiency studies of the ORT trigger.

Three LeCroy 8 bit, 8 channel ADC's digitized the 18 incoming phototube signals. Pedestal drifts were monitored every 10 minutes from the computer by pulsing the PHA gate ten times out of time with the beam pulses. Online monitoring of drifts gave quick indication of trouble (such as faulty power supplies). The gate pulse for the PHA's was set to 48 nsec by a 24 nsec clipping stub. The leading edge of the input pulses to be analyzed were set 10 nsec inside the front edge of the gate to allow for 6 nsec ADC activation time and up to 4 nsec forward time jitter in the signal.

The flag information is somewhat different from the PHA information as its time resolution was about 3 times better. The flag units were LeCroy discriminator-latch units into which the p- $\theta$  hodoscope phototube signals were directly fed. All other signals to the latch units went through separate discriminators first. The flag gate was set to 14 nsec using a 7 nsec clipping cable. The timing was set so that the leading edge of the flag signal fell in the center of the flag gate. The front end



discriminators in these units fired off the leading edge of the input signal and were clipped to 4 nsec internally. This, of course, generates problems with high rates, and deadtime-less operation of these units would have served us better.

The scalers were CAMAC "blind" scalers with 100 MHz counting rate capacity. These were read by the computer every 10 minutes during a "recess" which secured enough information from the equipment to end the data run at that time. This recess concept was used to protect against losing large amounts of data on a long run terminated by an unexpected "crash" of some kind.

The online XDS-9300 computer wrote 7-track, 800 BPI data tape for subsequent offline analysis. A total of 28 data tapes were made. The computer made various pulse height histograms and formed linear combinations of the hardware pulse heights with which to perform an online analysis. Various counter cross sections for the spectrometer setting as well as a missing mass spectrum for the entire line being run were stored and updated appropriately to help the experimenters monitor the functioning of the equipment.

In a dual experiment such as E-89 where two separate experiments are sharing the same target and beam, generating and maintaining a compatible run plan is a major project. The procedure was automated by reading preprogrammed run plans into both online computer at the start of each new incident energy and angle. This automatic sequencing of runs made it possible to make over 1700 runs on the 1.6-GeV spectrometer and about 1500

runs on the 20-GeV spectrometer.

## CHAPTER II REFERENCES

1. The Stanford Two-Mile Accelerator, R. B. Neal, Ed; Benjamin, New York (1968).
2. R. Anderson et al., Nucl. Instr. and Methods 66, 328 (1968).
3. Precision surveys and extensive magnetic measurements of the A-line result in between  $\pm .1\%$  and  $\pm .2\%$  absolute calibration in the energy determination of the center of the momentum slits.
4. R. S. Larsen and D. Horelick, Proceedings of the Symposium on Beam Intensity Measurement, Daresbury Nuclear Physics Laboratory (1968).
5. D. Yount, Nucl. Instr. and Methods 52, 1 (1967).
6. Bell et al., SLAC Pub 557 (1969).  
Mark et al., SLAC Pub 883 (1971).
7. L. A. Weber et al., Cryogenics 2, 236 (1962).
8. A. Bodek, Thesis, M.I.T. Laboratory for Nuclear Science, Report No. COO-3069-116 (1972).
9. Bubble Chamber Group Selected Cryogenic Data Notebook compiled by J. E. Jensen et al. (1966) BNL 10200.  
and H. M. Roder et al., "Survey of the Properties of Hydrogen Isotopes Below Their Critical Temperature," NBS Technical Note 641 (1973).

## CHAPTER III

### ELECTRON COUNTING AND EXPERIMENTAL CORRECTIONS

The analysis of the data proceeds in four steps referred to as "passes." The reduction of the data in each pass involves a loss of detailed information but results in a more compact data set. Each pass is carefully studied to ensure that the lost information is well understood at the time of discard. Our objective is to retain as much information as possible at a particular level to facilitate studies at that level, while keeping the data set and computer analysis time within reasonable bounds.

Briefly, the four passes are: Pass 1 launders the data and applies some corrections to provide clean events for Pass 2 which sorts out electrons and bins them into missing mass spectra for Pass 3 which calculates cross sections, subtracting off the empty target and positron contributions for Pass 4 which applies calculated corrections (radiation and Fermi motion effects) to the data to give proton and neutron cross sections. Table III - 1 shows the analysis scheme in more detail.

Passes 1 and 2 required the most computer time. Detailed studies of track reconstruction and efficiencies were done in these Passes, and the information contained in the events was processed and used to distinguish pions from electrons. Pass 1 reduced the data base stored on magnetic tape, and the results were stored on magnetic disk. Event by event information was retained at this level including 5 pulse height signals (PHS) and tracking

TABLE III - 1  
ANALYSIS SCHEME

PASS	COMPUTER TIME	EVENTS	ANALYSIS SUMMARY
1	6 hours	500K	Tracking: unique P, $\theta$ , $\phi$ and codes assigned each event PHS: position corrections, combining, leaving CT,TFT,MULT,TA1 and TA2. Monitor: target,spectrometer, electronics. Output: PASS1 disk data set (event by event). Microfilm summary of each run. Paper output summarizing job.
2	1.5 hours complete. 1-4 minutes typical study run.	100K	Most detailed analysis done at this level. Tracking: efficiencies, combining codes into codes classes. PHS: cut efficiencies,combining cut criterion into PHS classes. Output: final run produced measured missing mass spectra including all experimental corrections. Microfilm summary of each setting. Disk file of missing mass cross sections. Paper output summarizing job.
3	1 minute	9 lines	Reduced the 6 spectra per E and $\theta$ to final hydrogen and deuterium cross sections, (subtract empty target and positron signals).
4	1 hour	9 lines	Radiative corrections: elastic (and quasi-elastic) radiative tails subtracted. Inelastic radiative corrections. Neutron extraction: proton smearing, deuteron subtraction and neutron unsmearing. Output: disk file with final N, P and D cross sections.

information (hodoscope binning). Once the events were on disk, many detailed studies were carried out to determine tracking efficiencies and "cut" efficiencies on the PHS's. These studies culminated in Pass 2 to produce the line by line cross sections binned in missing mass. Pass 1 was done five times as information feedback from Pass 2 affected the Pass 1 analysis. Pass 2 was repeated many times. The data searching program allowed for concatenation of any subset of all the runs defined by run number, E',  $\theta$ , E<sub>0</sub> and target type. This made for easy testing of many systematic effects at the Pass 2 level. This type of computer job usually required between 1 and 4 minutes of computer time. All of the Pass 2 sub-programs were backwards compatible with Pass 1.

The processing of the events in Pass 1 and Pass 2 will be discussed in this Chapter. Corrections, theoretical and experimental (other than electron counting), are discussed in Chapter IV.

#### PULSE HEIGHT ANALYSIS

The counters in the experimental setup produced 18 pulse height signals (PHS) for each event. Some of the pulse height information was complementary, that is, two phototubes viewed the same light source (as in the CT, PRERAD left, PRERAD right, TA1 and TA2). Furthermore, many of the signals were highly correlated when an electron passed through the counter stack. The first

task was to reduce the original pulse heights to a small set of combined PHS's. The combining was done to optimize the resolution of the system for electrons. The assumption was made that optimizing the electron resolution would also nearly optimize  $\pi/e$  separation. The PHS analysis flow chart is shown in Fig. III-1.

All the PHA pedestals were monitored at ten minute intervals during the experiment. This information was used to subtract the pedestal from each PHS before further analysis. Tests on the PHA units used assured us that they were linear to better than 2% over an effective range of approximately 250 channels. The pedestal usually fell in channel 5 or 6.

One can easily derive the optimization rule for linearly combining  $n$  PHS's to minimize the resolution. Let  $e_{ij} = j^{\text{th}}$  PHS of the  $i^{\text{th}}$  event. Then for  $N$  events and  $n$  PHS's

$$S_j = \frac{1}{N} \sum_{i=1}^N e_{ij} \quad \text{is the first moment of the } j^{\text{th}} \text{ PHS.}$$

$$P_{ijk} = \frac{1}{N} \sum_{i=1}^N e_{ij} e_{ik} \quad \text{are the second moments.}$$

We wish to find a set of  $C_j$  so events defined by

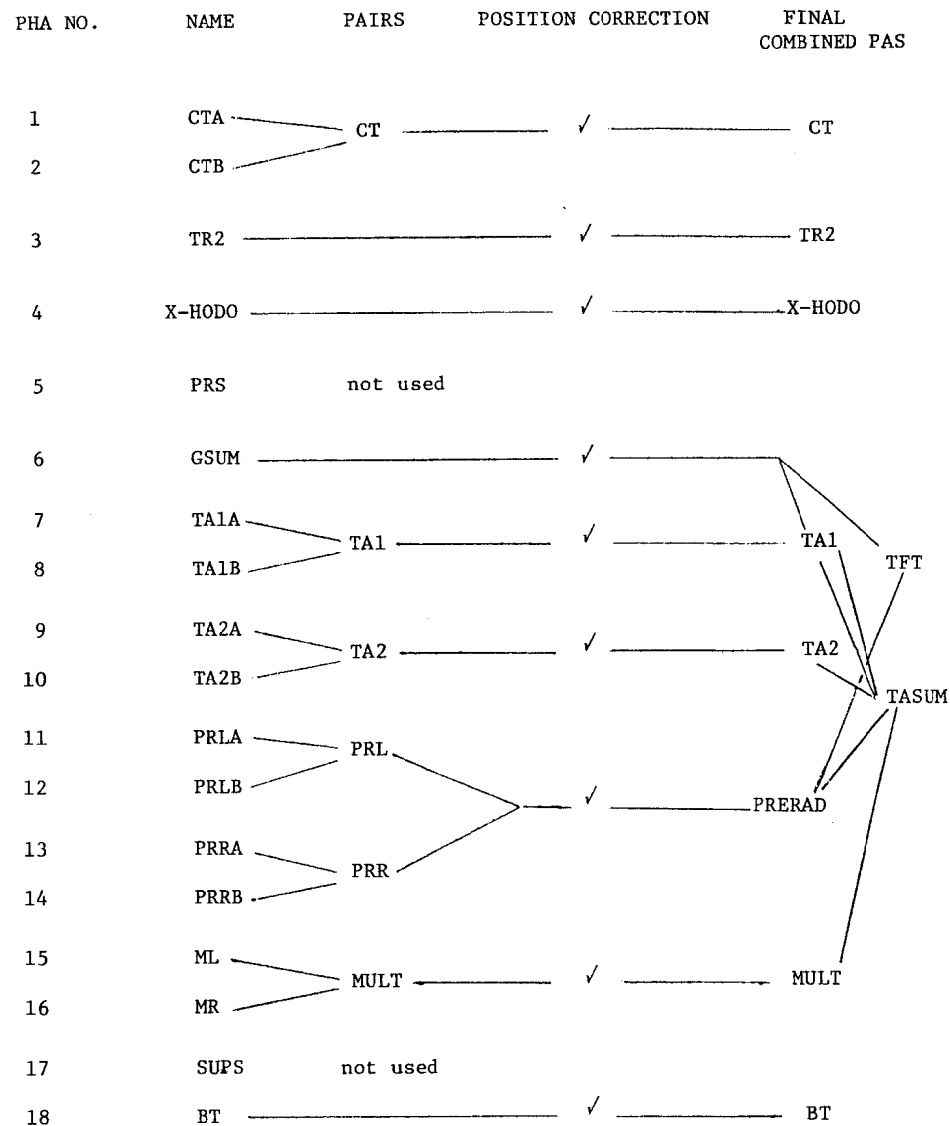
$$E_i = \sum_{j=1}^n C_j e_{ij} \quad \text{have optimal resolution,}$$

R(minimum width/mean).

$$\mu = \frac{1}{N} \sum_{i=1}^N E_i = \sum_{j=1}^n C_j S_j \equiv C_j S_j \quad (\text{repeated indices are}$$

summed over)

FIG. III - 1  
PULSE HEIGHT ANALYSIS  
FLOW CHART



$$\sigma^2 = \frac{1}{N} (E_i - \mu)^2 = C_i C_j P_{ij} - C_i C_j S_i S_j$$

$$R = \sqrt{\sigma^2 / \mu^2}$$

By differentiating R with respect to  $C_k$  one finds that the smallest R is given by

$$C_k = N_r (P_{jk})^{-1} S_j \text{ where } (P_{jk})^{-1} \text{ is inverse of the matrix of } P_{jk},$$

where  $N_r$  is an arbitrary normalization constant, (actually  $N_r = (C_j C_n P_{jn} / C_m S_m)$ , but since there are no unrepeat indices this is just a number that can be chosen to normalize the  $E_i$ ). This rule is quite general as we have only assumed the existence of the first and second moments of the PHS's (of the  $e_{ij}$ 's) input into the problem.

The procedure was to first combine all A,B pairs of phototube signals from the CT, the left and right PRERAD, TA1, and TA2. Optimization of each combination was performed using an almost pure electron sample from the high statistics (about 50K events) low  $E_0$  elastic peak runs taken near the end of the first data taking period (see Table I-1). Events were required to have a missing mass within 15 MeV of the proton mass, to have fired only one hodoscope slat in each of the hodoscopes and to fall within two hodoscope bins (about 2") of the center of the counter in question (to avoid spurious aperture effects). Typically, each pair was balanced with about 5K events satisfying these criteria. Also the left and right PHS's from the PRERAD and MULT were adjusted to have the same average pulse height and then combined to make a

single PHS at this stage.

The PHS's were then corrected for position to ensure that electrons of the same energy gave close to identical counter response independent of the measured X,Y, and  $\phi$  coordinates. The method here was to fit the means of the distributions from different regions of the counters to polynomials in the X, Y, and  $\phi$  coordinates and then to divide the resultant polynomials into the pulse height signals before further analysis. These corrections never exceeded 20%. This improved the resolution across the entire aperture and made discrimination curves insensitive to position. Cuts on these "flattened" pulse heights minimize spurious position dependent biases.

At this stage, most of the signals were ready for use in the analysis except for a total energy absorption signal, TASUM. By applying the combination formula previously derived the PHS's of the TA stack were added together linearly to obtain a final signal of good resolution. Choosing as a reference the minimum ionizing signals from each segment (i.e., adjust the gain of each signal from each section of glass to give the same average minimum ionizing pulse height) the optimal glass addition coefficients had the proportions 1:3:9 for GSUM:PRERAD:TA1. These corresponded to their radiation lengths as expected. It was found that small amounts of the MULT (1" plastic scintillator "multiplicity" counter located between PRERAD and TA1) and TA2

(the 9 radiation length lead-glass counter located directly behind TAl) gave noticeably better resolution (see Appendix B). The glass hodoscope signal, GSUM, and the PRERAD were added together for Pass 2 to make a TA Front Trigger, TFT. Figure III-2 shows the various final PHS distributions used in the analysis measured at elastic peak kinematics.

Pulse height discrimination curves were fit to integrated distributions like those shown in Fig. III-2 for energies from 0.830 GeV to 1.66 GeV using the various low  $E_0$  elastic peak data at 50 and 60 degrees and were used to calculate the fraction of the electron sample eliminated by making a cut on the data requiring that the PHS be greater than the cut value. The analysis strategy was to make low cuts on many distributions, rather than high cuts on a few. The order in which cuts were made for the analysis stream was TFT, TAl, CT and then TASUM. For example, Fig. III-3a shows a TFT vs TAl scatter plot of data taken at low  $E'$  and at an  $E_0$  of 19.5 GeV on deuterium. In Fig. III-3b, a scatter plot of low incident energy, elastic scattering data of approximately the same  $E'$  is shown for comparison. The two straight lines in Fig. III-3a indicate the cut positions of the two one-dimensional cuts used (TFT > 20 and TAl > 15). These two cuts eliminate electrons from opposite ends of the correlated electron signal (diagonal blob) and are uncorrelated in detection efficiency (we are not eliminating the same electrons twice).

Further  $\pi/e$  discrimination is possible. Consider a CT

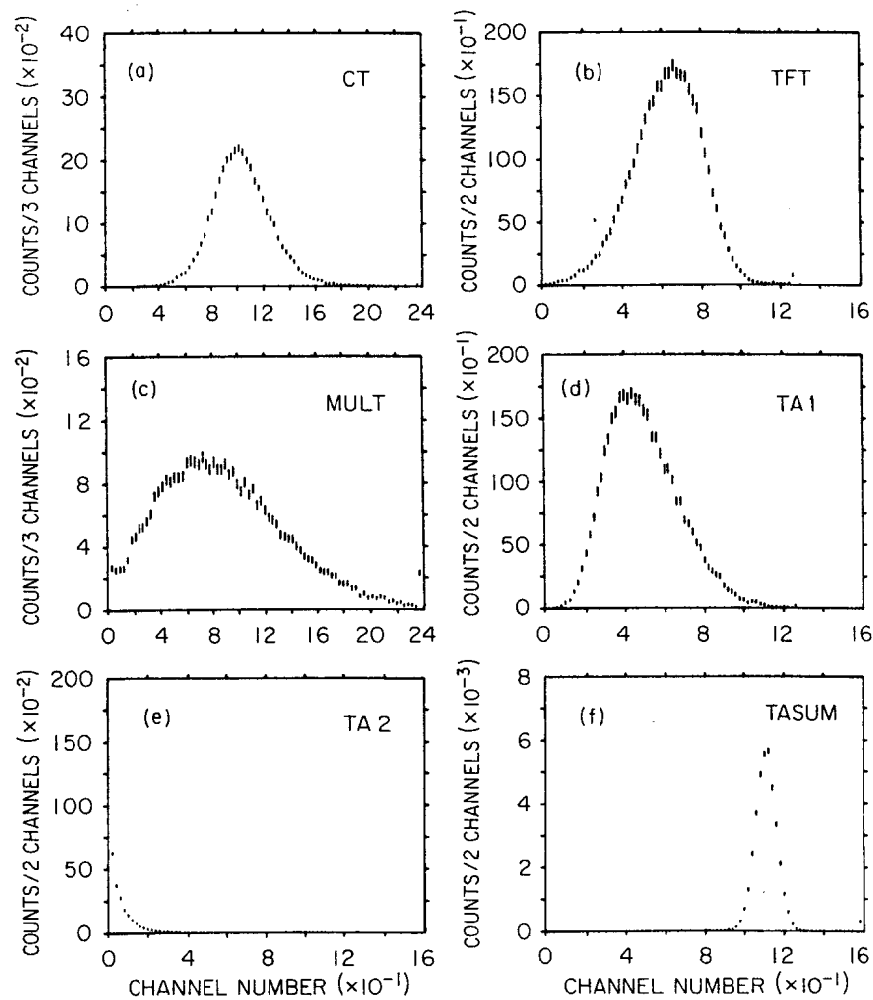


FIG. III-2

The six PHS's used in the analysis .

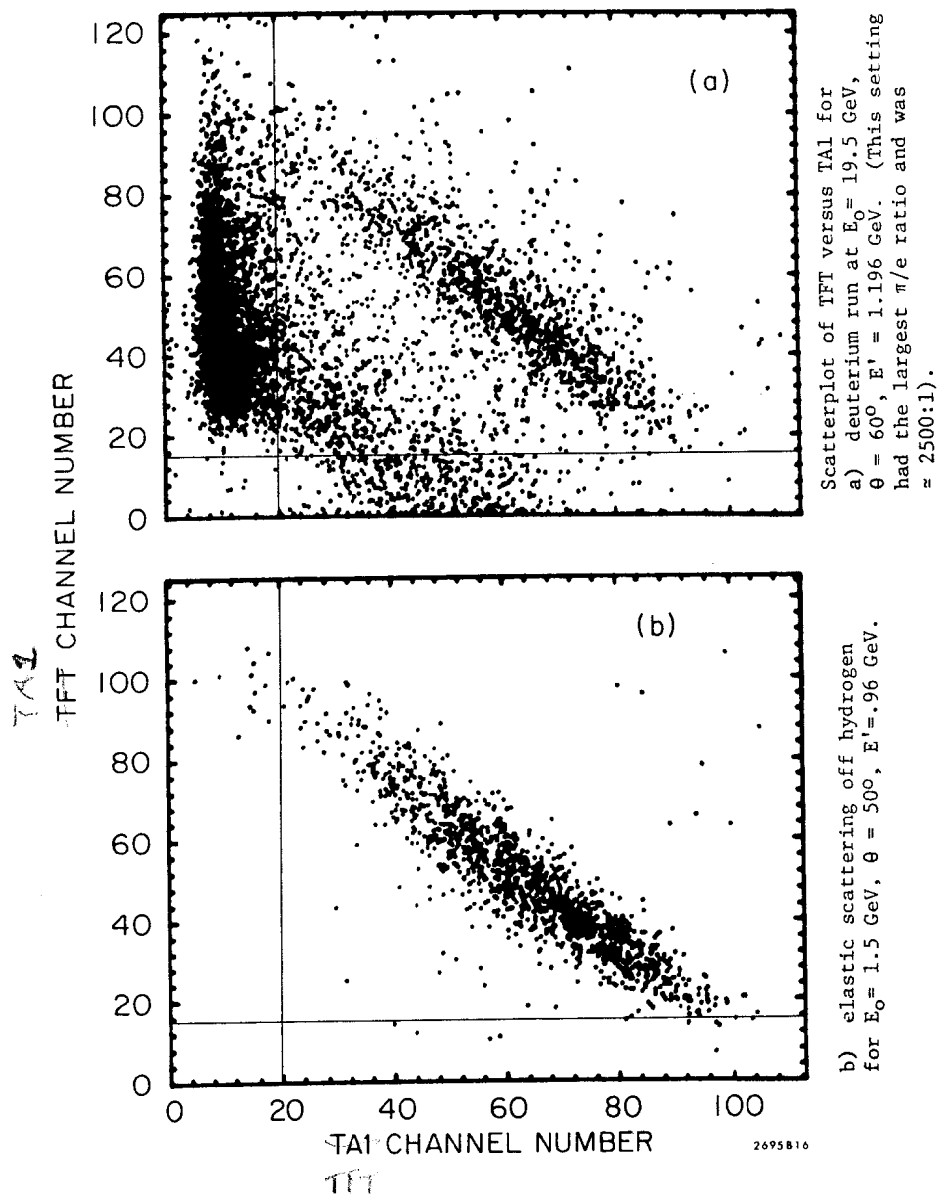
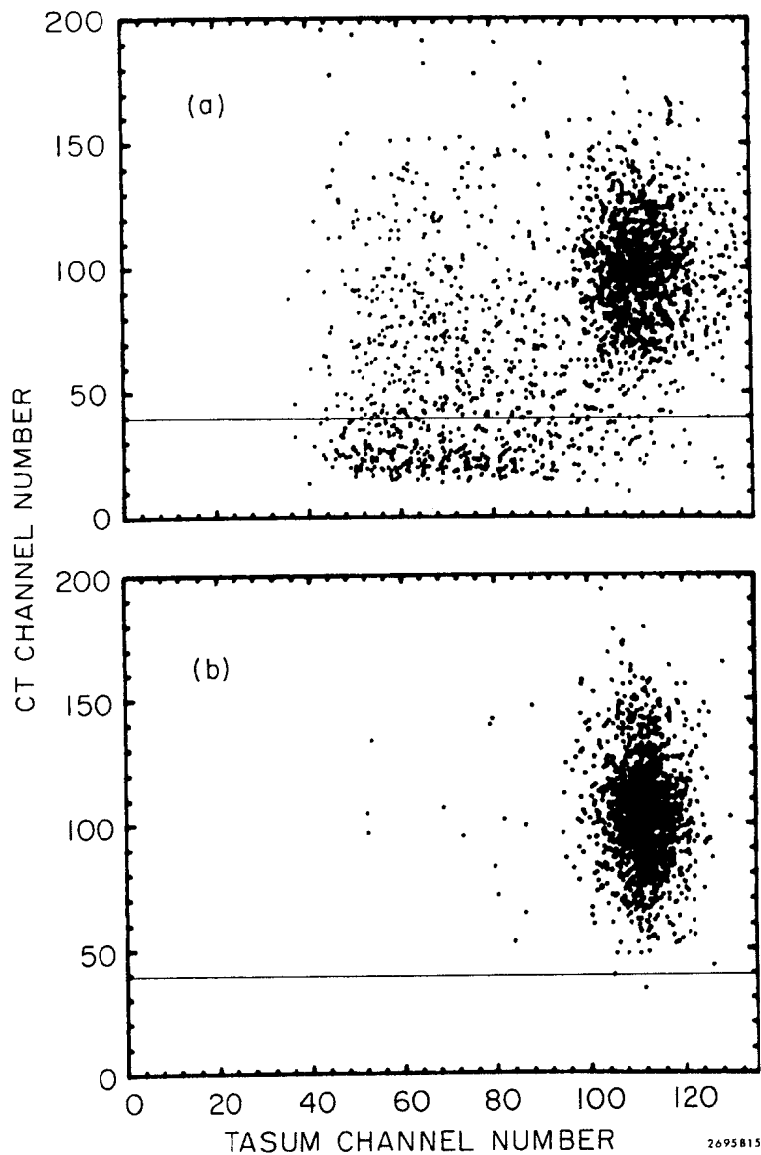


FIG. III-3

vs. TASUM scatter plot of the same data on which the previous two cuts have been applied (see Fig. III-4a). Again, the same elastic electron sample is shown in Fig. III-4b for comparison. The CT cut is indicated by the line in Fig. III-4a. Notice the electron signal from the TA package and the CT are uncorrelated. In Fig. III-5, the TASUM distribution before and after application of these three one-dimensional cuts is shown demonstrating that a large fraction of the pions have been rejected while retaining a high electron detection efficiency.

The remaining electron signal (the TASUM plot) is now cut at  $x_c$  as shown in Fig. III-6. A small pion tail remains underneath the electron peak. This distribution was fit to a pion shape and an electron shape as indicated by the curves. The pion spectrum was approximated by a falling exponential in the region of the electron peak. The shape of this function was modeled on data that satisfied the TFT and TAI cut conditions but had a small or zero CT PHS. The pion shape under the electron peak was not very sensitive to the TFT and TAI cut positions. The electron distribution was fit to two shapes: A Gaussian that accounted for most of the signal and a function similar to the pion function at higher pulse heights than the electron peak to account for "e +  $\pi$ " events. The fitted fraction of these e +  $\pi$  events, whose presence is seen as a shoulder on the high pulse height side of the electron peak in Fig. III-6, tracked well with the APE coincidence rate. The ratio of the fitted "noise"



Scatterplot of CT versus TASUM for the same data shown in Fig. III-3 after the TFT and TAI cuts have been applied. Again a) is deuterium for  $E_0 = 19.5$  GeV,  $\theta = 60^\circ$  and  $E' = 1.196$ .

b) elastic scattering off hydrogen for  $E_0 = 1.5$  GeV,  $\theta = 50^\circ$  and  $E' = .96$  GeV.

FIG. III-4

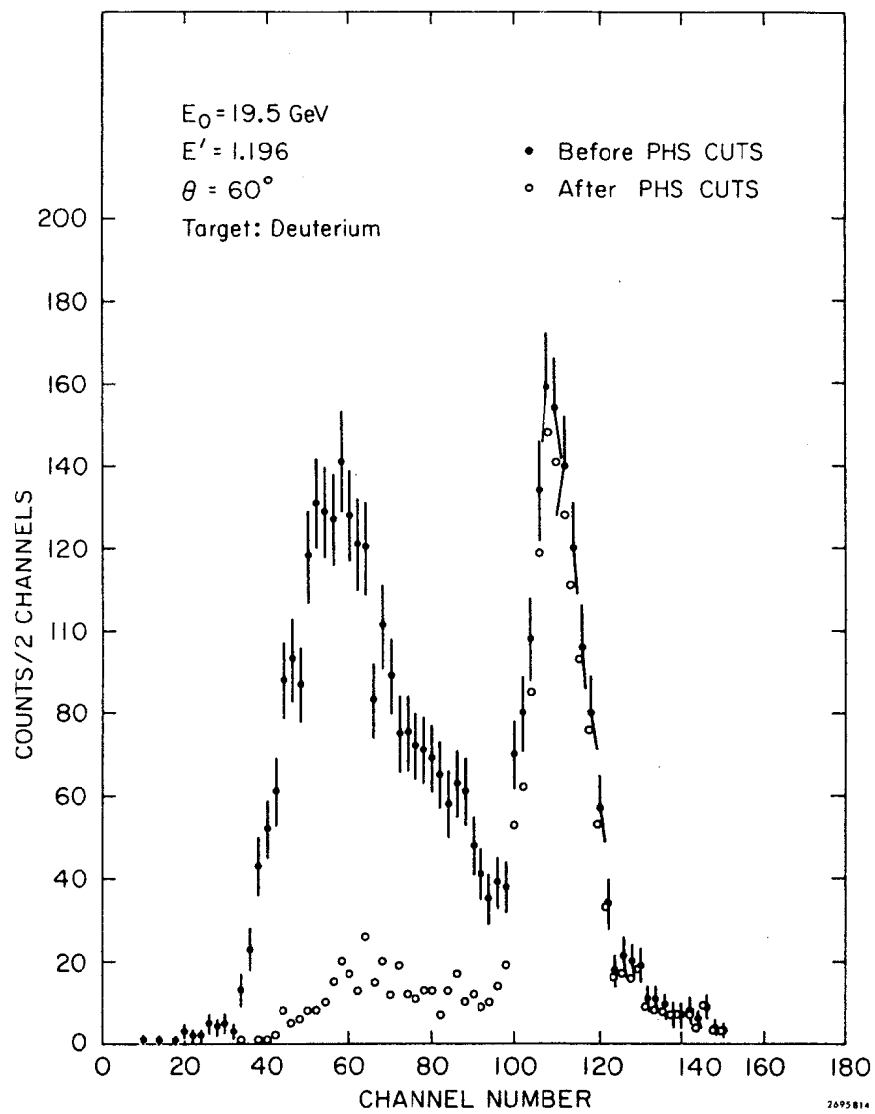


FIG. III-5

A plot of TASUM before and after the TFT, TAI and CT cuts have been applied.



Plot TASUM showing cut position,  $x_c$ , and fits used to estimate the electron detection efficiency and the pion subtraction factor.

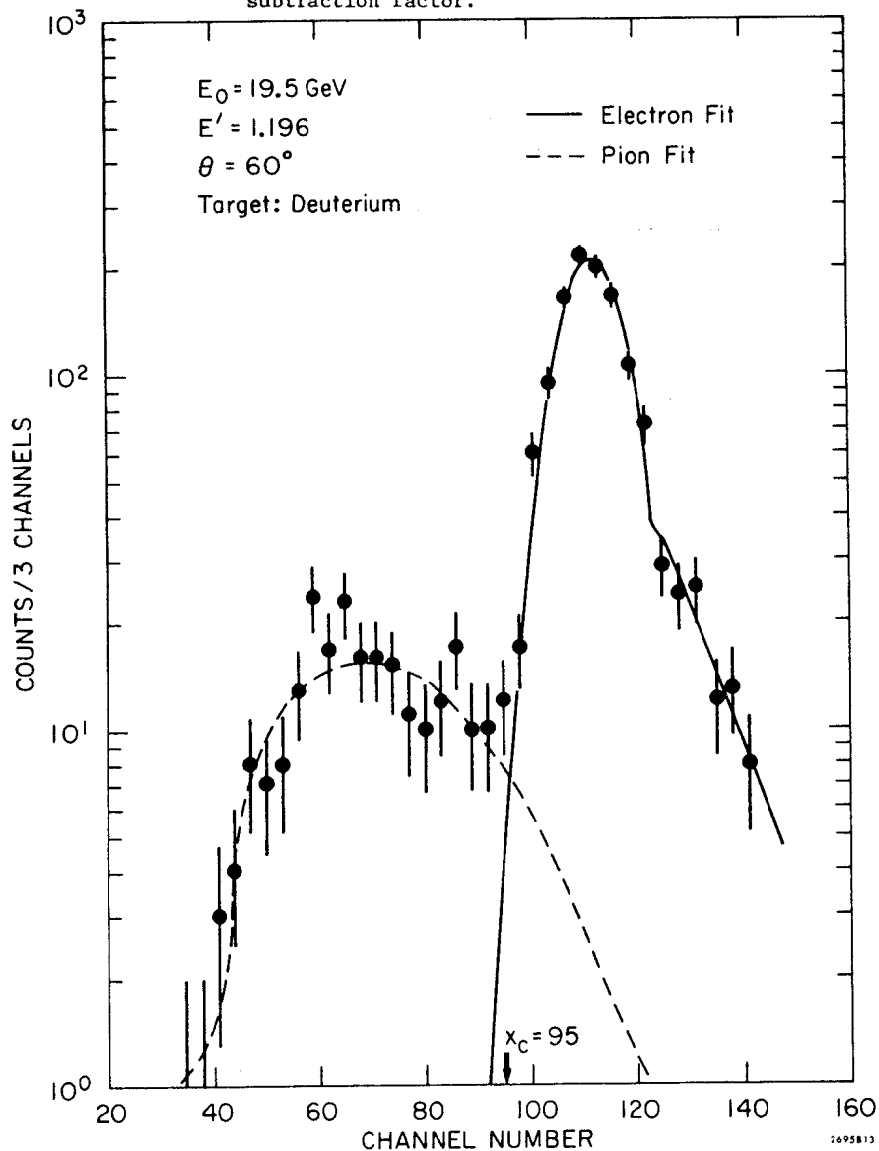


FIG. III-6

fraction  $(e + \pi)/e$  to the APE rate was approximately

40/1500 which is the PHA gate length/spill length.

A pion correction factor

$$C_{\pi} = \frac{\int_{x_c}^{\infty} f_e(x) dx}{\int_{x_c}^{\infty} (f_e(x) + f_{\pi}(x)) dx}$$

was calculated from the fitted functions  $f_e(x)$  (electron shape) and  $f_{\pi}(x)$  (pion shape). Also the electron efficiency factor

$$C_{eff} = \frac{\int_{x_c}^{\infty} f_e(x) dx}{\int_0^{\infty} f_e(x) dx}$$

was calculated. Both of these factors were used to correct the electron sample.

With five separate PHS's as well as a combined TASUM PHS, a variety of cut combinations are possible. To choose an optimal set of cuts (cuts which maximize  $\pi/e$  separation) at a given electron detection efficiency various possibilities were systematically considered. Table III-2 summarizes the results. This is a representation of a  $4 \times 4 \times 4 \times 4$  matrix with each of the 16 sub-boxes showing the  $4 \times 4$  expansion in the TPT and CT cut effectiveness. Each of the sub-boxes has a different TAL and/or MULT cut. The two entries for every cut condition are: 1) the calculated electron efficiency for those cuts, before a TASUM cut at  $x_c = 95$ , and 2) the number of counts less than 95 in TASUM divided by the number of counts greater than 95 (this gives a crude indication of  $\pi/e$  separation). (15% of this fraction is approximately

TABLE III - 2

		TA1 → 10				15				20				25			
		TFT →															
		10	20	30	40												
C	T	1.000	0.998	0.965	0.885	1.000	1.000	0.967	0.886	1.000	0.999	0.965	0.882	0.992	0.988	0.953	0.869
	30	0.443	0.246	0.168	0.098	0.393	0.199	0.130	0.075	0.344	0.155	0.097	0.056	0.299	0.118	0.070	0.040
U	40	1.000	0.996	0.963	0.884	1.000	0.999	0.965	0.884	1.000	0.997	0.962	0.880	0.991	0.986	0.950	0.867
	50	0.393	0.228	0.156	0.092	0.347	0.184	0.122	0.071	0.302	0.144	0.091	0.053	0.260	0.109	0.066	0.037
L	60	0.995	0.991	0.958	0.879	0.998	0.993	0.960	0.879	0.996	0.991	0.957	0.875	0.986	0.980	0.945	0.862
	70	0.340	0.204	0.143	0.084	0.298	0.164	0.110	0.065	0.257	0.127	0.083	0.049	0.220	0.096	0.060	0.035
T	80	0.979	0.974	0.942	0.863	0.981	0.976	0.943	0.863	0.979	0.974	0.940	0.860	0.968	0.962	0.928	0.847
	90	0.299	0.188	0.131	0.078	0.261	0.151	0.102	0.060	0.223	0.117	0.076	0.045	0.189	0.088	0.054	0.032
M	100	0.996	0.994	0.962	0.883	0.998	0.996	0.964	0.883	0.997	0.995	0.961	0.879	0.986	0.983	0.949	0.866
	110	0.409	0.225	0.156	0.092	0.367	0.184	0.122	0.071	0.324	0.144	0.092	0.053	0.283	0.111	0.066	0.038
5	120	0.995	0.993	0.960	0.881	0.997	0.994	0.962	0.881	0.996	0.992	0.959	0.877	0.985	0.991	0.947	0.864
	130	0.362	0.208	0.145	0.086	0.323	0.170	0.114	0.067	0.283	0.134	0.086	0.050	0.245	0.102	0.062	0.036
10	140	0.991	0.988	0.955	0.876	0.993	0.989	0.956	0.876	0.991	0.987	0.953	0.872	0.980	0.975	0.941	0.859
	150	0.312	0.186	0.132	0.079	0.277	0.151	0.103	0.062	0.241	0.119	0.078	0.047	0.207	0.090	0.056	0.033
15	160	0.974	0.970	0.939	0.861	0.976	0.971	0.940	0.861	0.974	0.969	0.937	0.857	0.963	0.957	0.924	0.844
	170	0.273	0.171	0.121	0.074	0.241	0.139	0.095	0.057	0.208	0.109	0.071	0.043	0.177	0.082	0.051	0.031
20	180	0.992	0.989	0.958	0.879	0.994	0.991	0.959	0.879	0.992	0.989	0.956	0.875	0.982	0.978	0.944	0.862
	190	0.367	0.215	0.149	0.088	0.348	0.177	0.118	0.068	0.309	0.140	0.089	0.052	0.271	0.108	0.065	0.037
25	200	0.991	0.987	0.956	0.877	0.993	0.989	0.957	0.877	0.991	0.987	0.954	0.873	0.980	0.976	0.942	0.860
	210	0.342	0.198	0.139	0.083	0.307	0.164	0.110	0.065	0.270	0.130	0.084	0.049	0.235	0.100	0.061	0.035
30	220	0.986	0.982	0.951	0.872	0.988	0.984	0.951	0.872	0.986	0.981	0.948	0.868	0.975	0.970	0.936	0.855
	230	0.295	0.177	0.126	0.076	0.262	0.146	0.100	0.059	0.230	0.115	0.076	0.046	0.198	0.088	0.055	0.033
35	240	0.970	0.965	0.934	0.857	0.971	0.966	0.935	0.857	0.969	0.964	0.932	0.853	0.958	0.952	0.920	0.840
	250	0.259	0.163	0.116	0.071	0.229	0.134	0.092	0.055	0.199	0.106	0.070	0.043	0.170	0.081	0.051	0.030
40	260	0.987	0.983	0.952	0.874	0.989	0.984	0.953	0.874	0.987	0.982	0.950	0.870	0.977	0.971	0.938	0.857
	270	0.314	0.198	0.141	0.084	0.279	0.164	0.111	0.066	0.244	0.131	0.085	0.050	0.211	0.102	0.063	0.036
45	280	0.986	0.981	0.950	0.872	0.988	0.983	0.951	0.872	0.986	0.980	0.948	0.868	0.975	0.969	0.936	0.855
	290	0.280	0.184	0.131	0.079	0.248	0.152	0.104	0.062	0.215	0.122	0.080	0.048	0.184	0.094	0.058	0.034
50	300	0.981	0.976	0.945	0.867	0.983	0.977	0.945	0.867	0.980	0.975	0.942	0.863	0.969	0.963	0.930	0.850
	310	0.243	0.165	0.119	0.073	0.214	0.136	0.095	0.057	0.184	0.108	0.073	0.044	0.156	0.083	0.053	0.032
55	320	0.965	0.959	0.929	0.852	0.966	0.960	0.929	0.852	0.963	0.957	0.926	0.848	0.952	0.946	0.914	0.835
	330	0.216	0.151	0.110	0.068	0.189	0.125	0.087	0.053	0.161	0.099	0.067	0.044	0.136	0.076	0.049	0.029

A 4x4x4x4 matrix showing various cut effects for TA1, CT, MULT and TFT. For each cut combination in the two entries are 1) electron detection efficiency and 2) pion contamination.

equal to  $(1 - C_{\pi})$  previously defined). The boxed-in elements indicate our choices for "optimal"  $\pi/e$  separation points in order of decreasing electron detection efficiency.

Six PHS classes were selected and are summarized in Table III-3. A test of the analysis procedure is how invariant the cross sections are to PHS class. Over the six classes the cross sections were usually found to vary less than 4% absolute while the detection efficiency varied by over 20% from the different PHS cuts made.

#### TRACKING AND CODES

The first task in analyzing a hodoscope system is to assign a unique slat to every event in each hodoscope. The backup coarse hodoscope on the  $p-\theta$  slats proved valuable in analyzing multiple slat events. For example, in an event consisting of a cluster of hit slats along with a single separate slat, we found that the backup hodoscope information favored assigning the event to the single slat as often as to the cluster. Events requiring the coarse hodoscope information were called "saved" events. Four hit patterns were recognized and classified: 1) a single slat, 2) two adjacent slats, 3) two slats separated by one blank slat, and 4) three slats with one imbedded blank slat or four adjacent slats. Each event had a tracking code (numbered 0-8) assigned to each hodoscope. Odd code numbers (1, 3, 5, 7) were given hodoscope patterns that didn't require saving and even numbered codes (2, 4, 6, 8) were the corresponding codes for saved patterns. The code number 0

TABLE III - 3  
PHS CLASSES

CLASS	CT	TFT	MULT	TA1	TASUM	EFFICIENCY (TYP)
I	30	10	-	10	95	.998
II	40	20	-	15	95	.980
III	50	20	-	20	95	.969
IV	60	30	-	25	95	.910
V	60	40	15	25	95	.792
VI	60	40	15	25	100	.771

The Table shows the various cut conditions selected for optimal  $\pi/e$  separation.

All cuts pass events which have a pulse height signal greater than the value shown. Class II is our choice for the analysis class.

referred to the case where no slats in a hodoscope fired. In Fig. III-7, typical hit patterns and their code and bin assignments are shown.

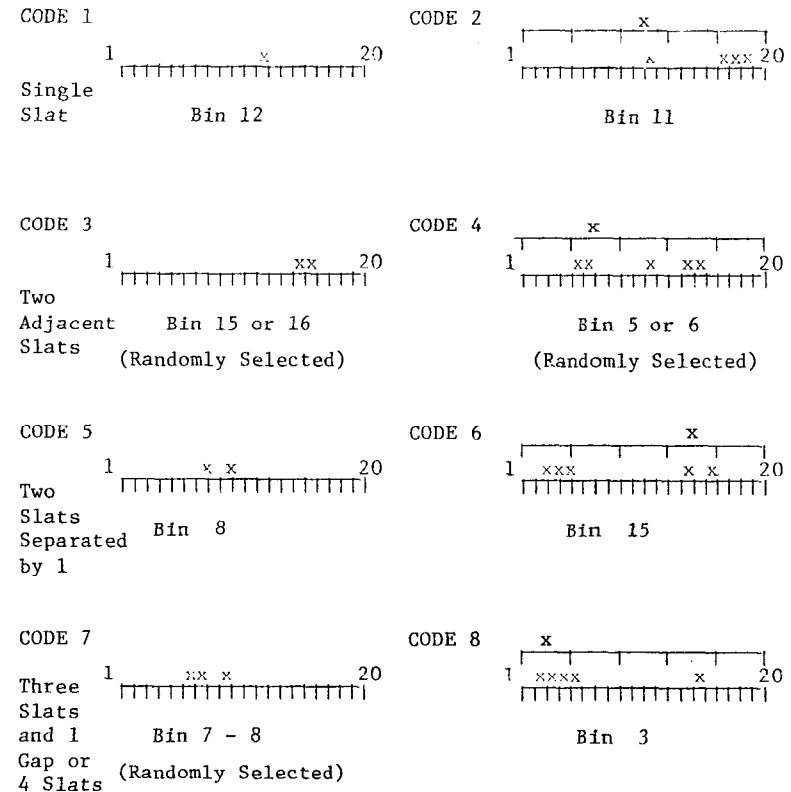
As the Y-hodoscope had no backup coarse hodoscope, optics information was used to project an allowed hit range for the +40 mrad to -50 mrad slits at the spectrometer's entrance. The events resolved in this manner are the "saved" events for this hodoscope. If no Y bin showed a hit, the event was assigned a random  $\phi$  angle that fell within the acceptance.

Different tracking criteria can have different  $\pi/e$  mixtures. Multiple  $\pi$  events can masquerade as electrons but have a high probability of giving bad codes (multiple tracks). To examine this, we first selected events in the analysis class passing the TFT,TA1 and CT cuts. If the event fell above 95 in TASUM it was called an electron and below 95, a pion. Table III-4 shows p codes vs.  $\theta$  codes with the upper entry being the fraction of PHS analysis class events with those codes, and the lower entry the  $\pi/e$  ratio.

One sees that the  $\pi/e$  ratio is large away from unique single tracks i.e., the (1,1) box. On the basis of Table III-4, six code classes were established of increasing track quality. These are summarized in Table III-5, which shows the code class (1-6) assigned to each (P, $\theta$ ) code.

The efficiency for each code class was fit to a second order polynomial in the counting rate of the APE2 coincidence (a coincidence between the Y hodoscope, the X hodoscope and TR2), and of the TR2 counter. This tracking efficiency correction was calculated for each run and applied to the

### HODOSCOPE PATTERNS



ALL OTHER PATTERNS WERE CONSIDERED UNRESOLVABLE AND LABELED "ZOO EVENTS"

FIG. III - 7

TABLE III - 4

		θ Code →							
		1	2	3	4	5	6	7	8
P C o d e ↓	1	0.8176	0.0394	0.0125	0.0007	0.0048	0.0004	0.0004	0.0080
		0.1770	0.4893	0.5532	1.6667	0.7706	1.1000	1.4444	0.4667
	2	0.0403	0.0041	0.0017	0.0002	0.0017	0.0002	0.0001	0.0003
		0.6839	1.9032	2.6154	5.7500	2.8462	5.0000	7.6667	3.1429
	3	0.0354	0.0032	0.0018	0.0002	0.0012	0.0000	0.0001	0.0004
		0.2900	1.1389	1.5000	2.0000	2.4643	8.0000	4.0000	1.2500
	4	0.0032	0.0004	0.0003	0.0	0.0001	0.0000	0.0000	0.0000
		0.7917	2.7000	1.1429	3.0000	5.0000	8.0000	4.0000	8.0000
5	0.0083	0.0008	0.0012	0.0001	0.0006	0.0	0.0001	0.0001	
	0.7433	3.1111	1.7308	4.5000	3.5000	6.0000	3.5000	2.0000	
6	0.0004	0.0001	0.0000	0.0	0.0001	0.0	0.0	0.0	
	2.5556	3.0000	7.0000	1.0000	2.3333	0.0	4.0000	1.0000	
7	0.0027	0.0004	0.0004	0.0	0.0002	0.0000	0.0	0.0000	
	0.8226	2.6667	1.1250	5.0000	3.6000	4.0000	9.0000	5.0000	
8	0.0050	0.0002	0.0001	0.0	0.0000	0.0	0.0	0.0001	
	1.5893	3.2000	4.6667	3.0000	8.0000	0.0	3.0000	5.5000	

TABLE III - 5

		θ Code →									
		0	1	2	3	4	5	6	7	8	>8
P C o d e ↓	0	1	1	1	1	1	1	1	1	1	1
	1	1	6	5	5	3	4	3	3	4	1
	2	1	4	2	2	2	2	2	2	2	1
	3	1	5	3	3	2	2	2	2	2	1
	4	1	4	2	2	2	2	2	2	2	1
	5	1	4	2	2	2	2	2	2	2	1
	6	1	2	2	2	2	2	2	2	2	1
	7	1	4	2	3	2	2	2	2	2	1
	8	1	4	2	2	2	2	2	2	2	1
>8	1	1	1	1	1	1	1	1	1	1	

data. The analysis stream used only events with code classes 4-6.

The average efficiency for electron data runs was 98% and never lower than 94%.

#### ACCIDENTALS

Random master trigger coincidences were created by splicing the TA1D trigger CT signal together with the rest of the information from the TA2D trigger. These events were uniquely tagged by the trigger flags (ORT false and ORA true). Each accidental event that passed the analysis class criteria (PHS classes 4-6 and code classes 4-6) was used to decrement the missing mass histogram and final TASUM PHS plot by 1.176 (this factor is the short spill correction). The accidental rate was highest for the cross section measured off deuterium at 60 degrees, 19.5 GeV incident. For those settings the number of accidentals that was subtracted from the analysis class sample amounted to 2% of the total. For the bulk of the data the percentage contribution was much less than 1%.

#### OVER-ONE CORRECTION

We could accept at most one event per pulse as the electronics had only one set of PHA's and flag units. As counting rates on the main trigger, ORT, were very low (usually less than .01 per pulse) this was not the source of much data loss. Missed ORT events were corrected for by using the ORTK scaler information. Missed accidental events were corrected by using the TA2D scaler and a count of the number of TA2D events read by the computer (gotten by counting events with a TA2D flag set true). These two over-one corrections were

combined in a single correction consistent with the decrementation scheme explained in the last section:

$$C_1 = \frac{ORT_{as} \left( \frac{ORT_{sc}}{ORTK_{sc}} \right) - 1.176 TA2D_{as} \left( \frac{TA2D_{sc}}{TA2D_{sfc}} \right)}{ORT_{as} - 1.176 TA2D_{as}}$$

where subscripts as = analysis class event count, sc = scaler event count, sfc = software flag scaler event count, and the 1.176 is the short spill correction (previously mentioned).

#### EVENT BINNING

At a particular setting (same  $E_o$ ,  $E'$ ,  $\theta$ , and target) there are 20 p bins x 15  $\theta$ -bins into which events can fall. As a TR2 signal is required of all events, the p-bin range is limited to 2-19, and the  $\theta$  bin range is limited to 2-14. The maximum  $\phi$  acceptance is set by the fixed slit at the entrance to the spectrometer. We required that  $-60 \text{ mrad} < \phi < 50 \text{ mrad}$  as reconstructed from the hodoscope information. Typical p,  $\theta$  and  $\phi$  distributions are shown in Fig. III-8. The solid line on the  $\phi$  distribution is a Monte Carlo prediction based on the 1.6 optics (see Appendix D). Similar predictions for p and  $\theta$  were not made as real events are not expected to be uniformly distributed in p and  $\theta$ . The solid angle for each of the 234 p- $\theta$  bins was calculated using a Monte Carlo program and stored (on disk) for both 50 and 60 degrees. Bins of constant missing mass cut across the p- $\theta$  plane diagonally. A particular p- $\theta$  bin is included in a mass bin if its center falls inside the boundaries of that bin.

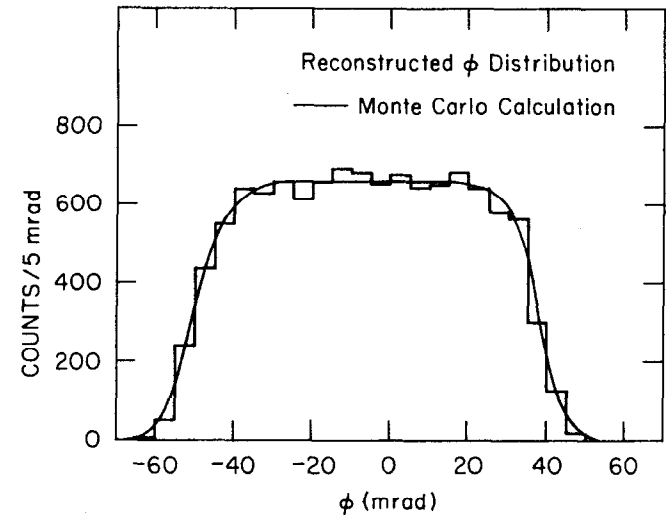
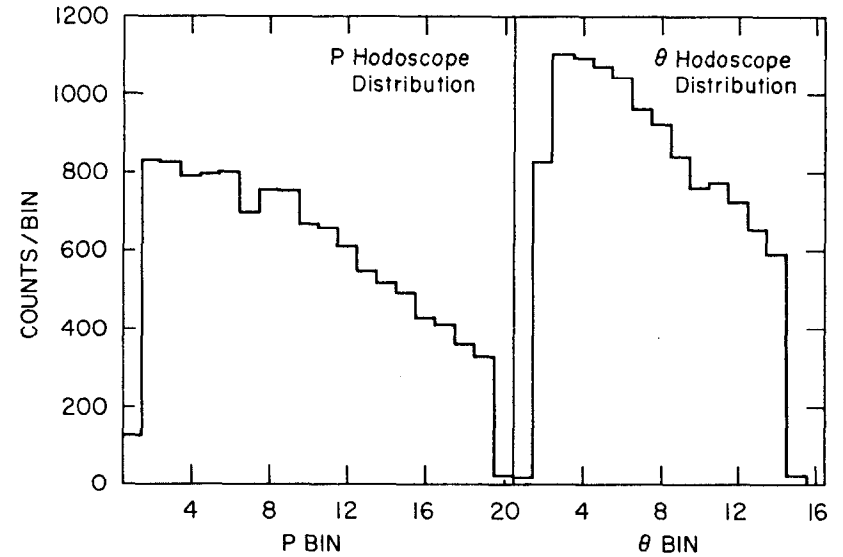


FIG. III-8

Hodoscope Distributions

The data were taken with overlapping momentum settings of the spectrometer. This "scanning" was done by lowering the momentum by one third of the total momentum acceptance for each new setting. There results a high degree of overlap among the settings comprising a line. The "counts" (number of electrons) and "weights" (the solid angle, correction factors, incident flux, etc.) for each missing mass bin were concatenated over the entire line and subsequently stored on disk.

#### RUN WEEDING

There were 1760 runs taken in the experiment. One hundred thirty runs were found to be unacceptable. Ninety three of these were abnormally terminated due to major equipment malfunctions or experimenter error. Twenty one runs were excluded by examining compatability with similar runs. All runs taken at the same setting were required to give reasonable  $\chi^2$  comparisons of the cross sections into the full acceptance. Runs so eliminated were found to have notes made in the experiment's log books that the beam was mis-steered or badly focused, the target had problems, or the electronics or the computer had some minor malfunction. The various run correction factors were scanned on a run-by-run basis and runs with large deviations examined carefully. The mean and width of each of the five PHS's were scanned to look for malfunctioning detectors. Large jumps in these quantities corresponded to changes in  $E_0$ ,  $\theta$  and sign of  $E'$ . Tracking efficiency scans unearthed a few runs with dead hodoscope slats not noted in the log book. These types of comparisons

lead us to discard another sixteen runs.

#### TESTING THE ANALYSIS PROCEDURE

After run weeding we felt confident in concatenating runs into settings (i.e., same target,  $E_0$ ,  $E'$  and  $\theta$ ). At this level of reduction, two tests were made. The first was designed to test tracking and PHS efficiencies, and the second was sensitive to cross section variation across the acceptance and setting to setting compatability.

The efficiency test was easily made. As described earlier in this Chapter, we derive 6 PHS classes and 6 tracking classes. We can analyze our data using 36 different criteria with PHS efficiencies running from 99.9% to 80% and tracking efficiencies ranging from 99% to 80%. The pion contamination varies from several percent (depending on running conditions) to virtually nil (<.5%) over the 36 PHS tracking classes. The total electron detection efficiency ranges from 100% to 64%. The analysis class was selected as the reference point and the 35 other cross section compared to it. Table III-6 shows a typical comparison for all the hydrogen running for  $E'$  between 1.200 GeV and 1.400 GeV for electrons at 60 degrees (the concatenation over  $E'$  was done to increase the statistics). For each line, each setting was so examined. We found no statistically significant deviation. This leads us to believe we know our inefficiencies to about 20% of their value for both the PHS efficiency and the tracking efficiency. As seen from Table III-6 there is no definite correlation between PHS efficiency and tracking efficiency.

TABLE III - 6

## MINIMUM CODE CLASS vs. PULSE HEIGHT CLASS

PH CLASS ↓	1	2	3	4	5	6
1	2512.2 1.001+0.020 0.99706 0.01832	2486.4 0.997+0.020 0.99493 0.01340	2445.4 0.991+0.020 0.98830 0.00963	2434.4 0.991+0.020 0.98386 0.00942	2273.4 0.988+0.021 0.92375 0.00787	2054.5 0.989+0.022 0.83523 0.00575
2	2479.3 1.011+0.020 0.97913 0.01286	2454.3 1.006+0.020 0.97705 0.01036	2416.3 1.000+0.020 0.97056 0.00741	2405.3 1.000+0.020 0.96619 0.00696	2246.3 0.997+0.021 0.90710 0.00512	2030.3 0.997+0.022 0.82022 0.00457
ANALYSIS CLASS						
3	2459.3 1.018+0.021 0.96892 0.00874	2434.3 1.011+0.021 0.96691 0.00683	2398.3 1.005+0.021 0.96056 0.00490	2387.3 1.005+0.021 0.95624 0.00476	2231.3 1.001+0.021 0.89777 0.00400	2016.3 1.001+0.022 0.81178 0.00373
4	2277.6 1.011+0.021 0.90972 0.00201	2255.6 1.003+0.021 0.90791 0.00178	2222.6 0.995+0.021 0.90220 0.00154	2211.6 0.995+0.021 0.89816 0.00150	2069.6 0.992+0.022 0.84328 0.00126	1866.6 0.989+0.023 0.76260 0.00110
5	2040.6 1.041+0.023 0.79210 0.00083	2021.6 1.034+0.023 0.79061 0.00080	1999.3 1.026+0.023 0.78564 0.00053	1982.6 1.025+0.023 0.78212 0.00053	1853.6 1.020+0.024 0.73476 0.00046	1670.6 1.016+0.025 0.66467 0.00040
6	1968.6 1.032+0.023 0.77104 0.00056	1951.6 1.025+0.023 0.76974 0.00054	1928.6 1.018+0.023 0.76579 0.00037	1918.6 1.017+0.023 0.76254 0.00037	1793.6 1.012+0.024 0.71637 0.00032	1614.6 1.008+0.025 0.64789 0.00028

The four numbers shown in the Table are: 1) number of electrons corrected for accidentals; 2) ratio to analysis class cross section; 3) electron detection efficiency; and 4) the pion subtraction factor. The data were taken on hydrogen with  $E_0 = 19.5$ ,  $\theta = 60^\circ$ , and for  $1.2 \text{ GeV} < E' < 1.4 \text{ GeV}$ .



Typically, we assign a 3.2% systematic error from tracking and PHS efficiency.

The second test we made on the data was a cross section comparison. Every line with few exceptions was measured three times in each scan (some of the low  $E_0$  lines at the low  $E'$  were taken in bigger than 1/3 acceptance jumps). Except for the beginning and end of each line we have three cross section measurements of the same points which we can compare. A reference cross section is gotten by concatenating the counts and weights for the three partial cross sections. This is then compared to individual cross sections.

A  $\chi^2$  test is also made by forming the residuals

$$R_{ij} = \frac{\sigma_i - \sigma_j}{\sqrt{\Delta\sigma_i^2 + \Delta\sigma_j^2}}, \quad i \text{ and } j = 1, 2, 3, i \neq j$$

A histogram of the residuals for the 50 and 60 degree data is shown in Fig. III-9. The distribution is what one expects normally distributed data to produce. We conclude that there are no serious aperture biases in the analysis.

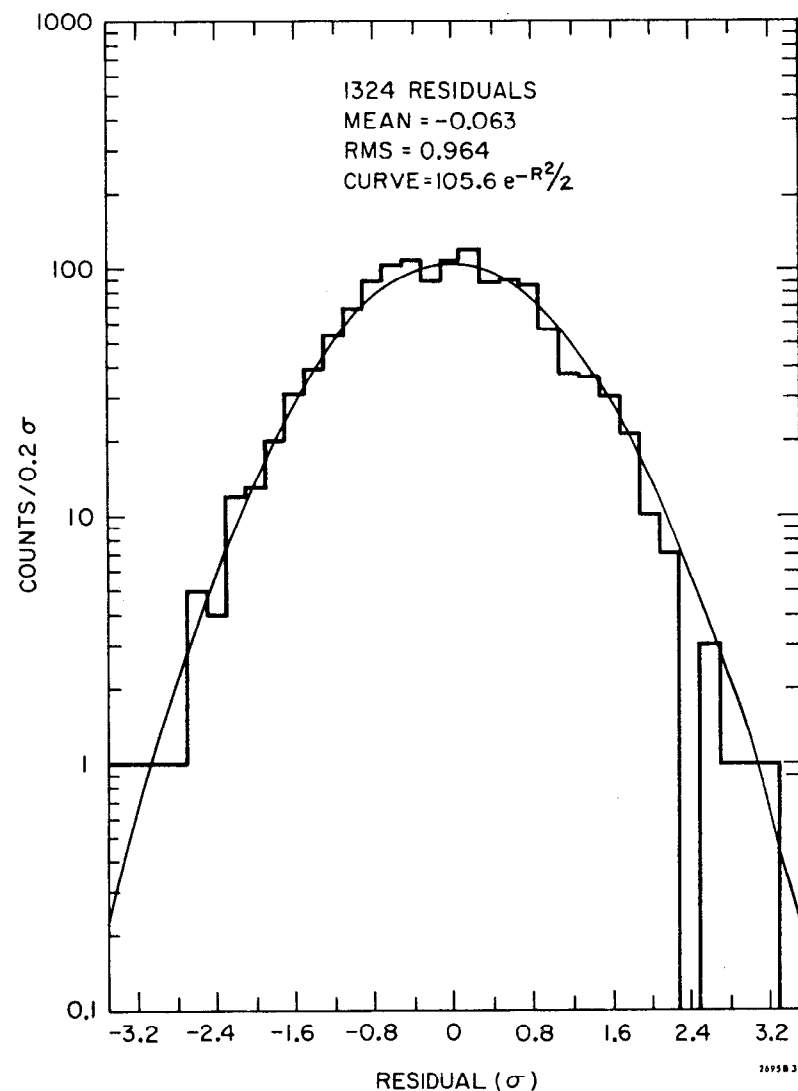


FIG. III-9  
 A histogram of the residuals  $R_{ij}$ .  
 The curve is what one expects normally distributed data to give.

## CHAPTER IV

### CALCULATED AND MEASURED CORRECTIONS

#### MEASURED CORRECTIONS

The full target yields include contributions from the target walls and from processes which produce both positrons and electrons. To remove these unwanted contributions we measured these yields besides the full target electron yields. These were the empty target cross-sections measured for both scattered electrons and positrons and the full target measured for scattered positrons. The prescription used to correct the full target cross section is given by

$$(4.1) \quad \sigma_{COR} = \sigma_{FULL} - \sigma_{MT}^- - (\sigma_{FULL}^+ - \sigma_{MT}^+).$$

The signal from the empty target typically amounted to about 6% of the full target signal for hydrogen and 4% for deuterium. The fraction of the measured cross section accounted for by charge symmetric processes depends on  $E_0$ ,  $E'$ , and  $\theta$  and in general increases as  $E'$  decreases. This correction, made by subtracting the measured positron yield from the electron yield, was a primary factor in determining the lowest  $E'$  at which data were taken. Most lines were run until the ratio of positron to electron yield on the full target reached .35 ( $\sigma_{FULL}^+ / \sigma_{FULL}^- = .35$ ).

The assumption used in Eq. 4.1 is that there are no important sources of electrons (other than scattered beam particles) which are not charge symmetric. A test of this assumption was recently made experimentally (Ref. IV-1) during the second cycle of E-89 by measuring the electron yield from the target using a positron beam

and comparing that to the charge symmetric situation with electrons incident in the same experiment. This wrong sign signal was equal for the two signs of the incident particle charge to within the accuracy of that experiment (5% at  $Q^2 = 3 \text{ GeV}^2$  to 10% at  $Q^2 = 15 \text{ GeV}^2$ ).

For both the empty target and positron signals we make the hypothesis that the structure in missing mass is smooth. We take smooth analytic representations of these data as our best estimate of their actual value. We are assuming that neighboring data points are not independent but contain similar physical information. Using the bulk of the data rather than the individual data points can improve estimates of these corrections.

Plots of these data show that the double differential cross sections are approximately exponential at these large angles. We find the following simple parametrization

$$(4.2) \quad \sigma_{pos} = 10^6 (a + b E_0 + c E_0^2) e^{-d E' \sin \theta} \text{ (pb/GeV-sr)}$$

works well for the positron cross sections. The resulting fit parameters are given in Table IV-1 for the various  $E_0$ 's,  $\theta$ 's and targets. To propagate the error introduced by these subtractions, we estimate that the functions thus fitted give the correct cross sections to

$$(4.3) \quad \Delta\sigma/\sigma = \text{MAX} (.1, .3 - .1 W \text{ (GeV)})$$

This gives an error in this correction of 20% in the elastic peak regions decreasing to a minimum of 10% for  $W > 2 \text{ GeV}$ . This error approximation does not significantly improve the errors over what the measured data would yield. The prescription of subtracting

TABLE IV - 1  
POSITIVE SUBTRACTION

$$\sigma_{\text{POS}} = \sigma_{\text{FULL}}^+ - \sigma_{\text{MT}}^+ = 10^6 (a + bE_0 + cE_0^2) e^{-d P_t} \left( \frac{\text{pb}}{\text{GeV-sr}} \right)$$

	a	b	c	d	$\chi^2/N_D$
60°, H	-13.3290	4.25038	-0.0484835	16.4419	85.7/112
60°, D	-13.2485	3.76622	-0.0684701	15.1213	153/130
50°, H	-19.3759	4.52011	-0.0766568	14.4748	41.1/37
50°, D	-9.52999	3.43338	-0.0555869	13.6932	31.0/43

EMPTY TARGET SUBTRACTION

$$\sigma_{\text{MT}}^- = a e^{(bW + cW^2)} \left( \frac{\text{pb}}{\text{GeV-sr}} \right)$$

Line	$E_0$	$\theta$	a	b	c	$\chi^2/N_D$
1	19.5	60°	0.160334E-1	-.970139	.536463	18.7/24
2	16.0		0.201885E-3	2.59807	-.0407573	15.0/17
3	13.3		0.902831E-2	-.292653	.591770	71.8/78
4	10.4		0.158756E-1	-.499663	.789576	17.4/25
5	6.5		0.250682E-2	2.89575	.179453	92.4/63
6	19.5	50°	0.195994E-4	2.62323	.0310931	13.7/9
7	16.0		0.268996E-4	3.21611	-.0468157	13.2/11
8	13.5		0.601734E-2	.237730	.445982	13.0/17
9	7.0		0.339265E-1	.986842	.521663	12.5/19

For  $D_2$  divide result by 1.16 (empty target only).

models allows us to treat all the data in the same manner (we did not measure all the quantities in Eq. 4.1 for about 30% of the data, as these corrections were small, and we felt confident in our ability to estimate them from the measured data). These errors will be taken as part of the systematic error in the final cross sections. The  $\chi^2$ 's quoted in Table IV-1 were evaluated using the statistical counting errors.

An interesting side note and source of puzzlement to us was that the empty target (stainless steel) cross sections were appreciably different in character from the deuterium cross sections. Our expectation would be that iron could be well approximated by a "bag" of deuterons. Fermi motion effects would tend to be similar. But, the ratio of the iron cross sections to the  $LD_2$  cross sections for wrong sign running is  $E'$  dependent, increasing with  $E'$ . The growth is as much as a factor of two for the highest incident energy lines and always at least a factor of two more than what would be expected. This means that the size of the empty target cross section was larger than expected from simple nucleon counting. The corrected empty target cross section,  $\sigma_{\text{MT}}^- - \sigma_{\text{MT}}^+$ , is the right size for scattered beam particles, but the charge symmetric part is anomalously large and increases relative to the signal as  $E'$  is increased. We doubt that this effect has been generated by a measurement or analysis error.

#### CALCULATED CORRECTIONS

It is traditional to correct the data for the effects of radiation in the target and in the scattering process itself. For deuterium, the motion of the bound neutron and proton provide additional correction. We have applied three calculated corrections to this electroproduction data. First, the elastic and quasi-elastic (as appropriate to deuterium) radiative tails were subtracted. The "tail subtracted" data were then corrected to account for radiation which shifts the theoretical electron yields to higher missing mass. The deuterium cross sections are the source of the neutron data, and corrections for Fermi-motion effects were calculated and applied before comparisons with the hydrogen data were made.

#### ELASTIC TAIL SUBTRACTION

The elastic tail was calculated by the methods given in G. Miller's thesis (Ref. IV-2). The elastic tails come from incident electrons radiating energy through photon emission and elastically (or quasi-elastically) scattering off the target particle. The energy degradation can occur before and after the elastic scatter. Both produce scattered electrons of lower energy than elastically scattered beam particles. These lower energy electrons enhance the cross sections measured at missing masses higher than the proton mass. The materials in the beam before and after the scatter are referred to as "real radiators" and are summarized in Table II-2. In addition to the effect of this real radiator, there are the quantum

electrodynamic processes involving radiation from the electron being accelerated during the elastic scatter. This source of radiation is often discussed in terms of the "internal" or "equivalent" radiator, as such radiation is similar to that caused by the real material in the beam. An approximate expression for the equivalent radiator is

$$(4.4) \quad t_{eq} = \frac{\alpha}{\pi} (\ln(Q^2/m_e^2) - 1)$$

For  $Q^2 = 20 \text{ GeV}^2$ ,  $t_{eq} = .04$ . The expressions given by Tsai (Ref. IV-3) were used to calculate this correction exactly to lowest order in  $\alpha$  and are used in Miller's approach.

Smaller corrections also included are an estimate of multiple photon emission and target radiation from the recoiling proton (only in the case of hydrogen). The elastic tail calculation requires knowledge of the form factors  $G_E$  and  $G_M$  for  $Q^2$  less than the effective  $Q^2$  of the point being corrected (the effective  $Q^2 = 4 E'^2 \sin^2(\theta/2) / (1 - 2 E' \sin^2(\theta/2)/M)$ ). We have assumed form factor scaling ( $G_E = G_M/\mu_p \equiv G_E^S$ ) and a fit to the measured elastic scattering data for  $G_E^S$  (see Chap. V). The exact expressions used for the elastic tails (as well as the inelastic radiative corrections) are given in Ref. IV-4.

Plotted in Fig. IV-1 are the elastic tail fractions, that is the elastic radiative tails divided by the raw cross section for representative lines at 50 deg. and 60 deg. for both hydrogen and deuterium targets.

For the deuterium quasi-elastic peak, we used the procedure given in Ref. IV-5 (also see Appendix C) to compute the quasi-elastic cross section which was then radiated to produce a "quasi-elastic" tail. The Reid hard-core wave function (Ref. IV-6) for the deuteron has been used in all the smearing and quasi-elastic calculations.

We take the error in the elastic and quasi-elastic tails to be the same as those estimated in Ref. IV-4 ( $\pm 5\%$ ) plus an additional  $\text{MAX}(5, Q^2(\text{GeV}^2))\%$  to account for the high  $Q^2$  uncertainty of the squared form factors. This gives  $\pm \text{MAX}(10, 5 + Q^2(\text{GeV}^2))\%$  error on the tail subtraction. This error usually contributes less than 2.5% to the systematic error.

#### INELASTIC RADIATIVE CORRECTIONS

The inelastic radiative corrections are applied to the tail-subtracted data. This correction accounts for the radiation from scatters occurring at low missing mass giving events at higher measured missing mass. We have used a new technique involving an iterative procedure with an analytic representation of all data taken at one angle on the same target.

The exact radiation calculation (as done for the elastic tails) would take too much computer time (as presently coded). Instead, an equivalent radiator is used to simulate internal bremsstrahlung. The hard radiation of this internal radiator is strongly peaked along the incoming and the outgoing directions of the electron, hence little angular deflection in the trajectory of

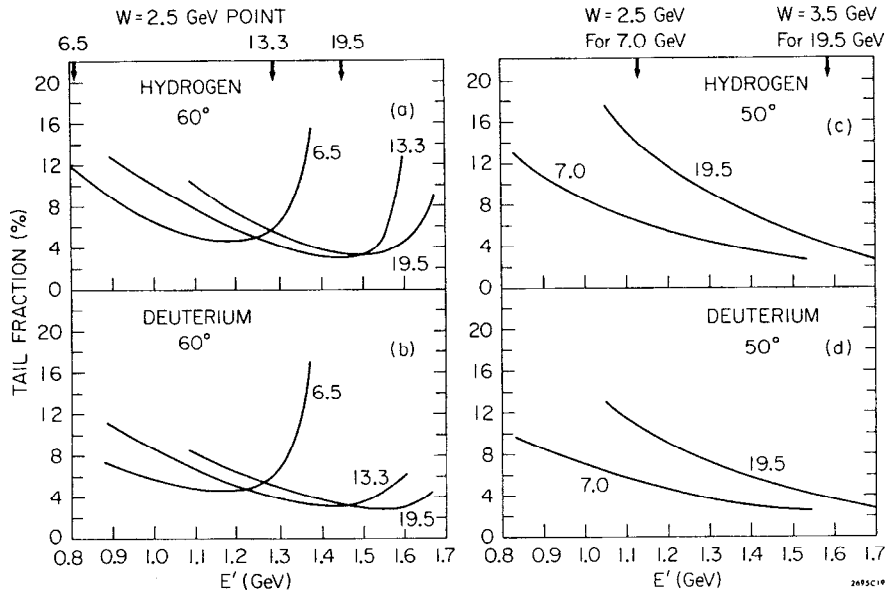


FIG. IV-1

The elastic radiative tail fraction for representative lines at  $50^\circ$  and  $60^\circ$ . These arrows at the top of the graph indicate where a missing mass,  $W$ , of 2.5 GeV falls for  $E_0 = 6.5, 13.3$  and 19.5 GeV at  $60^\circ$  and  $W = 2.5$  for  $E_0 = 7.0$  GeV and  $W = 3.5$  for  $E_0 = 19.5$  GeV at  $50^\circ$ .

the electron occurs. Usually an "angle peaking" approximation is used which includes only radiation along these two directions. As the electron can be degraded in energy both before and after the scatter, we must, in principle, integrate over all  $E_0$ 's and higher  $E'$ 's that can contribute to scattering at the measured point. Examination of this double integration shows that most of the contribution to the integral comes from either radiation before or radiation after the scatter, but not both. One takes advantage of this by an "energy peaking" approximation. The two-dimensional integral in  $E_0$  and  $E'$  is well approximated by three terms: a) scattering at the measured  $E_0$  of the beam with contributions coming from all allowed higher  $E$ 's; b) scattering at the measured  $E'$  with contributions coming from incident energies down to the lowest allowed  $E_0$ 's (determined by one pion threshold); and c) scatters in the "near" region with soft photon emission.

The new technique uses the fact that radiating "known" cross sections involves only integrals. What is done in practice is to start with a reasonable model of the data (such as an  $\omega'$  fit (Ref. IV-7)). Using the model, a radiative correction ratio  $R_{rad} = \sigma_{model} / \sigma_{model-radiated}$  is calculated for each data point, and a radiatively corrected set of cross sections is formed by multiplying the data and its error point-for-point by this ratio. The model is then refit to the data. New radiative corrections are calculated and reapplied to the tail subtracted data. A flow chart of the procedure is shown in Fig. IV-2. The major part of the correction

### RADIATIVE CORRECTION FLOW CHART

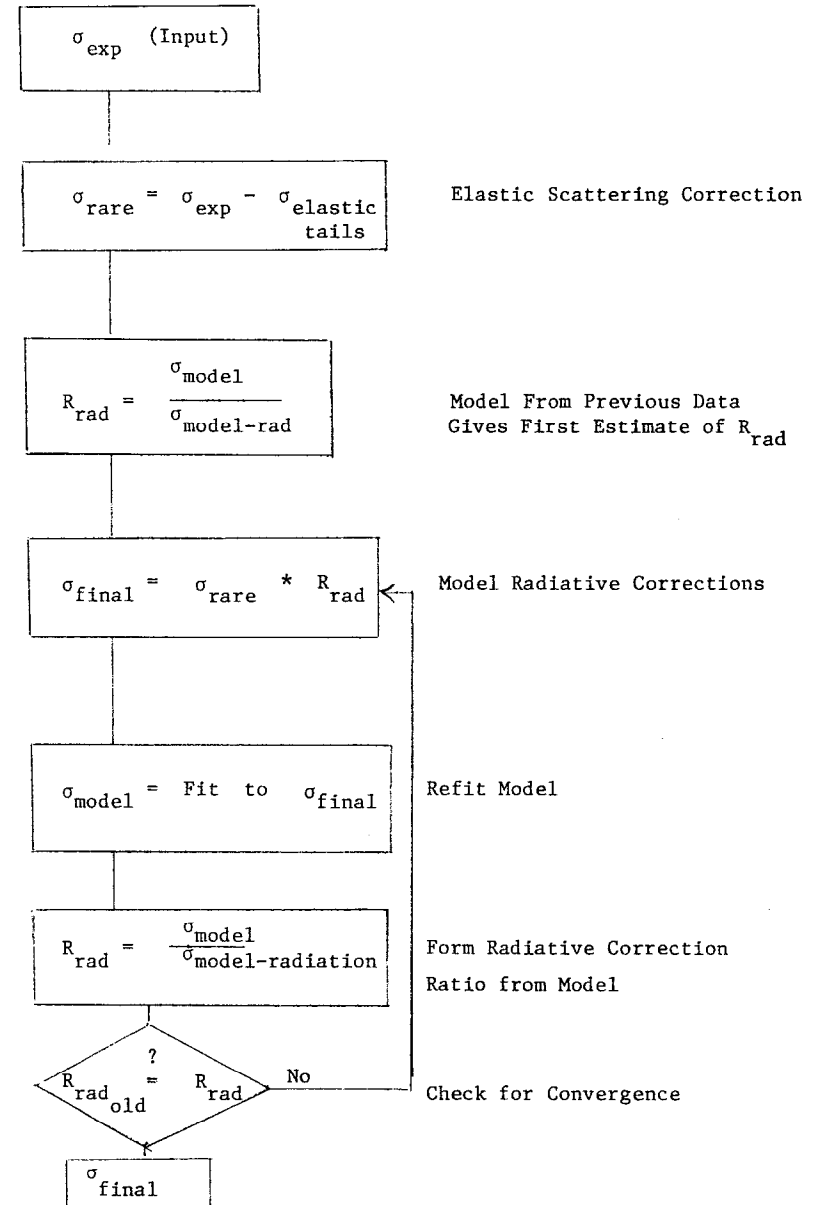


FIG. IV-2

comes from energies near the measured energies, and since the cross sections are quite smooth, convergence occurs after a few iterations. The model used has no resonance structure past a  $W = 2.0$  GeV. Any high mass resonance ( $W > 2.0$  GeV) will not have the appropriate radiative correction enhancement. This probably is a valid assumption as no high mass resonances have been observed for  $W < 5.7$  GeV for the process  $e+p \rightarrow e'+X$  (Ref. IV-8) for  $Q^2$ 's of approximately  $1 \text{ GeV}^2$ . The radiative correction ratios for some of the lines are shown in Fig. IV-3. The deuterium ratios are within .02 of the plotted hydrogen ratios. The formulas used for radiating the fitted cross sections are given in Ref. IV-4.

Some questions arise as to the correctness of the peaking approximation used in the radiative correction procedure. To check its validity, the "exact" (as in the elastic case) radiative correction ratios were recalculated at some  $W$  points spanning the range of the present data, again using an  $\omega'$  model as the source of the  $W_1$  and  $W_2$  structure functions. Two independent programs agreed to better than 5% with the peaking approximations and the equivalent radiator used for  $W < 4.5$  GeV (Ref. IV-9).

We quote the systematic error given in Ref. IV-4 for the radiative correction ratio:  $\pm 3\%$  near threshold ( $W = 1.3$  GeV) growing to  $\pm 5\%$  at the lowest values of  $E'$ . This error is considered systematic and will be combined with the other sources of systematic error.

The radiative correction ratios for representative incident energies at  $50^\circ$  and  $60^\circ$ . The ratios are plotted for  $W > 1.75$  GeV.

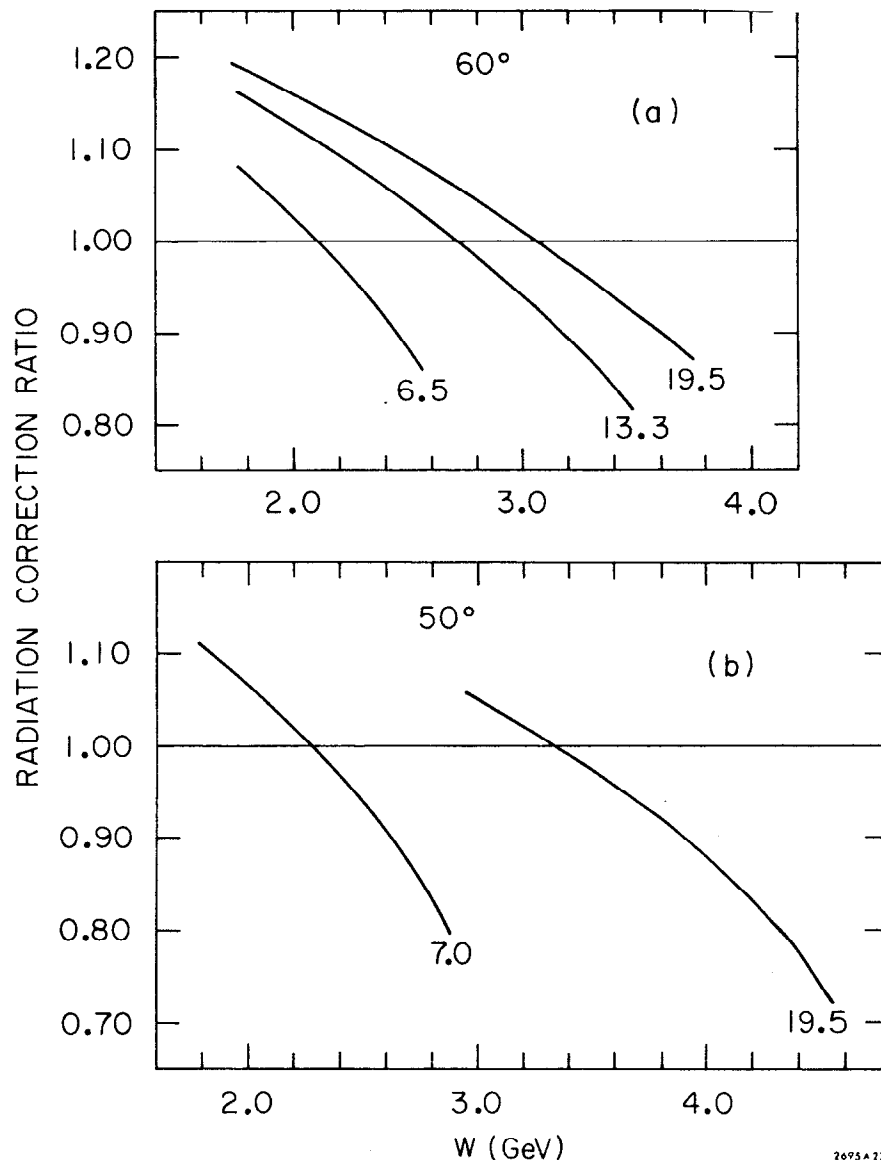


FIG. IV-3

## SMEARING CORRECTIONS

The deuteron is a very loosely bound structure consisting of a neutron and a proton. A first approximation for the deuteron cross section would be the sum of the proton and the neutron cross sections. This approximation is wrong to the extent that the motion of the nucleons inside the deuteron distort the free nucleon structure functions. Structure functions so modified are referred to as "smeared" structure functions.

The smearing effect is most pronounced for quasi-elastic scattering where the electron scatters elastically off one of the nucleons inside the deuteron resulting in nuclear breakup. The narrow electron elastic peak which results from scattering off free nucleons is broadened or "smeared out" because of the target particle's motion.

The smearing correction is done within the framework of the impulse approximation. The electron is assumed to interact with only one of the nucleons, the other nucleon being "spit" off as a free "spectator." Taking the Fermi-motion into account relativistically (that is conserving energy and momentum at all times) puts the interacting nucleon off its mass-shell. So not only is the target particle not in its rest frame, but it is off its mass shell. The first effect blurs the angular resolution of the scattering and both effects shift the invariant mass of the interaction. We follow the procedure given in Appendix C to calculate smeared structure functions from unsmeared ones. The smearing

correction for the inelastic structure functions is often parameterized as a smearing ratio,  $S_i = W_{1i}/W_{1i}(\text{SMEARED})$ . More analysis of the smearing problem is detailed in Appendix C.

The hydrogen cross section subtraction from the deuterium data was done with a smooth analytic function representing the proton data appropriately smeared. This procedure is preferable over point-for-point data subtraction corrected by a smearing ratio. Smearing ratios are not model insensitive because of the large kinematic range of the smearing integrals (typically  $\pm .2$  units in  $\omega'$ ). The calculated smeared cross sections are less model sensitive because of this. Forming a smearing ratio reintroduces the model in a local manner. Furthermore, the same arguments given for the empty target subtraction and the positron subtraction by a model subtraction are valid here too. The error assigned to this procedure was  $\pm 5\%$  of the  $\sigma_p(\text{model-smeared})$  and was considered as part of the systematic error in  $\sigma_N$ . The smeared neutron  $W_{1N}$  structure function can be obtained by subtracting the calculated smeared proton contribution from the deuteron:

$$(4.5) \quad W_{1N}(\text{SMEARED}) = W_{1D} - W_{1P}(\text{SMEARED})$$

The smearing procedure like radiative corrections is not invertible. An iterative procedure, similar to that used to account for radiation processes, was used to extract the unsmeared neutron structure functions. To extract an unsmeared neutron, we have to use the smearing ratios despite their model sensitivity. The first estimate



of the neutron smearing ratios are the calculated proton smearing ratios. This yields an "unsmeared" neutron which generates new smearing ratios through a fitted model to that neutron data and so on. A diagram of the logic flow is shown in Fig. IV-4. We take the error in the smearing ratios to be similar to that calculated in Ref. IV-9 and is typically less than  $\pm 1.5\%$ .

The principal problem that arises with smearing compared with radiation is that smearing extends over a larger kinematic range (see Appendix C). The principal smearing contribution comes from approximately  $\pm 2$  units in  $\omega'$  about the  $\omega'$  for which the calculation is being made. This aspect of smearing makes convergence occur slowly in this iteration procedure, especially for non-linear parameterizations of structure such as in the resonance region.

The maximum deviation of the smearing ratios from unity occurs as  $x' \rightarrow 1$  ( $S_p = .62$  for  $x' = .92$ , but for 90% of the data where  $x' < .8$  the ratio lies in the range  $0.90 < S_p < 1.02$ ). The smearing ratios calculated for this experiment are shown in Fig. IV-5.

#### THE EXTRACTION OF $W_1$

As stated in Chapter I, the large angle cross sections are insensitive to the value of  $R \equiv \sigma_s / \sigma_t$  used in extracting  $W_1$  from the cross sections due to the smallness of  $\epsilon$  in the measured region. The contribution of  $\sigma_s$  is always less than 4.5% for  $R = .18$ . We

UNSMEARING FLOW CHART

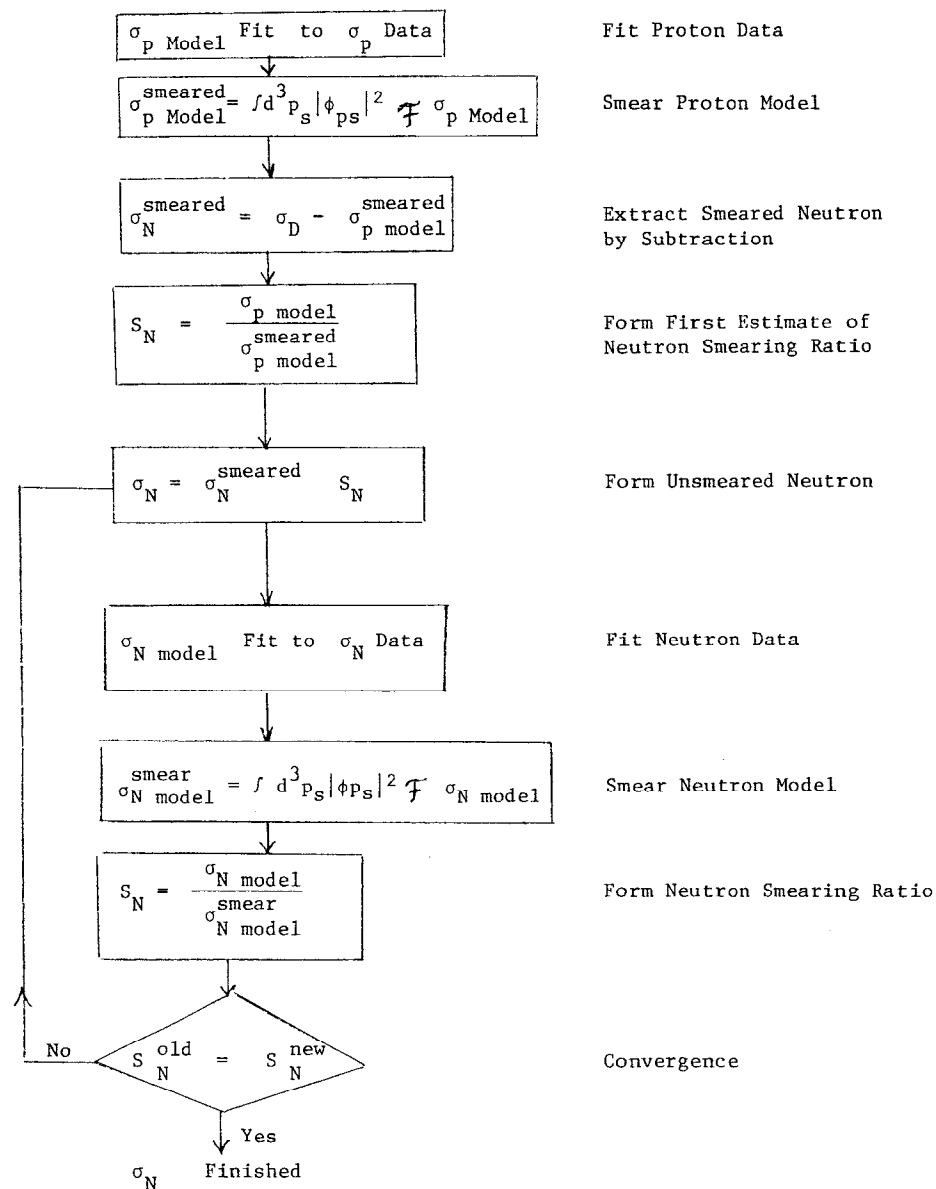


FIG. IV-4

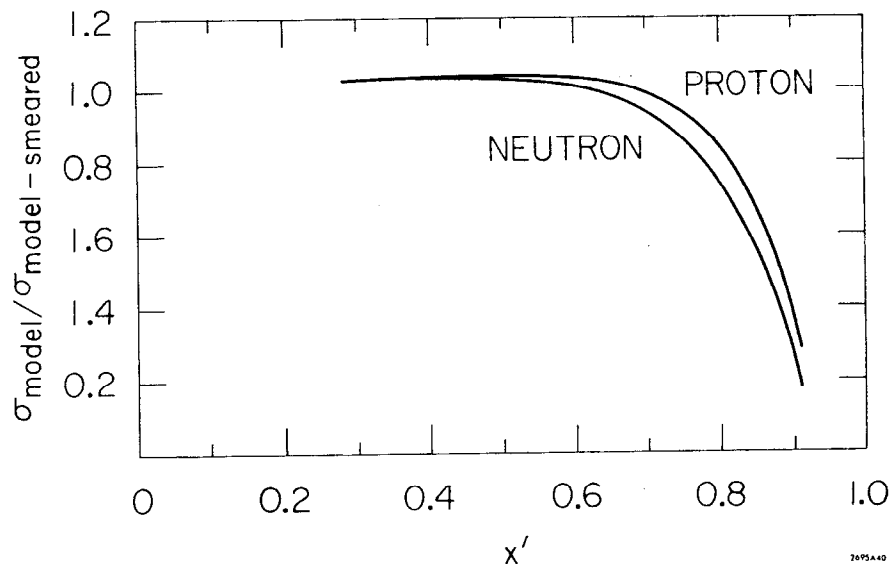


FIG. IV - 5

The smearing ratios ( $\sigma_{\text{model}}/\sigma_{\text{model smeared}}$ )  
for the neutron,  $S_N$ , and the proton,  $S_P$ .

calculated  $W_1$  by

$$(4.6) \quad W_1 = \frac{\sigma_{\text{exp}}}{\sigma_{\text{mott}}} \frac{1}{2 \tan^2(\theta/2)} \frac{1 - \epsilon}{1 + \epsilon R}$$

We assign an error of  $\pm .5 \epsilon R$  to this procedure, and this error is taken as part of the total systematic error. A value of .18 was used for  $R$ .

#### SUMMARY OF SYSTEMATIC ERRORS

Systematic errors of two types are considered: 1) point-to-point errors and 2) overall normalizations errors. Counter efficiencies, tracking efficiencies, the pion subtraction factor, and the fast electronic flag efficiencies are considered here as sources of point-to-point fluctuations. As it is unclear what correlations may exist between these contributions, the conservative approach of adding them linearly together has been adopted. The detailed contributions and the typical sizes of the estimated errors are given in Table IV-2.

The overall systematic errors which contribute are given in Table IV-3. In each category the detailed contributions with typical values of the error are shown. We choose to combine these errors by adding all contributions to a particular category together linearly and then combining the various categories in quadrature (see #3 at the bottom of Table IV-3). For the N/P determination many systematic errors tend to cancel, such as those associated with the beam, the spectrometer, the inelastic radiative corrections, and the  $W_1$  extraction. Others will partially cancel, such as point-to-

TABLE IV - 2

## POINT-TO-POINT SYSTEMATIC ERRORS

Contribution	Size (%)	
	P	D
PHS Cuts: CT	.05	.05
TFT	.5	.5
TA1	.05	.05
TASUM	.2	.2
Codes: $\phi$ Cut	.2	.2
P <sub>2-19</sub> Cut	.3	.3
$\theta_{2-14}$ Cut	.3	.3
Code Class 4-6	.5	.8
Flags: ORX	.5	.8
STR2	.05	.05
Over One:	0.0	0.0
Pion Subtraction Factor:	.5	1.0
Linear Sum:	3.2	4.3

TABLE IV - 3

## OVERALL SYSTEMATIC ERRORS

Category	Contribution	Typical Size (%)		
		P	D	N
Beam	E <sub>0</sub>	.8	.8	-
	Flux	.6	.6	-
	Halo	.2	.2	-
Target	Density	.5	.5	-
	Purity	.5	.5	-
	Length	.5	.5	-
Spectrometer	Solid Angle	1.	1.	-
Measured Subtraction	Empty Target	.7	.4	-
	Positron Yields	2.	2.	-
Radiative Corrections	Tails	1.	.8	-
	Inelastic	4.	4.	-
W <sub>1</sub> Extraction		1.	1.	
Neutron Extraction	P Subtraction	-	-	3
	Unsmearing	-	-	2
1) Linear Addition		11.9	12.3	17.3
2) Quadrature Addition		5.0	5.0	6.2
3) Contributions Linear, Categories quadratically		6.3	6.0	7.8
4) 3) Added in quadrature to Point-to Point Error		7.1	7.4	8.9
4) For N/P = 6.0%				

point systematics, radiative tails, and the measured subtractions. For these the average of the P and D errors were used and added in quadrature with the other contributing sources of error. The resulting systematic error in the N/P ratio is approximately  $\pm 6.0\%$  including the point-to-point contribution ( $\pm 4.9\%$  excluding point-to-point errors).

These Tables include various kinematic quantities, the cross sections for P, D, and N, and  $W_1$  for P and D. Given in the parenthesis for each P and D measurement are: 1) the statistical counting errors and 2) the total systematic error for that point. For the neutron cross sections the "counting" error includes the 5% hydrogen subtraction error added in quadrature to the statistical counting error of the deuterium cross section.

THIS PAGE LEFT BLANK

TABLE IV - 4

19.5 GeV 50<sup>0</sup>

W (GeV)	Q <sup>2</sup> (GeV <sup>2</sup> )	ε	x	x'	$\frac{d^2\sigma}{d\Omega dE'} \left( \frac{\text{pb}}{\text{GeV-sr}} \right)$	2M W <sub>1</sub> <sup>P</sup>
PROTON						
3.100	24.555	0.1428	0.738	0.719	2.973 ± (0.668, 0.135)	0.03054 ± (0.00686, 0.00138)
3.200	24.000	0.1397	0.719	0.701	3.218 ± (0.435, 0.173)	0.03319 ± (0.00449, 0.00178)
3.300	23.427	0.1365	0.701	0.683	3.752 ± (0.351, 0.220)	0.03887 ± (0.00364, 0.00228)
3.400	22.836	0.1332	0.681	0.664	4.616 ± (0.330, 0.279)	0.04803 ± (0.00344, 0.00291)
3.500	22.228	0.1298	0.662	0.645	5.931 ± (0.340, 0.353)	0.06199 ± (0.00356, 0.00369)
3.600	21.603	0.1263	0.641	0.625	7.369 ± (0.390, 0.443)	0.07737 ± (0.00410, 0.00465)
3.700	20.959	0.1227	0.621	0.605	7.652 ± (0.424, 0.557)	0.08073 ± (0.00447, 0.00588)
3.800	20.298	0.1189	0.600	0.584	10.059 ± (0.508, 0.707)	0.10664 ± (0.00539, 0.00750)
3.900	19.620	0.1151	0.578	0.563	12.063 ± (0.581, 0.899)	0.12853 ± (0.00619, 0.00958)
4.000	18.924	0.1112	0.556	0.542	13.680 ± (0.673, 1.155)	0.14652 ± (0.00721, 0.01237)
4.100	18.210	0.1071	0.533	0.520	15.486 ± (0.849, 1.511)	0.16674 ± (0.00914, 0.01627)
4.200	17.478	0.1029	0.510	0.498	19.058 ± (1.157, 2.001)	0.20630 ± (0.01253, 0.02166)
4.300	16.729	0.0986	0.487	0.475	23.916 ± (1.510, 2.759)	0.26033 ± (0.01644, 0.03003)
4.400	15.963	0.0943	0.463	0.452	29.137 ± (1.895, 3.978)	0.31896 ± (0.02075, 0.04355)
4.500	15.178	0.0897	0.439	0.428	29.083 ± (2.622, 5.990)	0.32021 ± (0.02887, 0.06595)
4.600	14.376	0.0851	0.415	0.405	39.494 ± (6.186, 9.499)	0.43740 ± (0.06851, 0.10520)

W (GeV)	$\frac{d^2\sigma}{d\Omega dE'} \left( \frac{\text{pb}}{\text{GeV-sr}} \right)$	$\frac{d^2\sigma}{d\Omega dE'} \left( \frac{\text{pb}}{\text{GeV-sr}} \right)$	2M W <sub>1</sub> <sup>D</sup>
DEUTERON		NEUTRON	
3.100	3.90 ± (0.80, 0.22)	1.29 ± (0.80, 0.20)	0.04007 ± (0.00818, 0.00224)
3.200	3.81 ± (0.50, 0.28)	0.69 ± (0.52, 0.26)	0.03933 ± (0.00514, 0.00286)
3.300	5.10 ± (0.43, 0.35)	1.27 ± (0.47, 0.34)	0.05283 ± (0.00443, 0.00365)
3.400	6.94 ± (0.42, 0.45)	2.27 ± (0.48, 0.44)	0.07213 ± (0.00436, 0.00465)
3.500	7.93 ± (0.41, 0.57)	2.30 ± (0.50, 0.56)	0.08243 ± (0.00431, 0.00591)
3.600	10.34 ± (0.49, 0.72)	3.58 ± (0.59, 0.72)	0.10856 ± (0.00510, 0.00754)
3.700	13.02 ± (0.54, 0.92)	4.94 ± (0.72, 0.93)	0.13732 ± (0.00620, 0.00967)
3.800	16.72 ± (0.74, 1.19)	7.12 ± (0.88, 1.21)	0.17728 ± (0.00781, 0.01263)
3.900	18.20 ± (0.85, 1.56)	6.79 ± (1.03, 1.60)	0.19388 ± (0.00905, 0.01664)
4.000	24.09 ± (1.07, 2.08)	10.69 ± (1.27, 2.14)	0.25804 ± (0.01141, 0.02229)
4.100	28.50 ± (1.37, 2.63)	12.76 ± (1.59, 2.72)	0.30689 ± (0.01473, 0.02837)
4.200	30.99 ± (1.87, 3.46)	12.46 ± (2.10, 3.58)	0.33544 ± (0.02025, 0.03743)
4.300	38.90 ± (2.74, 4.80)	17.36 ± (2.96, 4.98)	0.42340 ± (0.02986, 0.05223)
4.400	51.97 ± (3.69, 6.93)	27.14 ± (3.92, 7.21)	0.56895 ± (0.04039, 0.07590)
4.500	51.20 ± (4.93, 10.49)	22.10 ± (5.16, 10.91)	0.56372 ± (0.05427, 0.11549)
4.600	77.90 ± (11.79, 16.57)	45.02 ± (11.95, 17.25)	0.86272 ± (0.13061, 0.18354)

TABLE IV - 4

16.0 GeV 50<sup>0</sup>

W (GeV)	Q <sup>2</sup> (GeV <sup>2</sup> )	c	x <sup>-</sup>	x <sup>+</sup>	$\frac{d^2\sigma}{dQdE'} (\frac{pb}{GeV\text{-sr}})$	2H W <sub>1</sub> <sup>P</sup>
PROTON						
2.700	20.285	0.1732	0.760	0.736	3.207 ± (1.043, 0.158)	0.02128 ± (0.00692, 0.00105)
2.800	19.812	0.1695	0.740	0.716	2.819 ± (0.588, 0.208)	0.01880 ± (0.00392, 0.00139)
2.900	19.323	0.1655	0.720	0.697	4.484 ± (0.539, 0.272)	0.03007 ± (0.00361, 0.00182)
3.000	18.816	0.1614	0.699	0.676	5.967 ± (0.544, 0.352)	0.04024 ± (0.00367, 0.00238)
3.100	18.292	0.1572	0.677	0.656	8.144 ± (0.618, 0.454)	0.05524 ± (0.00419, 0.00308)
3.200	17.751	0.1527	0.655	0.634	10.711 ± (0.798, 0.581)	0.07308 ± (0.00544, 0.00396)
3.300	17.192	0.1482	0.632	0.612	10.637 ± (0.884, 0.742)	0.07303 ± (0.00607, 0.00510)
3.400	16.617	0.1435	0.609	0.590	15.507 ± (1.144, 0.951)	0.10715 ± (0.00791, 0.00657)
3.500	16.024	0.1386	0.585	0.567	19.369 ± (1.402, 1.218)	0.13471 ± (0.00975, 0.00847)
3.600	15.414	0.1335	0.561	0.545	19.451 ± (1.431, 1.562)	0.13620 ± (0.01002, 0.01094)
3.700	14.787	0.1283	0.536	0.519	26.463 ± (1.727, 2.025)	0.18658 ± (0.01218, 0.01427)
3.800	14.143	0.1229	0.511	0.495	30.870 ± (2.054, 2.672)	0.21920 ± (0.01459, 0.01897)
3.900	13.482	0.1174	0.485	0.470	36.776 ± (2.559, 3.640)	0.26304 ± (0.01831, 0.02604)
4.000	12.803	0.1117	0.459	0.445	39.231 ± (3.060, 5.199)	0.28270 ± (0.02205, 0.03747)
4.100	12.107	0.1058	0.432	0.419	46.261 ± (3.885, 7.852)	0.33591 ± (0.02821, 0.05702)
4.200	11.394	0.0998	0.405	0.392	50.718 ± (5.697, 12.562)	0.37116 ± (0.04169, 0.09193)

W (GeV)	$\frac{d^2\sigma}{dQdE'} (\frac{pb}{GeV\text{-sr}})$	$\frac{d^2\sigma}{dQdE'} (\frac{pb}{GeV\text{-sr}})$	2H W <sub>1</sub> <sup>D</sup>
	DEUTERON		
	NEUTRON		
2.700	6.22 ± ( 1.56, 0.25)	2.71 ± ( 1.56, 0.23)	0.04130 ± (0.01035, 0.00166)
2.800	7.40 ± ( 1.02, 0.33)	3.10 ± ( 1.04, 0.30)	0.04938 ± (0.00679, 0.00218)
2.900	7.63 ± ( 0.77, 0.42)	2.41 ± ( 0.81, 0.40)	0.05116 ± (0.00518, 0.00284)
3.000	9.40 ± ( 0.76, 0.55)	2.95 ± ( 0.82, 0.53)	0.06338 ± (0.00513, 0.00370)
3.100	11.26 ± ( 0.83, 0.71)	3.33 ± ( 0.92, 0.70)	0.07639 ± (0.00565, 0.00480)
3.200	15.21 ± ( 1.13, 0.92)	5.48 ± ( 1.23, 0.92)	0.10381 ± (0.00769, 0.00628)
3.300	18.45 ± ( 1.39, 1.20)	6.61 ± ( 1.51, 1.21)	0.12667 ± (0.00951, 0.00826)
3.400	22.08 ± ( 1.61, 1.58)	7.74 ± ( 1.76, 1.61)	0.15259 ± (0.01111, 0.01091)
3.500	24.80 ± ( 1.87, 2.07)	7.47 ± ( 2.07, 2.12)	0.17249 ± (0.01304, 0.01440)
3.600	35.17 ± ( 2.48, 2.70)	14.52 ± ( 2.69, 2.78)	0.24624 ± (0.01734, 0.01888)
3.700	40.21 ± ( 3.38, 3.54)	15.34 ± ( 3.61, 3.65)	0.28352 ± (0.02385, 0.02493)
3.800	59.61 ± ( 4.84, 4.62)	30.75 ± ( 5.07, 4.79)	0.42325 ± (0.03436, 0.03282)
3.900	57.60 ± ( 4.92, 6.26)	23.03 ± ( 5.24, 6.52)	0.41196 ± (0.03522, 0.04489)
4.000	57.77 ± ( 4.89, 8.97)	16.69 ± ( 5.33, 9.33)	0.41626 ± (0.03522, 0.06462)
4.100	87.41 ± ( 5.56, 13.56)	40.06 ± ( 6.09, 14.11)	0.63457 ± (0.04037, 0.09846)
4.200	107.46 ± ( 7.80, 21.77)	52.40 ± ( 8.33, 22.66)	0.78639 ± (0.05706, 0.15930)

TABLE IV - 4

13.5 GeV 50°

W (GeV)	Q <sup>2</sup> (GeV <sup>2</sup> )	ε	x''	x'	$\frac{d^2\sigma}{dQdE'} (\frac{pb}{GeV-sr})$	2M W <sub>1</sub> <sup>P</sup>
PROTON						
2.400	17.122	0.2030	0.778	0.748	3.869 ± (0.969, 0.240)	0.01753 ± (0.00439, 0.00109)
2.500	16.712	0.1985	0.757	0.728	4.395 ± (1.109, 0.311)	0.02004 ± (0.00505, 0.00142)
2.600	16.285	0.1938	0.735	0.707	7.810 ± (1.184, 0.406)	0.03585 ± (0.00543, 0.00186)
2.700	15.841	0.1889	0.712	0.682	10.028 ± (1.119, 0.501)	0.04635 ± (0.00517, 0.00232)
2.800	15.381	0.1838	0.688	0.662	11.449 ± (1.127, 0.664)	0.05330 ± (0.00525, 0.00309)
2.900	14.904	0.1784	0.664	0.639	14.362 ± (1.241, 0.874)	0.06736 ± (0.00582, 0.00410)
3.000	14.410	0.1729	0.640	0.616	18.431 ± (1.462, 1.090)	0.08711 ± (0.00691, 0.00515)
3.100	13.899	0.1671	0.614	0.591	20.588 ± (1.814, 1.368)	0.09808 ± (0.00884, 0.00652)
3.200	13.372	0.1611	0.588	0.566	24.944 ± (2.181, 1.757)	0.11981 ± (0.01048, 0.00844)
3.300	12.828	0.1549	0.562	0.541	33.571 ± (2.518, 2.284)	0.16262 ± (0.01220, 0.01107)
3.400	12.267	0.1485	0.535	0.515	41.059 ± (3.162, 3.000)	0.20063 ± (0.01545, 0.01466)
3.500	11.689	0.1418	0.507	0.488	47.265 ± (3.504, 3.914)	0.23304 ± (0.01727, 0.01930)
3.600	11.095	0.1349	0.479	0.461	53.889 ± (3.570, 5.329)	0.26816 ± (0.01776, 0.02652)
3.700	10.484	0.1278	0.450	0.434	67.394 ± (4.565, 7.605)	0.33854 ± (0.02293, 0.03820)
3.800	9.856	0.1204	0.421	0.406	73.099 ± (6.374, 11.205)	0.37078 ± (0.03233, 0.05684)

W (GeV)	$\frac{d^2\sigma}{dQdE'} (\frac{pb}{GeV-sr})$	$\frac{d^2\sigma}{dQdE'} (\frac{pb}{GeV-sr})$	2M W <sub>1</sub> <sup>P</sup>
	DEUTERON	NEUTRON	
2.400	5.80 ± ( 1.97, 0.85)	1.57 ± ( 1.97, 0.75)	0.02627 ± (0.00892, 0.00386)
2.500	7.14 ± ( 1.56, 0.80)	1.70 ± ( 1.59, 0.74)	0.03256 ± (0.00712, 0.00366)
2.600	10.40 ± ( 1.42, 0.59)	3.36 ± ( 1.47, 0.56)	0.04775 ± (0.00654, 0.00269)
2.700	11.27 ± ( 1.26, 0.81)	2.53 ± ( 1.33, 0.78)	0.05208 ± (0.00581, 0.00372)
2.800	16.17 ± ( 1.39, 1.02)	5.11 ± ( 1.50, 1.01)	0.07526 ± (0.00649, 0.00474)
2.900	21.26 ± ( 1.65, 1.26)	7.50 ± ( 1.79, 1.28)	0.09970 ± (0.00775, 0.00600)
3.000	27.65 ± ( 2.13, 1.65)	10.63 ± ( 2.30, 1.65)	0.13063 ± (0.01008, 0.00772)
3.100	29.90 ± ( 2.95, 2.20)	8.95 ± ( 3.13, 2.25)	0.14243 ± (0.01404, 0.01049)
3.200	39.31 ± ( 4.11, 3.10)	13.72 ± ( 4.32, 3.19)	0.18881 ± (0.01975, 0.01491)
3.300	50.47 ± ( 4.96, 3.77)	19.49 ± ( 5.22, 3.89)	0.24447 ± (0.02404, 0.01827)
3.400	62.25 ± ( 5.98, 4.96)	24.93 ± ( 6.29, 5.14)	0.30425 ± (0.02925, 0.02424)
3.500	72.89 ± ( 5.99, 6.71)	28.04 ± ( 6.44, 6.96)	0.35940 ± (0.02955, 0.03307)
3.600	93.15 ± ( 6.05, 9.19)	34.88 ± ( 6.66, 9.55)	0.46352 ± (0.03012, 0.04571)
3.700	101.11 ± ( 6.64, 13.17)	37.46 ± ( 7.41, 13.71)	0.50792 ± (0.03334, 0.06617)
3.800	121.10 ± ( 8.69, 20.24)	46.00 ± ( 9.54, 21.07)	0.61429 ± (0.04406, 0.10269)

TABLE IV - 4

7.0 GeV 50°

W (GeV)	Q <sub>2</sub> <sup>2</sup> (GeV <sup>2</sup> )	ε	x <sup>-</sup>	x <sup>+</sup>	$\frac{d^2\sigma}{d\Omega dE'} \left( \frac{pb}{GeV-sr} \right)$	2M W <sub>1</sub> <sup>P</sup>
PROTON						
2.000	7.283	0.3058	0.700	0.645	69.54 ± ( 6.57, 4.32)	0.07247 ± (0.00685, 0.00450)
2.100	6.985	0.2950	0.664	0.613	82.03 ± ( 7.14, 5.74)	0.08698 ± (0.00758, 0.00609)
2.200	6.672	0.2835	0.628	0.580	112.96 ± ( 9.55, 7.55)	0.12197 ± (0.01031, 0.00815)
2.300	6.345	0.2713	0.590	0.545	155.33 ± (11.11, 10.10)	0.17095 ± (0.01223, 0.01111)
2.400	6.003	0.2583	0.552	0.510	187.54 ± (12.03, 13.33)	0.20830 ± (0.01350, 0.01496)
2.500	5.647	0.2446	0.513	0.475	237.86 ± (13.94, 17.26)	0.27263 ± (0.01598, 0.01979)
2.600	5.276	0.2300	0.473	0.438	300.61 ± (14.80, 22.73)	0.35208 ± (0.01734, 0.02662)
2.700	4.891	0.2146	0.433	0.402	387.83 ± (16.35, 30.75)	0.46455 ± (0.01959, 0.03683)
2.800	4.491	0.1984	0.392	0.364	460.71 ± (19.41, 40.38)	0.56482 ± (0.02380, 0.04950)
2.900	4.076	0.1813	0.351	0.326	530.56 ± (28.07, 56.81)	0.67385 ± (0.03526, 0.07134)

W (GeV)	$\frac{d^2\sigma}{d\Omega dE'} \left( \frac{pb}{GeV-sr} \right)$	$\frac{d^2\sigma}{d\Omega dE'} \left( \frac{pb}{GeV-sr} \right)$	2M W <sub>1</sub> <sup>D</sup>
DEUTERON		NEUTRON	
2.000	97.33 ± ( 7.77, 6.34)	32.02 ± ( 8.82, 6.46)	0.10144 ± (0.00810, 0.00661)
2.100	139.14 ± ( 8.49, 8.39)	49.99 ± ( 9.61, 8.63)	0.14754 ± (0.00900, 0.00890)
2.200	189.78 ± (11.30, 11.50)	74.40 ± (12.77, 11.97)	0.20493 ± (0.01220, 0.01248)
2.300	224.46 ± (12.23, 16.03)	75.94 ± (14.42, 16.67)	0.24703 ± (0.01346, 0.01765)
2.400	271.43 ± (13.83, 21.61)	82.77 ± (16.87, 22.52)	0.30472 ± (0.01553, 0.02426)
2.500	368.26 ± (17.44, 29.54)	133.57 ± (21.24, 30.80)	0.42210 ± (0.01999, 0.03386)
2.600	472.68 ± (21.05, 38.00)	183.25 ± (25.85, 39.61)	0.55362 ± (0.02465, 0.04451)
2.700	588.90 ± (24.17, 48.41)	204.17 ± (30.39, 50.37)	0.66945 ± (0.02895, 0.05799)
2.800	700.62 ± (25.09, 63.74)	270.59 ± (33.62, 66.13)	0.85895 ± (0.03076, 0.07814)
2.900	763.88 ± (35.72, 83.95)	240.80 ± (45.74, 86.84)	0.95934 ± (0.04486, 0.10543)



TABLE IV - 4

19.5 GeV 60°

W (GeV)	Q <sup>2</sup> (GeV <sup>2</sup> )	c	x	x'	$\frac{d^2\sigma}{dQdE'} (\frac{pb}{GeV-sr})$ PROTON	2M W <sub>1</sub> <sup>P</sup>
2.000	30.544	0.1151	0.907	0.884	0.053 ± (0.010, 0.004)	0.00079 ± (0.00015, 0.00006)
2.100	30.170	0.1137	0.895	0.872	0.053 ± (0.011, 0.006)	0.00080 ± (0.00017, 0.00008)
2.200	29.778	0.1123	0.883	0.860	0.131 ± (0.015, 0.008)	0.00196 ± (0.00022, 0.00011)
2.300	29.367	0.1108	0.869	0.847	0.140 ± (0.016, 0.010)	0.00210 ± (0.00024, 0.00015)
2.400	28.938	0.1093	0.856	0.834	0.244 ± (0.020, 0.014)	0.00367 ± (0.00031, 0.00021)
2.500	28.491	0.1077	0.841	0.820	0.304 ± (0.024, 0.019)	0.00458 ± (0.00037, 0.00028)
2.600	28.026	0.1060	0.827	0.806	0.379 ± (0.030, 0.025)	0.00573 ± (0.00045, 0.00038)
2.700	27.543	0.1043	0.811	0.791	0.563 ± (0.037, 0.034)	0.00852 ± (0.00056, 0.00051)
2.800	27.041	0.1025	0.795	0.775	0.716 ± (0.044, 0.045)	0.01086 ± (0.00067, 0.00068)
2.900	26.521	0.1006	0.779	0.759	0.922 ± (0.055, 0.060)	0.01402 ± (0.00084, 0.00091)
3.000	25.983	0.0986	0.762	0.743	1.039 ± (0.067, 0.079)	0.01585 ± (0.00102, 0.00121)
3.100	25.426	0.0966	0.744	0.726	1.383 ± (0.090, 0.105)	0.02114 ± (0.00138, 0.00160)
3.200	24.852	0.0945	0.726	0.708	1.825 ± (0.119, 0.138)	0.02797 ± (0.00183, 0.00211)
3.300	24.259	0.0923	0.708	0.690	2.317 ± (0.147, 0.181)	0.03562 ± (0.00226, 0.00279)
3.400	23.648	0.0901	0.689	0.672	2.997 ± (0.180, 0.238)	0.04620 ± (0.00277, 0.00368)
3.500	23.018	0.0878	0.669	0.653	3.508 ± (0.201, 0.315)	0.05423 ± (0.00311, 0.00487)
3.600	22.370	0.0854	0.649	0.633	4.730 ± (0.234, 0.418)	0.07335 ± (0.00362, 0.00648)
3.700	21.704	0.0829	0.629	0.613	5.679 ± (0.266, 0.560)	0.08835 ± (0.00414, 0.00870)
3.800	21.020	0.0804	0.608	0.593	6.348 ± (0.346, 0.760)	0.09906 ± (0.00541, 0.01186)
3.900	20.318	0.0778	0.586	0.572	7.509 ± (0.346, 1.051)	0.11758 ± (0.00542, 0.01646)
W (GeV)	$\frac{d^2\sigma}{dQdE'} (\frac{pb}{GeV-sr})$ DEUTERON	$\frac{d^2\sigma}{dQdE'} (\frac{pb}{GeV-sr})$ NEUTRON			2M W <sub>1</sub> <sup>D</sup>	
2.000	0.145 ± (0.019, 0.010)	0.009 ± (0.016, 0.004)			0.00217 ± (0.00028, 0.00015)	
2.100	0.176 ± (0.019, 0.013)	0.011 ± (0.016, 0.006)			0.00264 ± (0.00028, 0.00019)	
2.200	0.305 ± (0.023, 0.017)	0.057 ± (0.020, 0.009)			0.00456 ± (0.00034, 0.00025)	
2.300	0.336 ± (0.025, 0.022)	0.053 ± (0.027, 0.013)			0.00505 ± (0.00037, 0.00032)	
2.400	0.429 ± (0.028, 0.026)	0.076 ± (0.032, 0.018)			0.00645 ± (0.00042, 0.00042)	
2.500	0.484 ± (0.033, 0.037)	0.063 ± (0.038, 0.026)			0.00729 ± (0.00049, 0.00055)	
2.600	0.682 ± (0.042, 0.048)	0.136 ± (0.048, 0.035)			0.01029 ± (0.00063, 0.00072)	
2.700	0.826 ± (0.049, 0.062)	0.155 ± (0.058, 0.049)			0.01261 ± (0.00074, 0.00074)	
2.800	1.344 ± (0.065, 0.081)	0.454 ± (0.075, 0.067)			0.02039 ± (0.00098, 0.00133)	
2.900	1.342 ± (0.074, 0.106)	0.302 ± (0.088, 0.091)			0.02041 ± (0.00112, 0.00161)	
3.000	1.774 ± (0.095, 0.138)	0.477 ± (0.113, 0.123)			0.02705 ± (0.00145, 0.00211)	
3.100	2.306 ± (0.127, 0.182)	0.703 ± (0.148, 0.166)			0.03526 ± (0.00194, 0.00278)	
3.200	2.589 ± (0.156, 0.239)	0.647 ± (0.183, 0.224)			0.03969 ± (0.00240, 0.00367)	
3.300	3.620 ± (0.198, 0.317)	1.226 ± (0.229, 0.302)			0.05565 ± (0.00304, 0.00487)	
3.400	4.505 ± (0.238, 0.421)	1.597 ± (0.277, 0.408)			0.06945 ± (0.00367, 0.00649)	
3.500	5.672 ± (0.282, 0.566)	2.154 ± (0.331, 0.557)			0.08769 ± (0.00436, 0.00875)	
3.600	7.032 ± (0.338, 0.761)	2.796 ± (0.398, 0.757)			0.10906 ± (0.00524, 0.01180)	
3.700	8.611 ± (0.416, 1.031)	3.537 ± (0.488, 1.037)			0.13296 ± (0.00647, 0.01604)	
3.800	9.785 ± (0.573, 1.417)	3.721 ± (0.690, 1.437)			0.15272 ± (0.00894, 0.02212)	
3.900	11.749 ± (0.873, 1.983)	4.312 ± (0.650, 2.025)			0.18396 ± (0.00897, 0.03106)	

TABLE IV - 4

16.0 GeV 60°

W (GeV)	Q <sup>2</sup> (GeV <sup>2</sup> )	ε	x <sup>-</sup>	x <sup>+</sup>	$\frac{d^2\sigma}{d\Omega dx'} (\frac{pb}{GeV-sr})$ PROTON	2M W <sub>1</sub> <sup>P</sup>
2.000	24.085	0.1336	0.885	0.858	0.203 ± (0.021, 0.012)	0.00199 ± (0.00020, 0.00011)
2.100	23.718	0.1317	0.870	0.843	0.362 ± (0.027, 0.016)	0.00355 ± (0.00026, 0.00016)
2.200	23.333	0.1297	0.855	0.828	0.461 ± (0.033, 0.023)	0.00455 ± (0.00032, 0.00023)
2.300	22.930	0.1276	0.839	0.813	0.565 ± (0.043, 0.032)	0.00558 ± (0.00043, 0.00032)
2.400	22.509	0.1254	0.822	0.796	0.748 ± (0.056, 0.045)	0.00741 ± (0.00056, 0.00044)
2.500	22.071	0.1231	0.804	0.779	1.138 ± (0.075, 0.061)	0.01132 ± (0.00074, 0.00061)
2.600	21.614	0.1207	0.786	0.762	1.327 ± (0.090, 0.084)	0.01324 ± (0.00090, 0.00084)
2.700	21.140	0.1182	0.767	0.744	1.872 ± (0.120, 0.113)	0.01873 ± (0.00120, 0.00113)
2.800	20.648	0.1155	0.748	0.725	2.439 ± (0.156, 0.152)	0.02449 ± (0.00156, 0.00153)
2.900	20.137	0.1128	0.728	0.705	3.087 ± (0.196, 0.204)	0.03111 ± (0.00197, 0.00205)
3.000	19.609	0.1100	0.707	0.685	3.353 ± (0.221, 0.271)	0.03291 ± (0.00224, 0.00274)
3.100	19.063	0.1071	0.686	0.665	4.673 ± (0.262, 0.359)	0.04744 ± (0.00266, 0.00365)
3.200	18.499	0.1041	0.664	0.644	5.516 ± (0.323, 0.477)	0.05622 ± (0.00329, 0.00486)
3.300	17.918	0.1009	0.642	0.622	7.578 ± (0.480, 0.634)	0.07754 ± (0.00491, 0.00649)
3.400	17.318	0.0977	0.619	0.600	9.528 ± (0.776, 0.852)	0.09790 ± (0.00797, 0.00875)
3.500	16.700	0.0944	0.595	0.577	11.109 ± (0.776, 1.159)	0.11463 ± (0.00800, 0.01196)

W (GeV)	$\frac{d^2\sigma}{d\Omega dx'} (\frac{pb}{GeV-sr})$ NEUTRON	$\frac{d^2\sigma}{d\Omega dx'} (\frac{pb}{GeV-sr})$ NEUTRON	2M W <sub>1</sub> <sup>D</sup>
2.000	0.425 ± (0.032, 0.025)	0.055 ± (0.036, 0.014)	0.00416 ± (0.00032, 0.00023)
2.100	0.574 ± (0.037, 0.033)	0.094 ± (0.042, 0.021)	0.00564 ± (0.00036, 0.00033)
2.200	0.730 ± (0.046, 0.045)	0.126 ± (0.053, 0.030)	0.00720 ± (0.00045, 0.00044)
2.300	0.942 ± (0.060, 0.060)	0.174 ± (0.069, 0.043)	0.00931 ± (0.00059, 0.00059)
2.400	1.243 ± (0.080, 0.080)	0.260 ± (0.091, 0.062)	0.01232 ± (0.00079, 0.00079)
2.500	1.710 ± (0.102, 0.106)	0.442 ± (0.117, 0.087)	0.01700 ± (0.00102, 0.00106)
2.600	1.916 ± (0.116, 0.141)	0.360 ± (0.137, 0.121)	0.01911 ± (0.00116, 0.00141)
2.700	2.734 ± (0.148, 0.189)	0.732 ± (0.176, 0.168)	0.02735 ± (0.00149, 0.00189)
2.800	3.608 ± (0.185, 0.254)	1.087 ± (0.220, 0.233)	0.03622 ± (0.00185, 0.00253)
2.900	4.799 ± (0.223, 0.338)	1.641 ± (0.270, 0.318)	0.04835 ± (0.00225, 0.00340)
3.000	5.753 ± (0.265, 0.453)	1.851 ± (0.327, 0.435)	0.05818 ± (0.00268, 0.00458)
3.100	7.215 ± (0.307, 0.611)	2.393 ± (0.388, 0.597)	0.07323 ± (0.00311, 0.00620)
3.200	8.798 ± (0.360, 0.831)	2.872 ± (0.465, 0.824)	0.08966 ± (0.00367, 0.00847)
3.300	10.559 ± (0.489, 1.114)	3.307 ± (0.609, 1.117)	0.10804 ± (0.00501, 0.01140)
3.400	14.049 ± (0.832, 1.545)	5.230 ± (0.943, 1.564)	0.14436 ± (0.00854, 0.01587)
3.500	17.185 ± (0.832, 2.174)	6.289 ± (0.943, 2.218)	0.17733 ± (0.00858, 0.02243)

TABLE IV - 4

13.3 GeV  $60^\circ$

W (GeV)	Q <sup>2</sup> (GeV <sup>2</sup> )	ε	x <sup>-</sup>	x <sup>+</sup>	$\frac{d^2\sigma}{dQdE'} (\frac{pb}{GeV-sr})$	2M W <sub>1</sub> <sup>P</sup>
PROTON						
2.000	19.120	0.1523	0.860	0.827	0.656 ± (0.066, 0.043)	0.00434 ± (0.00044, 0.00028)
2.100	18.761	0.1497	0.842	0.810	0.940 ± (0.069, 0.064)	0.00622 ± (0.00046, 0.00042)
2.200	18.384	0.1469	0.823	0.792	1.342 ± (0.093, 0.128)	0.00891 ± (0.00062, 0.00085)
2.300	17.990	0.1440	0.803	0.773	1.689 ± (0.114, 0.164)	0.01126 ± (0.00076, 0.00109)
2.400	17.578	0.1409	0.783	0.753	2.455 ± (0.149, 0.173)	0.01644 ± (0.00100, 0.00116)
2.500	17.148	0.1377	0.762	0.733	3.099 ± (0.183, 0.237)	0.02085 ± (0.00123, 0.00159)
2.600	16.702	0.1343	0.740	0.712	3.792 ± (0.227, 0.385)	0.02562 ± (0.00154, 0.00260)
2.700	16.237	0.1308	0.717	0.690	4.849 ± (0.313, 0.578)	0.03292 ± (0.00212, 0.00393)
2.800	15.755	0.1271	0.694	0.668	6.611 ± (0.469, 0.801)	0.04509 ± (0.00320, 0.00546)
2.900	15.256	0.1233	0.670	0.645	8.823 ± (0.646, 0.967)	0.06048 ± (0.00443, 0.00663)
3.000	14.739	0.1194	0.645	0.621	11.855 ± (0.877, 1.017)	0.08169 ± (0.00604, 0.00701)
3.100	14.204	0.1153	0.619	0.596	16.603 ± (1.247, 1.280)	0.11641 ± (0.00864, 0.00887)
3.200	13.652	0.1110	0.593	0.571	17.300 ± (1.321, 1.846)	0.12052 ± (0.00921, 0.01286)
3.300	13.083	0.1066	0.567	0.546	24.100 ± (1.264, 2.444)	0.16886 ± (0.00886, 0.01713)
3.400	12.495	0.1020	0.539	0.519	29.057 ± (1.518, 3.161)	0.20480 ± (0.01070, 0.02228)

W (GeV)	$\frac{d^2\sigma}{dQdE'} (\frac{pb}{GeV-sr})$	$\frac{d^2\sigma}{dQdE'} (\frac{pb}{GeV-sr})$	2M W <sub>1</sub> <sup>D</sup>
DEUTERON		NEUTRON	
2.000	1.198 ± (0.069, 0.085)	0.220 ± (0.104, 0.063)	0.00790 ± (0.00059, 0.00056)
2.100	1.635 ± (0.092, 0.127)	0.364 ± (0.108, 0.100)	0.01082 ± (0.00061, 0.00084)
2.200	2.267 ± (0.121, 0.152)	0.600 ± (0.142, 0.127)	0.01506 ± (0.00081, 0.00101)
2.300	2.802 ± (0.148, 0.183)	0.690 ± (0.177, 0.161)	0.01869 ± (0.00099, 0.00122)
2.400	3.501 ± (0.182, 0.297)	0.803 ± (0.222, 0.270)	0.02345 ± (0.00122, 0.00199)
2.500	5.020 ± (0.247, 0.356)	1.510 ± (0.298, 0.334)	0.03375 ± (0.00166, 0.00240)
2.600	5.938 ± (0.325, 0.574)	1.506 ± (0.389, 0.549)	0.04012 ± (0.00220, 0.00388)
2.700	8.229 ± (0.440, 0.701)	2.573 ± (0.519, 0.685)	0.05586 ± (0.00298, 0.00476)
2.800	10.704 ± (0.561, 0.851)	3.576 ± (0.662, 0.845)	0.07301 ± (0.00382, 0.00580)
2.900	12.725 ± (0.657, 1.364)	3.805 ± (0.793, 1.369)	0.08723 ± (0.00450, 0.00935)
3.000	18.025 ± (0.854, 1.771)	6.924 ± (1.019, 1.796)	0.12421 ± (0.00588, 0.01220)
3.100	22.619 ± (1.255, 2.103)	8.909 ± (1.435, 2.151)	0.15671 ± (0.00870, 0.01457)
3.200	28.236 ± (2.183, 2.815)	11.405 ± (2.348, 2.897)	0.19671 ± (0.01521, 0.01961)
3.300	33.456 ± (4.265, 4.522)	12.854 ± (4.399, 4.673)	0.23441 ± (0.02988, 0.03168)

TABLE IV - 4

10.4 GeV 60°

W (GeV)	Q <sup>2</sup> (GeV <sup>2</sup> )	x	x'	x''	$\frac{d^2\sigma}{d\Omega dE'} (\frac{pb}{GeV-sr})$	2M W <sub>1</sub> <sup>P</sup>
PROTON						
2.000	13.890	0.1783	0.817	0.776	3.066 ± (0.242, 0.185)	0.01195 ± (0.00094, 0.00072)
2.100	13.543	0.1742	0.793	0.754	4.529 ± (0.303, 0.250)	0.01775 ± (0.00119, 0.00098)
2.200	13.179	0.1699	0.769	0.731	6.535 ± (0.407, 0.346)	0.02576 ± (0.00161, 0.00136)
2.300	12.797	0.1654	0.744	0.708	8.826 ± (0.525, 0.503)	0.03501 ± (0.00208, 0.00200)
2.400	12.399	0.1606	0.718	0.683	11.352 ± (0.654, 0.682)	0.04533 ± (0.00261, 0.00272)
2.500	11.984	0.1557	0.691	0.657	14.777 ± (0.798, 0.907)	0.05941 ± (0.00321, 0.00365)
2.600	11.552	0.1505	0.663	0.631	18.640 ± (0.918, 1.246)	0.07546 ± (0.00372, 0.00505)
2.700	11.103	0.1450	0.634	0.604	23.521 ± (1.049, 1.671)	0.09593 ± (0.00428, 0.00682)
2.800	10.637	0.1393	0.604	0.576	30.076 ± (1.285, 2.305)	0.12360 ± (0.00528, 0.00947)
2.900	10.154	0.1334	0.574	0.547	37.634 ± (1.718, 3.145)	0.15589 ± (0.00712, 0.01333)
3.000	9.655	0.1272	0.543	0.518	47.507 ± (2.438, 4.403)	0.19841 ± (0.01018, 0.01839)
3.100	9.138	0.1208	0.511	0.487	59.928 ± (4.701, 6.120)	0.22715 ± (0.01980, 0.02578)

W (GeV)	$\frac{d^2\sigma}{d\Omega dE'} (\frac{pb}{GeV-sr})$	$\frac{d^2\sigma}{d\Omega dE'} (\frac{pb}{GeV-sr})$	2M W <sub>1</sub> <sup>D</sup>
	DEUTERON	NEUTRON	
2.000	4.77 ± (0.31, 0.28)	1.12 ± (0.36, 0.24)	0.01860 ± (0.00121, 0.00109)
2.100	6.81 ± (0.39, 0.39)	1.95 ± (0.45, 0.35)	0.02670 ± (0.00152, 0.00154)
2.200	9.58 ± (0.50, 0.53)	3.15 ± (0.59, 0.49)	0.03776 ± (0.00199, 0.00210)
2.300	12.29 ± (0.63, 0.74)	3.94 ± (0.75, 0.70)	0.04877 ± (0.00251, 0.00293)
2.400	15.84 ± (0.80, 1.02)	5.00 ± (0.96, 0.99)	0.06324 ± (0.00319, 0.00407)
2.500	19.61 ± (0.95, 1.42)	5.66 ± (1.18, 1.41)	0.07881 ± (0.00381, 0.00572)
2.600	26.43 ± (1.16, 1.99)	8.55 ± (1.46, 2.01)	0.10700 ± (0.00469, 0.00807)
2.700	35.17 ± (1.49, 2.72)	12.50 ± (1.88, 2.77)	0.14342 ± (0.00608, 0.01111)
2.800	43.82 ± (2.02, 3.84)	15.29 ± (2.49, 3.94)	0.18009 ± (0.00831, 0.01577)
2.900	56.90 ± (2.92, 5.38)	21.32 ± (3.44, 5.55)	0.23570 ± (0.01208, 0.02229)
3.000	68.62 ± (4.34, 7.83)	24.47 ± (4.90, 8.12)	0.28660 ± (0.01815, 0.03271)
3.100	90.90 ± (9.25, 10.44)	36.80 ± (9.70, 10.85)	0.38286 ± (0.03896, 0.04398)

TABLE IV - 4

6.5 GeV 60°

W (GeV)	Q <sup>2</sup> (GeV <sup>2</sup> )	c	x''	x'	$\frac{d^2\sigma}{dQ^2 dx'' dx'} \left( \frac{pb}{GeV-sr} \right)$ PROTON	2M W <sub>1</sub> <sup>P</sup>
1.075	9.251	0.2838	0.971	0.889	-0.218 ± (0.206, -0.000)	-0.00028 ± (0.00027, -0.00000)
1.100	9.209	0.2827	0.965	0.884	0.207 ± (0.233, 0.076)	0.00027 ± (0.00030, 0.00010)
1.125	9.166	0.2816	0.960	0.879	0.542 ± (0.248, 0.082)	0.00071 ± (0.00032, 0.00011)
1.150	9.122	0.2805	0.954	0.873	0.962 ± (0.261, 0.094)	0.00126 ± (0.00034, 0.00012)
1.175	9.077	0.2794	0.948	0.868	0.442 ± (0.200, 0.074)	0.00058 ± (0.00026, 0.00010)
1.200	9.031	0.2782	0.942	0.862	1.504 ± (0.277, 0.110)	0.00198 ± (0.00036, 0.00014)
1.225	8.984	0.2770	0.935	0.857	1.879 ± (0.282, 0.124)	0.00247 ± (0.00037, 0.00016)
1.250	8.936	0.2758	0.929	0.851	2.068 ± (0.287, 0.131)	0.00273 ± (0.00038, 0.00017)
1.275	8.887	0.2745	0.923	0.845	2.484 ± (0.303, 0.147)	0.00328 ± (0.00040, 0.00019)
1.300	8.837	0.2732	0.916	0.839	3.469 ± (0.340, 0.186)	0.00462 ± (0.00045, 0.00025)
1.325	8.786	0.2719	0.909	0.833	3.000 ± (0.322, 0.170)	0.00398 ± (0.00043, 0.00023)
1.350	8.734	0.2706	0.903	0.827	4.014 ± (0.352, 0.211)	0.00534 ± (0.00047, 0.00028)
1.375	8.681	0.2692	0.896	0.821	4.442 ± (0.362, 0.231)	0.00592 ± (0.00048, 0.00031)
1.400	8.627	0.2678	0.889	0.815	5.083 ± (0.422, 0.283)	0.00759 ± (0.00056, 0.00038)
1.425	8.572	0.2664	0.882	0.808	6.479 ± (0.424, 0.319)	0.00867 ± (0.00057, 0.00043)
1.450	8.517	0.2649	0.875	0.802	6.967 ± (0.464, 0.343)	0.00935 ± (0.00062, 0.00046)
1.475	8.460	0.2634	0.867	0.795	9.519 ± (0.560, 0.451)	0.01280 ± (0.00075, 0.00061)
1.500	8.402	0.2619	0.860	0.789	13.267 ± (0.644, 0.609)	0.01788 ± (0.00087, 0.00082)
1.525	8.343	0.2604	0.852	0.782	13.895 ± (0.679, 0.643)	0.01877 ± (0.00092, 0.00087)
1.550	8.284	0.2588	0.845	0.775	11.633 ± (0.620, 0.558)	0.01575 ± (0.00084, 0.00076)
1.575	8.223	0.2572	0.837	0.768	10.733 ± (0.611, 0.530)	0.01457 ± (0.00083, 0.00072)
1.600	8.162	0.2556	0.829	0.761	11.903 ± (0.658, 0.588)	0.01620 ± (0.00089, 0.00080)
1.625	8.099	0.2539	0.821	0.754	12.925 ± (0.669, 0.641)	0.01763 ± (0.00091, 0.00087)
1.650	8.036	0.2522	0.814	0.747	17.549 ± (0.809, 0.847)	0.02400 ± (0.00111, 0.00116)
1.675	7.971	0.2505	0.805	0.740	21.931 ± (0.944, 1.046)	0.03007 ± (0.00129, 0.00143)
1.700	7.906	0.2487	0.797	0.732	25.538 ± (1.013, 1.216)	0.03511 ± (0.00139, 0.00167)
1.725	7.839	0.2469	0.789	0.725	24.795 ± (1.026, 1.202)	0.03418 ± (0.00141, 0.00166)
1.750	7.772	0.2451	0.781	0.717	28.350 ± (1.086, 1.375)	0.03919 ± (0.00150, 0.00190)
1.775	7.703	0.2432	0.772	0.710	26.288 ± (1.079, 1.308)	0.03644 ± (0.00150, 0.00181)
1.800	7.634	0.2414	0.764	0.702	27.751 ± (1.132, 1.396)	0.03858 ± (0.00157, 0.00194)
1.825	7.564	0.2394	0.755	0.694	31.461 ± (1.237, 1.585)	0.04389 ± (0.00172, 0.00221)
1.850	7.492	0.2375	0.747	0.686	32.169 ± (1.308, 1.645)	0.04498 ± (0.00183, 0.00230)
1.875	7.420	0.2355	0.738	0.679	36.085 ± (1.451, 1.852)	0.05060 ± (0.00203, 0.00260)
1.900	7.347	0.2335	0.729	0.671	37.611 ± (1.557, 1.957)	0.05290 ± (0.00219, 0.00275)
1.925	7.273	0.2314	0.720	0.662	43.562 ± (1.734, 2.266)	0.06145 ± (0.00245, 0.00320)
1.950	7.197	0.2294	0.711	0.654	45.129 ± (1.823, 2.382)	0.06385 ± (0.00258, 0.00337)
1.975	7.121	0.2272	0.702	0.646	51.844 ± (1.942, 2.738)	0.07359 ± (0.00276, 0.00389)

TABLE IV - 4

6.5 GeV 60°

W (GeV)	Q <sup>2</sup> (GeV <sup>2</sup> )	c	x <sup>-</sup>	x <sup>+</sup>	$\frac{d^2\sigma}{d\Omega dE'} \left( \frac{pb}{GeV-sr} \right)$	2M W <sub>1</sub> <sup>P</sup>
PROTON						
2.000	7.044	0.2251	0.693	0.638	55.29 ± ( 1.07, 3.32)	0.07873 ± (0.00152, 0.00473)
2.100	6.726	0.2161	0.656	0.604	75.04 ± ( 1.16, 4.63)	0.10825 ± (0.00167, 0.00669)
2.200	6.392	0.2066	0.618	0.569	97.71 ± ( 1.45, 6.98)	0.14291 ± (0.00213, 0.00963)
2.300	6.043	0.1965	0.578	0.533	128.22 ± ( 2.77, 9.29)	0.19025 ± (0.00412, 0.01378)
2.400	5.679	0.1858	0.538	0.496	157.98 ± ( 7.15, 13.63)	0.23798 ± (0.01077, 0.02053)
2.500	5.298	0.1744	0.497	0.459	202.57 ± (11.40, 21.27)	0.31001 ± (0.01745, 0.03255)
2.600	4.903	0.1625	0.455	0.420	288.77 ± (16.48, 25.33)	0.44928 ± (0.02563, 0.03942)

W (GeV)	$\frac{d^2\sigma}{d\Omega dE'} \left( \frac{pb}{GeV-sr} \right)$	$\frac{d^2\sigma}{d\Omega dE'} \left( \frac{pb}{GeV-sr} \right)$	2M W <sub>1</sub> <sup>D</sup>
DEUTERON		NEUTRON	
2.000	77.46 ± ( 1.74, 4.90)	25.78 ± ( 3.47, 4.97)	0.11030 ± (0.00248, 0.00698)
2.100	103.32 ± ( 2.03, 7.25)	31.97 ± ( 4.14, 7.44)	0.14905 ± (0.00293, 0.01046)
2.200	140.80 ± ( 3.30, 9.80)	47.06 ± ( 5.94, 10.14)	0.20592 ± (0.00512, 0.01434)
2.300	190.14 ± ( 6.14, 14.39)	68.91 ± ( 8.75, 14.96)	0.28213 ± (0.00911, 0.02135)
2.400	244.67 ± ( 7.42, 20.41)	89.53 ± (10.92, 21.28)	0.36857 ± (0.01116, 0.03075)
2.500	311.06 ± ( 7.42, 25.40)	114.83 ± (12.56, 26.50)	0.47604 ± (0.01136, 0.03888)
2.600	391.62 ± ( 7.42, 31.35)	146.16 ± (14.69, 32.68)	0.60930 ± (0.01153, 0.04877)

CHAPTER IV - REFERENCES

1. L. S. Rochester et al. (to be published).
2. G. Miller, Ph.D. Thesis, Stanford University, SLAC Report No. 129 (1971).
3. L. W. Mo and Y. S. Tsai, Rev. Mod. Phys. 41, 205 (1969); also Y. S. Tsai, "Radiative Corrections to Electron Scattering," SLAC-PUB-848 (1971).
4. S. Stein et al., SLAC-PUB-1528 (1975).
5. W. B. Atwood and G. B. West, Phys. Rev. D 7, 773 (1973).
6. R. V. Reid, Jr., Ann. Phys. (N.Y.) 50, 411 (1968).
7. J. I. Friedman et al., SLAC-PUB-707 (1971).
8. R. L. A. Cottrell et al. (to be published).
9. E. D. Bloom, private communication; E. Allton, private communication.
10. *A. Bodak, Ph.D. Thesis, MIT Laboratory for Nuclear Science Report No. COO-3069-116 (1972)*

CHAPTER V - RESULTS AND CONCLUSIONS

INTRODUCTION

The measured cross sections at  $50^\circ$  and  $60^\circ$  cover a wide range of kinematics and give new information about the nucleons for both elastic and inelastic electron scattering. A general form of the cross section

$$(5.1) \quad \frac{\partial^2 \sigma}{\partial \Omega \partial E'} = \frac{\alpha^2}{4E_0^2} \sin^4 \theta/2 \cos^2 \theta/2 \left( \frac{\nu W_2}{\nu} + \frac{2M W_1}{M} \tan^2 \theta/2 \right)$$

indicates that for small angles and energy loss the measurements will be dominated by the behavior of  $W_2$ .  $W_2$  has been carefully measured in previous experiments (Ref. V-1). For the measurements reported here at large angles and energy losses the contribution of  $W_1$  to the cross section is much larger than that of  $W_2$ .

In a composite model of the proton (with spin 1/2 and spin 0 constituents)  $W_1$  is determined by the scattering from the particles with spin 1/2, but for  $W_2$  particles of both spin 0 and spin 1/2 can contribute. Thus in a simple quark model  $W_1$  directly measures scattering off the quarks, where  $W_2$  might contain contributions from spin 0 "glue" particles.

The measurements at  $50^\circ$  and  $60^\circ$  were carried out in a region where the total mass of the recoiling hadronic state is small compared with the momentum transferred to it. (This region is referred to as the "threshold region"). Because of kinematics, the fragments all travel away from the collision with small relative momentum compared to the total momentum given to the hadronic system by the incident electron.

For the large values of momentum transfer covered in this experimer

the interaction is occurring over very short distances compared with typical nucleon dimensions (for  $Q^2=20 \text{ GeV}^2$  we are probing distances of approximately 1/20 of a nucleon diameter). Thus a very small fraction of the total volume of the proton is "hit." In a simple picture, the large momentum transfer must be absorbed by a small part of the nucleon. Nevertheless in the threshold region the whole nucleon and any other particles produced must share this momentum in order to recoil in a state of small mass. The cross section is therefore suppressed in this region.

Elastic scattering is the extreme case: a single recoiling particle carrying away all of the momentum transferred. If the proton is a composite particle, it is difficult for all the parts to stay together in high energy collisions. This is particularly true if all the momentum transfer is to a single constituent. We therefore expect small elastic cross sections.

The range of the interaction for inelastic scattering is also small. The large inelastic cross sections support the thesis that the nucleon can be described by small charged constituents rather than a smooth charge distribution. In the simple quark model the neutron and the proton have different quark constituents which naturally leads to a difference in the total scattering strength of these two systems. Electroproduction experiments have demonstrated that the two nucleons do have different scattering strengths and this difference is largest in the threshold region (Ref. V-2) ( $W < |\vec{q}|$ ). One of the goals of the

the present experiment was a measurement of the N/P ratio in this region.

This chapter proceeds as follows: Elastic scattering is discussed first and a comparison to previous data is made. The behavior of the  $W_1$  structure function of the proton is detailed next. The extension of previous parameterizations of older data does not agree with the present data and alternate solutions are studied. The chapter concludes with the neutron to proton ratio. In the analysis only the statistical counting errors are used when plotting and when fitting functions to the new data (except where noted for elastic scattering).

#### ELASTIC SCATTERING

Elastic scattering from protons was measured for incident energies of 6.5 GeV, 13.3 GeV and 19.5 GeV at a scattering angle of  $60^\circ$ . Some lower  $Q^2$  elastic peaks were measured at  $50^\circ$  and  $60^\circ$  with incident energies ranging from 1.5 GeV to 4.5 GeV during the experimental "check out" periods.

These low  $Q^2$  elastic peaks are high statistics runs and clearly show the elastic radiative tail between the proton mass and one pion threshold. Empty target contributions were measured for each point and subtracted from the data. An unfolding technique was employed (Ref. V-3) to account for the radiation processes. Of the higher  $Q^2$  data only the measurement made at  $E_0=6.5 \text{ GeV}$  had sufficient statistical accuracy to allow use of the unfolding methods.

The measured data for the two highest  $Q^2$  points are shown in



Fig. V-1. Also shown in this figure are the measured empty target contributions. The empty target cross sections were measured to be "flat" in the elastic peak region and all the empty target data for  $W < 1.075$  GeV were combined to reduce the error introduced by this correction.

The radiative corrections were made using the formula given by Tsai (Ref. V-4). An energy resolution equal to the missing energy between the elastic peak and one pion threshold,  $\Delta E' = E'(\text{elastic}) - E'(M + M_\pi)$  was used. The final values of elastic scattering cross sections are given in Table V-1.

The elastic cross section can be written in terms of the two form factors  $G_E$  and  $G_M$  as

$$(5.2) \quad \frac{\partial \sigma}{\partial \Omega} = \sigma_{NS} \frac{(G_E^2 + \tau G_M^2 + 2\tau \tan^2 \theta/2 G_M^2)}{1 + \tau}$$

$$\sigma_{NS} = \frac{\alpha^2}{4E_0^2} \frac{\cos^2 \theta/2}{\sin^4 \theta/2} \frac{1}{1 + 2E_0(\sin^2 \theta/2)/M}; \text{ and } \tau = Q^2/4M^2$$

At high  $Q^2$  and large scattering angles the  $G_M$  contribution to the cross section dominates. The assumption of form factor scaling, i.e.  $G_E = G_M/\mu_p$ , is often made although there is some indication that  $G_E$  falls faster than this (Ref. V-5). Form factor scaling predicts that by a  $Q^2$  of 5 GeV<sup>2</sup> and  $\theta = 60^\circ$ ,  $G_E$  contributes only 3.3% to the cross section. Thus, measurements at large angles are insensitive to  $G_E$ , if  $G_E$  is not larger than predicted by form factor scaling.  $G_M^{S^2}$  is given in Table V-1 along with the measured cross sections, where  $G_M^{S^2}$  is defined by

$$(5.3) \quad \frac{d\sigma}{d\Omega} = \sigma_{NS} (G_M^S)^2 \frac{(1/p^2 + \tau + 2\tau \tan^2 \theta/2)}{1 + \tau}$$

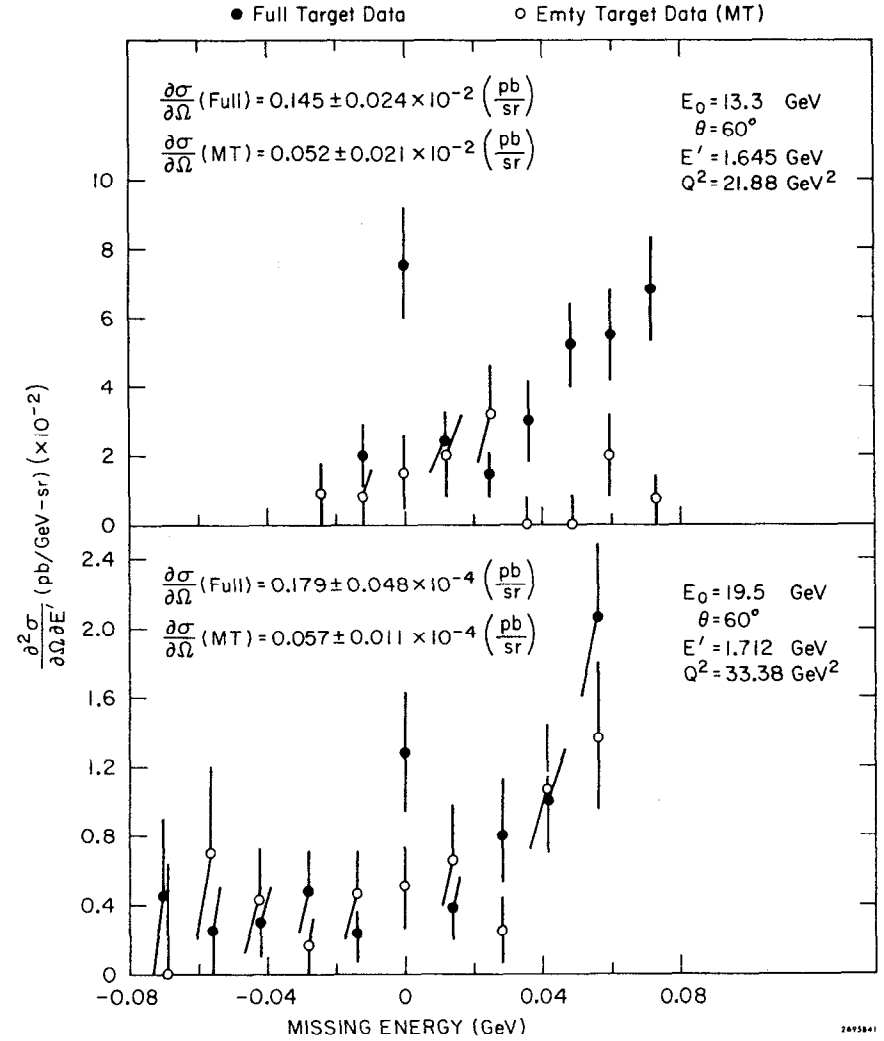


FIG. V - 1

The measured elastic peak cross sections off hydrogen and the empty target cross sections for  $Q^2 = 21.8$  GeV<sup>2</sup> and 33.4 GeV<sup>2</sup>.

Adopting the ideas of Brodsky and Farrar (Ref. V-6), we plot  $Q^4 G_M^S / \mu_p$  for our data and previous SLAC data in Fig. V-2 (Ref. V-3 and Ref. V-7). The data are not in conflict with an asymptotic behavior of  $1/Q^4$  for the form factor.

Also plotted on this figure (dashed line) is the "dipole" formula times  $Q^4$ :  $Q^4 / (1+Q^2/.71)^2$ . The data seem to reach the asymptotic  $1/Q^4$  behavior faster than the dipole formula. The difference in the rates at which the data and the dipole reach the  $1/Q^4$  behavior is the cause of the data "oscillating" about the dipole fit.

We have tried various fits to  $(G_M^S / \mu_p)^2$ . To include systematic errors in an approximate way between the different experiments fit, we set the minimum error in any of the measured cross sections used to be  $\pm 2.5\%$  even though the statistical accuracy of much of the data is considerably better.

The functional forms, parameters, and  $\chi^2$ 's for various fits are given in Table V-2. The last, an ad hoc parameterization, was adjusted to have the observed  $1/Q^4$  behavior at large  $Q^2$  and the value of 1 as  $Q^2 \rightarrow 0$ . This form has no other physical significance but does reproduce the measured data for  $.1 \text{ GeV}^2 < Q^2 < 33.4 \text{ GeV}^2$  reasonably well. It is plotted as a solid line in Fig. V-2.

#### THE $W_1$ STRUCTURE FUNCTION OF THE PROTON

A first approach to new data is usually "how well does the measurement match what we thought we would measure?" The size of  $W_1$  can be estimated from previous measurements at smaller angles by making an

ELASTIC SCATTERING CROSS SECTIONS FOR  $50^\circ$  AND  $60^\circ$

TABLE V - 1

$E_0$ (GeV)	$\theta^\circ$	$Q^2$ (GeV <sup>2</sup> )	$\frac{d\sigma}{d\Omega} \left( \frac{\text{cm}^2}{\text{Sr}} \right)$	$(G_M^S)^2$
1.501	59.87	1.249	$.132 \pm .004 \times 10^{-32}$	$.144 \pm .004 \times 10^0$
1.502	50.0	1.0254	$.401 \pm .003 \times 10^{-32}$	$.236 \pm .002 \times 10^0$
2.492	49.96	2.275	$.232 \pm .008 \times 10^{-33}$	$.280 \pm .009 \times 10^{-1}$
3.491	49.96	3.736	$.252 \pm .013 \times 10^{-34}$	$.515 \pm .026 \times 10^{-2}$
4.484	49.96	5.303	$.507 \pm .032 \times 10^{-35}$	$.158 \pm .010 \times 10^{-2}$
6.461	60.02	9.397	$.149 \pm .014 \times 10^{-36}$	$.174 \pm .016 \times 10^{-3}$
13.302	60.00	21.876	$.120 \pm .042 \times 10^{-38}$	$.550 \pm .194 \times 10^{-5}$
19.499	60.00	33.379	$.184 \pm .073 \times 10^{-40}$	$.177 \pm .070 \times 10^{-5}$

TABLE V - 2

Functional Form	Parameters	$\chi^2/N_D$
$\frac{1}{(1+C_1q^2)^2}$	$C_1 = 1.4062 \pm .0031$ ( $1/C_1 = .711$ )	226.4/28
$\frac{C_1}{(1+C_2q^2)^2} + \frac{1-C_1}{(1+C_3q^2)^2}$	$C_1 = 1.0013 \pm .0004$ $C_2 = 1.3699 \pm .0054$ ( $1/C_2 = .730$ ) $C_3 = .0432 \pm .0171$ ( $1/C_3 = 23.15$ )	76.5/26
$\frac{C_1(1-e^{-q^2/C_2})(1-e^{-q^2/C_3})}{q^4} + \frac{A}{q^4+C_4}$	$C_1 = .402 \pm .003$ $C_2 = 1.651 \pm .027$ $C_3 = .317 \pm .013$ $C_4 = .00795 \pm .00189$ $A = (1-C_1/C_2C_3) C_4 = .00184$	33.2/25

Various functions fit to the elastic data with parameters and  $\chi^2$ . The minimum error was taken to be  $\pm 2.5\%$  of the cross section.

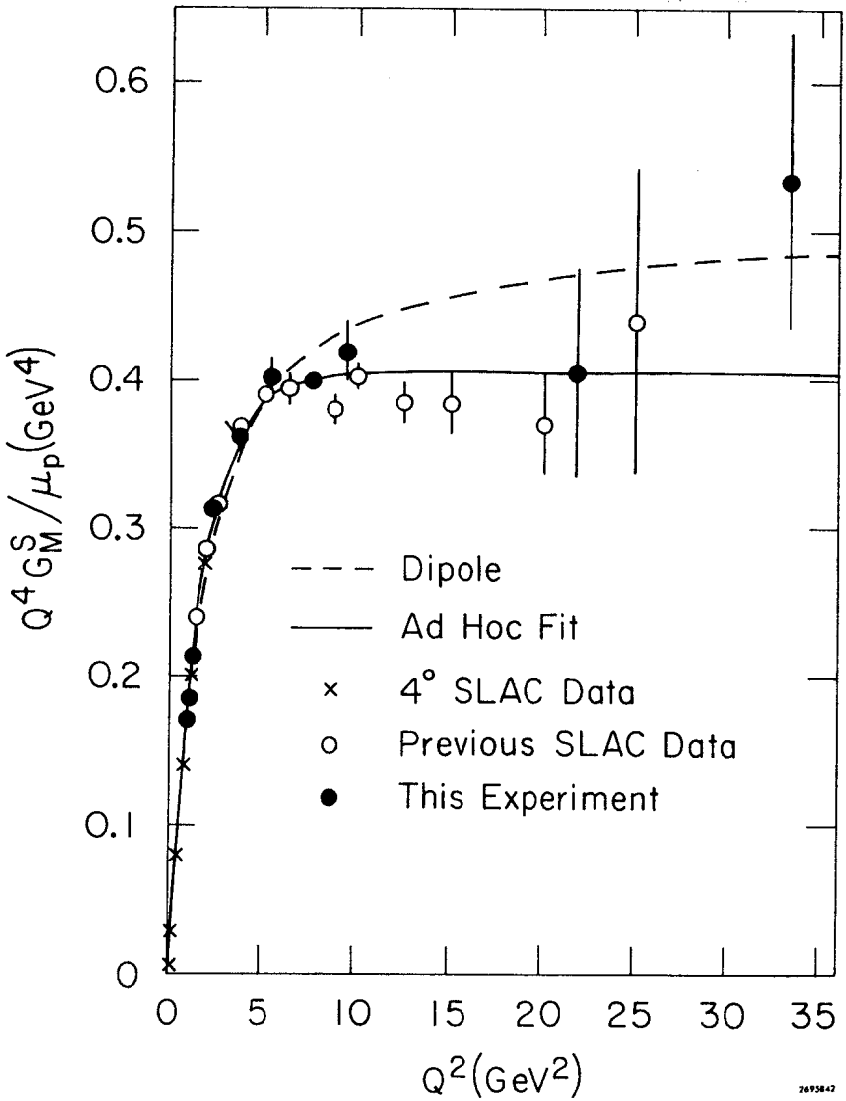


FIG. V - 2

A plot of  $Q^4 G_M^S / \mu_p$  versus  $Q^2$ . The dashed line is the dipole fit and the solid line is the ad hoc fit.

assumption about R (we choose R=.18). Shown in Fig. V-3 is the  $W_1$  structure function extracted from the cross sections using R=.18 plotted against the scaling variable  $x' = Q^2/(W^2+Q^2)$  (we have only included data with  $W > 2.0$  GeV). Over-plotted in this figure is what one would predict using

$$(5.4) \quad \nu W_2 = .6453(1-x')^3 + 1.902(1-x')^4 - 2.343(1-x')^5$$

where  $R=.18$  (Ref.V-8),  $2MW_1 = \omega \nu W_2 (1 + Q^2/\nu^2)/(1+R)$  and  $\omega = 2M\nu/Q^2$ .

The  $W_1$  structure function is seen to have a strong dependence on  $x'$  and decreases rapidly with increasing  $x'$ . It is clear that the general scaling nature of the proton data in  $x'$  works to 30% for over a factor of 1000 in the size of  $2MW_1$ . Of course for R constant  $W_1$  cannot scale in  $x'$  if  $\nu W_2$  scales perfectly in  $x'$ , but for small values of R this is a small effect and is the reason for plotting different predicted  $W_1$ 's for different incident energies.

The impression of the "goodness" of scaling changes when the data are more closely scrutinized. For both of the scaling variables  $x(=Q^2/2M\nu)$  and  $x'$ ,  $W_1$  falls off as  $Q^2$  rises. To examine this we have interpolated a combined data set to fixed values of  $x'$  and plot  $2M W_1$  versus  $Q^2$  as shown in Fig. V-4. All of the data fall off with increasing  $Q^2$ . The non-scaling behavior becomes obvious when trying to fit the data, resulting in poor  $\chi^2$ 's for simple polynomial fits in  $(1-x')$  and  $(1-x)$  as shown in Table V-3.

The first question that arises is "can we fix this non-scaling behavior in  $W_1$  by taking a different R"? The cross section as given

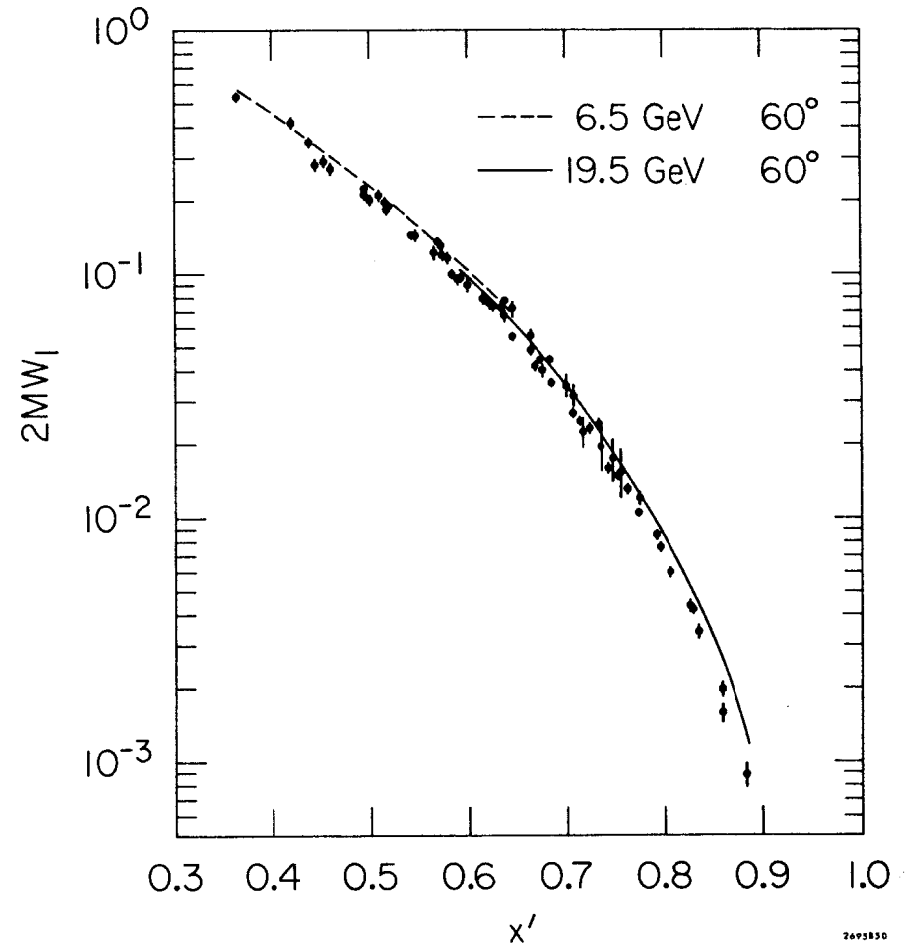


FIG. V - 3

$2MW_1$  (for  $R = .18$ ) plotted versus  $x'$ . The lines indicate the predicted values of  $2MW_1$  for  $E_0 = 6.5$  GeV and  $E_0 = 19.5$  GeV.

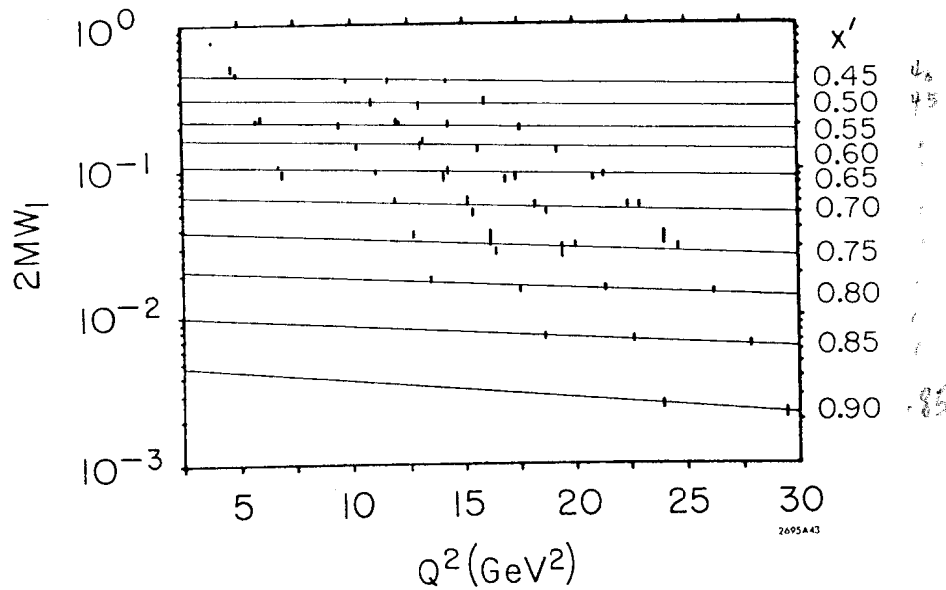


FIG. V - 4

The  $2MW_1$  data interpolated to fixed values of  $x'$  (indicated on the right) plotted against  $Q^2$ .

in Eq. 4.6 shows that  $W_1$  is proportional to  $(1-\epsilon)/(1+\epsilon R)$  where  $\epsilon$  is the photon polarization parameter and is less than .3 for our data. If we can take  $R$  to be increasing with increasing  $Q^2$ , the "scale breaking" of  $W_1$  becomes larger as  $Q^2$  increases. We can take  $R$  to be decreasing with increasing  $Q^2$  and account for some of the observed effect. To account for the whole effect  $R$  would have to have a value near 2 in the low  $Q^2$  region and decrease to zero in the high  $Q^2$  region. This solution is in contradiction with the measured values of  $R$  for  $Q^2 < 10 \text{ GeV}^2$ . Thus the non-scaling behavior of the measured data cannot be successfully accounted for by modifying  $R$  within reasonable bounds.

We can accept the non-scaling behavior of  $W_1$  and ask what kind of  $R$  values might result. To do this we will need to make some assumptions. First we assume scaling for  $\nu W_2$  in the  $x'$  variable and that the value of  $\nu W_2$  is correctly given by Eq. 5.4. This is an extrapolation for much of our data in  $Q^2$  and is therefore sensitive to the scaling variable  $x'$ . Also for the large  $x'$ 's we must extrapolate the fit in the scaling variable (Eq. 5.4 was fit to data for which  $x'$  was mostly less than .6). The value of  $R$  for each of the data points is then calculated using

$$(5.5) \quad R = (F - \sigma_H) / (\sigma_H - \epsilon F)$$

$$\text{where} \quad F = \frac{4\pi^2 \alpha}{K} (1 + \nu^2/Q^2) \frac{\nu W_2}{\nu}$$

$$K = \frac{W^2 - M^2}{2M}$$

$$\text{and} \quad \sigma_H = \sigma_{\text{exp}} / \Gamma_t$$

$$\Gamma_t = \frac{\alpha}{4\pi^2} \frac{2KE'}{E_0 Q^2 (1-\epsilon)}$$

TABLE V - 3

FITS TO THE  $W_1$  STRUCTURE FUNCTION OF THE PROTON

Scaling Variable	Functional Form	R = .18 Parameters	$\frac{\chi^2}{N_D}$	R = .5 Parameters	$\chi^2$	R = $Q^2/\nu^2$ Parameters	$\chi^2$
x	$\sum_{n=3}^6 a_n (1-x)^n$	$a_3 = .30 \pm .16$ $a_4 = 7.69 \pm 1.51$ $a_5 = -10.29 \pm 4.47$ $a_6 = 4.52 \pm 4.11$	$\frac{1744}{122}$	$a_3 = .31 \pm .15$ $a_4 = 7.21 \pm 1.44$ $a_5 = -9.49 \pm 4.28$ $a_6 = 4.01 \pm 3.94$	$\frac{1562}{122}$	$a_3 = .31 \pm .16$ $a_4 = 7.67 \pm 1.52$ $a_5 = -10.27 \pm 4.51$ $a_6 = 4.61 \pm 4.15$	$\frac{1631}{122}$
x	$\left(\frac{1}{1+Q^2/\Lambda^2}\right)^2 \sum_{n=3}^6 a_n (1-x)^n$	$a_3 = 2.57 \pm .35$ $a_4 = 5.44 \pm 2.99$ $a_5 = -10.48 \pm 8.34$ $a_6 = 4.60 \pm 7.29$ $(1/\Lambda^2) = .0233 \pm .00077$	$\frac{222}{121}$	$a_3 = 2.31 \pm .32$ $a_4 = 5.00 \pm 2.74$ $a_5 = -9.05 \pm 7.65$ $a_6 = 3.65 \pm 6.70$ $(1/\Lambda^2) = .0214 \pm .00074$	$\frac{221}{121}$	$a_3 = 2.50 \pm .35$ $a_4 = 5.21 \pm 2.94$ $a_5 = -9.71 \pm 8.21$ $a_6 = 4.24 \pm 7.19$ $(1/\Lambda^2) = .0221 \pm .00075$	$\frac{211}{121}$
x'	$\sum_{n=3}^5 a_n (1-x')^n$	$a_3 = .075 \pm .131$ $a_4 = 4.114 \pm 1.212$ $a_5 = .279 \pm 3.437$ $a_6 = -2.941 \pm 3.039$	$\frac{348}{122}$	$a_3 = .066 \pm .126$ $a_4 = 4.091 \pm 1.162$ $a_5 = -.356 \pm 3.289$ $a_6 = -2.226 \pm 2.904$	$\frac{282}{122}$	$a_3 = .063 \pm .132$ $a_4 = 4.340 \pm 1.223$ $a_5 = -.532 \pm 3.468$ $a_6 = -2.061 \pm 3.067$	$\frac{303}{122}$
x'	$\left(\frac{1}{1+Q^2/\Lambda^2}\right)^2 \sum_{n=3}^5 a_n (1-x')^n$	$a_3 = .139 \pm .179$ $a_4 = 6.838 \pm 1.593$ $a_5 = -7.261 \pm 4.417$ $a_6 = 2.866 \pm 3.814$ $(1/\Lambda^2) = .00775 \pm .00059$	$\frac{134}{121}$	$a_3 = .118 \pm .160$ $a_4 = 6.192 \pm 1.457$ $a_5 = -6.227 \pm 4.052$ $a_6 = 2.330 \pm 3.506$ $(1/\Lambda^2) = .00630 \pm .00056$	$\frac{135}{121}$	$a_3 = .121 \pm .172$ $a_4 = 6.776 \pm 1.563$ $a_5 = -7.348 \pm 4.346$ $a_6 = 3.260 \pm 3.762$ $(1/\Lambda^2) = .00687 \pm .00057$	$\frac{130}{121}$
$x_B$	$\sum_{n=4}^5 a_n (1-x_B)^n$ $x_B = \frac{1}{\frac{2M\nu}{Q^2} + \frac{M_B^2}{Q^2}}$	$a_4 = 3.429 \pm .112$ $a_5 = -.509 \pm .189$ $M_B^2 = 1.473 \pm .042$	$\frac{129}{123}$	$a_4 = 3.543 \pm .113$ $a_5 = -.896 \pm .191$ $M_B^2 = 1.368 \pm .042$	$\frac{130}{123}$	$a_4 = 3.599 \pm .116$ $a_5 = -.715 \pm .197$ $M_B^2 = 1.405 \pm .042$	$\frac{126}{123}$

The resulting values of  $\nu R$  so calculated are plotted in Fig. V-5 versus  $Q^2$ . This clearly results in large scale breaking of  $\nu R$  and it would be hard for the standard parton models to accommodate such behavior. Intuitively one would not expect the longitudinal virtual photoabsorption cross section corresponding to large values of  $R$  to dominate in the threshold region. This leads us to suspect the assumption of scaling in  $x'$  and/or the extrapolation of the fit given in Eq. 5.4 to the region of large  $x'$ . We now leave the question of  $R$  and focus our attention on the behavior of  $W_1$  itself.

Many theorists have speculated about the structure functions eventually not scaling as the range of the data was extended to high  $Q^2$ . One such model was put forward by Drell and Chanowitz (Ref. V-9). In this model, the structure functions fall off at high  $Q^2$  (compared to the scaling prediction) due to the form factors of the constituents. G. B. West (Ref. V-10) considered the possibility that the quarks in the model could have anomalous magnetic moments as well. Then one can construct a fortuitous cancellation of terms so that  $\nu W_2$  continues to scale for high  $Q^2$ , but no such cancellation occurs for  $W_1$  and it should fall as  $1/(1+Q^2/\Lambda^2)^2$  with respect to its "scaling" value. We tried fits to our data of the form "scaling function" times a propagator for the scaling variables  $x$  and  $x'$ ; the parameters and  $\chi^2$ 's are given in Table V-3. The data is not in contradiction with this notion for the scaling variable  $x'$ . But a scaling function in the variable  $x$  is incompatible with the data even with propagator scale breaking.

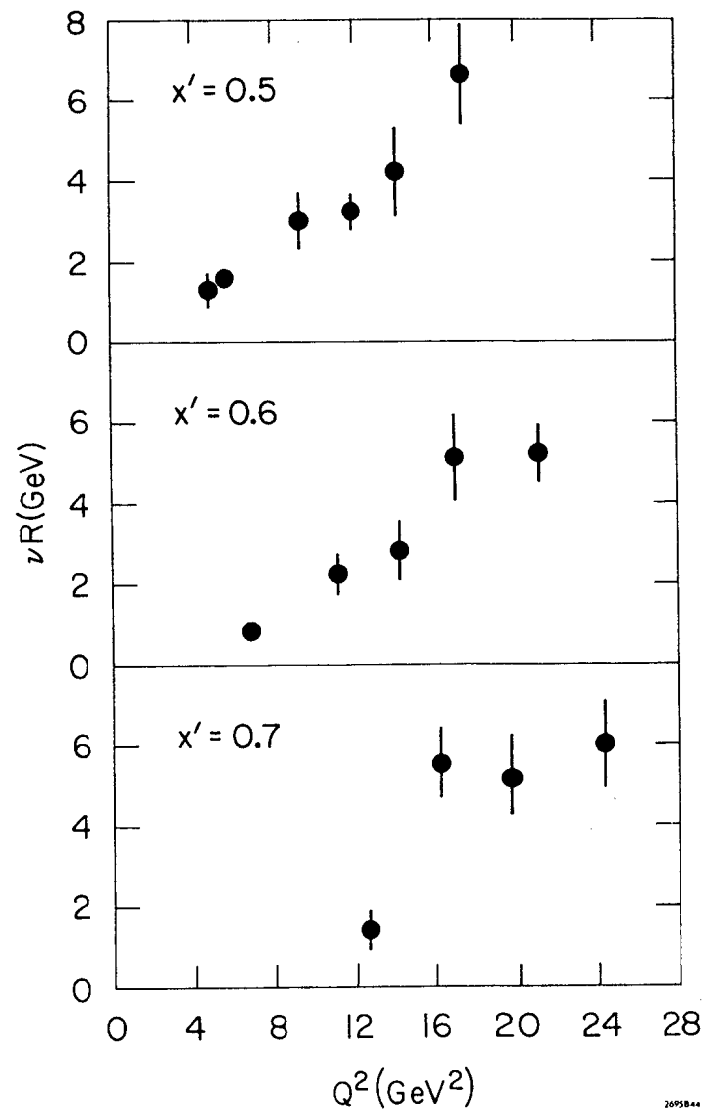


FIG. V - 5

$\nu R$  extracted from the data (assuming  $\nu W_2$  given by Eq. 5.4) plotted against  $Q^2$  for various values of  $x'$ .

The undesirable features of this interpretation are: 1) we have had to introduce more free parameters into the theory (namely two - the propagator mass and the anomalous quark magnetic moment) and 2) the same theory would have the elastic scattering form factor fall off faster than  $1/Q^4$  due to the parton's form factor. The second point is in mild contradiction with the measured data presented in the last section. The ideas of propagator scale breaking factors were originally motivated by the rising ratio of  $e^+e^-$  annihilation cross sections into hadrons compared to muon production by the same process. Better data has converted the smooth rise into a step indicative of some new threshold and the propagator ideas no longer seem to be necessary to explain that data.

Another alternative to "explain" the  $W_1$  data is to change the definition of the scaling variable. Theoretically the approach of the scaling variable to the asymptotic form,  $v/Q^2$ , is not understood. The introduction of terms like  $M^2/Q^2$  into the definition of the scaling variable has had some degree of success, and  $\omega'$  has supplanted  $\omega$  as a scaling variable which describes the data better. Consider the variable

$$(5.5) \quad \omega_s = 2Mv/Q^2 + M_S^2/Q^2$$

where we will let the data determine the best value of  $M_S^2$ .

The scaling variables  $\omega$  and  $\omega'$  are the special cases of  $M_S^2$  equal to zero and  $M^2$ . We fitted the  $W_1$  structure function in  $\omega_s$  allowing the mass parameter to vary, with  $W_1$  extracted from the data using various values for  $R$ . The results are given at the bottom of Table V-3. The  $\chi^2$ 's for these fits are the best of those given in Table V-3 and are

very close to one per degree of freedom (recall that only statistical counting errors have been used in the data to which the fits were made).

The leading power of  $(1-x')$  or  $(1-x_s)$  is of interest for it determines the fall off of the structure functions at high  $Q^2$  for fixed  $W$ .  $W_1$  is found to be mostly accounted for by  $(1-x_s)^4$ . The third power is not required at all and the best  $\chi^2$ 's were obtained by including a small amount of the fifth power. To illustrate the power law dependence we have plotted  $2M W_1/(1-x_s)^4$  in Fig. V-6a versus  $Q^2$  and in Fig. V-6b versus  $x_s$ . The curves in Fig. V-6b show what the third and the fifth power would look like.

This power law is different from what was expected. The  $1/Q^4$  behavior of  $G_M^S$  and the Drell-Yan-West relation (Ref. V-12) would predict that  $W_1$  should fall as  $1/Q^6$  for fixed  $W$  and not as  $1/Q^8$  (from the fourth power of  $(1-x_s)$ ). The data on  $W_1$  show little dependence on the third power for fits using  $(1-x')$  or  $(1-x_s)$ .

The simple parton model given in Chapter I tells us that  $vW_2 = xf(x)$  and  $2M W_1 = f(x)$ . The new data gives  $f(x_s) = c(1-x_s)^4$ . M. Mestayer has pointed out (Ref. V-11) that fits in  $x'$  such as that given in Eq. 5.4 can be refactored into a form surprisingly close to  $x'(1-x')^4$ . For the region of  $x'$  between .3 and .7 where most of the data falls, the factor  $x'(1-x')$  is quite flat so that  $x'(1-x')^4$  and  $(1-x')^3$  have nearly the same shape in this region. This suggests that the previous data on  $vW_2$  should be refit in the form of  $vW_2/x$  to powers in  $(1-x')$  or  $(1-x_s)$  to see if it is compatible with the  $f(x_s)$  obtained from fitting  $2M W_1$ .



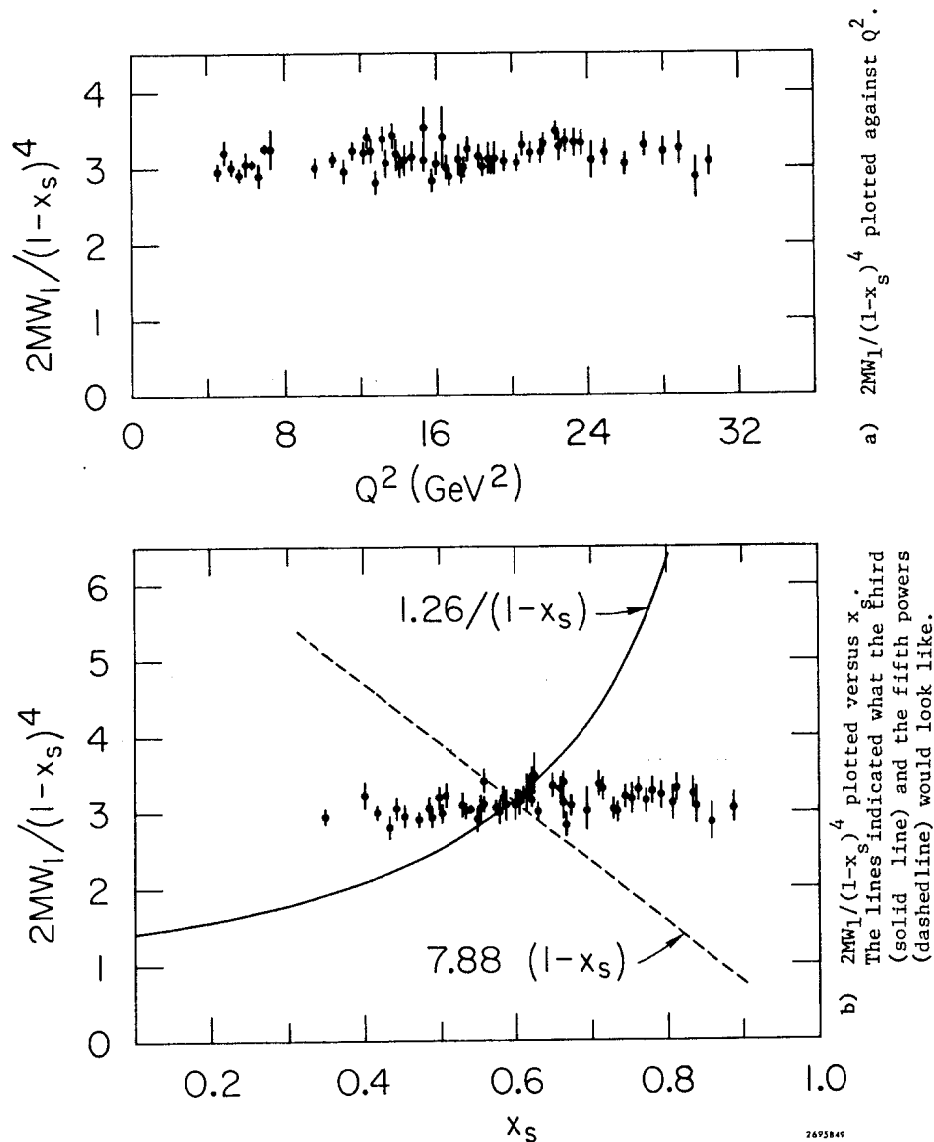


FIG. V - 6

One way of showing the effect of the scaling variable on the  $Q^2$  dependence is to plot the slope in  $Q^2$  obtained by fitting data at constant  $x_s$  versus  $x_s$  for various values of  $M_S^2$ . The results are shown in Fig. V-7 for  $M_S^2=0, M^2, 1.42 \text{ GeV}^2$ . Clearly  $W_1$  scales well in  $x_s$ . We note that the variable  $\omega_s$  is very similar to  $\omega_W$  introduced by Rittenberg and Rubinstein (Ref. V-14), and that the value of  $M_S^2 = 1.42$  is close to that found for the equivalent  $\omega_W$  parameter,  $M_W$  (Ref. V-15).

THE PROTON CROSS SECTIONS FOR  $W < 2.0 \text{ GeV}$

There is some interest in whether or not the nucleon resonances excited in electroproduction persist as  $Q^2$  is increased. The data taken with 6.5 GeV incident energy at  $60^\circ$  were scanned with high statistics through the mass region  $M < W < 3.0 \text{ GeV}$ . The cross sections plotted against  $W$  are shown in Fig. V-8. Also shown on the top scale of the figure are the corresponding values of  $Q^2$ . The resonance enhancements located at  $W=1512 \text{ MeV}$  and  $W=1700 \text{ MeV}$  are large with respect to the background but the first resonance located at  $1238 \text{ MeV}$  is small suggesting that its form factor falls with increasing  $Q^2$  faster than the background under it. The statistical accuracy of the data is too poor to afford much comment on the fourth resonance enhancement around  $W=1950 \text{ MeV}$ .

#### NEUTRON/PROTON COMPARISON

We have combined our N/P data into bins of  $.025$  in  $x'$ . We have used the model subtraction techniques described in Chapter IV, but instead of assigning  $\pm 5\%$  error on a point-to-point basis, we used the error of the measured hydrogen cross section for that point. The calculated N/P values are given in Table V-4 and are plotted in

The slope in  $Q^2$  for fixed values of the scaling variable for values of  $M_S^2 = 0, M^2,$  and  $1.42$ . The poor  $\chi^2$  for  $M_S^2 = 0$  and  $M^2$  indicate that the  $Q^2$  dependence is not well parameterized by a straight line.

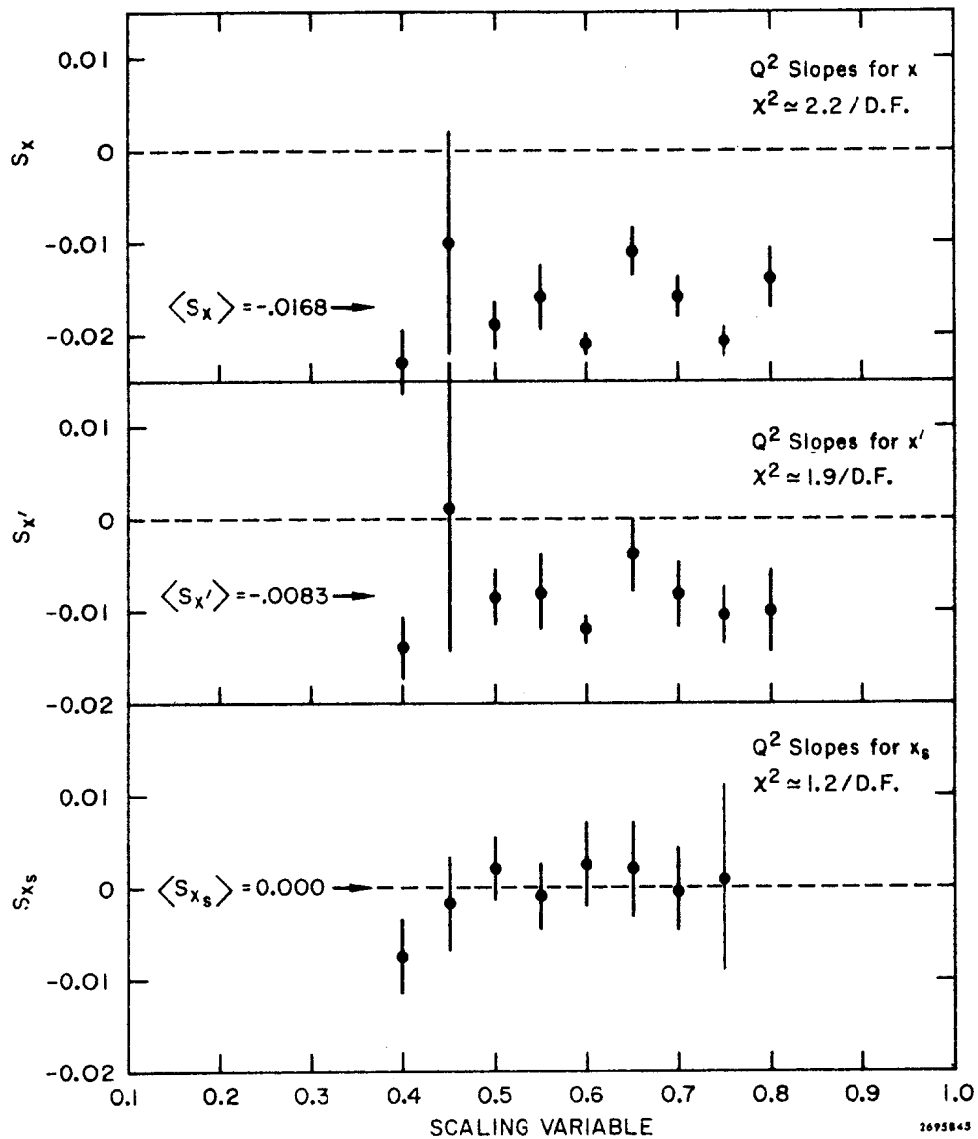


FIG. V - 7

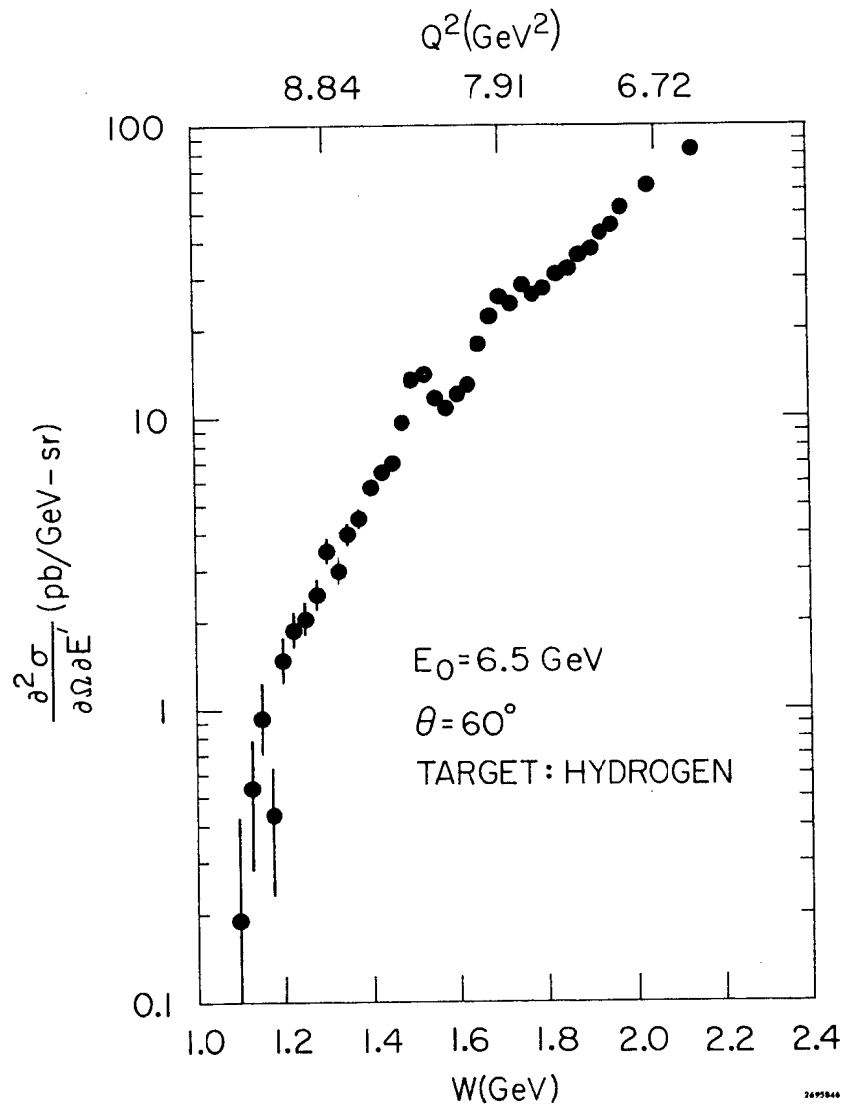


FIG. V - 8

Resonance region data for  $6.9 \text{ GeV}^2 < Q^2 < 9.2 \text{ GeV}^2$ .

TABLE V - 4

x'	x' Range of Smearing	N/P	Systematic Error
.325	.31 - .35	.525 ± .085	± .031
.375	.35 - .41	.606 ± .100	± .031
.400	.37 - .44	.508 ± .054	± .031
.425	.39 - .46	.599 ± .123	± .031
.450	.41 - .50	.602 ± .059	± .031
.475	.43 - .53	.598 ± .064	± .031
.500	.46 - .56	.602 ± .099	± .031
.525	.48 - .59	.553 ± .060	± .031
.550	.50 - .62	.572 ± .049	± .031
.575	.52 - .65	.506 ± .054	± .031
.600	.54 - .68	.470 ± .031	± .031
.625	.56 - .71	.490 ± .030	± .031
.650	.58 - .75	.414 ± .036	± .031
.675	.60 - .78	.435 ± .038	± .031
.700	.61 - .81	.430 ± .044	± .031
.725	.63 - .85	.455 ± .055	± .031
.750	.65 - .88	.349 ± .049	± .033
.775	.67 - .92	.409 ± .062	± .034
.800	.69 - .95	.360 ± .057	± .034
.825	.71 - .99	.284 ± .057	± .035
.850	.73 - 1.00	.271 ± .068	± .036
.875	.74 - 1.00	.251 ± .163	± .038

The measure N/P ratios for 50° and 60°. The systematic errors include target uncertainties and smearing errors.

Fig. V-9 together with the data from Ref. V-7 and from Ref. V-3. The new data is in fair agreement with the previous measurements. The N/P ratio near x' equal to 1 should be considered very cautiously as the neutron information really represents an average over the cross section for values of x' from 1 to .7 with the bulk of the contribution coming from the lower x's (see Appendix C). The ratio N/P is expected to be in the range of  $1/4 < N/P < 4$  on rather general grounds, and we have no evidence that the lower limit is violated.

We have also considered the neutron data separately and performed a similar analysis of scale breaking. We found that the neutron data favored simple scaling in x' with no propagator scale breaking. Going to the  $x_s$  variable increases the  $\chi^2$  of the fit by a factor of two. This suggests the possibility that N/P does not scale, but the statistical accuracy of the data and uncertainties in the neutron extraction do not allow firm conclusions to be made.

#### A SUMMARY OF THE PHYSICS RESULTS

The elastic scattering measurements made on hydrogen are consistent with a  $1/Q^4$  fall off of the form factor for values of  $Q^2$  as high as  $33.4 \text{ GeV}^2$  as predicted by Brodsky and Farrar.

The behavior of the inelastic  $W_1$  structure function is roughly what one would have expected but a close examination reveals inconsistencies.  $W_1$  does not scale in x' and this situation cannot be repaired by choosing various values of R consistent with previous data.  $W_1$  does not scale in x. Propagator scale breaking is consistent with the measurements when

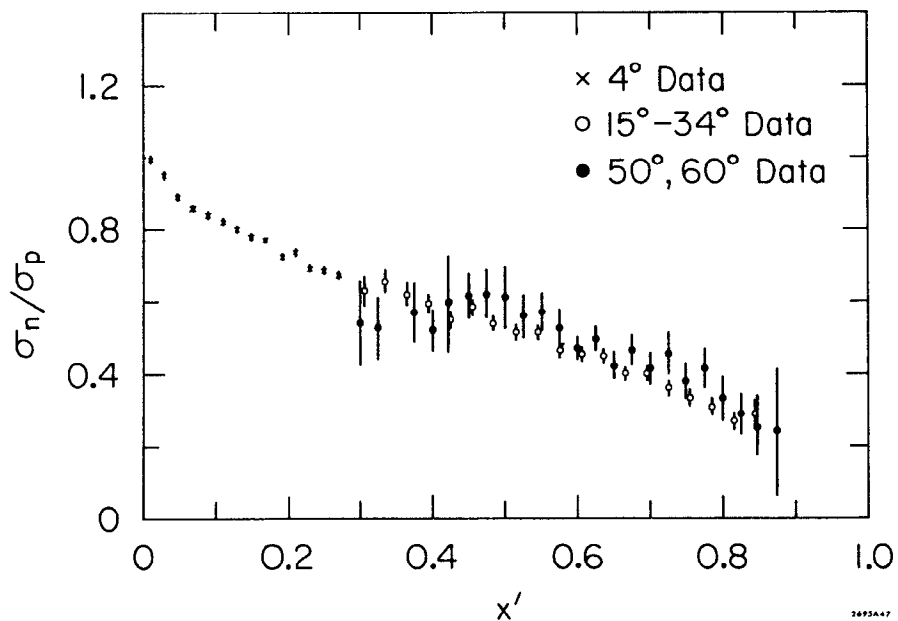


FIG. V - 9

The N/P ratio plotted versus  $x'$ .

the  $x'$  scaling variable is used. Also changing the scaling variable to  $\omega_s = \omega + M_s^2/Q^2$  with  $M_s^2 = 1.42$  results in  $W_1$  scaling with a simple  $(1-x_s)^4$  power law dependence. This power law for  $W_1$  and the  $1/Q^4$  behavior of  $G_M$  are in conflict with the Drell-Yan-West relation.

The various proton resonances at high  $Q^2$  have different dependences on  $Q^2$ . The "1238" is not seen in the data for  $Q^2 = 9 \text{ GeV}^2$  while the second and third resonance regions remain comparable to the background.

The N/P ratio is consistent with previous measurements.

## CHAPTER V - REFERENCES

1. G. Miller, Ph.D. Thesis, SLAC Report No. 129, January 1971.  
J. S. Poucher et al., Phys. Rev. Letters 32, 118 (1974).
2. E. D. Bloom et al., "Recent Results in Inelastic Electron Scattering," SLAC-PUB-796, 1970; (A report presented to the XV International Conference on High Energy Physics, Kiev, U.S.S.R., 1970).
3. P. N. Kirk et al., Phys. Rev. D8, 63 (1973); also H. W. Kendall and D. Isabelle, Bull. Am. Phys. Soc. 9, 94 (1964).
4. Y. S. Tsai, Phys. Rev. 122, 1898 (1961).
5. R. Wilson, "Elastic Scattering and Resonance Electroproduction," Proceedings 1971 International Symposium on Electron and Photon Interactions at High Energy (Cornell University, Ithaca, N.Y. 1971).
6. S. Brodsky and G. Farrar, SLAC-PUB-1473 (1974).
7. S. Stein et al., SLAC-PUB-1528.
8. J. I. Friedman et al., SLAC-PUB-907
9. M. Chanowitz and S. D. Drell, Phys. Rev. Letters 30, 807 (1973).
10. G. B. West, Stanford University Preprint 1974, (unpublished).
11. M. Mestayer, private communication.
12. S. D. Drell and T. M. Yan, Phys. Rev. Letters 24, 181 (1970);  
and G. B. West, Phys. Rev. Letters 24, 1206 (1970).

## CHAPTER V - REFERENCES (continued)

13. A. Bodek et al., Phys. Letters 51B 417 (1974).
14. V. Rittenberg and H. R. Rubinstein, Phys. Letters 35B, 50 (1971).
15. F. W. Brasse et al., Nucl. Phys. B39 421-431 (1972).

APPENDIX A - THE CERENKOV COUNTER

A major component of the electron detection/pion rejection system was a large aperture, threshold gas Cerenkov counter. This appendix presents specific details about its design and its functioning in the experiment.

As shown in Fig. A-1, an aluminum frame supported the mirror assembly and phototubes. Two beam windows of .002" aluminum foil and 1/16" aluminum walls attached to the frame formed the gas enclosure. The beam windows were made as thin as possible to reduce knock-on electron production. The mirror blank was formed from a 1/4" sheet of plexiglas slump molded on a spherical carbon mold with a radius of 138 cm. After cutting the blank to 26"x 26", the mirror was coated by vapor depositing aluminum to a thickness of 2500 Å. A 200 Å over-coating of MgF<sub>2</sub> was deposited on the front surface of the mirror immediately after the aluminum was deposited to protect the aluminum from oxidation. The backside of the mirror was coated with aluminum to trap Cerenkov light produced inside the plexiglass.

The phototube assembly consisted of two Amperex 58 DUVP photomultipliers placed side by side. A double conical aluminized light collector helped to reflect the Cerenkov light onto the photocathodes. This assembly as well as the mirror was aligned in the Cerenkov counter using a small optical laser. The focusing properties of the mirror were optimized and checked using a conical plexiglass lens system to simulate the Cerenkov light radiation pattern. These adjustments were made by warping the mirror using the turnbuckles.

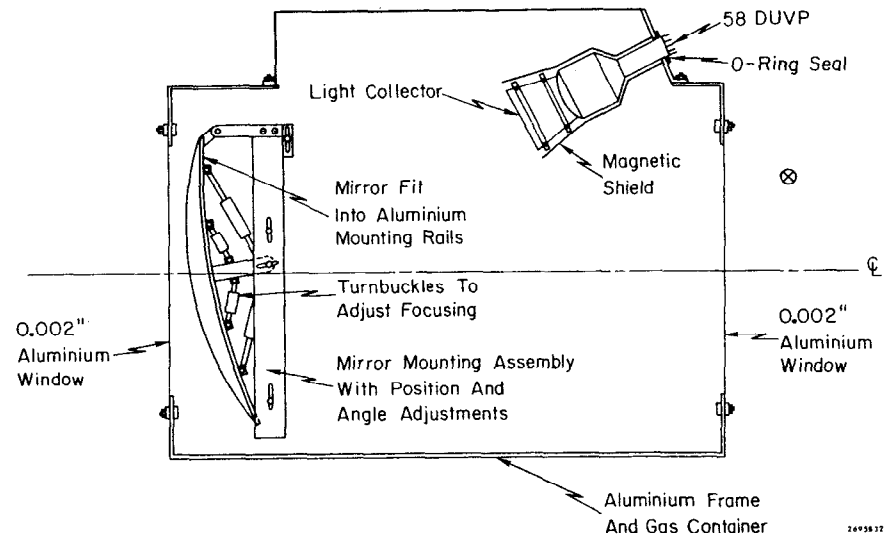


FIG. A-1

A layout of the isobutane threshold gas Cerenkov counter used in E-89.

TABLE A - 1

PHYSICAL PROPERTIES OF GASES USED IN THRESHOLD CERENKOV COUNTERS  
 PION MOMENTUM OF 1500.0 MeV GIVES KNOCK-ON  $E_{MAX} = 112.22$  MeV

Gas	$n$ (r/cc)	Z	M	$(n-1) \times 10^4$	$\gamma_t$	$E_{th}$ (MeV)	$\pi_{th}$ (GeV)	$N_g$ (r's/m)	$n$ (knock-ons/m)
N <sub>2</sub>	0.00114	7	14	2.699	43.05	21.998	5.941	41.231	0.1944E-03
C <sub>2</sub> H <sub>4</sub>	0.00166	22	40	7.401	26.01	13.299	3.589	112.942	0.6674E-03
C <sub>3</sub> H <sub>8</sub>	0.00184	26	44	9.203	23.32	11.919	3.219	140.399	0.9235E-03
CH <sub>3</sub> CO	0.00210	26	50	15.202	18.16	9.278	2.506	231.778	0.1292E-02
C <sub>4</sub> H <sub>10</sub>	0.00246	34	58	13.103	19.55	9.991	2.698	199.817	0.1550E-02
C <sub>4</sub> H <sub>10</sub> (ISO)	0.00257	34	58	13.704	19.12	9.771	2.639	208.954	0.1667E-02
C <sub>4</sub> H <sub>10</sub>	0.00370	42	88	4.196	34.53	17.643	4.765	64.082	0.8542E-03
CCl <sub>4</sub>	0.00430	50	104	7.296	26.19	13.384	3.614	111.343	0.1496E-02
CCl <sub>2</sub> F <sub>2</sub>	0.00510	58	120	10.500	21.84	11.160	3.014	160.217	0.2288E-02
SF <sub>6</sub>	0.00640	70	146	7.200	26.36	13.473	3.638	109.890	0.2201E-02
C <sub>2</sub> C <sub>2</sub> F <sub>4</sub>	0.00730	82	171	13.504	19.26	9.843	2.658	205.907	0.3836E-02

156

mounted on the mirror support frame (see Fig. A-1).

In Table A-1 some physical properties of several gases are shown. The data on the various gases were compiled from Ref. A-1. All densities and indexes of refraction are quoted for 26.5° at 1 atm. pressure. The number of Cerenkov photons,  $N_g$  was calculated using

$$(A.1) \quad \frac{dN_g}{dLd\lambda} = 2\pi\alpha \left( 1 - \frac{1}{n^2\beta^2} \right) \frac{1}{\lambda^2}$$

where  $n$  is the index of refraction,  $\beta = P/E$  ( $\beta = 1$  for energetic electrons), and  $\alpha = 1/137$  (the fine structure constant). The limits of integration were 3000 Å to 6000 Å, and  $n$  was assumed to be constant over this interval. In column 7 the  $\gamma_t = 1/\sqrt{1 - 1/n^2}$  is given.

The next two columns give the threshold energies for pions,  $\pi_{th}$ , and electrons,  $E_{th}$ , to count. In column 10 is a calculation of the maximum knock-on production per meter of gas from 1.5 GeV pions using (Ref. A-2).

$$(A.2) \quad n = 2 \left( \frac{.15 Z}{A} \right) \frac{m_e}{\beta_{\pi} E_{th}} \left( 1 - \frac{E_{th}}{E_{max}} \left( 1 + \beta_{\pi}^2 \ln(E_{max}/E_{th}) \right) \right)$$

where  $Z =$  atomic number,  $A =$  atomic weight,  $E_{max} = m_e \left( \frac{1 + \beta_{cm}^2}{1 - \beta_{cm}^2} \right)$

( $\beta_{cm} = P_{\pi}/(E_{\pi} + m_e)$ ), and  $E_{th} =$  threshold energy for electrons to count.

Despite the obvious drawback of high flamability, isobutane was selected for the following three reasons: 1) large Cerenkov light output per unit path length, 2) compared to the Cerenkov light output it has a low knock-on electron efficiency, and 3)

it has good light transmission far into the ultraviolet (the light transmission cuts off at approximately 2200 Å). Isobutane is considerably superior to the Freons in all of these categories.

Data on elastically scattered electrons using a 1.5 GeV incident beam were taken at the beginning and end of the first data run and at the beginning of the second data run (see Table I - 1). At the beginning and end of each data taking period, parts of the 6.5 GeV incident energy line at 60° were taken to monitor any equipment changes. These test runs revealed a small gradual improvement in the Cerenkov counter over the course of the experiment probably due to the continuously flowing isobutane purging the counter of impurities.

Threshold gas Cerenkov counters fail to give 100% particle discrimination primarily through knock-on electron production in front of the counter as well as in the gas itself. Sometimes other mechanisms such as Cerenkov light produced in the mirror or scintillation of the gas can spoil a counter's discrimination capability. The raw rejection of pions to electrons for this counter in the environment of the 1.6 GeV Spectrometer counter cave varied from 350:1 to a low of 200:1, depending on beam and target conditions. This rejection corresponded to our on-line hardware discriminator cut place in PHA channel 15 (see Fig. II - 9). This cut had no measureable inefficiency for electron detection.

There are numerous ways in which pions can count in this counter: 1) electrons produced by particles hitting the end of the 1.6 aluminum vacuum tank (referred to as "spray"); 2) knock-on electrons produced in the exit beam window of the spectrometer or Y-hodoscope; 3) particles striking the phototubes directly; 4) Cerenkov light produced in the mirror and light collection cones; and 5) scintillation of the gas. Of these, only the first three are real problems, as 4) and 5) probably contribute little because of the counter's design.

Knock-on electrons produced near the top of the 1.6 Spectrometer vacuum tank and near the bottom of the counter cave were quickly found to be the most serious problem for this Cerenkov counter. During the first checkout runs in June and July of 1973, before the installation of the Y-hodoscope, a remotely controlled moveable two-piece counter made of 1/8" plastic scintillator (TR1) was positioned in front of the Cerenkov counter. It was determined that the "noise" rate in the Cerenkov counter was less when this counter covered the magnet's exit aperture. Presumably some of the soft spray coming up the vacuum tank was absorbed by this counter. We verified that the "spray" was coming up the vacuum tank rather than penetrating the shielding by closing the moveable slits in front of the spectrometer and observing a much reduced counting rate. It was decided that the knock-on electrons produced in the material of the hodoscope (equivalently TR1) were less



damaging to the pion rejection capability of the counter than this spray. The Y-hodoscope replaced the moveable TR1 for the rest of the experiment.

This Cerenkov counter gave approximately 44 photoelectrons (using a factor of 1.3 for first dynode fluctuations(Ref. A-3)) in the phototubes per passage of an electron. The value calculated from Table A-1 for 1.24 meters of Isobutane is 259 photons incident on the photocathodes. This would indicate an average quantum efficiency of 17% for these Amperex DUVF photomultipliers weighted with a Cerenkov light spectrum. The knock-on efficiency is calculated to be 1/484 for the gas and 1/154 for the hodoscope in front of the counter. As the calculation is the maximum number of knock-ons produced, a reduction of a factor of two is reasonable.

#### REFERENCES FOR APPENDIX A

1. This is a partial list of the gases compiled by D. Trines (Group-A Internal Memo, 1972) from Matheson Gas Data Book, Fourth Edition, the Matheson Company, Inc. (1966).
2. V. S. Vorenko et al., Soviet Physics Uspekhi 6(6), 794 (1964).
3. C. Y. Prescott, private communication.

## APPENDIX B - DESIGN CONSIDERATIONS FOR LEAD GLASS SHOWER COUNTERS

High energy electrons and photons incident on matter form electromagnetic cascade showers. Rossi (Ref. B-1) discusses shower theory in detail. We shall only sketch the shower process here. Upon entering matter, high energy electrons or photons ( $E_{e,\gamma} > 100 \text{ MeV}$ ) start to lose energy through the emission of energetic photons or by pair production. The created particles then continue the process, thus producing still more particles. The resulting avalanche continues to build up until the typical energy of the photons has dropped to less than about 10 MeV. Below this energy, Compton scattering dominates over pair production. When the electrons (positrons) have less energy than the critical energy,  $E_{cr}$  (typical values are 8 MeV for Pb and 15 MeV for lead glass) ionization losses dominate over bremsstrahlung losses.

The characteristic distance within matter for an electron (positron) bremsstrahlung is approximately equal to the distance for pair production by a photon at high energies. This electromagnetic interaction length is referred to as the radiation length,  $\chi_0$ , and depends on the specific atomic properties (principally the atomic number and the density) of the shower medium. Shower characteristics can be discussed in units of radiation lengths and be somewhat independent of the specific material.

A crude picture of a shower is as follows. An incident high energy electron starts an electromagnetic cascade shower which builds up exponentially with a doubling length of approximately a

radiation length. This build-up ceases when the typical energy of the shower photons reach an energy of about 10 MeV (i.e., where pair production and Compton scattering are equal). At this "shower maximum" point given by (Ref. B-1)

$$\chi_{0 \text{ max}} = 1.01 (\ln(E_{inc}/E_{cr}) - 1) \text{ where } E_{inc} \text{ is the incident particles' energy.}$$

The shower has a charge multiplicity of approximately

$$\Pi_{\text{max}} = \frac{.31}{(\ln(E_{inc}/E_{cr}) - .37)^{1/2}} \frac{E_{inc}}{E_{cr}}$$

The shower now starts to fade, less rapidly than its build-up, through ionization loss. Processes such as Moller scattering, Bhabha scattering, and Compton scattering disperse the shower. A simple picture of the transverse shower development caused by a high energy incident particle is a narrow "core" of energetic components which have little deflection from the incident particle's trajectory, surrounded by a "fuzz" of soft Compton and Moller scattered electrons. The radial spread is typically  $2 \chi_0 - 3 \chi_0$  and occurs after shower maximum. Shower maximum occurs at  $3-6 \chi_0$  for energies of 1-10 GeV and varies logarithmically with energy. The shower tail (after shower maximum) can be as long as  $14 \chi_0$  long and is insensitive to incident energy. For an incident photon the same picture is approximately correct except that one should add a radiation length for the photon to convert into an electron-positron pair, but then the shower begins with a multiplicity of two.

The shower loses energy to the material in which it occurs, mainly through ionization losses. To the extent that ionization

loss is independent of the particle's energy, the total charged particle path length,  $\tau$ , will be proportional to the energy of the particle initiating the shower. In lead glass particle counters, charged particles produce light via Cerenkov radiation. The total Cerenkov light output for shower particles with velocities near the speed of light is proportional to the charged particle path length.

The fluctuations in short counters are due primarily to the initial shower development. Typically the point of the first interaction is a radiation length into the material, but on a shower-to-shower basis this point will fluctuate by approximately a radiation length, thus shifting the whole shower back and forth by a radiation length. This can cause more or less leakage from the back of the counter.

We now examine shower development in lead glass. The principal physical properties of several commercially available lead glasses are shown in Table B-1 (Ref. B-2). The light transmission of these glasses is shown in Fig. B-1 for a length of  $11 \chi_0$  of glass (Ref. B-2). Also plotted in Fig. B-1 are the approximate quantum efficiencies of AVP and DVP photocathodes.

Using a crude shower model that has all the shower particles going in the same direction with approximately the right buildup and decay in multiplicity, we can fold in the glass transmission and photocathode response to estimate the total photoelectron yield. Figure B-2a shows the photon number spectrum per  $\lambda$  for a 1 GeV shower in a  $16 \chi_0$  counter that would be transmitted by the glass to

TABLE B - 1  
LEAD GLASS PROPERTIES

No.	Schott	Ohara	Ref. Index	Density (gr/cc)	% PbO	Rad. Len. (cm)	Int. Len. (cm)	I.L./R.L.
1a	F2	PEMG2A	1.6200	3.63	45.0	3.22	28.0	8.7
1b	-	PEMG2	1.6200	3.63	45.0	3.22	28.0	8.7
2	SF2	PEMG1	1.6477	3.85	50.0	2.84	27.3	9.6
3	SF5	PEMG4	1.6727	4.08	55.0	2.54	25.6	10.1
4	SF1	PEMG5	1.7174	4.47	61.0	2.17	24.9	11.5
5a	SF6	PEMG3A	1.8052	5.20	71.0	1.68	22.7	13.5
5b	-	PEMG3	1.8052	5.20	71.0	1.68	22.7	13.5

Some physical properties of various commercial lead glasses.

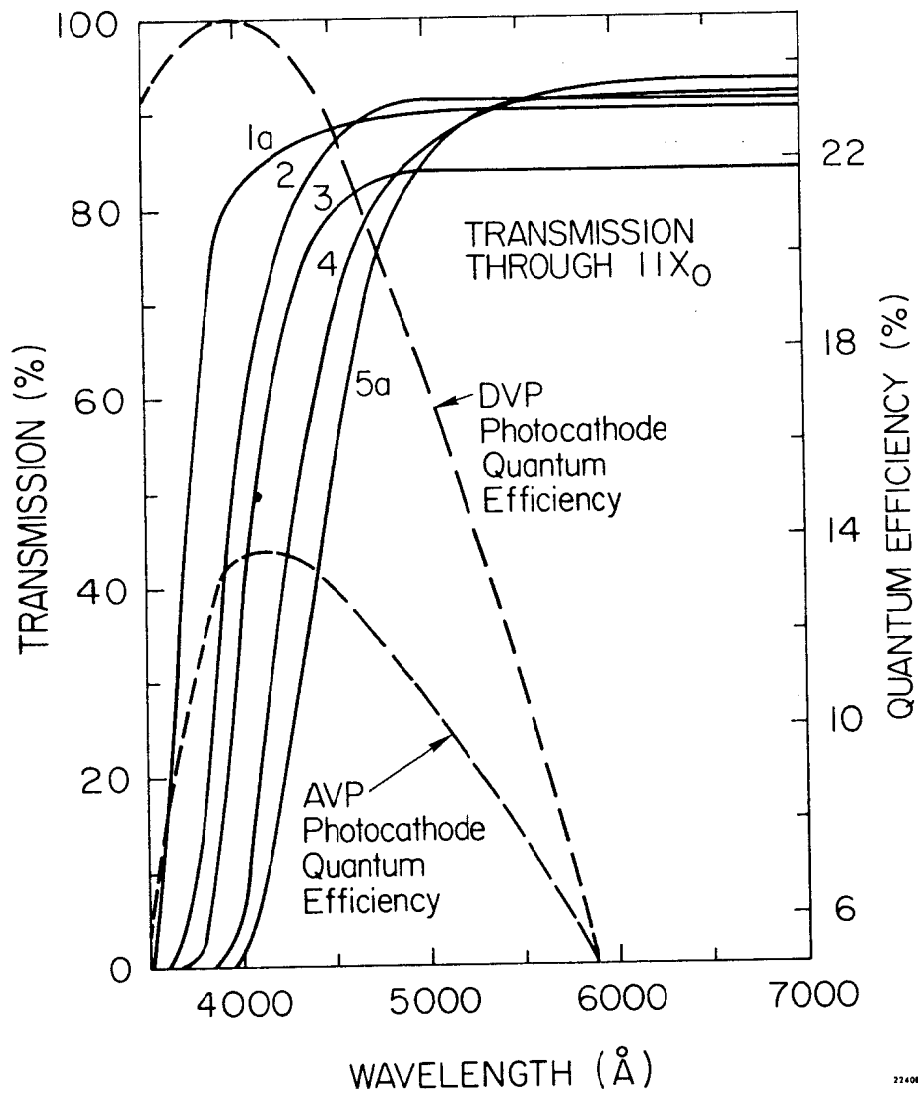


FIG. B-1

Transmission curves for lead glass types 1a, 2, 3, 4, 5a (see Table B-1). Dash lines and right-hand scale show AVP and DVP photocathode response.

Number of photons produced from a 1 GeV electron shower and transmitted through a  $16 X_0$  long counter.

Number of photoelectrons expected for a 1 GeV shower for various glass types. No light collection efficiency has been included in the calculation.

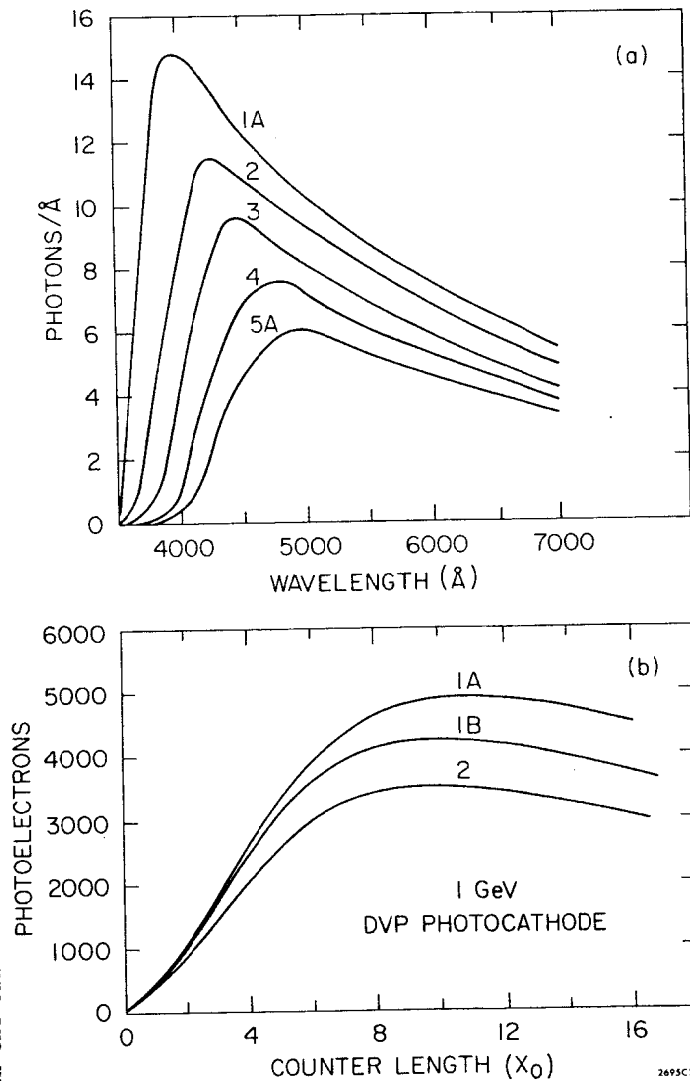


FIG. B-2

the photocathodes located at the opposite end of the counter from the entering particle. The curves in the red end of the spectrum are separated by approximately the ratio of their radiation lengths, while the short wavelength cutoff is determined by the transmission properties of the particular glass type. The least dense glass (longest  $\chi_0$ ) gives the largest number of photons for both of the above reasons. This photon number spectrum was then folded against the photocathode response of a DVP bialkali and the calculated number of photoelectrons versus counter length is shown in Fig. B-2b for 1.0 GeV showers. No light collection efficiency has been included in the calculation, so these numbers corrected for collection efficiency will depend on the particular geometry, and, in our case, were perhaps a factor of 5 too large.

Shower fluctuations in spatial development and charged particle path lengths were studied using a shower program initially written by Nagel (Ref. B-3) and modified by R. Ford (Ref. B-4). For lead glass Cerenkov shower counters, an interesting quantity to calculate is the charged particle path length adjusted for decreasing Cerenkov light intensity as  $\beta$  falls away from unity.

$$\tilde{\tau} = \tau \frac{(1 - \frac{1}{n^2\beta^2})}{(1 - \frac{1}{n^2})}$$

This effective charge particle pathlength,  $\tilde{\tau}$ , cuts off the low energy shower particles as they do not radiate Cerenkov light as effectively. By generating Monte Carlo showers using the program the spread in various shower parameters can be estimated. The

medium in which showers were generated corresponded to the mixture of elements found in Schott F2 glass. The shower tails were followed until particles had less than 1.0 MeV of energy ( $\beta^2 = .739$  for electrons). The showers developed in 40  $\chi_0$  (dia.) by 41  $\chi_0$  (long) counter geometries. The shower development was binned in radial and longitudinal bins of 1  $\chi_0$  width. The incident particles were normal to the front surface and centered on it.

In Tables B-2a through B-2c, we present the results of such Monte Carlo shower simulations for 1, 5 and 20 GeV incident electrons. Several interesting quantities may be plotted from such tables. In Fig. B-3, the fraction of the shower contained versus the length and the radius of the counter is plotted. A spread in the lines plotted for different energies indicates non-linear energy responses for that geometry. The conclusions are: 1) the radial containment is insensitive to incident energy and thus does not affect the linearity; and, 2) for energies in the 1-20 GeV range, counters appreciably shorter than 18  $\chi_0$  will not have a linear energy response.

Shower resolution is a more sensitive parameter to both depth and radius. Fig. B-4a shows that the RMS shower fluctuations in  $\tilde{\tau}$  improve approximately exponentially, finally reaching a minimum at 18  $\chi_0$  for 1.0 GeV and 26  $\chi_0$  for 20 GeV. The resolution sensitivity to radial size is less dramatic and tends to become less dependent on the radius as the energy increases (see Fig. B-4b).

In Fig. B-5, we show the calculated counter resolution versus energy for a 22  $\chi_0$  by a 4  $\chi_0$  radius counter. We have used 5000

TABLE B - 2a

FRACTIONAL SHOWER PATH LENGTHS FOR 1.000 GEV ELECTRONS, AVERAGE MAX. PATH LENGTH= 49.81 R.L., 500 SHOWERS

DEPTH	RACIAL													
	1		2		3		4		5		6		7	
0	0.0	+0.0	0.0	+0.0	0.0	+0.0	0.0	+0.0	0.0	+0.0	0.0	+0.0	0.0	+0.0
1	0.04118	-0.4831	0.04129	-0.4833	0.04134	-0.4830	0.04142	-0.4839	0.04146	-0.4841	0.04147	-0.4841	0.04148	-0.4841
2	0.14116	-0.4381	0.14155	-0.4391	0.14184	-0.4392	0.14202	-0.4394	0.14210	-0.4393	0.14214	-0.4394	0.14215	-0.4394
3	0.28667	-0.3653	0.28844	-0.3665	0.28898	-0.3669	0.28933	-0.3670	0.28947	-0.3670	0.28954	-0.3671	0.28961	-0.3671
4	0.43519	-0.2958	0.44043	-0.2977	0.44180	-0.2977	0.44251	-0.2978	0.44283	-0.2977	0.44296	-0.2977	0.44307	-0.2978
5	0.56476	-0.2414	0.57639	-0.2429	0.57910	-0.2430	0.58026	-0.2433	0.58088	-0.2433	0.58111	-0.2433	0.58127	-0.2434
6	0.66327	-0.1975	0.68342	-0.1987	0.68839	-0.1989	0.69033	-0.1992	0.69130	-0.1993	0.69169	-0.1994	0.69193	-0.1994
7	0.73354	-0.1587	0.76306	-0.1602	0.77023	-0.1607	0.77301	-0.1609	0.77436	-0.1611	0.77498	-0.1611	0.77534	-0.1611
8	0.78528	-0.1251	0.82436	-0.1256	0.83404	-0.1264	0.83776	-0.1265	0.83957	-0.1267	0.84041	-0.1267	0.84088	-0.1267
9	0.81876	-0.0988	0.86585	-0.0981	0.87839	-0.0987	0.88324	-0.0989	0.88566	-0.0990	0.88686	-0.0989	0.88749	-0.0989
10	0.83934	-0.0793	0.89272	-0.0768	0.90759	-0.0772	0.91356	-0.0774	0.91641	-0.0776	0.91784	-0.0775	0.91862	-0.0774
11	0.85319	-0.0647	0.91210	-0.0600	0.92916	-0.0596	0.93624	-0.0597	0.93558	-0.0599	0.94123	-0.0597	0.94211	-0.0596
12	0.86185	-0.0557	0.92522	-0.0477	0.94414	-0.0461	0.95224	-0.0457	0.95613	-0.0458	0.95794	-0.0455	0.95893	-0.0454
13	0.86722	-0.0505	0.93397	-0.0398	0.95445	-0.0370	0.96343	-0.0362	0.96775	-0.0362	0.96980	-0.0358	0.97096	-0.0357
14	0.87107	-0.0467	0.94023	-0.0336	0.96202	-0.0291	0.97177	-0.0280	0.97640	-0.0277	0.97867	-0.0271	0.97991	-0.0271
15	0.87369	-0.0447	0.94437	-0.0298	0.96702	-0.0239	0.97730	-0.0221	0.98218	-0.0214	0.98459	-0.0208	0.98594	-0.0208
16	0.87490	-0.0440	0.94677	-0.0282	0.97015	-0.0215	0.98077	-0.0190	0.98589	-0.0180	0.98840	-0.0174	0.98987	-0.0172
17	0.87535	-0.0438	0.94789	-0.0277	0.97180	-0.0204	0.98265	-0.0177	0.98787	-0.0167	0.99042	-0.0160	0.99198	-0.0155
18	0.87576	-0.0436	0.94862	-0.0272	0.97275	-0.0197	0.98390	-0.0167	0.98926	-0.0156	0.99186	-0.0150	0.99347	-0.0144
19	0.87601	-0.0435	0.94925	-0.0270	0.97358	-0.0193	0.98488	-0.0161	0.99037	-0.0149	0.99305	-0.0141	0.99467	-0.0135
20	0.87619	-0.0435	0.94963	-0.0269	0.97413	-0.0191	0.98554	-0.0158	0.99106	-0.0145	0.99377	-0.0136	0.99542	-0.0130
21	0.87632	-0.0435	0.94991	-0.0270	0.97453	-0.0190	0.98598	-0.0157	0.99151	-0.0143	0.99426	-0.0134	0.99592	-0.0127
22	0.87643	-0.0434	0.95012	-0.0270	0.97480	-0.0190	0.98634	-0.0156	0.99188	-0.0142	0.99465	-0.0133	0.99633	-0.0126
23	0.87650	-0.0434	0.95025	-0.0269	0.97500	-0.0189	0.98658	-0.0155	0.99214	-0.0141	0.99497	-0.0132	0.99667	-0.0124
24	0.87650	-0.0434	0.95029	-0.0269	0.97508	-0.0189	0.98666	-0.0155	0.99225	-0.0142	0.99511	-0.0131	0.99681	-0.0124
25	0.87651	-0.0434	0.95031	-0.0270	0.97514	-0.0189	0.98673	-0.0155	0.99233	-0.0142	0.99519	-0.0131	0.99689	-0.0124
26	0.87655	-0.0434	0.95035	-0.0269	0.97518	-0.0189	0.98678	-0.0155	0.99238	-0.0141	0.99525	-0.0131	0.99696	-0.0124
27	0.87655	-0.0434	0.95035	-0.0269	0.97518	-0.0189	0.98679	-0.0155	0.99243	-0.0141	0.99532	-0.0131	0.99702	-0.0124
28	0.87655	-0.0434	0.95035	-0.0269	0.97519	-0.0189	0.98679	-0.0155	0.99244	-0.0141	0.99532	-0.0131	0.99703	-0.0124
29	0.87655	-0.0434	0.95035	-0.0270	0.97519	-0.0189	0.98680	-0.0155	0.99244	-0.0141	0.99532	-0.0131	0.99703	-0.0124
30	0.87655	-0.0434	0.95036	-0.0269	0.97520	-0.0189	0.98681	-0.0155	0.99246	-0.0141	0.99534	-0.0131	0.99707	-0.0124
31	0.87655	-0.0434	0.95036	-0.0269	0.97520	-0.0189	0.98681	-0.0155	0.99246	-0.0141	0.99534	-0.0131	0.99707	-0.0124
32	0.87655	-0.0434	0.95036	-0.0269	0.97520	-0.0189	0.98681	-0.0155	0.99246	-0.0141	0.99534	-0.0131	0.99707	-0.0124
33	0.87655	-0.0434	0.95036	-0.0269	0.97520	-0.0189	0.98681	-0.0155	0.99246	-0.0141	0.99534	-0.0131	0.99707	-0.0124
34	0.87655	-0.0434	0.95036	-0.0269	0.97520	-0.0189	0.98681	-0.0155	0.99246	-0.0141	0.99534	-0.0131	0.99707	-0.0124
35	0.87655	-0.0434	0.95036	-0.0269	0.97520	-0.0189	0.98681	-0.0155	0.99246	-0.0141	0.99534	-0.0131	0.99707	-0.0124
36	0.87655	-0.0434	0.95036	-0.0269	0.97520	-0.0189	0.98681	-0.0155	0.99246	-0.0141	0.99534	-0.0131	0.99707	-0.0124
37	0.87655	-0.0434	0.95036	-0.0269	0.97520	-0.0189	0.98681	-0.0155	0.99246	-0.0141	0.99534	-0.0131	0.99707	-0.0124
38	0.87655	-0.0434	0.95036	-0.0269	0.97520	-0.0189	0.98681	-0.0155	0.99246	-0.0141	0.99534	-0.0131	0.99707	-0.0124
39	0.87655	-0.0434	0.95036	-0.0269	0.97520	-0.0189	0.98681	-0.0155	0.99246	-0.0141	0.99534	-0.0131	0.99707	-0.0124
40	0.87655	-0.0434	0.95036	-0.0269	0.97520	-0.0189	0.98681	-0.0155	0.99246	-0.0141	0.99534	-0.0131	0.99707	-0.0124
41	0.87655	-0.0434	0.95036	-0.0269	0.97520	-0.0189	0.98681	-0.0155	0.99246	-0.0141	0.99534	-0.0131	0.99707	-0.0124

TABLE B - 2b

FRACTIONAL SHOWER PATH LENGTHS FOR 5.000 GEV ELECTRONS, AVERAGE MAX. PATH LENGTH= 248.85 R.L., 117 SHOWERS

DEPTH	RADIAL													
	1		2		3		4		5		6		7	
0	0.0	+0.0	0.0	+0.0	0.0	+0.0	0.0	+0.0	0.0	+0.0	0.0	+0.0	0.0	+0.0
1	0.01151	+0.5184	0.01153	+0.5186	0.01155	+0.5191	0.01157	+0.5190	0.01158	+0.5183	0.01159	+0.5186	0.01161	+0.5168
2	0.05123	+0.4560	0.05134	+0.4562	0.05141	+0.4564	0.05146	+0.4564	0.05151	+0.4568	0.05154	+0.4568	0.05158	+0.4562
3	0.12900	+0.3881	0.12963	+0.3890	0.12988	+0.3892	0.12999	+0.3893	0.13010	+0.3892	0.13016	+0.3893	0.13025	+0.3890
4	0.23636	+0.3248	0.23858	+0.3260	0.23921	+0.3260	0.23948	+0.3261	0.23965	+0.3262	0.23975	+0.3263	0.23986	+0.3262
5	0.35806	+0.2645	0.36342	+0.2663	0.36467	+0.2667	0.36528	+0.2666	0.36560	+0.2668	0.36579	+0.2668	0.36595	+0.2668
6	0.47931	+0.2124	0.49002	+0.2143	0.49255	+0.2151	0.49359	+0.2152	0.49414	+0.2154	0.49441	+0.2154	0.49462	+0.2155
7	0.58437	+0.1755	0.60176	+0.1771	0.60584	+0.1774	0.60753	+0.1776	0.60835	+0.1778	0.60878	+0.1779	0.60906	+0.1779
8	0.66887	+0.1449	0.69449	+0.1468	0.70076	+0.1470	0.70330	+0.1472	0.70444	+0.1474	0.70504	+0.1476	0.70537	+0.1476
9	0.73326	+0.1169	0.76731	+0.1191	0.77591	+0.1198	0.77945	+0.1200	0.78105	+0.1203	0.78186	+0.1204	0.78231	+0.1205
10	0.78041	+0.0917	0.82251	+0.0945	0.83361	+0.0954	0.83818	+0.0959	0.84031	+0.0962	0.84138	+0.0964	0.84196	+0.0965
11	0.81340	+0.0719	0.86210	+0.0742	0.87562	+0.0752	0.88128	+0.0755	0.88392	+0.0758	0.88526	+0.0760	0.88598	+0.0761
12	0.83516	+0.0582	0.88971	+0.0599	0.90528	+0.0609	0.91204	+0.0612	0.91511	+0.0615	0.91669	+0.0617	0.91758	+0.0618
13	0.85207	+0.0440	0.91183	+0.0452	0.92935	+0.0460	0.93702	+0.0463	0.94050	+0.0465	0.94240	+0.0467	0.94347	+0.0468
14	0.86150	+0.0317	0.92457	+0.0322	0.94355	+0.0329	0.95194	+0.0332	0.95586	+0.0335	0.95794	+0.0337	0.95912	+0.0338
15	0.86785	+0.0249	0.93355	+0.0238	0.95372	+0.0241	0.96253	+0.0243	0.96681	+0.0246	0.96910	+0.0248	0.97043	+0.0248
16	0.87189	+0.0224	0.93980	+0.0196	0.96100	+0.0194	0.97026	+0.0196	0.97483	+0.0199	0.97729	+0.0200	0.97867	+0.0200
17	0.87447	+0.0201	0.94392	+0.0154	0.96587	+0.0145	0.97584	+0.0147	0.98070	+0.0148	0.98331	+0.0149	0.98475	+0.0148
18	0.87564	+0.0188	0.94604	+0.0132	0.96865	+0.0116	0.97901	+0.0118	0.98409	+0.0117	0.98686	+0.0116	0.98840	+0.0115
19	0.87648	+0.0183	0.94771	+0.0118	0.97075	+0.0098	0.98132	+0.0098	0.98650	+0.0097	0.98934	+0.0094	0.99096	+0.0094
20	0.87718	+0.0180	0.94889	+0.0112	0.97214	+0.0085	0.98286	+0.0084	0.98817	+0.0081	0.99113	+0.0078	0.99286	+0.0078
21	0.87760	+0.0179	0.94953	+0.0113	0.97299	+0.0081	0.98390	+0.0077	0.98932	+0.0073	0.99237	+0.0069	0.99411	+0.0069
22	0.87778	+0.0179	0.94986	+0.0112	0.97345	+0.0080	0.98443	+0.0073	0.98993	+0.0070	0.99305	+0.0065	0.99483	+0.0064
23	0.87782	+0.0179	0.95000	+0.0111	0.97370	+0.0080	0.98475	+0.0074	0.99030	+0.0070	0.99345	+0.0064	0.99530	+0.0063
24	0.87789	+0.0179	0.95021	+0.0111	0.97396	+0.0079	0.98507	+0.0073	0.99065	+0.0068	0.99383	+0.0062	0.99569	+0.0062
25	0.87796	+0.0179	0.95043	+0.0112	0.97424	+0.0080	0.98538	+0.0073	0.99096	+0.0068	0.99420	+0.0062	0.99607	+0.0061
26	0.87799	+0.0180	0.95053	+0.0112	0.97436	+0.0080	0.98557	+0.0072	0.99116	+0.0066	0.99440	+0.0060	0.99628	+0.0060
27	0.87801	+0.0179	0.95060	+0.0112	0.97446	+0.0080	0.98569	+0.0071	0.99130	+0.0066	0.99454	+0.0060	0.99642	+0.0060
28	0.87801	+0.0179	0.95061	+0.0113	0.97448	+0.0080	0.98573	+0.0072	0.99133	+0.0065	0.99459	+0.0060	0.99647	+0.0059
29	0.87801	+0.0179	0.95061	+0.0113	0.97448	+0.0080	0.98574	+0.0071	0.99135	+0.0065	0.99460	+0.0060	0.99649	+0.0059
30	0.87801	+0.0179	0.95062	+0.0113	0.97449	+0.0080	0.98575	+0.0071	0.99136	+0.0065	0.99463	+0.0059	0.99652	+0.0059
31	0.87801	+0.0179	0.95062	+0.0113	0.97449	+0.0080	0.98575	+0.0071	0.99136	+0.0065	0.99463	+0.0059	0.99652	+0.0059
32	0.87801	+0.0175	0.95062	+0.0113	0.97449	+0.0080	0.98575	+0.0071	0.99136	+0.0065	0.99463	+0.0059	0.99652	+0.0059
33	0.87801	+0.0175	0.95062	+0.0113	0.97449	+0.0080	0.98575	+0.0071	0.99136	+0.0065	0.99463	+0.0059	0.99652	+0.0059
34	0.87801	+0.0179	0.95062	+0.0113	0.97449	+0.0080	0.98575	+0.0071	0.99136	+0.0065	0.99463	+0.0059	0.99652	+0.0059
35	0.87801	+0.0179	0.95062	+0.0113	0.97449	+0.0080	0.98575	+0.0071	0.99136	+0.0065	0.99463	+0.0059	0.99652	+0.0059
36	0.87801	+0.0175	0.95062	+0.0113	0.97449	+0.0080	0.98575	+0.0071	0.99136	+0.0065	0.99463	+0.0059	0.99652	+0.0059
37	0.87801	+0.0179	0.95062	+0.0113	0.97449	+0.0080	0.98575	+0.0071	0.99136	+0.0065	0.99463	+0.0059	0.99652	+0.0059
38	0.87801	+0.0179	0.95062	+0.0113	0.97449	+0.0080	0.98575	+0.0071	0.99136	+0.0065	0.99463	+0.0059	0.99652	+0.0059
39	0.87801	+0.0179	0.95062	+0.0113	0.97449	+0.0080	0.98575	+0.0071	0.99136	+0.0065	0.99463	+0.0059	0.99652	+0.0059
40	0.87801	+0.0179	0.95062	+0.0113	0.97449	+0.0080	0.98575	+0.0071	0.99136	+0.0065	0.99463	+0.0059	0.99652	+0.0059
41	0.87801	+0.0179	0.95062	+0.0113	0.97449	+0.0080	0.98575	+0.0071	0.99136	+0.0065	0.99463	+0.0059	0.99652	+0.0059

TABLE B - 2c

FRACTIONAL SHOWER PATH LENGTHS FOR 20,000 GEV ELECTRONS, AVERAGE MAX. PATH LENGTH= 995.03 R.L., 28 SHOWERS

DEPTH	RADIAL															
	1	2	3	4	5	6	7	1	2	3	4	5	6	7		
0	0.0	+0.0	0.0	+0.0	0.0	+0.0	0.0	+0.0	0.0	+0.0	0.0	+0.0	0.0	+0.0	0.0	+0.0
1	0.00292+	-0.5683	0.00293+	-0.5671	0.00294+	-0.5612	0.00295+	-0.5603	0.00296+	-0.5586	0.00298+	-0.5590	0.00299+	-0.5579	0.00299+	-0.5579
2	0.01926+	-0.5245	0.01932+	-0.5228	0.01936+	-0.5216	0.01938+	-0.5215	0.01940+	-0.5214	0.01944+	-0.5210	0.01945+	-0.5207	0.01945+	-0.5207
3	0.06031+	-0.4240	0.06060+	-0.4238	0.06073+	-0.4227	0.06081+	-0.4223	0.06094+	-0.4227	0.06094+	-0.4226	0.06094+	-0.4226	0.06091+	-0.4225
4	0.12865+	-0.3574	0.12949+	-0.3576	0.12979+	-0.3575	0.12998+	-0.3574	0.13006+	-0.3575	0.13006+	-0.3575	0.13012+	-0.3575	0.13015+	-0.3574
5	0.22492+	-0.2992	0.22748+	-0.2994	0.22914+	-0.2992	0.22850+	-0.2990	0.22865+	-0.2990	0.22878+	-0.2990	0.22884+	-0.2989	0.22884+	-0.2989
6	0.33653+	-0.2422	0.34196+	-0.2433	0.34331+	-0.2433	0.34391+	-0.2432	0.34418+	-0.2432	0.34437+	-0.2432	0.34437+	-0.2432	0.34446+	-0.2432
7	0.44624+	-0.1933	0.45663+	-0.1963	0.45930+	-0.1964	0.46011+	-0.1962	0.46059+	-0.1963	0.46090+	-0.1962	0.46106+	-0.1962	0.46106+	-0.1962
8	0.54422+	-0.1594	0.56141+	-0.1626	0.56548+	-0.1630	0.56683+	-0.1631	0.56757+	-0.1631	0.56806+	-0.1631	0.56832+	-0.1631	0.56832+	-0.1631
9	0.62704+	-0.1354	0.65176+	-0.1379	0.65793+	-0.1385	0.66007+	-0.1385	0.66109+	-0.1385	0.66178+	-0.1384	0.66211+	-0.1385	0.66211+	-0.1385
10	0.69322+	-0.1213	0.72550+	-0.1238	0.73399+	-0.1242	0.73691+	-0.1242	0.73832+	-0.1242	0.73925+	-0.1242	0.73966+	-0.1242	0.73966+	-0.1242
11	0.74307+	-0.1087	0.78319+	-0.1109	0.79424+	-0.1111	0.79800+	-0.1110	0.79983+	-0.1111	0.80095+	-0.1111	0.80146+	-0.1111	0.80146+	-0.1111
12	0.78108+	-0.0955	0.82813+	-0.0978	0.84115+	-0.0980	0.84608+	-0.0979	0.84836+	-0.0980	0.84975+	-0.0980	0.85035+	-0.0980	0.85035+	-0.0980
13	0.80970+	-0.0802	0.86280+	-0.0828	0.87800+	-0.0830	0.88402+	-0.0830	0.88671+	-0.0831	0.88834+	-0.0831	0.88907+	-0.0831	0.88907+	-0.0831
14	0.82972+	-0.0640	0.88182+	-0.0669	0.90545+	-0.0674	0.91244+	-0.0673	0.91556+	-0.0675	0.91742+	-0.0675	0.91833+	-0.0676	0.91833+	-0.0676
15	0.84433+	-0.0502	0.90650+	-0.0521	0.92538+	-0.0538	0.93324+	-0.0536	0.93697+	-0.0536	0.93899+	-0.0536	0.94012+	-0.0536	0.94012+	-0.0536
16	0.85425+	-0.0384	0.91935+	-0.0407	0.93951+	-0.0416	0.94824+	-0.0414	0.95232+	-0.0415	0.95459+	-0.0413	0.95588+	-0.0414	0.95588+	-0.0414
17	0.86134+	-0.0280	0.92983+	-0.0302	0.94999+	-0.0310	0.95930+	-0.0308	0.96374+	-0.0309	0.96619+	-0.0308	0.96756+	-0.0308	0.96756+	-0.0308
18	0.86648+	-0.0200	0.93574+	-0.0222	0.95776+	-0.0230	0.96762+	-0.0226	0.97224+	-0.0228	0.97482+	-0.0228	0.97627+	-0.0227	0.97627+	-0.0227
19	0.86989+	-0.0148	0.94071+	-0.0169	0.96349+	-0.0175	0.97375+	-0.0170	0.97868+	-0.0171	0.98140+	-0.0169	0.98291+	-0.0170	0.98291+	-0.0170
20	0.87207+	-0.0113	0.94390+	-0.0124	0.96737+	-0.0128	0.97795+	-0.0123	0.98312+	-0.0123	0.98598+	-0.0121	0.98760+	-0.0122	0.98760+	-0.0122
21	0.87332+	-0.0096	0.94576+	-0.0096	0.96970+	-0.0097	0.98047+	-0.0091	0.98569+	-0.0091	0.98866+	-0.0088	0.99035+	-0.0090	0.99035+	-0.0090
22	0.87437+	-0.0097	0.94731+	-0.0078	0.97173+	-0.0078	0.98272+	-0.0071	0.98805+	-0.0069	0.99108+	-0.0067	0.99281+	-0.0067	0.99281+	-0.0067
23	0.87491+	-0.0082	0.94815+	-0.0056	0.97282+	-0.0063	0.98393+	-0.0056	0.98940+	-0.0052	0.99248+	-0.0049	0.99422+	-0.0051	0.99422+	-0.0051
24	0.87520+	-0.0079	0.94858+	-0.0061	0.97339+	-0.0056	0.98463+	-0.0050	0.99016+	-0.0047	0.99330+	-0.0042	0.99509+	-0.0041	0.99509+	-0.0041
25	0.87558+	-0.0077	0.94905+	-0.0056	0.97405+	-0.0049	0.98541+	-0.0042	0.99095+	-0.0040	0.99410+	-0.0031	0.99592+	-0.0035	0.99592+	-0.0035
26	0.87564+	-0.0077	0.94921+	-0.0054	0.97428+	-0.0044	0.98565+	-0.0039	0.99123+	-0.0038	0.99441+	-0.0032	0.99624+	-0.0033	0.99624+	-0.0033
27	0.87571+	-0.0077	0.94935+	-0.0054	0.97457+	-0.0041	0.98598+	-0.0038	0.99157+	-0.0035	0.99477+	-0.0027	0.99660+	-0.0031	0.99660+	-0.0031
28	0.87573+	-0.0077	0.94944+	-0.0053	0.97469+	-0.0040	0.98613+	-0.0037	0.99175+	-0.0035	0.99496+	-0.0028	0.99681+	-0.0031	0.99681+	-0.0031
29	0.87574+	-0.0077	0.94947+	-0.0053	0.97472+	-0.0039	0.98619+	-0.0037	0.99184+	-0.0034	0.99506+	-0.0029	0.99692+	-0.0028	0.99692+	-0.0028
30	0.87574+	-0.0077	0.94947+	-0.0053	0.97473+	-0.0040	0.98620+	-0.0037	0.99185+	-0.0033	0.99507+	-0.0028	0.99693+	-0.0028	0.99693+	-0.0028
31	0.87574+	-0.0077	0.94947+	-0.0053	0.97473+	-0.0040	0.98620+	-0.0037	0.99185+	-0.0033	0.99507+	-0.0028	0.99693+	-0.0028	0.99693+	-0.0028
32	0.87574+	-0.0077	0.94947+	-0.0053	0.97472+	-0.0040	0.98620+	-0.0037	0.99185+	-0.0033	0.99507+	-0.0028	0.99693+	-0.0028	0.99693+	-0.0028
33	0.87574+	-0.0077	0.94947+	-0.0053	0.97473+	-0.0040	0.98620+	-0.0037	0.99185+	-0.0033	0.99507+	-0.0028	0.99693+	-0.0028	0.99693+	-0.0028
34	0.87574+	-0.0077	0.94947+	-0.0053	0.97473+	-0.0040	0.98620+	-0.0037	0.99185+	-0.0033	0.99507+	-0.0028	0.99693+	-0.0028	0.99693+	-0.0028
35	0.87574+	-0.0077	0.94947+	-0.0053	0.97473+	-0.0040	0.98620+	-0.0037	0.99185+	-0.0033	0.99507+	-0.0028	0.99693+	-0.0028	0.99693+	-0.0028
36	0.87574+	-0.0077	0.94947+	-0.0053	0.97473+	-0.0040	0.98620+	-0.0037	0.99185+	-0.0033	0.99507+	-0.0028	0.99693+	-0.0028	0.99693+	-0.0028
37	0.87574+	-0.0077	0.94947+	-0.0053	0.97473+	-0.0040	0.98620+	-0.0037	0.99185+	-0.0033	0.99507+	-0.0028	0.99693+	-0.0028	0.99693+	-0.0028
38	0.87574+	-0.0077	0.94947+	-0.0053	0.97473+	-0.0040	0.98620+	-0.0037	0.99185+	-0.0033	0.99507+	-0.0028	0.99693+	-0.0028	0.99693+	-0.0028
39	0.87574+	-0.0077	0.94947+	-0.0053	0.97473+	-0.0040	0.98620+	-0.0037	0.99185+	-0.0033	0.99507+	-0.0028	0.99693+	-0.0028	0.99693+	-0.0028
40	0.87574+	-0.0077	0.94947+	-0.0053	0.97473+	-0.0040	0.98620+	-0.0037	0.99185+	-0.0033	0.99507+	-0.0028	0.99693+	-0.0028	0.99693+	-0.0028
41	0.87574+	-0.0077	0.94947+	-0.0053	0.97473+	-0.0040	0.98620+	-0.0037	0.99185+	-0.0033	0.99507+	-0.0028	0.99693+	-0.0028	0.99693+	-0.0028



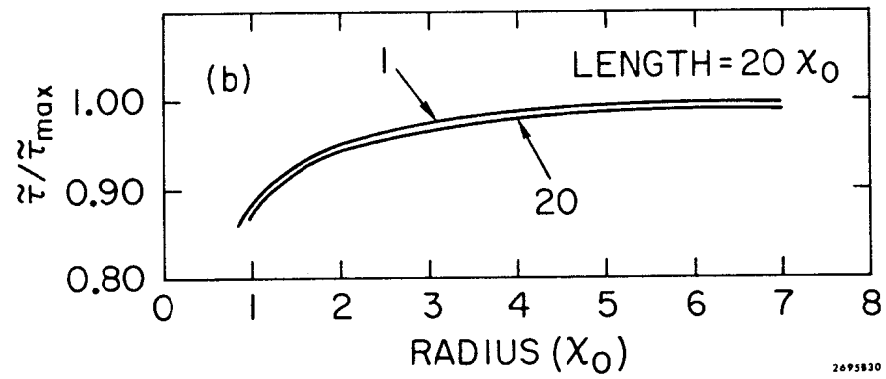
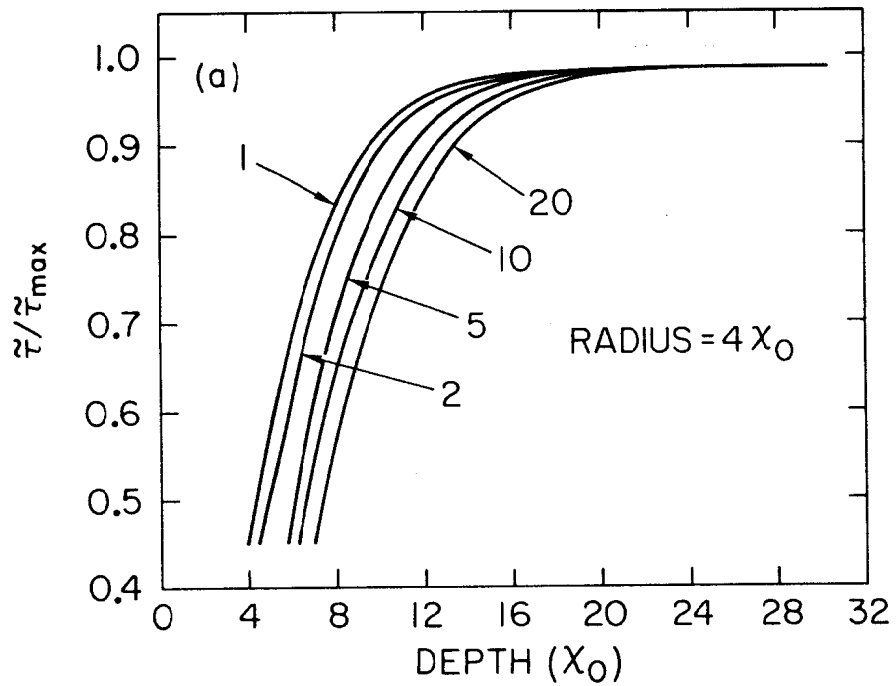


FIG. B-3  
Fractional containment of showers for 1, 2, 5, 10 and 20 GeV incident electrons versus a) counter length and b) counter radius.

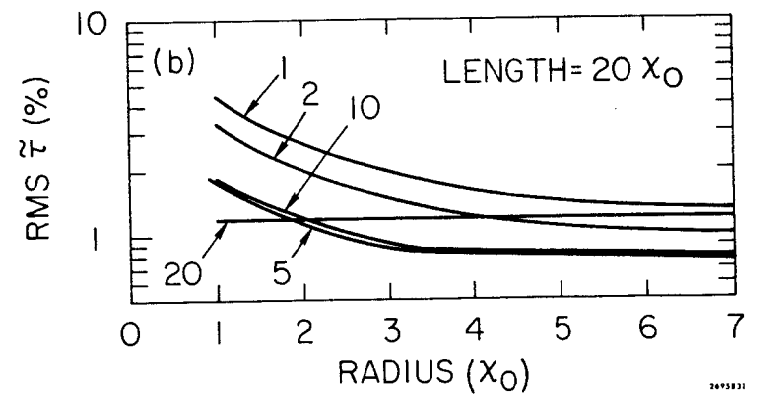
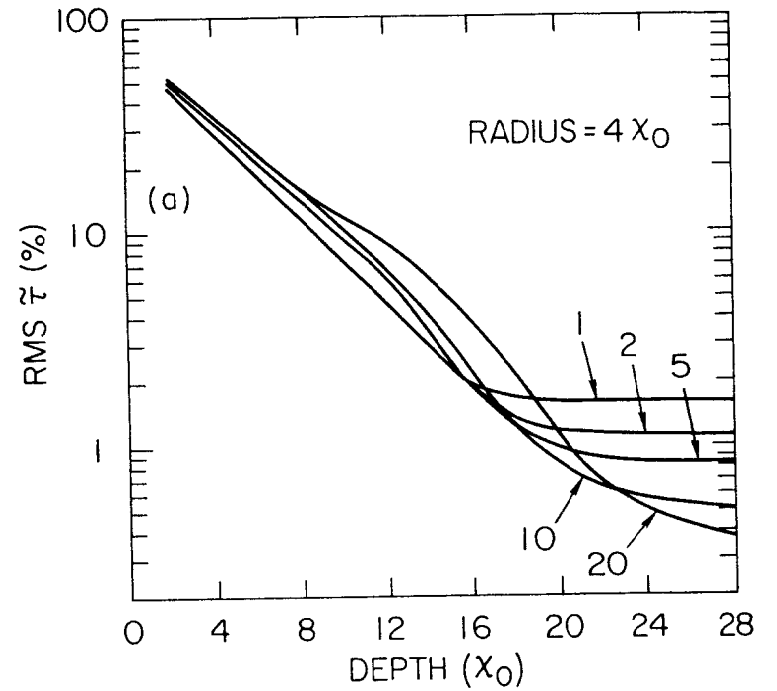


FIG. B-4  
Shows fluctuations for 1, 2, 5, 10 and 20 GeV incident electrons versus a) counter length and b) counter width.

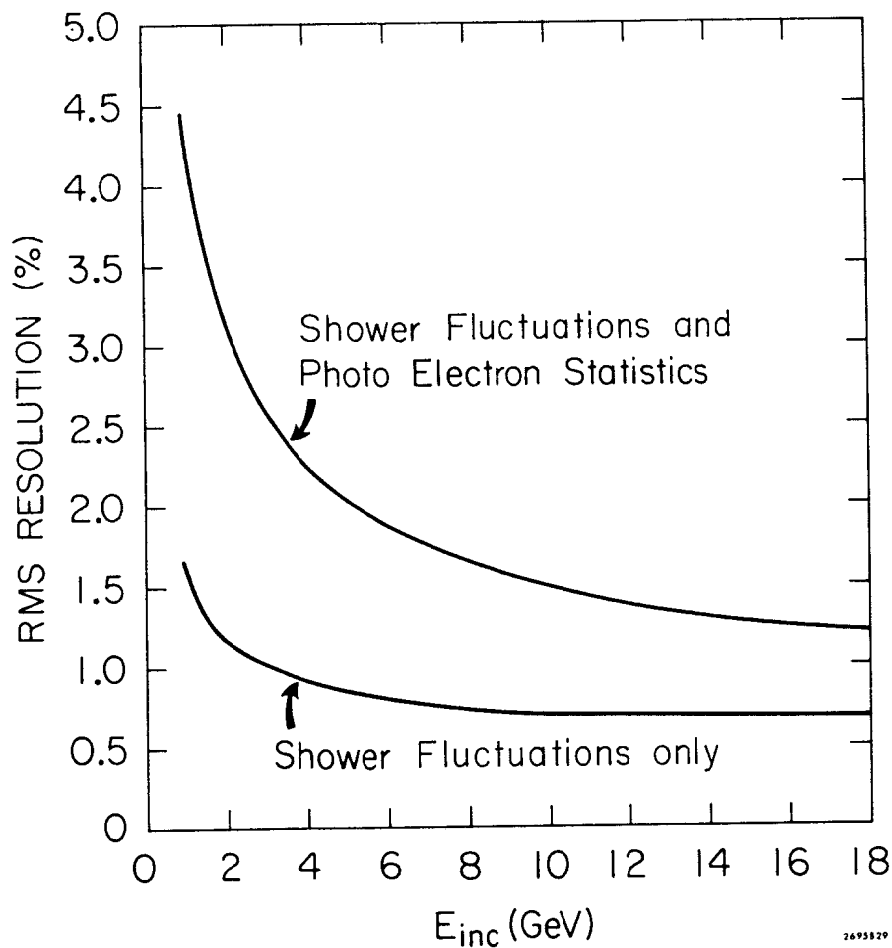


FIG. B-5

Calculated RMS resolution for a lead glass counter (see text) using 20% light collection efficiency.

photoelectrons for a 1 GeV shower times a 20% light collection efficiency (so chosen to match the E-89 counter). The photoelectron fluctuations were increased by 30% to account for amplification fluctuations in the first few dynodes of the phototubes. The resultant resolution was folded in quadrature with the shower fluctuations calculated by the shower program. The important features of Fig. B-5 are: 1) for the 1-10 GeV energy region, lead glass counter resolution is dominated by photoelectron statistics and improves approximately as  $1/\sqrt{E_{inc}}$ ; and 2) at high energies ( $E_{inc} > 10$  GeV) the resolution should improve more slowly approaching a  $1/E_{inc}^{1/4}$  response similar to that of NaI(Tl).

As photoelectron statistics are the dominant contribution to the resolution, care should be taken to obtain optimum light collection. To examine the Cerenkov radiation pattern in glass counters, we have plotted  $\tilde{\tau}$  versus  $\cos(\theta_i)$  where  $\theta_i$  is the angle of the path length with respect to the incident direction in Fig. B-6. The forward peaking is a factor of about 2 over the backwards contribution. This gives a Cerenkov radiation pattern somewhat peaked at the Cerenkov angle ( $\theta_c = 51.9$  deg. for F2 glass) with respect to the incident direction and a large flat background of more or less isotropically distributed light. One probably optimizes light collection by having the phototubes "look" into the shower direction. The E-89 counter was not constructed in this way.

A proper index match from the glass to the phototube is also important. For the counter constructed for E-89, oil light pipes

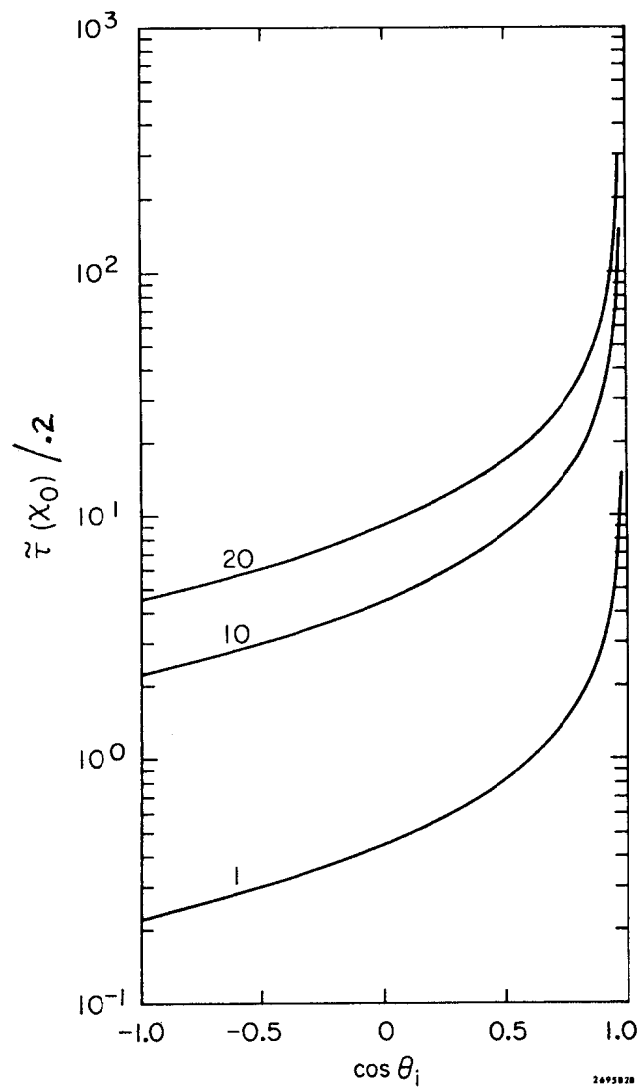


FIG. B-6

Plot of  $\tilde{z}$  versus cosine of its angle from particle's direction for 1, 10 and 20 GeV electrons.

filled with high index fluid ( $n = 1.58$ , immersion liquid) were used. The light pipes were aluminum frames glued to the glass and the phototubes with RTV to make the seals. The system continues to work well after two years of service.

## APPENDIX B REFERENCES

1. B. Rossi, "High Energy Particles," Prentice-Hall Inc., Englewood Cliffs, N.J. (1952).
2. Bourns Optical Glass, "Specification Sheet for PEMG," 1790A Springfield Avenue, New Providence, N.J. 97974.
3. H. H. Nagel, "Elektron-Photon-Kaskaden in Blei," Z.für Physik 186, 319-346 (1965); SLAC-TRANS-28; and D.F. Nicoli, "The Application of Monte Carlo Cascade Shower Generation in Lead in the Several BeV Energy Region," MIT B.S. Thesis, June 15, 1966, MIT, LNS Internal Report; also U. Volkel, DESY 67/16 (May 1967); U. Volkel, DESY 65/6 (July 1965); SLAC-TRANS-41, W.V. Jones, Physical Review 187, 1868-1879 (25 Nov. 1969); Crawford and Messel, "Electron Photon Shower Distribution Functions," (Pergamon Press, N.Y., 1970).
4. The shower programs used were obtained from R. L. Ford who also provided a preprocessor to calculate the various input parameters for the shower program for mixtures of elements.
5. L. P. Cargille Laboratory, Cedar Grove, New Jersey.

## APPENDIX C - A QUASI-ELASTIC APPROACH TO SMEARING

In this Appendix, smearing is reviewed, and a unified method of handling quasi-elastic scattering and inelastic smearing is developed. The term smearing refers to the effect of the Fermi motion of the nucleons within a nucleus on measured particle cross sections. In electroproduction data the effect is perhaps most graphically seen in quasi-elastic scattering where the narrow electron-nucleon elastic scattering peak is broadened out by this Fermi-motion effect. First, the quasi-elastic formalism as put forward by G. B. West (Ref. C-1) is reviewed for the case of arbitrary target, spectator, and produced hadronic masses. This formalism is then taken over to the inelastic case. The kinematic regions over which smearing is important are reviewed.

In electroproduction, we assume an impulse approximation for the interaction of the electron and nucleon within the target nucleus (see Fig. C-1). The notation used in this Appendix is given in Table C-1. Each nucleon is considered to be "free" and interacts independently of the rest of the nucleus (no interference terms) but with shifted kinematics resulting from its motion. This interacting nucleon leaves behind a spectator particle of equal but opposite momentum. Due to conservation of momentum at the breakup of the target particles, the probability of finding an interacting nucleon of a given momentum is equally well given by that of finding a spectator of opposite momentum.

These ideas are expressed in the following equations relating

TABLE C - 1

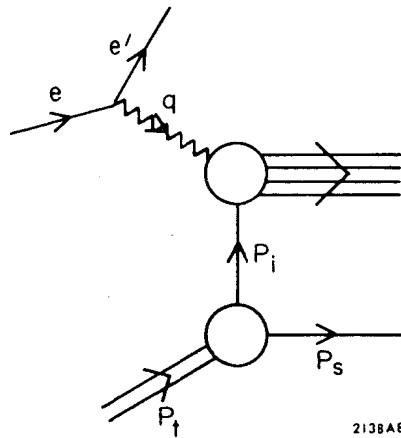


FIG. C-1

Feynman diagram of electron-deuteron scattering in the impulse approximation.

Quantity	Definition
$M$	Mass of the proton
$M_S$	Mass of the free spectator particle
$M_i$	Mass of the interacting particle were it on its mass shell
$M_t$	Mass of the target particle
$P_s$	Magnitude of the 3 momentum of the spectator particle
$E_s = \sqrt{P_s^2 + M_s^2}$	Energy of the spectator particle
$P_i = (P_o, P_x, P_y, P_z)$	Four vector of the interacting particle (note $P_i^2 \neq M_i^2$ )
$q = (\nu, \vec{q})$	Four vector of the virtual photon ( $q$ is the magnitude of $\vec{q}$ and $q^2 = -Q^2$ )
$P_t = (M_t, \vec{0})$	Four vector of the target particle in the laboratory

Definition of the variables used in the equations of Appendix C.

the nucleon structure functions to that of the target particle

(we consider here the deuteron case):

$$(C-1) \quad W_{\mu\nu}^D = \int \frac{d^3\mathbf{p}_s}{E_s/M_s} |\phi(\mathbf{p}_s)|^2 \{ W_{\mu\nu}^p + W_{\mu\nu}^N \}$$

$$\text{where} \quad W_{\mu\nu}^k = -W_1^k \left( q_{\mu\nu} - \frac{q_\mu q_\nu}{q^2} \right) + \frac{W_2^k}{M^2} \left( p_\mu^k - \frac{p_\mu^k \cdot q}{q} \right) \left( p_\nu^k - \frac{p_\nu^k \cdot q}{q} \right)$$

$|\phi(\mathbf{p}_s)|^2$  is the square of the relativistic momentum wave function of the spectator particle.

Defining  $\vec{q}$  along the z-axis, examination of the various tensor components of equation C-1 yields the following two equations for the smearing of the  $W_1$  and the  $W_2$  structure functions:

$$(C-2a) \quad W_1^S(\nu, Q^2) = \int \frac{d^3\mathbf{p}_s}{E_s/M_s} |\phi(\mathbf{p}_s)|^2 \{ W_1(W^2, Q^2) + \frac{P_X^2}{M^2} W_2(W^2, Q^2) \}$$

$$(C-2b) \quad W_2^S(\nu, Q^2) = \int \frac{d^3\mathbf{p}_s}{E_s/M_s} |\phi(\mathbf{p}_s)|^2 \mathcal{F}(P_i, \nu, q) W_2(W^2, Q^2)$$

and

$$\mathcal{F}(P_i, \nu, q) = \frac{1}{M^2} \left[ \left( P_o - \frac{\nu}{q} P_Z \right)^2 - \frac{q^2}{2} P_X^2 \right]$$

Consider the general case of  $(P_i + q)^2 = W^2$ . In the case of quasi-elastic scattering, the condition that the interacting nucleon be put onto its mass-shell,  $(P_i + q)^2 = M^2$ , in the final state is imposed.

We set

$$(C-3a) \quad W_1(W^2, Q^2) \equiv G_1(Q^2, S) \delta(S - W^2)$$

$$(C-3b) \quad W_2(W^2, Q^2) \equiv G_2(Q^2, S) \delta(S - W^2)$$

(for quasi-elastic scattering  $S = M_1^2$ )

Transforming the invariant phase-space volume element to the C.M. system (denoted by a tilde) of the photon-target particle system, the delta function is used against the  $d\mathbf{p}_s$  integration. This leaves only the angle integration  $d \cos(\tilde{\theta}_s)$  to be performed. Specifically, we have

$$(C-4a) \quad W_1^{SQ}(W^2, Q^2) = G_1(Q^2, W^2) I_1 + G_2(Q^2, W^2) I_2$$

$$(C-4b) \quad W_2^{SQ}(W^2, Q^2) = G_2(Q^2, W^2) I_3$$

where

$$(C-5a) \quad I_1 = \pi M \frac{\sqrt{s_t} + 1}{\sqrt{s_t} - 1} \int d \cos \tilde{\theta}_s |\phi(\tilde{\mathbf{p}}_s)|^2$$

$$(C-5b) \quad I_2 = \pi M \frac{\sqrt{s_t} + 1}{\sqrt{s_t} - 1} \int d \cos \tilde{\theta}_s |\phi(\tilde{\theta}_s)|^2 \frac{P_X^2}{M^2}$$

$$(C-5c) \quad I_3 = \pi M \frac{\sqrt{s_t} + 1}{\sqrt{s_t} - 1} \int d \cos \tilde{\theta}_s |\phi(\tilde{\mathbf{p}}_s)|^2 \mathcal{F}(P_i, \nu, q)$$

and

$$S_t = (P_t + q)^2 = M_t^2 + 2M_t \nu - Q^2$$

$$\tilde{p}_s^2 = \frac{S_t}{4} - \frac{1}{2} (W^2 + M^2) + \frac{1}{4S_t} (W^2 - M^2)^2$$

$$\tilde{E}_s = \sqrt{\tilde{p}_s^2 + M_s^2}$$

$$P_x^2 = \frac{1}{2} (1 - \cos^2 \tilde{\theta}_s) \tilde{p}_s^2$$

$$P_Z = \frac{1}{\sqrt{s_t}} \left( (M_t + \nu) \tilde{p}_s \cos \tilde{\theta}_s - q \tilde{E}_s \right)$$

$$P_s = \sqrt{2P_x^2 + P_Z^2}$$

The quasi-elastic case is the special one where  $S = M_1^2$  and  $G_1 = 2M\tau G_M^2$ ,  $G_2 = 2M(G_E^2 + \tau G_M^2)/(1 + \tau)$ ,  $\tau = Q^2/4M^2$ . The inelastic case is gotten by using the identity  $W_1(W^2, Q^2) = \int_{W_T^2}^{W_M^2} dS W_1(S, Q^2) \delta(S - W^2)$

where we have substituted  $W_1$  for  $G_1$ , and the limits of integration contain  $W^2$ . We then write

$$(C-7a) \quad W_1^S(\nu, Q^2) = \int_{W_T^2}^{W_M^2} dW^2 \{W_1(W^2, Q^2) I_1 + W_2(W^2, Q^2) I_2\}$$

$$(C-7b) \quad W_2^S(\nu, Q^2) = \int_{W_T^2}^{W_M^2} dW^2 W_2(W^2, Q^2) I_3$$

where

$$W^2 = (P_i + q)^2 = P_i^2 + 2 P_i \cdot q - Q^2$$

$$W_T^2 = (M + M\pi)^2 = \text{one pion threshold}$$

$$W_M^2 = (\sqrt{S_t} - M_s)^2 = \text{maximum producible hadronic mass off the interacting nucleon.}$$

We now have an identical formalism for handling quasi-elastic scattering and inelastic smearing. The convolution function  $I_1$ ,  $I_2$  and  $I_3$  are responsible for the quasi-elastic peak shape. One might find this formalism more attractive than previous methods since: 1) the limits of integration of the  $d \cos(\tilde{\theta}_s)$  integral and of the  $dW^2$  are physically simple to understand; and 2) the structure function is not buried inside two integral signs, and the smearing formalism now appears as a simple convolution integral over quasi-elastic peak shapes (of course if one chooses a mixed variable approach (Ref. C-2) you lose this simplicity).

We have chosen what A. Bodek (Ref. C-2) calls the "off shell kinematics" - "on shell dynamics" formalism. Stated plainly we use only  $W^2$  and  $Q^2$  to describe the photon-nucleon vertex. As the interacting nucleon is off its mass-shell, the structure functions could, in principle, depend on  $\nu$  of the photon as well. Using such a prescription that has an additional  $\nu$  dependence might suggest that the elastic form factors for off mass-shell nucleons would also have a  $\nu$  dependence thus resulting in a different  $Q^2$  dependence from free nucleons (the quasi-elastic case is fixed by requiring  $W^2 = M^2$ ). Experimentally this is probably impossible to resolve as any  $Q^2$  variation of the quasi-elastic cross section would be interpreted as information about  $G_E(N)$  and  $G_M(N)$ . There are simply too many undetermined functions. In any case, for the present, we adopt the prescription in which only  $W^2$  and  $Q^2$  figure in the dynamics at the nucleon photon vertex.

We can easily transform Eq. C-2a,b to a scaling form by defining

$$\omega \equiv 2M\nu/Q^2$$

$$\omega_W \equiv \frac{W^2 - M^2}{Q^2} + 1$$

Then, for example, Eq. C-7a becomes

$$(C-8) \quad W_1^S(\nu, Q^2) = \int_{\omega_T}^{\omega_M} d\omega_W Q^2 \{W_1(W^2, Q^2) I_1 + W_2(W^2, Q^2) I_2\}$$

where

$$\omega_{T,M} = \frac{W_{M,T}^2 - M^2}{Q^2} + 1$$

The principal contribution to  $W_1$  smearing comes from the

$I_1$  term in C-8. The quantity

$$(C-9) \quad \Gamma_\omega = Q^2 I_1(Q^2, \omega, \omega_W)$$

is shown by Fig. C-2 for various values of  $\omega$  versus the integration variable  $\omega_W$ . This quantity scales remarkably well (i.e., it is insensitive to  $Q^2$ ). *The width of the convolution function (Γ) has been found to scale in ω and is approximately 1ω.* It is also quite independent of  $\omega$  in its shape — all the curves in Fig. C-2 have approximately the same width independent of  $\omega$ . The insensitivity to  $Q^2$  of the convolution function reveals the "scaling" nature of smearing. Perhaps "scaling" always results when the impulse approximation is used. The convolution function  $\Gamma$  may also be expressed in terms of the scaling variable  $\omega'$ . A plot of  $\Gamma_\omega = Q^2 I_1(Q^2, \omega', \omega'_W)$  versus  $\omega'_W = W^2/Q^2 + 1$  for fixed  $\omega' = 2M\nu/Q^2 + M^2/Q^2$  shows that  $\Gamma_\omega$  scales even better in  $\omega'$  than it does in  $\omega$  (see Fig. C-2b, 2c and 2d).

In Fig. C-3, we show the convolution function expressed in terms of missing mass variables

$$\Gamma_W = 2W I_1(Q^2, W_i, W)$$

for various values of the input missing mass  $W_i^2 = M^2 + 2M\nu - Q^2$  versus  $W$ . These curves show the range in  $W$  and size of the convolution function over which the structure functions contribute. These curves are of course equivalent to the  $\omega$  curves in Fig. C-2 and dramatically show that  $\pm 0.2$  units of  $\omega$  can mean very different ranges in  $W$  depending on  $Q^2$ .

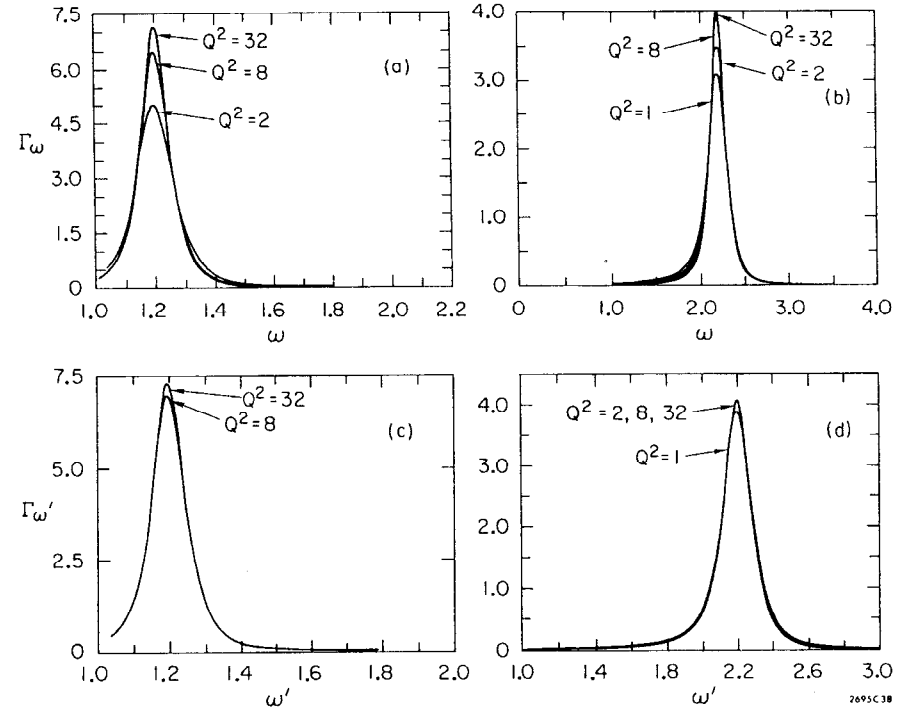


FIG. C-2

Graphs of the convolution function  $\Gamma_\omega$  for input ( $\omega'$ )'s of a) 1.2 and b) 2.2 for various values of  $Q^2$ .



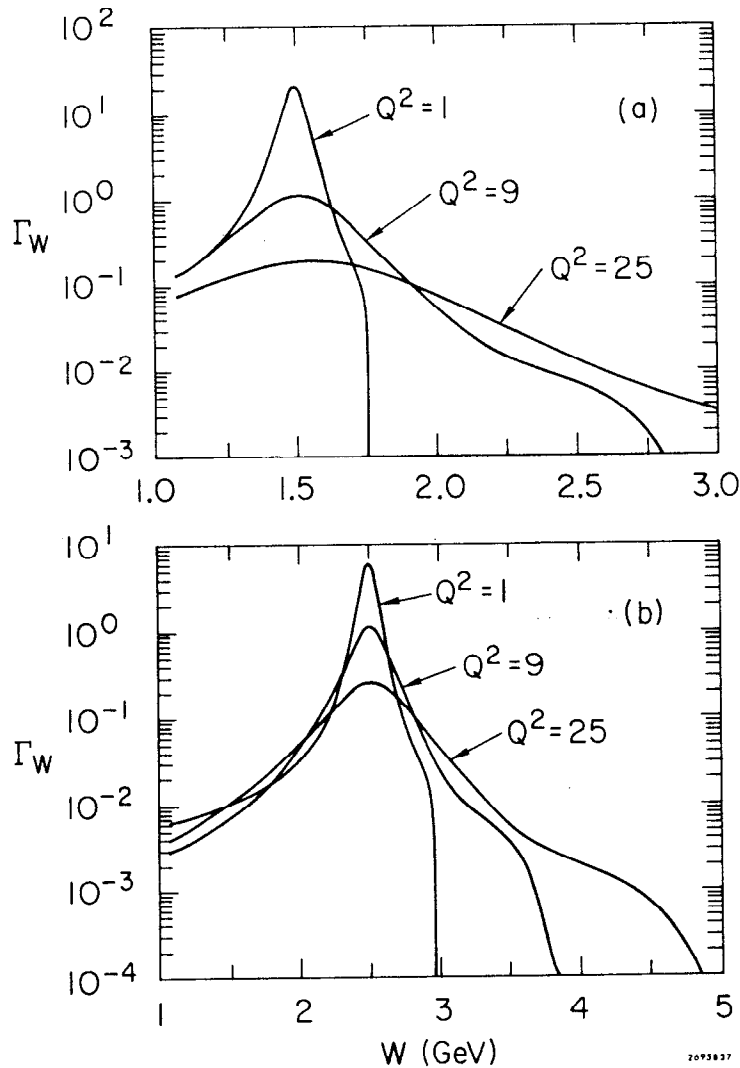


FIG. C-3  
The convolution function  $\Gamma_W$  for input  $W$ 's of a) 1.5 GeV and b) 2.5 GeV for various values of  $Q^2$ .

The  $\Gamma_W$  curves also demonstrate another interesting feature of smearing. As  $Q^2$  increases for fixed  $W$  any missing mass structure is more and more washed out. For example at  $Q^2 = 4 \text{ GeV}^2$  the resonances should be broader by a factor of approximately 2.

We have used the Reid hard core wave function to describe the spectator momentum within the deuteron. It is of some interest to find the region in  $|\vec{p}_s|$  which contributes to the smearing integrals. To do this, we revert back to the previous formalism (Ref. C-1) and define a  $\Gamma_{ps}$  by

$$W_1^S(\nu, Q^2) = \int_0^\infty dP_s \Gamma_{ps}(\nu, Q^2, P_s)$$

$\Gamma_{ps}$  involves the structure functions (as well as  $|\phi(P_s)|^2$  for which we have used

$$\nu W_2 = (1 - x')^3 (.6453 + 1.902(1 - x') - 2.343(1 - x')^2)$$

$$2M W_1 = \frac{\omega}{1+R} (1 + Q^2/\nu^2) \nu W_2$$

$$x' = \frac{1}{\omega'} = \frac{Q^2}{Q^2 + W^2}$$

and  $R = \sigma_s/\sigma_t = .18$ .

Fig. C-4 shows  $\Gamma_{ps}$  versus  $P_s$  for  $\omega = 2.2$  and  $Q^2$  values from 1-25  $\text{GeV}^2$ . The rapid fall off is caused by the wave function. The smearing functions at best linearly enhance the high  $p_s$  regions over which  $|\phi(P_s)|^2$  can contribute to smearing and these functions eventually fall to zero as physical final states can no longer be produced off such

virtual nucleons. This figure shows why the smearing formalism is so insensitive to various deuteron wave functions. Where the wave functions exhibit large differences (at large  $p_s$ ), little contribution to smearing occurs.

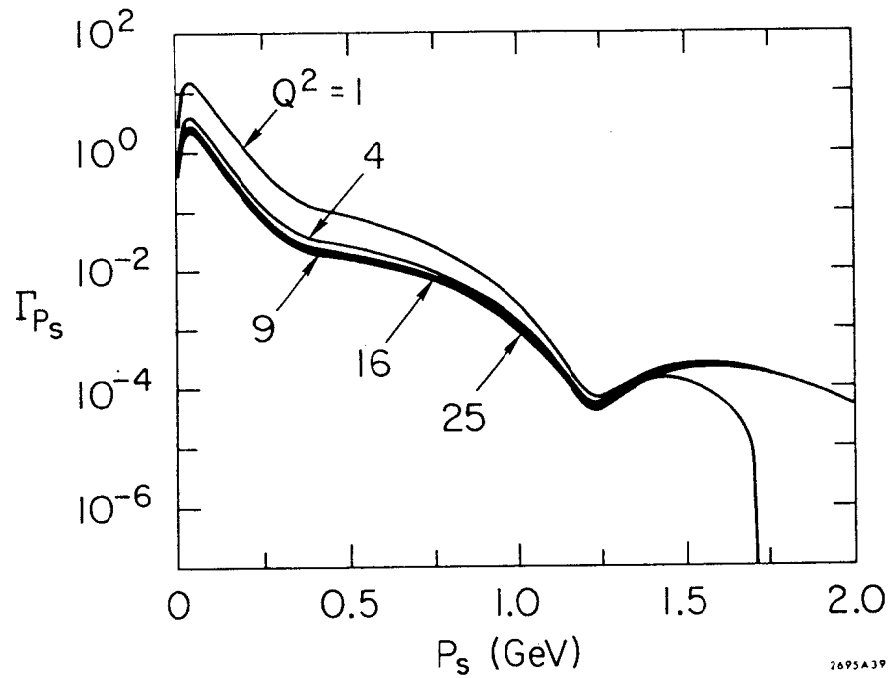


FIG. C-4

The function  $\Gamma_{P_s}$  shows where the contributions to smearing come from in the squared momentum wave function.

#### APPENDIX C - REFERENCES

1. G. B. West, Phys. Letters 37B, 509 (1971) and W. B. Atwood and G. B. West, Phys. Rev. 7D, 773 (1973).
2. A. Bodek, Ph.D. Thesis, MIT Laboratory for Nuclear Science Technical Report No. C00-3069-116.

#### APPENDIX D - WIRE ORBIT OF THE 1.6 GeV SPECTROMETER

The optical properties of the 1.6 GeV spectrometer were originally calculated using a Transport model (Ref. D-1) of the magnet. Optical coefficients were then measured by Group-F at SLAC using two techniques. Before the magnet was raised into its carriage and was lying horizontally on the End Station floor, the momentum dispersion and  $\phi$  angle focusing properties were measured using wire orbit techniques. With the magnet in place, the optics were again measured using the primary electron beam positioned and steered at the magnet entrance by magnets placed in the beam line of ESA. Both sets of measurements agreed with the values calculated from Transport to within their measured accuracy (Ref. D-2).

In 1970, the 1.6 suffered an accident. The magnet was left on without cooling water circulating through the coil. Subsequently, in 1971, two of the 144 turns in the coil shorted due to the poor condition of epoxy insulation. To "temporarily" fix the situation the two symmetric turns on the other half of the aperture were shorted. Remeasurements of elastic proton peaks showed no appreciable change in the optics.

At the end of data taking for E-89, Group-A decided to remeasure the optics coefficient and the limiting apertures in the 1.6 GeV spectrometer to confirm the values of the optics coefficient and solid angle of this instrument. To accomplish this measurement, we used wire orbit techniques.

An elementary analysis shows that a current carrying wire under tension will follow the trajectory of a charged particle through a magnetic field. The relationship between tension (resulting from a weight of mass M (kg) hung on the wire), current I (amps), and equivalent momentum pc(GeV) is

$$pc(\text{GeV}) = \frac{gc}{10^9} \frac{M(\text{kg})}{I(\text{amps})}$$

(The classical current flow is in the same direction as the momentum of a negatively charged particle). The measurements of the magnet were carried out by passing the current carrying wire through the magnet field and measuring the input and output trajectories of this wire "orbit." To achieve stable orbits in a magnet system that is focusing, the wire cannot be held at both foci but must be held inside at least one of the foci. The weight of the wire makes the tension in the wire depend on the mass of the wire as well as the weight, M, hung on it. This effect must be measured experimentally to make absolute calibrations between the magnet field strength and the momentum.

The coordinate systems used are shown in Fig. D-1. The laboratory coordinates (subscript l) are related to the input spectrometer coordinates (subscript i) by a 60° rotation about the Y<sub>l</sub> axis. The counter cave coordinates are rotated by 90° about the X<sub>i</sub> axis with respect to the input coordinates. This makes the Z axis roughly the direction of the flight path of particles as they traverse the magnet. The coordinates used by Group-F are

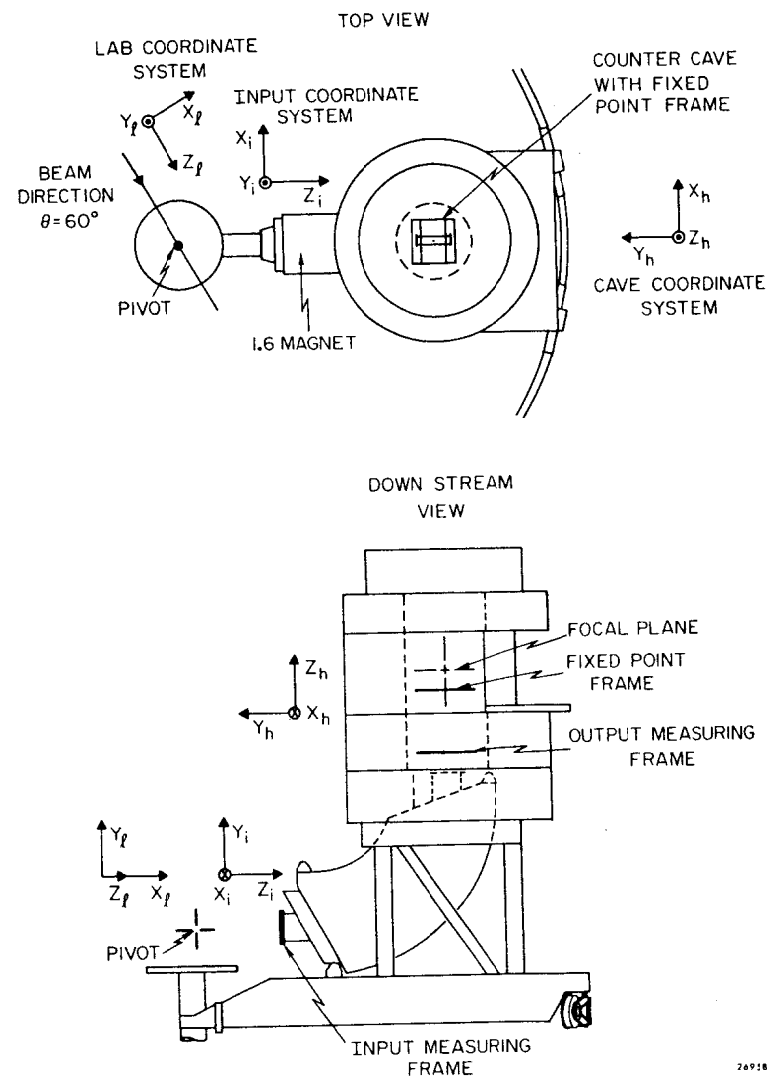


FIG. D-1

Definitions of the various co-ordinate systems used to describe the 1.6 GeV spectrometer optics.

different from the ones used here, and the correspondences are given in Table D-1.

The experimental setup used had an air bearing pulley positioned at the pivot on a travelling screw table allowing for positioning along the beam direction ( $Z_q$ ). The spectrometer was positioned at  $60^\circ$  with respect to the beam line. A phosphor-bronze wire (.010" dia.) was draped over the pulley with a weight hung on the side away from the spectrometer. The input trajectory of the wire was measured using an aluminum frame with sensing devices mounted on moveable arms. This frame was mounted on the magnet (see Fig. D-1) and was surveyed in place to an accuracy of  $\pm .010''$  with respect to the pivot.

Inside the counter cave, two more similar frames were mounted; one to hold the wire and the other to measure its position near the exit of the magnet. Both of these frames were aligned using the laser system (See Chapter II) and leveled.

The power supply for the wire was a precision current regulated supply, and the current in the wire was obtained by measuring the voltage drop across a .9835( $\pm .05\%$ ) ohm resistor (calibrated with a precision current source) with a digital voltmeter (DVM).

A four man team performed the measurements; two located at the pivot and two in the counter cave. The measuring frames had photo diode sensors to measure the wire position (without touching the wire) and were accurate to approximately  $\frac{1}{2}$  the wire diameter (.005"). When the wire triggered the photodiode sensor, an indicator lamp was

TABLE D - 1

COORDINATE SYSTEM CONVERSIONS FOR INPUT AND OUTPUT TRAJECTORIES

No.	Group-A	Group-F
1	-Y	X
2	$-\phi$	$\theta$
3	X	Y
4	$\theta$	$\phi$
5	Z	Z
6	$\delta$	$\delta$

Group-F input coordinates were subscripted with o, e.g.,

$(-Y_i |_A = X_o |_F)$  and the output coordinates had no subscript e.g.,  $(\phi_h |_A = \theta |_F)$ .

lit on each measuring frame, one in the counter cave and one at the pivot. This made it possible to measure both the input and the output trajectories simultaneously (we required that both indicator lamps be lit at the time of the measurement) without touching the wire at the measuring points. As the sensing devices only allowed a measurement in one direction, two such systems were made for measuring the X and the Y coordinates. Simultaneously with the Y coordinate measurement (corresponding to momentum and  $\phi$ ) the DVM reading of the shunt voltage for the current in the wire was recorded. The overall accuracy of this system was  $\pm .010''$  for all the coordinates and  $\pm .001$  volts for the DVM. The magnetic field strength was measured using an NMR (see Chapter II). A total of 167 orbits were measured at 1.00 GeV and 159 orbits at 1.68 GeV.

Different orbits were achieved by varying the current in the wire, the position of the air bearing pulley at the pivot, and the X and Y positions of the fixed point in the counter cave, a total of four variables. Measurements were made over the entire aperture and covered 7.0" of travel at the pivot,  $\pm 8\%$  changes in the current in the wire, and fixed positions in the counter cave corresponding to changes in  $\theta_i$  of  $\pm 20$  mrad and changes in  $\phi_i$  of  $\pm 80$  mrad.

The first task in the analysis was to establish a central orbit. To do this, the measured current, I, was fit to a function of  $X_i$ ,  $\theta_i$ ,  $\phi_i$ ,  $X_h$  and  $Y_h$ . We then selected  $X_i = Y_i = X_h = Y_h = 0$  and  $\theta_i = \phi_i = 0$  as defining the central orbit. From the fit we calculated the current in the wire,  $I_o$ , for this orbit. This was done for both values of magnet field for

which orbits were measured. For all the measured orbits, the deviation from the central momentum,  $\delta$ , was then calculated by

$$\delta = (P_o - P)/P_o = \frac{I - I_o}{I}$$

The absolute value of the tension in the wire doesn't enter into the determination of  $\delta$  if the tension remains constant for all orbits (different orbits can have different path lengths with different lengths of wire, thus changing the tension slightly due to the finite wire mass). The resistance of the shunt and the values of g and c also cancel in the determination of  $\delta$ .

Optics coefficients were determined by fitting coordinates of the input trajectories as functions of the coordinates of the output trajectories and vice-versa. Since we didn't vary the coordinates transverse to the beam direction,  $Y_\ell$  and  $X_\ell$ , the optics coefficients that depend on these coordinates are not determined. We assumed all optics coefficients involving these coordinates to be given by the calculated numbers in Ref. D-2. We found no significant differences in the optics coefficients between the high and the low momentum measurements, so we fit the optics coefficients to the combined data set. The optics coefficients through second order are given in Table D-2 for transforming input trajectories to output trajectories (i.e., lab. coordinates to hut coordinates). In Table D-3 the inverse fits are given using the three counter cave coordinates measured in E-89, namely  $X_h$ ,  $Y_h$  and  $\phi_h$ . One difference between these coefficients and Transport coefficients should be noted. As we have

TABLE D - 2

OPTICS COEFFICIENTS FOR THE 1.6 GeV SPECTROMETER

OFFSETS			
1	CORRECTED OFFSET#	C.76731E-01	
2	CORRECTED OFFSET#	0.11991E 02	
3	CORRECTED OFFSET#	0.14310E 00	
4	CORRECTED OFFSET#	0.40520E 00	

FIRST ORDER COEFFICIENTS					
1 1	-0.66100E 00	1 2	-0.54541E-02	1 3	-0.30558E-01
1 3	0.0	1 4	-0.13383E-01	1 5	0.0
2 1	-0.46100E 01	2 2	-0.15295E 01	2 3	-0.35858E-01
2 4	-0.11458E-01	2 5	0.0	2 6	0.65220E 01
3 1	0.0	3 2	-0.55978E-02	3 3	0.23352E-01
3 4	0.81439E 00	3 5	0.0	3 6	0.87498E-02
4 1	0.0	4 2	-0.97021E-02	4 3	-0.11853E 01
4 4	0.13401E 01	4 5	0.0	4 6	0.15554E-01
5 1	-0.15090E 01	5 2	-0.63000E 00	5 3	0.0
5 4	0.0	5 5	0.10000E 01	5 6	-0.14600E 01
6 1	0.0	6 2	0.0	6 3	0.0
6 4	0.0	6 5	0.0	6 6	0.10000E 01

SECOND ORDER COEFFICIENTS					
1 11	-0.64100E-03	1 22	-0.21389E-03	1 33	-0.44978E-02
1 13	0.0	1 23	0.35629E-03	1 34	-0.93230E-03
1 14	0.0	1 24	0.39720E-04	1 35	0.0
1 15	0.0	1 25	0.0	1 36	-0.19655E-02
1 16	0.11410E-01	1 26	-0.42816E-03	1 36	-0.19655E-02
2 11	0.18000E-01	2 22	-0.10913E-02	2 33	-0.35632E-01
2 12	0.41300E-02	2 23	0.11672E-02	2 34	-0.99902E-02
2 13	0.0	2 24	0.19579E-03	2 35	0.0
2 14	0.0	2 25	0.0	2 36	-0.30677E-04
2 15	0.0	2 26	-0.32404E-01	2 44	0.15055E-02
2 16	-0.21290E-01	2 26	-0.32404E-01	2 45	0.0
3 11	0.0	3 22	-0.40593E-04	3 33	-0.23377E-02
3 12	0.0	3 23	0.22451E-02	3 34	-0.16642E-02
3 13	0.29730E-01	3 24	0.17625E-03	3 35	0.0
3 14	0.53320E-02	3 25	0.0	3 36	0.11624E-01
3 15	0.0	3 26	-0.36688E-03	3 44	-0.38987E-03
3 16	0.0	3 26	-0.36688E-03	3 45	0.0
4 11	0.0	4 22	-0.14931E-03	4 33	-0.51896E-02
4 12	0.0	4 23	0.37188E-02	4 34	-0.37111E-02
4 13	0.57705E-01	4 24	0.46000E-03	4 35	0.0
4 14	0.79293E-02	4 25	0.0	4 36	0.31917E-01
4 15	0.0	4 26	-0.37454E-03	4 44	-0.85559E-03
4 16	0.0	4 26	-0.37454E-03	4 45	0.0
5 11	0.29600E-02	5 22	-0.58000E-03	5 33	-0.10300E-01
5 12	-0.17100E-03	5 23	0.0	5 34	-0.37600E-02
5 13	0.0	5 24	0.0	5 44	-0.85440E-03
5 14	0.0	5 25	0.0	5 45	0.0
5 15	0.0	5 26	-0.39570E-03	5 55	0.0
5 16	0.41100E-02	5 26	-0.39570E-03	5 56	0.0
6 11	0.0	6 22	0.0	6 33	0.0
6 12	0.0	6 23	0.0	6 34	0.0
6 13	0.0	6 24	0.0	6 35	0.0
6 14	0.0	6 25	0.0	6 36	0.0
6 15	0.0	6 26	0.0	6 44	0.0
6 16	0.0	6 26	0.0	6 45	0.0
6 16	0.0	6 26	0.0	6 46	0.0
6 66	0.0			6 55	0.0
6 66	0.0			6 56	0.0

$$x_{hi}^o = x_i^o + \sum_{j=1}^6 C_{ij}^1 x_{lj} + \sum_{j,k=1}^6 C_{ijk}^2 x_{lj} x_{lk}$$

where

$x_{hi}^o$  are the hut coordinates

$x_{li}$  are the laboratory (input) coordinates

$x_i^o$  are the offsets

$C_{ij}^1$  are the first order coefficients

and

$C_{ijk}^2$  are the second order coefficients

TABLE D - 3

INPUT COORDINATES AS FUNCTIONS OF OUTPUT

COORDINATES  $x_h, Y_h$  AND  $\phi_h$

OFFSETS			
2	7.3070E00		
4	-.25683E-01		
6	.28116E-01		

FIRST ORDER			
2 1	.99721E00	4 1	.80756E-02
2 2	-.65255E00	4 2	-.45699E-02
2 3	.32008E-02	4 3	1.2193E00
6 1	.24608E00	6 1	.24608E00
6 2	-.12124E-02	6 2	-.12124E-02
6 3	.27510E-02	6 3	.27510E-02

SECOND ORDER			
2 11	-.95704E-02	2 22	-.21912E-03
2 12	.38169E-02	2 23	-.15397E-03
2 13	-.82572E-04	2 33	.22228E-02
4 11	-.45948E-04	4 22	.27021E-04
4 12	-.94906E-04	4 23	.23560E-03
4 13	-.43377E-02	4 33	-.38951E-03
6 11	.84475E-03	6 22	.20106E-04
6 12	-.71581E-04	6 23	.56203E-05
6 13	.10472E-03	6 33	.12579E-03

$$x_{li} = x_{hi}^o + \sum_{j=1}^3 \tilde{C}_{ij}^1 x_{hj} + \sum_{k,j=1}^3 \tilde{C}_{ijk}^2 x_{hj} x_{hk}$$

where

$x_{li}$  are the laboratory (input) coordinates

$x_{hi}^o$  are the counter cave coordinates

$x_i^o$  are the offsets

$\tilde{C}_{ij}^1$  are the first order coefficients

$\tilde{C}_{ijk}^2$  are the second order coefficients

TABLE D - 4

COEFFICIENT ERROR ESTIMATES FOR 40 TRIALS FOR  
OFFSETS AND FIRST ORDER COEFFICIENTS

made a physical measurement on a real magnet, we have chosen a specific, fixed coordinate system. This procedure can introduce non-zero constants (offsets) into the fits.

To estimate the error in our numbers, we randomized the measurements within the measured accuracy of  $\pm .010''$  for the coordinates and  $\pm .001$  volts in the DVM and repeated the fitting procedure many times. The RMS deviations calculated from 40 such trials for the important first order coefficients are given in Table D-4. The residuals of the fits for some of the important first order coefficients are histogrammed in Fig. D-2. Also shown in Fig. D-2 are the hodoscope bin widths used in E-89.

The fits were calculated only through second order in the input (output) coordinates. We tested the self consistency and the resolution of this system (the hodoscope bin widths and the forward and backward spectrometer optical models) by Monte Carlo techniques. In Fig. D-3 we show the difference between the reconstructed coordinates and their starting values. We calculate from these the following resolutions (RMS deviations):  $\phi \pm 5.08$  mrad,  $\theta \pm 1.16$  mrad, and  $\delta \pm .23\%$ . These are comparable to the RMS deviations of the residuals shown in Fig. D-2. Since the coefficients are those of finite Taylor expansions about our chosen central ray, second order coefficients will fail to describe significant third or higher order effects away from the central orbit. The spread in the residuals in Fig. D-2 is thought not to be caused by measurement error but by the use of

## OUTPUT AS FUNCTIONS OF INPUT

## OFFSETS

1	.0191	2	.0543	3	.0137	4	.0468
---	-------	---	-------	---	-------	---	-------

## FIRST ORDER

1	2	.431E-3	2	2	.126E-2	3	2	.257E-3	4	2	.861E-3
1	3	.176E-2	2	3	.417E-2	3	3	.126E-2	4	3	.463E-2
1	4	.839E-3	2	4	.234E-2	3	4	.523E-3	4	4	.172E-2
1	6	.300E-2	2	6	.645E-2	3	6	.196E-2	4	6	.618E-2

## INPUT AS FUNCTIONS OF OUTPUT

## OFFSETS

2	.230E-1	4	.135E-1	6	.475E-2
---	---------	---	---------	---	---------

## FIRST ORDER

2	1	.618E-3	4	1	.693E-3	6	1	.195E-3
2	2	.243E-3	4	2	.175E-3	6	2	.563E-4
2	3	.959E-3	4	3	.633E-3	6	3	.218E-3



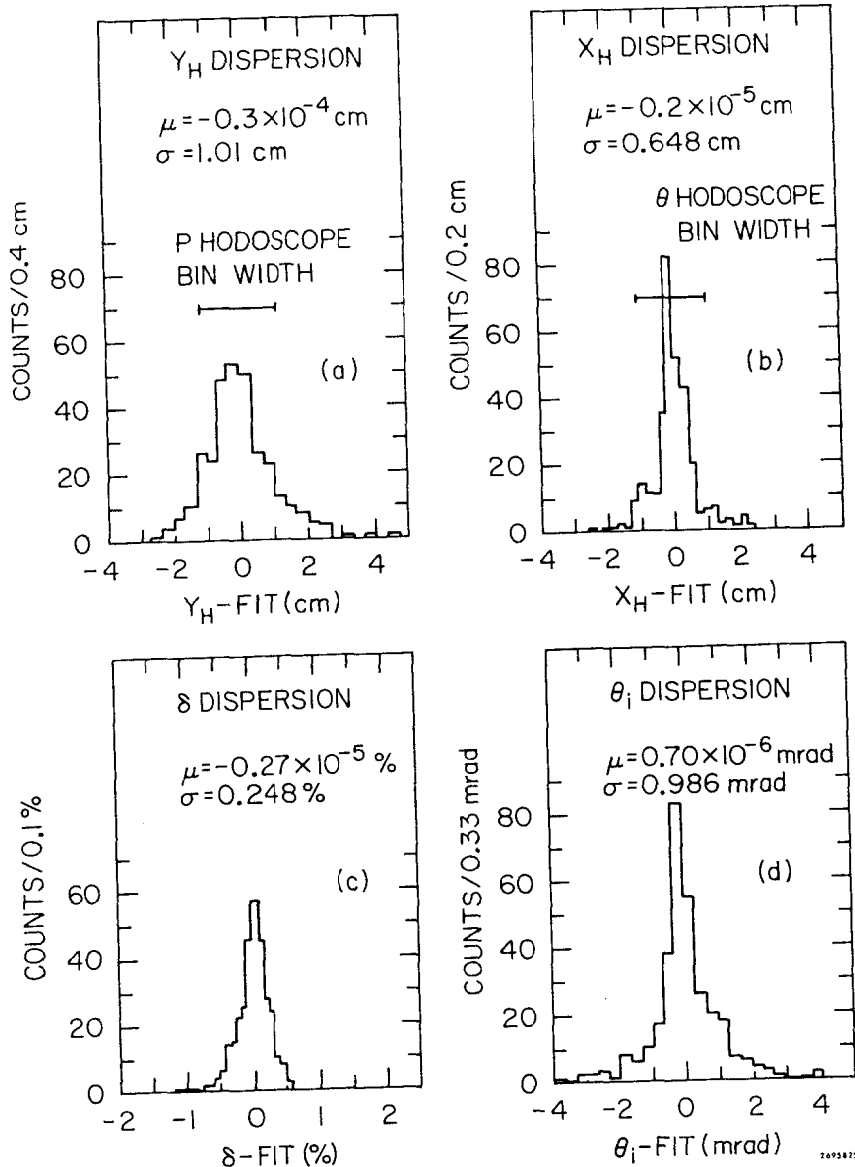


FIG. D-2

Histograms of the residuals for the fits to the optics coefficients. The mean,  $\mu$ , and RMS deviations,  $\sigma$ , of each histogram is shown.

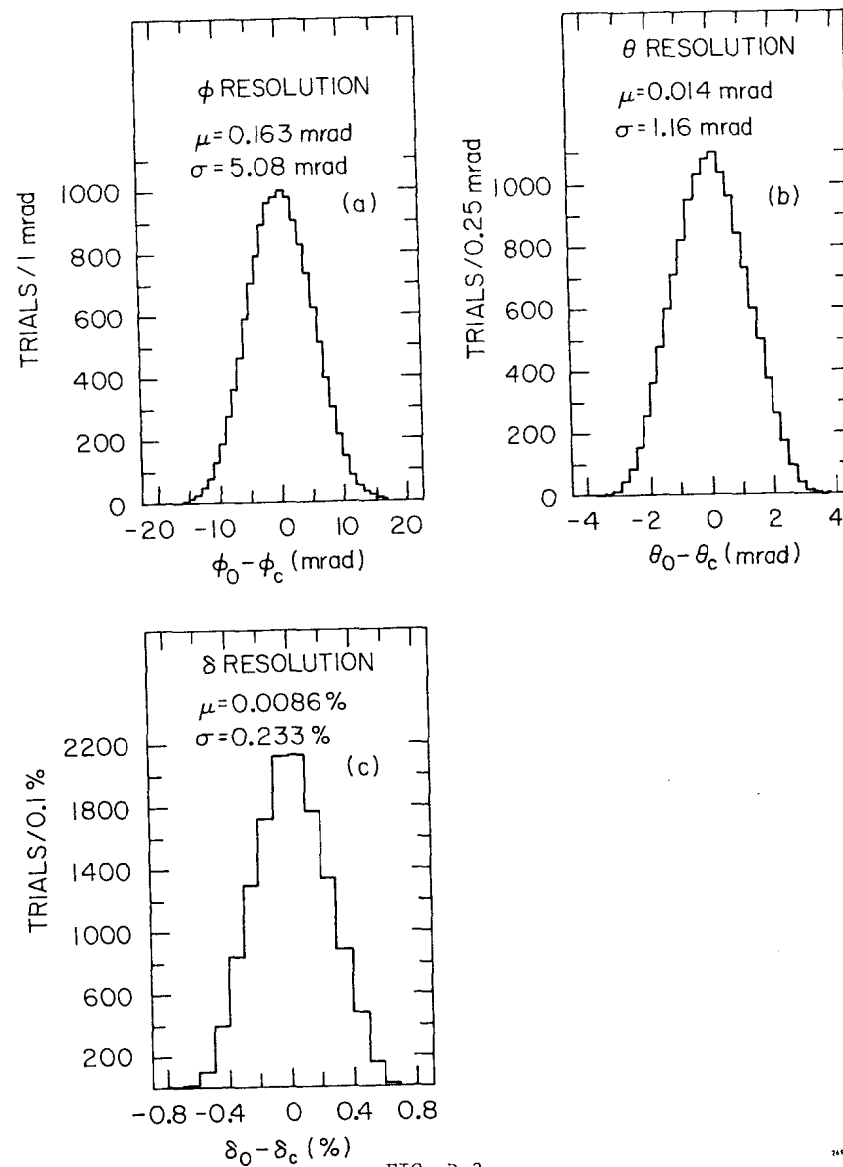


FIG. D-3

Calculated resolutions of the optics for the 1.6 using the fitted optics coefficients and hodoscope bin widths.

a finite Taylor expansion to approximate the optical properties of the 1.6-GeV spectrometer.

The improvement made in the resolution of the 1.6 is marginal using our new fits over that obtained from the previous measurements. The only place where differences were noticed was for the elastic peaks. The resolution in missing mass improved about 10% over that obtained using the simple first order prescription of the original Group-F coefficients. The resolutions of the hodoscope bin widths used for E-89 are comparable to the resolution gotten with the second order optics coefficients. Further refinements of the optics (such as third order coefficients) are unnecessary for our present purposes.

To test the absolute quality of the measurements, we changed the weight and current in the wire while keeping the ratio fixed for several orbits with the spectrometer set for approximately 1 GeV. The weights used ranged from .401 kg to .772 kg. For all these orbits the ratio of the current in the wire to the weight on it was held approximately constant. From the measured orbits we calculated  $\delta$  using the coordinates measured in the cave and corrected each orbit for slight missettings of the ratio, M/I. The central momentum was calculated using

$$P_o^c = \frac{gc}{10^9} \frac{M(\text{kg})}{I(\text{amps})} \frac{1}{(1+\delta)}$$

(the range of  $\delta$  was  $-.0067 < \delta < -.0052$ )

In Fig. D-4 we have plotted the calculated  $P_o^c$  (GeV) versus the reciprocal of the tension (1/Mg). We have used the values of .98062 m/sec<sup>2</sup> for g and  $2.9979 \times 10^9$  m/sec for the speed of light, c. The error bars indicate the full spread of the data measured using a particular weight. A straight line extrapolated to 1/Mg = 0 gives an absolute calibration of magnetic field strength in momentum for the central ray. We find this to be .9984 GeV. The NMR frequency, measured with a deuterium probe, was 8.6905 MHz corresponding to a field strength of 13.30 kgauss. This calibration was compared to that obtained from the position of the elastic peaks in missing mass. The elastic peak calibration predicts a momentum of .9981 GeV for this NMR frequency ( $P_o^c$  (MeV) =  $17.63 \times 6.51436 \times f_{\text{NMR}}$  (MHZ)). This fortuitous agreement between the wire float calibration and the elastic peak calibration should be taken with a grain of salt as the magnet power supply current regulation was only  $\pm .03\%$ .

The limiting apertures in the 1.6-GeV spectrometer were measured using the wire orbits. The volume of phase space accepted by the spectrometer relevant to E-89 is shown in Fig. D-5 with the various limiting apertures denoted on the drawing. The limiting aperture measurements showed the largest differences between the high and the low momentum data, and the data are plotted in Fig. D-5. The solid line is the Monte Carlo results for the optics coefficients fit to the combined data set. The difference in the solid angle between the high and the low momentum measurements was calculated to be approximately .5%. We take the uncertainty in our solid angle

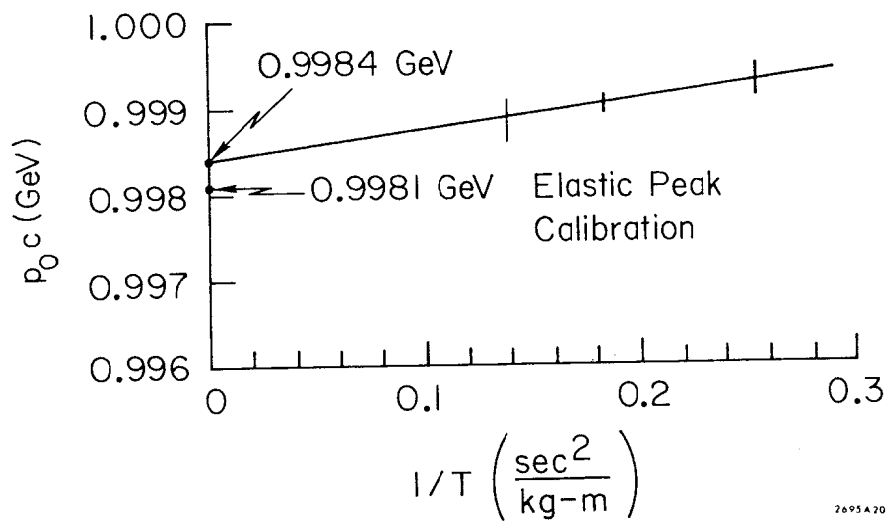


FIG. D-4

Calculated values of  $p_{0c}$  for various values of (1/tension).

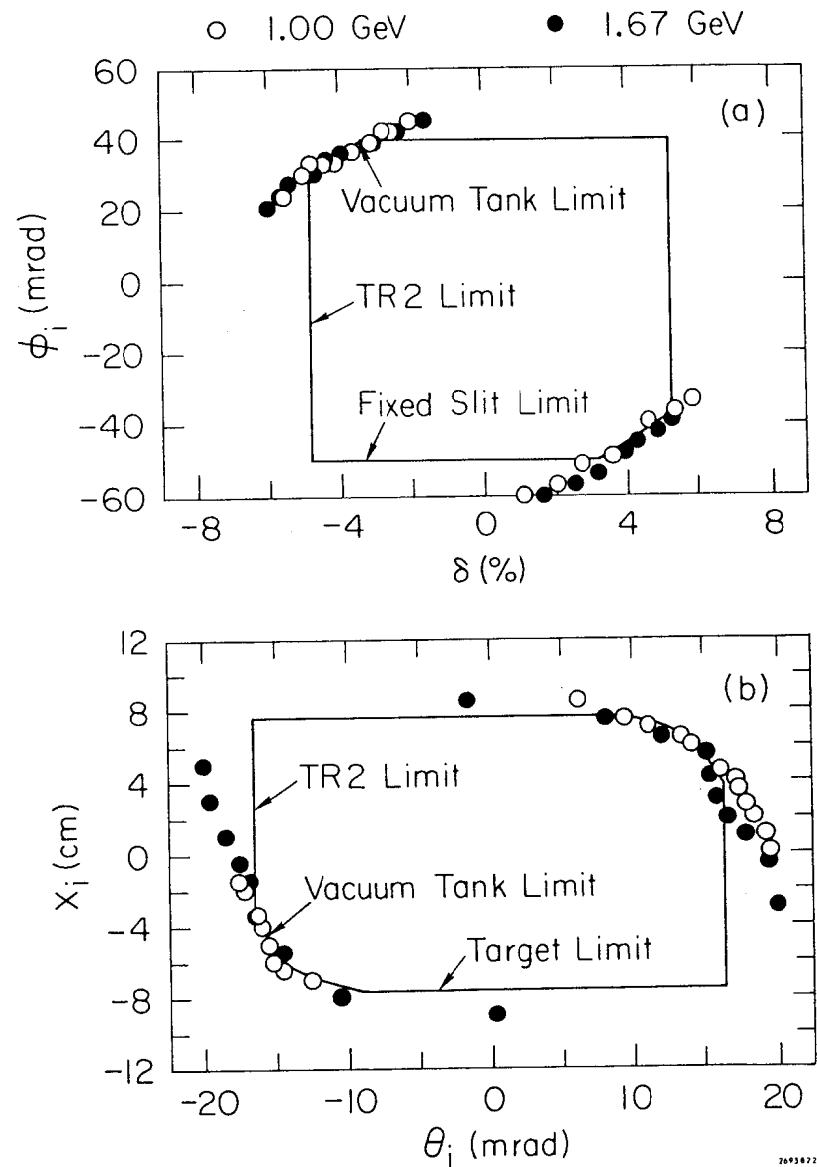


FIG. D-5

The limiting apertures of the 1.6 GeV spectrometer for a)  $\phi_i$  (vertical projected scattering angle) versus  $\delta$  (deviation in momentum from the central ray), b)  $X_i$  (target length) versus  $\theta_i$  (horizontal projected scattering angle).

determination to be  $\pm 1.0\%$ . The solid angle subtended by our counter package was limited by the TR2 counter. Averaged over a 17.7 cm target the solid angle was calculated by Monte Carlo techniques to be 2.904 msr - 10% ( $\Delta p/p$ ) at  $60^\circ$  and 2.955 msr - 10% ( $\Delta p/p$ ) at  $50^\circ$ . The contribution to the TR2 solid angle from each  $p-\theta$  bin was calculated, and these were applied to the data on a bin-by-bin basis.

#### APPENDIX D - REFERENCES

1. K. Brown, SLAC Report No. 75, 1967.
2. R. Anderson et al., Nuclear Instr. and Methods 66, 328 (1968).